INFORMATION TO USERS

This manuscript has been reproduced from the microfilm master. UMI films the text directly from the original or copy submitted. Thus, some thesis and dissertation copies are in typewriter face, while others may be from any type of computer printer.

The quality of this reproduction is dependent upon the quality of the copy submitted. Broken or indistinct print, colored or poor quality illustrations and photographs, print bleedthrough, substandard margins, and improper alignment can adversely affect reproduction.

In the unlikely event that the author did not send UMI a complete manuscript and there are missing pages, these will be noted. Also, if unauthorized copyright material had to be removed, a note will indicate the deletion.

Oversize materials (e.g., maps, drawings, charts) are reproduced by sectioning the original, beginning at the upper left-hand corner and continuing from left to right in equal sections with small overlaps.

Photographs included in the original manuscript have been reproduced xerographically in this copy. Higher quality 6" x 9" black and white photographic prints are available for any photographs or illustrations appearing in this copy for an additional charge. Contact UMI directly to order.

Bell & Howell Information and Learning
300 North Zeeb Road, Ann Arbor, MI 48106-1346 USA
800-521-0600

Fluid Dynamics of the Shock Wave Reactor

Robert K. Masse

A dissertation submitted in partial fulfillment of the requirements for the degree of

Doctor of Philosophy

University of Washington

2000

Program Authorized to Offer Degree: Aeronautics and Astronautics

In presenting this thesis in partial fulfillment of the requirements for the Doctoral degree at the University of Washington, I agree that the Library shall make its copies freely available for inspection. I further agree that extensive copying of the dissertation is allowable only for scholarly purposes, consistent with "fair use" as prescribed in the U.S. Copyright Law. Requests for copying or reproduction of this dissertation may be referred to University Microfilms, 1490 Eisenhower Place, P.O. Box 975, Ann Arbor, MI 48106, to whom the author has granted "the right to reproduce and sell (a) copies of the manuscript in microform and/or (b) printed copies of the manuscript made from microform."

Signature 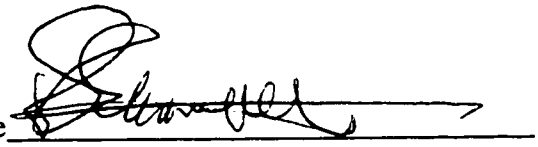

Date 3/8/00

University of Washington
Graduate School

This is to certify that I have examined this copy of a doctoral dissertation by

Robert K. Masse

And have found that it is complete and satisfactory in all respects,
and that any and all revisions required by the final
examining committee have been made.

Chair of Supervisory Committee:

David A. Russell

Reading Committee:

Abraham Hertzberg

Arthur T. Mattick

David A. Russell

Date: 3/8/00

University of Washington

Abstract

Fluid Dynamics of the Shock Wave Reactor

Robert K. Masse

Chairperson of the Supervisory Committee:
Professor David A. Russell
Aeronautics and Astronautics

High commercial incentives have driven conventional olefin production technologies to near their material limits, leaving the possibility of further efficiency improvements only in the development of entirely new techniques. One strategy known as the Shock Wave Reactor, which employs gas dynamic processes to circumvent limitations of conventional reactors, has been demonstrated effective at the University of Washington. Preheated hydrocarbon feedstock and a high enthalpy carrier gas (steam) are supersonically mixed at a temperature below that required for thermal cracking. Temperature recovery is then effected via shock recompression to initiate pyrolysis. The evolution to proof-of-concept and analysis of experiments employing ethane and propane feedstocks are presented.

The Shock Wave Reactor's high enthalpy steam and ethane flows severely limit diagnostic capability in the proof-of-concept experiment. Thus, a preliminary blow down supersonic air tunnel of similar geometry has been constructed to investigate recompression stability and (especially) rapid supersonic mixing necessary for successful operation of the Shock Wave Reactor. The mixing capabilities of blade nozzle arrays are therefore studied in the air experiment and compared with analytical models. Mixing is visualized through Schlieren imaging and direct photography of condensation in carbon dioxide injection, and interpretation of visual data is supported by pressure measurement and flow sampling. The influence of convective Mach number is addressed. Additionally, thermal behavior of a blade nozzle array is analyzed for comparison to data obtained in the course of succeeding proof-of-concept experiments.

Proof-of-concept is naturally succeeded by interest in industrial adaptation of the Shock Wave Reactor, particularly with regard to issues involving the scaling and refinement of the shock recompression. Hence, an additional, variable geometry air tunnel has been constructed to study the parameter dependence of shock recompression in ducts. Distinct variation of the flow Reynolds and Mach numbers and section height allow unique mapping of each of these parameter dependencies. Agreement with a new one-dimensional model is demonstrated, predicting an exponential pressure profile characterized by two key parameters, the maximum pressure recovery and a characteristic length scale. Transition from one to two-dimensional dependence of the length parameter is observed as the duct aspect ratio varies significantly from unity.

TABLE OF CONTENTS

LIST OF FIGURES

LIST OF TABLES

LIST OF SYMBOLS

Chapter 1

T_1 Mixed gas temperature upstream of shock

T_2 Mixed gas temperature downstream of shock

T_{oc} Carrier gas initial temperature

T_{of} Feedstock gas initial temperature

Chapter 2

a_1 Sound speed of faster stream in shear layer pair

a_2 Sound speed of slower stream in shear layer pair

$a_{compr.}$ Freestream speed of sound (compressible case)

A_1 Area of faster stream in shear layer pair

A_1' Area of stream exiting shear layer mixing stage adjacent to faster entering stream

A_2 Area of slower stream in shear layer pair

A_2' Area of stream exiting shear layer mixing stage adjacent to slower entering stream

$A/A^*|_f$ Feedstock nozzle exit-to-throat area ratio

$A/A^*|_p$ Plenum nozzle exit-to-throat area ratio

A_e Nozzle exit area

A_f Control volume exit area

$\mathbf{AR}_{inlet}$ Blade nozzle array inlet aspect ratio: $\mathbf{AR}_{inlet} \equiv H/W$

$\mathbf{AR}_{throat}$ Blade internal nozzle throat aspect ratio: $\mathbf{AR}_{throat} \equiv H/h_f^*$

A_u Entering stream area of shear layer mixing stage adjacent to unmixed exiting stream

A_u' Area of unmixed stream exiting shear layer mixing stage

d Nozzle spacing

d^* Nozzle throat height

F_{Ci} Convective Mach number factor for mixing stage i

h_f Feed nozzle exit height

h_f^* Feed nozzle throat height

h_t Transverse dimension of smallest entering stream for mixing stage i

h_p Plenum nozzle exit height

h_p^* Plenum nozzle throat height

h_t Total enthalpy

h_{t1}' Exit total enthalpy of shear layer mixing stage adjacent to faster stream

h_{t2}' Exit total enthalpy of shear layer mixing stage adjacent to slower stream

h_{te}	Total enthalpy of flow exiting nozzle
h_{tf}	Total enthalpy of flow exiting control volume
H	Blade span
$\dot{H}_{t1}$	Total enthalpy flux of faster stream in shear layer pair
$\dot{H}_{t2}$	Total enthalpy flux of slower stream in shear layer pair
$\dot{H}_{tu}$	Upstream Total Enthalpy flux of shear layer mixing stage adjacent to unmixed exiting stream
K	Defined compressibility parameter: $[K \equiv 2+(\gamma-1)\, M_{\theta e}{}^2]/M_{\theta e}{}^2$
K_A	Blade geometric feed parameter
L_D	Dimotakis mixing length
L_{mix}	Total mixing length
$\dot{m}_1$	Mass flow rate of faster stream in shear layer pair
$\dot{m}_1'$	Exit mass flow rate of shear layer mixing stage adjacent to faster entering stream
$\dot{m}_2$	Mass flow rate of slower stream in shear layer pair
$\dot{m}_2'$	Exit mass flow rate of shear layer mixing stage adjacent to slower entering stream
$\dot{m}_u$	Entering mass flow rate of shear layer mixing stage adjacent to unmixed exiting stream
$\dot{m}_u'$	Mass flow rate of unmixed exiting stream of shear layer mixing stage
M	Mach number
M_{c1}	Convective Mach number of faster stream in shear layer pair
M_{c2}	Convective Mach number of slower stream in shear layer pair
M_e	Mach number of flow exiting nozzle
M_f	Mach number of flow exiting control volume
M_f	Feedstock Mach number
M_f	Feedstock nozzle exit Mach number
M_{in}	Blade feed Mach number
M_p	Plenum nozzle exit Mach number
$(M.W.)_f$	Feedstock molecular weight
$(M.W.)_p$	Plenum gas molecular weight
$M_{\theta e}$	Eddie edge Mach number, nozzle feed Mach number
n_f	Total number of feedstock throats
n_{max}	Maximum allowable number of blades
n_p	Total number of plenum throats
p	Pressure
p_1	Pressure of faster stream in shear layer pair
p_1'	Exit pressure of shear layer mixing stage adjacent to faster entering stream
p_2	Pressure of slower stream in shear layer pair
p_2'	Exit pressure of shear layer mixing stage adjacent to slower entering stream

p_{Air}	Air feed pressure
p_b	Nozzle exit base area
p_{CO_2}	CO_2 feed pressure
p_e	Pressure of flow exiting nozzle
p_f	Pressure of flow exiting control volume, feed nozzle exit pressure
p_{He}	Helium feed pressure
p_{in}	Blade feed pressure
p_o	Freestream pressure
p_p	Plenum nozzle exit pressure
p_{te}	Total pressure of flow exiting nozzle
p_{tf}	Total pressure of flow exiting control volume, feed total pressure
p_{tp}	Plenum total pressure
p_u	Entering stream pressure of shear layer mixing stage adjacent to unmixed exiting stream
p_u'	Pressure of unmixed exiting stream of shear layer mixing stage
Δp	Maximum pressure drop across blade span
$\dot{Q}_1$	Momentum flux of faster stream in shear layer pair
$\dot{Q}_2$	Momentum flux of slower stream in shear layer pair
$\dot{Q}_u$	Upstream Momentum flux of shear layer mixing stage adjacent to unmixed exiting stream
r	Radial coordinate
R	Eddy radius
$\mathcal{R}$	Ideal gas constant
T_e	Temperature of flow exiting nozzle
T_f	Temperature of flow exiting control volume
T_{te}	Total temperature of flow exiting nozzle
T_{tf}	Total temperature of flow exiting control volume, feed flow total temperature
T_{tp}	Plenum flow total temperature
T_w	Wall temperature
u_θ	Tangential flow velocity
U	Velocity
U'	Exit velocity of simple shear layer mixing
U_1	Velocity of faster stream in shear layer pair
U_1'	Exit velocity of shear layer mixing stage adjacent to faster entering stream
U_2	Velocity of slower stream in shear layer pair
U_2'	Exit velocity of shear layer mixing stage adjacent to slower entering stream
U_c	Convective speed
U_e	Velocity of flow exiting nozzle

U_f	Velocity of flow exiting control volume, feed nozzle exit flow velocity
U_p	Plenum nozzle exit flow velocity
U_u'	Velocity of unmixed exiting stream of shear layer mixing stage
U_v	Blade spanwise internal flow velocity
U_θ	Tangential flow velocity at eddy edge
ΔU	Velocity difference across shear layer: $\Delta U \equiv U_1 - U_2$
w	Blade width
W	Total blade nozzle array inlet width
x	Distance downstream of origin of mixing
y	Normal distance from wall
α	Nozzle wall divergence angle
β	Generalized geometric parameter
γ	Ratio of specific heats
γ_1	Specific heat ratio of faster stream in shear layer pair
γ_2	Specific heat ratio of slower stream in shear layer pair
γ_f	Feedstock specific heat ratio
γ_p	Plenum specific heat ratio
δ	Mixed fluid layer thickness
δ^*	Boundary layer displacement thickness
Δ	Generalized geometric parameter
ϵ	Boundary layer energy thickness
ϵ^*	Boundary layer enthalpy: $\epsilon^* \equiv \delta^* + \epsilon$
θ	Boundary-layer momentum thickness
θ^*	Alternate boundary layer momentum thickness: $\theta^* \equiv \delta^* + \theta$
λ	Generalized geometric parameter
ρ	Density
ρ'	Exit density of simple shear layer mixing
ρ_1	Density of faster stream in shear layer pair
ρ_1'	Exit density of shear layer mixing stage adjacent to faster stream
ρ_2	Density of slower stream in shear layer pair
ρ_2'	Exit density of shear layer mixing stage adjacent to slower stream
ρ_c	Density at center of solid body eddy with $M_{\theta e} = M_c$
ρ_e	Density of flow exiting nozzle
ρ_f	Density of flow exiting control volume
ρ_o	Freestream density
σ	Mean-square standard deviation for flow samples

ϕ Plenum-to-feed mass flow rate ratio

Chapter 3

A Area

A_p Blade area wetted by plenum flow

C_{pf} Feedstock constant pressure specific heat

C_{vw} Blade wall specific heat

h Mixing section height

$(hA)_f$ Coefficient of total heat transfer over blade area wetted by feed flow

$(hA)_f^*$ Effective coefficient of total heat transfer over blade area wetted by feed flow

$(hA)_p$ Coefficient of total heat transfer over blade area wetted by plenum flow

$(h\hat{A})_p$ Coefficient of total heat transfer over blade area per unit span wetted by plenum flow

h_f Heat transfer coefficient from feed flow to nozzle blade

h_p Heat transfer coefficient from plenum flow to nozzle blade

$\hat{m}_w$ Mass per unit span of blade wall

$\dot{m}_f$ Feed mass flow rate

$\dot{m}_{feed}$ Feed mass flow rate (alternate notation used for clarification)

$\dot{m}_{steam}$ Steam mass flow rate

m_w Mass of blade wall

M Mach number

$(M.W.)$ Molecular weight

N Mole number

$N_{C_2H_6}$ C_2H_6 mole number

$\dot{N}_{C_2H_6}$ Reaction rate constant for breakup of C_2H_6 into CH_3 radicals

p pressure

Pr Prandtl number

$\dot{Q}$ Heat transfer per unit time

$\mathcal{R}$ Ideal gas constant

$\mathcal{R}_{mix}$ Ideal gas constant of mixture

t Time

t_o Initial time

T temperature

$T_{crit.}$ Temperature to initiate pyrolysis

T_p Plenum flow temperature

T_r Recovery temperature

T_t Total temperature

T_{tf} Feed flow total temperature

T_{tfe} Feed flow total temperature exiting blade nozzle

T_{tfo} Feed flow total temperature entering blade nozzle

T_{to} Initial total temperature

T_{tp} Plenum flow total temperature

T_w Blade wall temperature

T_w^* Equilibrium blade wall temperature

T_{wo} Initial blade wall temperature

ΔT_{tf} Change in feed flow total temperature from blade nozzle inlet to exit: $\Delta T_{tf} \equiv T_{tfe} - T_{tfo}$

$(\Delta T_{tf})_{max}$ Maximum possible change in feed flow total temperature: $\Delta T_{tf} \equiv T_w - T_{tfo}$

x Distance downstream of nozzle exit plane

β Area-averaged recovery factor

γ Ratio of specific heats

γ_{mix} Ratio of specific heats for mixture

τ Blade wall heating characteristic time constant

Chapter 4

a_1 Speed of sound in freestream flow

a_{t1} Stagnation speed of sound in freestream flow

A Channel cross-sectional area

A^* Throat area

b Transformation parameter: $b \equiv (\mu/\mu_{t1})/(T/T_{t1})$

D Hydraulic diameter

h Enthalpy, test section height

h_e^* Effective channel height downstream of recompression: $h_e^* \equiv 1 - 2\theta_e^*$

h_o^* Effective channel height upstream of recompression: $h_o^* \equiv 1 - 2\theta_o^*$

h_{t1} Freestream flow total enthalpy

h_{te} Freestream flow total enthalpy downstream of recompression region

h_{to} Freestream flow total enthalpy upstream of recompression region

$\tilde{K}$ Illingworth-Stewartson transformed shape parameter: $\tilde{K} \equiv (\tilde{\theta}^2/\mu_{t1})(d\tilde{u}_1/d\tilde{x})$

$\tilde{K}_{sep}$ Illingworth-Stewartson transformed shape parameter at separation

K_M Compressibility factor: $K_M \equiv (1 + \gamma M_1^2)/\pi(M_1)$

l Downstream distance measured from origin of boundary-layer growth

L Characteristic recompression length scale: $L \equiv \{1\text{-}2(\theta^*/h)\}[\delta/(d\delta/dx)]$

M_1 Freestream Mach number

$M_{cont.}$ Mach number computed from continuity equation

M_e	Freestream Mach downstream of recompression region
M_{ideal}	Mach number computed from flow area
$M_{isen.}$	Mach number computed from pressure assuming isentropicity
M_o	Freestream Mach upstream of recompression region
n	Boundary-Layer Reynolds number dependence exponent
p	Pressure
p_1	Freestream pressure ($\approx p$)
p_e	Recovered pressure
p_o	Pressure upstream of recompression
p_{t1}	Freestream total pressure
Δp_{∞}	Maximum pressure recovery
Δp_{sep}	Pressure rise required to separate boundary-layer
Pr	Prandtl number
Re_h	Reynolds number based on height h
Re_l	Reynolds number based on length l
S	Transformation parameter: $S \equiv (h + u^2/2)/h_{t1} - 1$
T	Temperature
T_{t1}	Freestream flow total temperature
u	Flow velocity tangential to wall
$\tilde{u}$	Illingworth-Stewartson transformed flow velocity tangential to wall
$\tilde{u}_1$	Illingworth-Stewartson transformed freesteam flow velocity
U	Freestream flow velocity
U_e	Freestream flow velocity downstream of recompression region
U_o	Freestream flow velocity upstream of recompression region
U_s	Separated region flow velocity
v	Flow velocity normal to wall
$\tilde{v}$	Illingworth-Stewartson transformed flow velocity normal to wall
w	Test section width
x	Streamwise coordinate
$\tilde{x}$	Illingworth-Stewartson transformed streamwise coordinate
x^*	Location of throat
x_o	Location of initial pressure rise
y	Normal-to-wall coordinate
$\tilde{y}$	Illingworth-Stewartson transformed streamwise coordinate
Γ_e	Shape parameter downstream of recompression region
Γ_o	Shape parameter upstream of recompression region

δ	Thickness of separated region
δ_e^*	Boundary-layer displacement thickness exiting recompression region
$\delta_{h,i}^*$	Displacement thickness on walls separated by distance h at location denoted by i
δ_o^*	Boundary-layer displacement thickness upstream of recompression region
$\delta_{w,i}^*$	Displacement thickness on walls separated by distance w at location denoted by i
Δ_e^*	Normalized effective mass-flow area downstream of recompression
Δ_o^*	Normalized effective mass-flow area upstream of recompression
ε_e^*	Boundary-layer energy thickness exiting recompression region
$\varepsilon_{h,i}^*$	Energy thickness on walls separated by distance h at location denoted by i
ε_o^*	Boundary-layer energy thickness upstream of recompression region
$\varepsilon_{w,i}^*$	Energy thickness on walls separated by distance w at location denoted by i
E_e^*	Normalized effective total enthalpy-flow area downstream of recompression
E_o^*	Normalized effective total enthalpy-flow area upstream of recompression
θ	Boundary-layer momentum thickness
$\tilde{\theta}$	Illingworth-Stewartson transformed boundary-layer momentum thickness
θ^*	Alternate boundary-layer momentum thickness as defined for Chapter 2
θ_e^*	Boundary-layer momentum thickness exiting recompression region
$\theta_{h,i}^*$	Momentum thickness on walls separated by distance h at location denoted by i
θ_o^*	Boundary-layer momentum thickness upstream of recompression region
$\theta_{w,i}^*$	Momentum thickness on walls separated by distance w at location denoted by i
Θ_e^*	Normalized effective momentum-flow area downstream of recompression
Θ_o^*	Normalized effective momentum-flow area upstream of recompression
μ	Coefficient of viscosity
μ_{t1}	Freestream flow stagnation coefficient of viscosity
ν_{t1}	Freestream flow stagnation coefficient of dynamic viscosity
$\pi(M)$	Pressure ratio across shock
ρ	Density
ρ_1	Freestream flow density
ρ_e	Freestream density downstream of recompression region
ρ_o	Freestream density upstream of recompression region
ρ_s	Separated region flow density
ρ_{t1}	Freestream flow stagnation density
τ_w	Sheer stress at wall

ACKNOWLEDGEMENTS

Grateful thanks to Professor Abraham Hertzberg for origination of the shock wave pyrolysis concept; to Professors David Russell and Tom Mattick, and Doctor Carl Knowlen, in assisting in the further conceptual advancement of, and, ultimately, obtaining funding for, a research program; and to the Department of Energy for its funding of the project. Special thanks to the University of Washington Office of Technology Transfer, and, in particualar, Greg Hauth and Pat Jones, for assistance in industry negotiations and for providing funds necessary to complete the final recompression studies of Chapter 4.

The author wishes to express appreciation for the faith of Professor David Russell in inviting him to participate as chief graduate student on the Shock Wave Reactor program, and for the continuous, inestimable contributions throughout seven fruitful years of research. The author wishes to extend equal gratitude to Professor Tom Mattick (the principal investigator) and Doctor Carl Knowlen as invaluable collaborators throughout the development of experiments and proof of the Shock Wave Reactor concept, and for numerical modeling of the chemistry. Additional thanks go to fellow students Mahmood Mahmoodian, for his thorough preliminary numerical chemistry modeling; Justin Lan, for his efforts in the development of control and diagnostic software; Julio Galarza, for tireless hours spent on gas chromatography; and Ryan Schwab, for assistance in the final assembly and operation of the apparatus employed in the experiments of Chapter 4.

The author wishes to acknowledge the developers of Microsoft Word as the seeds of hatred within a once less troubled soul, but hereby vows to curb all expression of that hatred, should it ever fall upon a fellow human being, to the recommendation of Microsoft Word to that unlucky individual.

Finally, the author would be remiss if he were not to express appreciation to Professors David Russell and Tom Mattick, and Doctor Carl Knowlen (who often lost as much sleep as the author) for keen editorship of each the various publications, including the present one, in which the author was involved.

For Lorraine,

with this finale I shed the final vestiges of bachelorhood.

1. Introduction

Ethylene. Though few among us know it by name, an ever increasing majority cannot remember, nor scarcely imagine, a world apart from its vast utility. It formulates the building block of modern society in as much as it serves as raw material for nearly all manufactured materials, including plastics, synthetic fibers and rubbers, adhesives and solvents, soaps and detergents, perfumes and cosmetics, paints, dyestuffs, anti-corrosives, pesticides and herbicides, fertilizers, animal feeds, pharmaceuticals, refrigerants, antifreeze, photographic supplies, and explosives[1]. (See Appendix A.) It permeates virtually every aspect of our physical existence.

1.1 The Ethylene Industry

Industrial processes represent approximately 40% of energy consumption in the developed world with more than 15% of that utilage attributed to chemical synthesis (more than any other process).[2] Given that ethylene manufacture consumes over half of this, one may estimate that it accounts for over 3% of the total global energy budget. At present, the world accomplishes over 95% of its commercial ethylene manufacture through thermal cracking of petroleum hydrocarbon feedstocks (pyrolysis), such as natural gases, napthas and gas oils (see Table 1.1). While napthas, obtained by distillation of crude oil, comprise the large majority of feedstocks used throughout the

Table 1.1 World fractional feedstock usage[3]

Feedstock	Usage, %		
	1978	1983	1998
Ethane	22.0	24.3	30.8
Propane	6.7	11.1	7.7
Butanes	1.6	0.9	2.8
Napthas	59.7	51.9	49.0
Gas Oils	8.7	10.6	5.4
Others	1.3	1.2	4.4

global petrochemical industry, ethane, despite contrary expectations in the late 80's, continues to represent the source of over 50% of U.S. ethylene production.

1.2 Production Capacity Surplus

Olefin market prices fluctuate as a simple function of the ratio of supply to demand. In response to steadily increasing world ethylene consumption, new plants are built and older ones enlarged to harvest emerging and expanding markets. Production capability grows not steadily, however, but surges forward with the completion of each typically large-scale expansion. Thus the price of olefins is seen to oscillate, depressing considerably as new facilities come on-line, and gradually recovering during periods where margins do not motivate further capacity increases.

Throughout the nineties, olefin production capacity development has outpaced demand growth, resulting in the greatest capacity surplus in thirteen years (Figure 1.1). Outages due to an explosion at Shell's olefin Unit 3 in Deer Park,[4] maintenance work and expansion at Chevron's facility in Port Arthur, Texas,[5] and retirement of Dow's LHC-6 ethylene unit at Freeport, Texas,[6] temporarily reduced U.S capacity by over 7% in the summer of 1997, delaying market softening and allowing world capacity to continue its

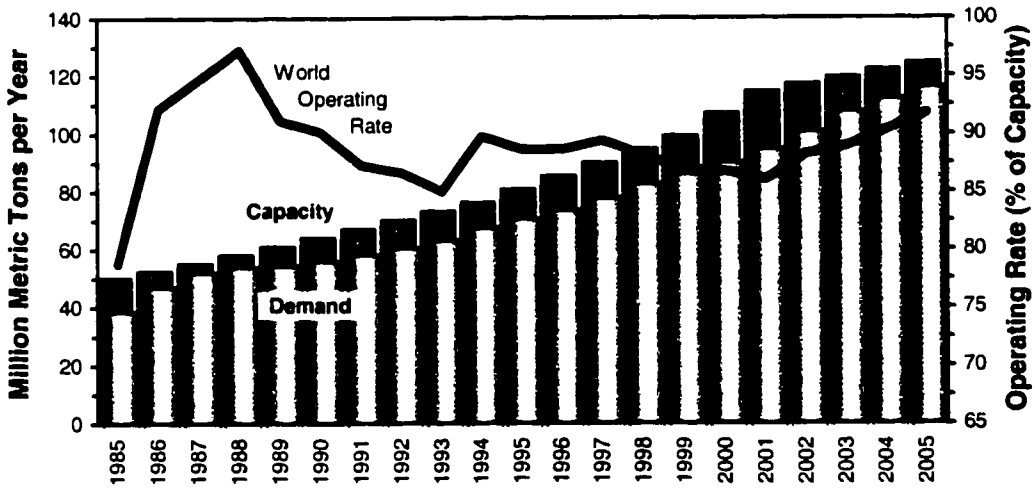

Figure 1.1 World ethylene demand, production capacity, and operating rate from 1985, projected through 2005.[7]

steady rise to 89.6 million metric tons by the beginning of 1998, representing a 5.4% increase from the previous year (as compared to an average growth rate of 4.3% over the preceding 10 years). Despite the fact that demand growth is predicted to fall short of even that which was previously expected due to the Asian financial crisis, several new plant and plant expansion projects are scheduled for completion before the year 2000. Chemical Marketing Associates Incorporated, a Houston based consulting firm, predict capacity to be 90 million metric tons at the millennium, and see the supply/demand gap widening for an additional two or three years, during which time operating rates will fall bellow 90%.[8] Smaller and older facilities have already begun to show a loss of viability[6] as efficiency considerations, driven by narrowing margins of the late 90's, incite ethylene suppliers to consolidate production through mergers and transfer of capacity to ever larger, more modern, higher efficiency plants. Technological advantage will be the scale upon which economic viability is measured in the first decade of the new millennium.

1.3 Conventional Technology

Hydrocarbon pyrolysis is basically achieved by rapid heating within furnace tubes and subsequent cooling of a feedstock, so as to effect endothermic rearrangement of chemical bonds and freeze the reaction at a desired state. Initially the feedstock is preheated within the convective region of the furnace to a temperature just below some critical value required to initiate pyrolysis. The feedstock is generally diluted approximately 25-45% by mass with steam which serves to lower the hydrocarbon partial pressure, thereby increasing reaction efficiency and reducing coking of furnace tube walls downstream in the process. The steam and feedstock may be preheated separately or as a mixture. Subsequent passage through radiant coils or tubes (most modern systems use tubes) heats the mixture to pyrolysis temperatures and provides energy for the endothermic reaction. Upon leaving the furnace, the reaction is terminated via rapid quench heat exchangers. Reaction temperatures generally range from 500-800°C at furnace tube inlet to 775-875°C with typical residence times of the order of hundreds of milliseconds, depending upon choice of feedstock, dilution, furnace design, etc. Figure 1.2 illustrates a typical configuration.

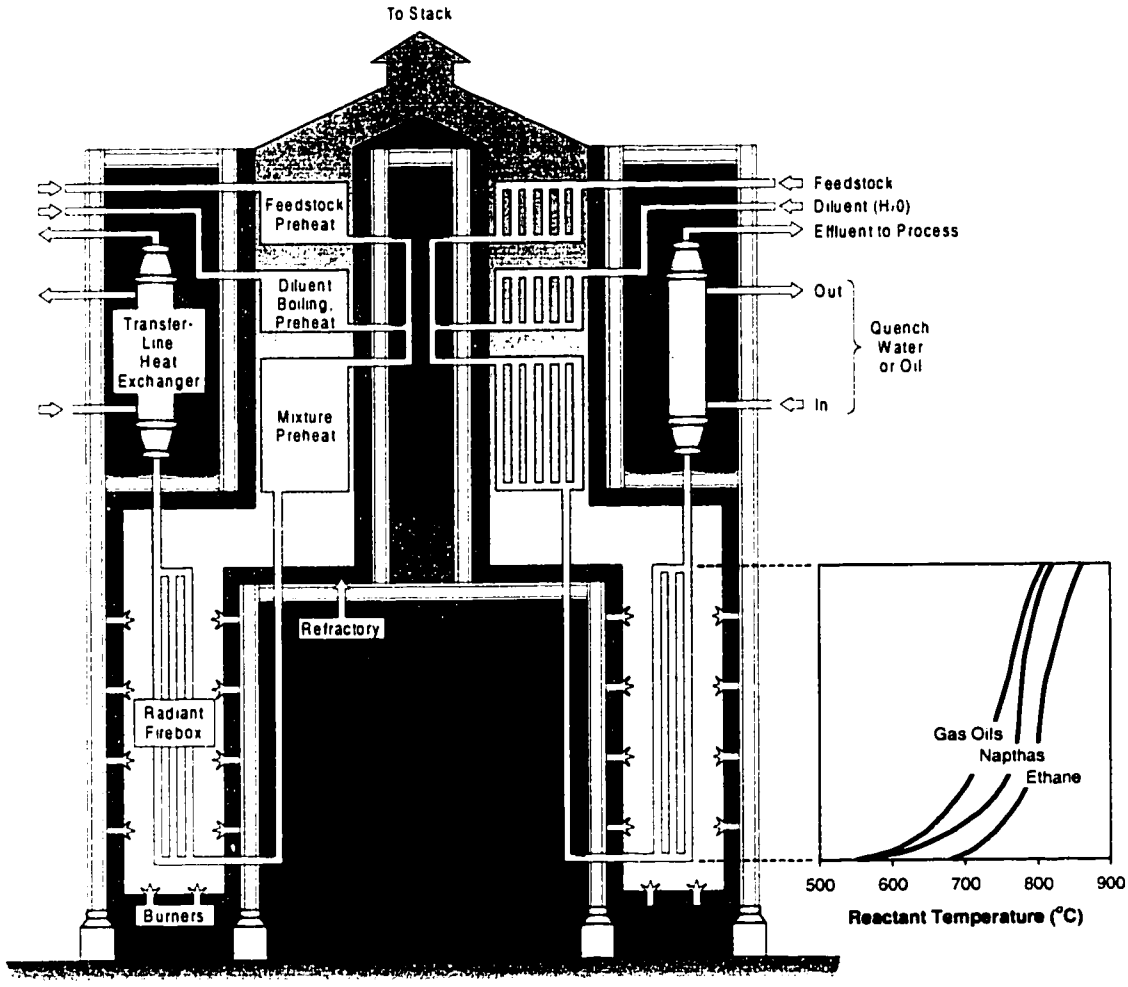

Figure 1.2 Typical furnace configuration and coil temperature profiles for various feedstocks.

Product selectivity varies as a function of reaction temperature-time history, and in accordance with chemical shock tube experiments by Hertzberg et al. (See Section 1.4) and numerical models, technological progress has led to ever increasing reaction temperatures and correspondingly shorter reaction durations throughout the five decades of pyrolysis reactor development. This has naturally corresponded to the development of multi-stage, special alloy furnace tubes of ever decreasing diameter to allow higher reaction temperatures and heat transfer rates, culminating in the Millisecond Furnace (M. W. Kellogg Co., Houston Texas) which reports substantial yield improvements as a result

of a relatively short 50-100 ms residence time and coil outlet temperature 50 °C higher than other modern designs.[9,10] Constraints on furnace tube architecture imposed by metallurgical temperature limits, as well as increased coking with increasing surface area-to-volume ratio as furnace tube diameter decreases, however, continue to be key design issues, and are unlikely to be much further relaxed by continuing research. In short, pyrolysis efficiency in conventional furnace tube type reactors seems to have approached a practical maximum. Further improvement in process effectiveness awaits the development of entirely new technologies.

1.4 Shock Wave Pyrolysis

In the 1950's Hertzberg et al., conducted chemical shock tube experiments designed to study reaction rates by employing shock waves to subject thermally reacting mixtures to a much elevated, shorter duration temperature pulse than is possible using convective heating (Figure 1.3). Shock wave induced pyrolysis demonstrated much improved conversion efficiencies as compared to conventional furnace tube reactors. This originated the idea that perhaps the batched shock tube process could be adapted for some application on an industrial scale and ultimately led, in 1955, to the concept of the "CAL (Cornell Aeronautics Lab) Pressure Wave Chemical Reactor"[12] which employed a battery of shock tubes positioned on the periphery of a rotating drum, each of which was loaded, reacted, and purged once per rotation, integrating to form a quasi-steady stream of output. The Pressure Wave Chemical Reactor was ultimately abandoned due to practical concerns with regard to its large degree of mechanical complexity. In 1991 a new technique involving the use of a standing shock wave in a truly steady state process to initiate pyrolysis was proposed by Hertzberg, Mattick, Russell, and Knowlen, known as the "Shock Wave Reactor".[13-16] The Shock Wave Reactor project received funding from the Department of Energy in June, 1993.[17] This dissertation presents the Shock Wave Reactor Concept, as well as the description, development and analysis of experiments undertaken to ascertain its efficacy.

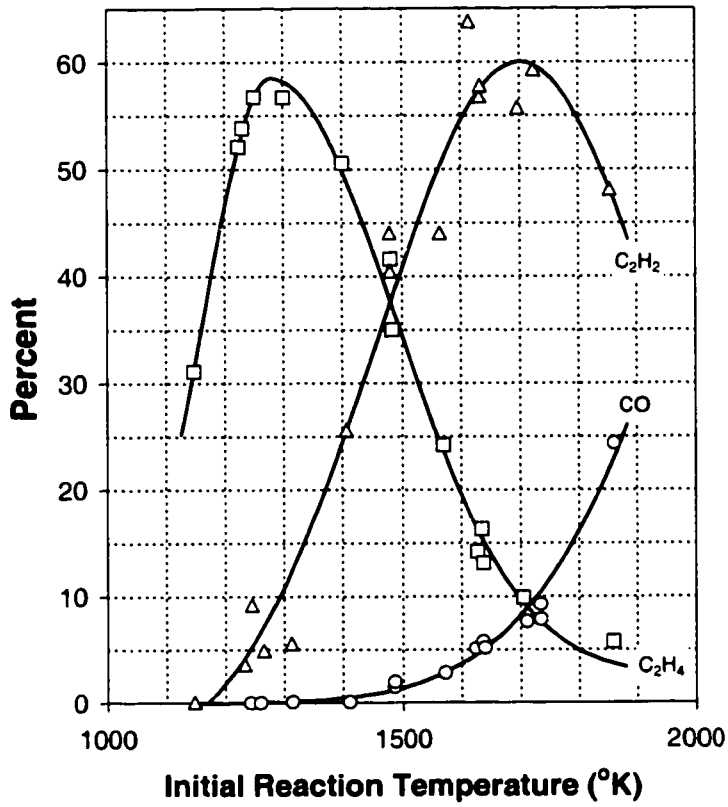

Figure 1.3 Ethylene and acetylene yield vs. reaction time.[11]

1.5 The Shock Wave Reactor

The basic Shock Wave Reactor concept is illustrated in Figure 1.4. A high temperature carrier gas is initially heated by a furnace to a temperature, T_{oc}, sufficiently elevated so as to be capable of initiating and providing enough energy to sustain thermal cracking in some feedstock. Steam is considered to be the preferred carrier gas as it is inert, so as not to participate chemically in the reaction; has a high specific heat, making it an effective transporter of energy; and is currently used as a diluent in commercial pyrolysis to lower hydrocarbon partial pressure. Similarly, as in common reactors, pure feedstock is preheated to a temperature, T_{of}, just below that required to initiate thermal cracking. The carrier and feedstock then accelerate and expand through a blade nozzle array such that they begin to mix supersonically, both now below the pyrolysis initiation

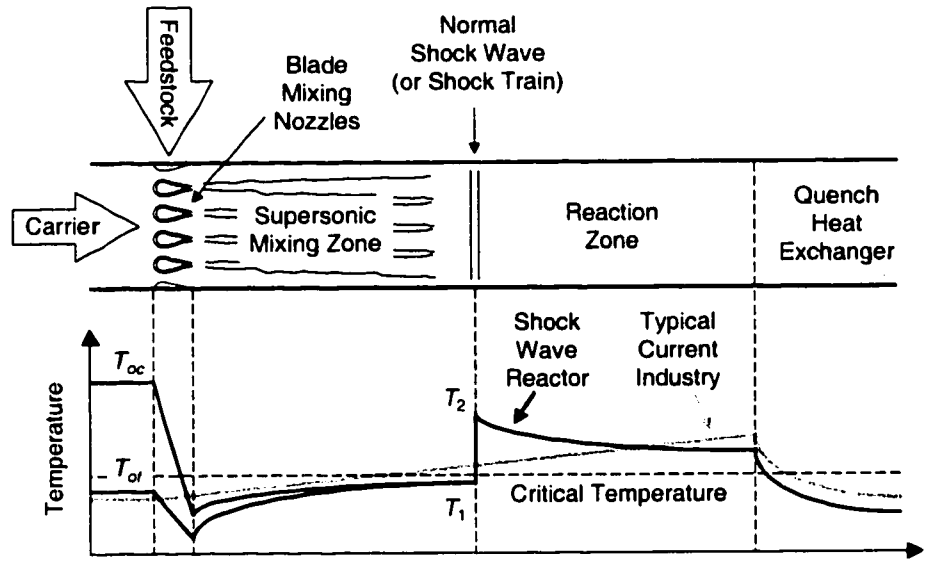

Figure 1.4 Shock Wave Reactor concept schematic.

temperature. The gases combine to form a chemically homogeneous mixture with a uniform temperature T_1, never exceeding critical reaction temperature. A standing shock wave then affects an ideally instantaneous onset of pyrolysis, raising the temperature to T_2. The endothermic chemistry gradually reduces the mixture temperature throughout the reaction zone, although subsonic diffusion may be employed to partially offset this effect, and is ultimately quenched after a yield-optimized interval by conventional means.

1.6 Advantages of the Shock Wave Reactor

The key advantage of performing pyrolysis in this way is that heating of feedstock during the thermal cracking process is no longer an energy transfer process, limited to convective heating rates, but merely one of energy conversion. Kinetic energy, already distributed throughout the fluid flow during the supersonic mixing process, may be converted virtually instantly into the thermal energy required to initiate the reaction. Thus, when combined with existing fast quench technologies, the Shock Wave Reactor can yield substantially shorter reaction times than conventional furnace tube heaters, allowing higher reaction temperatures.

Additionally, because the Shock Wave Reactor requires no heat transfer through

boundaries during the reaction, the metallurgical constraints associated with the inherent role of furnace tube walls in conventional processes are relaxed. In the volumetric Shock Wave Reactor process, a single, large diameter duct replaces the numerous small diameter furnace tubes of the conventional reactor; surface area-to-volume ratio is minimized. The process temperature may be significantly beyond the channel wall material limits, as the walls may be passively or actively maintained well below failure limits. Ultimately, waterwalls (parallel tubes with interconnected shells forming a jacket around the radiant firebox) of a steam superheating furnace do present a practical thermal limit for the Shock Wave Reactor, but one considerably less stringent than that of a pyrolysis furnace which must maintain a much higher temperature difference between the tube wall and internal flow to insure adequate heat transfer at a rate matched to the endothermy of the chemistry. No such requirement exists for a simple steam superheater where slower heating rates are not merely tolerable, but desirable.

Indeed, heat transfer to steam not only permits a higher fluid maximum temperature, but allows a higher furnace thermal efficiency, as well, for two reasons. Firstly, the lower entropy production, corresponding to lower heat transfer rates across a smaller temperature gradient, allows greater utilization of the total energy within the flue gas. Secondly, the typical pyrolysis furnace, in order to insure uniform radiative heating of all of the feedstock, must employ only a very limited array of tubes, centrally located

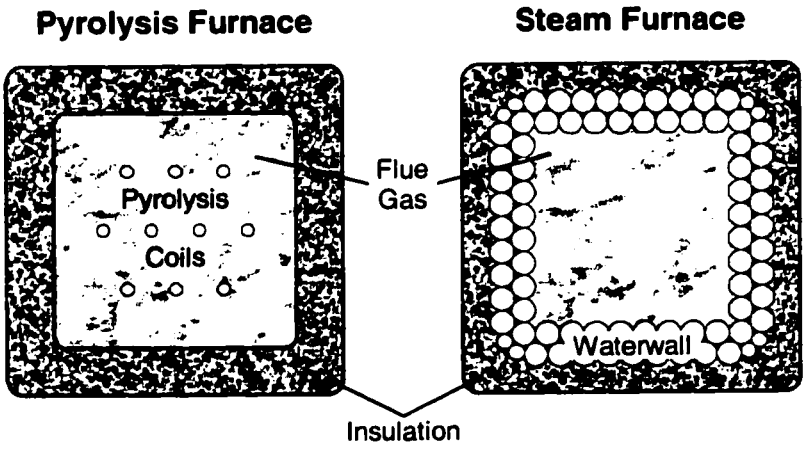

Figure 1.5 Comparison of pyrolysis and steam furnace cross sections.

within the furnace, to avoid shadowing effects between neighbors. (Non-uniform heating can lead to reduced yield optimization and excessive coking.[9]) Any heat escaping through the heavily insulated walls is simply lost to the environment. Wall loss is not fixed, but varies dramatically with external wind and temperature fluctuations, and increases as insulation deteriorates with age. In a steam superheater, however, the tubes containing the fluid to be heated are typically located within the furnace walls, and may make several passes from an outer shell inward. In this way, the heat from the radiant flue gas cannot escape, but must enter the fluid tubes. Since the outer shell of tubes is relatively cool, insulation is fairly simple and heat loss minimized.

One final important advantage of the Shock Wave Reactor process stems from the issue of coke formation. In a conventional wall-heated furnace coil, pyrolysis-formed acetylenic, diolefinic, and aromatic compounds (in a process which is not well understood) form large hydrocarbon chains at the hot wall surface, gradually reducing the effective heat transfer coefficient and ultimately occluding flow. To counter this fouling, radiant coils and downstream equipment must be occasionally de-coked either by disassembly and cleaning or, more modernly, on line by running pure steam or a steam-air mixture for a sufficient interval. Typical de-coking cycles for millisecond and more conventional coils are depicted in Figure 1.6. Even with regular de-coking, the coils

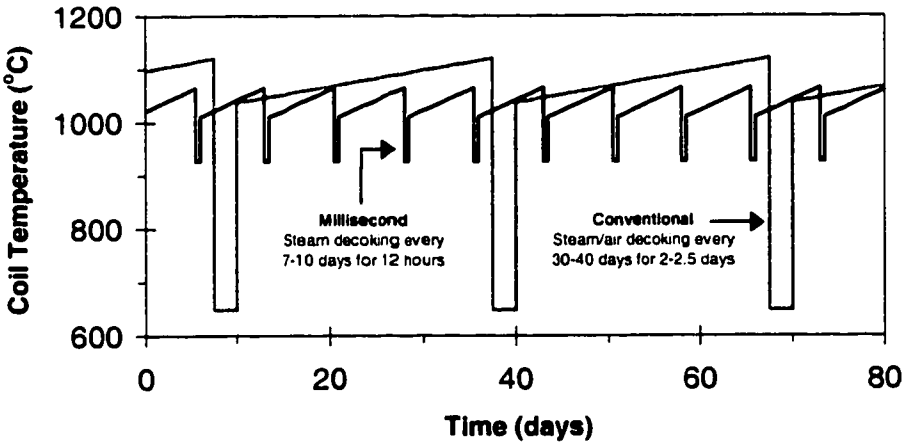

Figure 1.6 Typical operation and decoking cycles.[18]

must be replaced every 3-5 years at a cost totaling 3-7% that of the entire plant.[9] Continuous production may be sustained only through the use of multiple furnaces with staggered maintenance schedules.

By contrast, the Shock Wave Reactor process can be expected to generate virtually no coke formation whatever. As previously mentioned, the Shock Wave Reactor, in theory represents a wall-less design, where the short duration, high temperature, high dilution chemistry may be expected to be practically coke-free. In application, of course, walls must bound the flow. However, because the wall surface area is minimized and may be designed to remain at low temperature, the flow boundaries do not represent a potential source of coke production. Furthermore, as the process involves ducts of large cross-sectional area with no necessary heat transfer through the walls, occluding and insulating effects of any coke that should reside on channel surfaces are negligible. In short, coke formation in the Shock Wave Reactor should be functionally ignorable and economically negligible, representing a significant improvement indeed, for even assuming for purposes of comparison, conventional and shock wave devices of identical thermal efficiency, the simplicity, extended component life, and reduced down time of the Shock Wave Reactor prove great advantages.

1.7 Experiments

The Shock Wave Reactor represents a complex interdisciplinary application of fluid dynamic and chemical kinetic features. No single feature of the problem may be set aside and treated independently; the desired performance of the SWR inherently couples a numerous array of design elements, each of which are sufficiently challenging when completely abstracted from other considerations. While engineering of the Shock Wave Reactor may begin with analytic and numerical modeling, the inherent complexity of mixing and shock recovery dictate that proof-of-concept must inevitably befall experiment.

Because the high enthalpies associated with pyrolysis severely limit diagnostics, cold air studies were conducted in parallel to design of the major auxiliary components

(steam and feedstock supply, dump-tank) of the proof-of-concept experiment throughout the first year of the development effort. This involved the construction of a facility of nearly identical proportions to the expected mixing and reaction duct components of the high enthalpy facility, but with large glass windows along the sidewalls of each section to allow flow visualization. Described in Chapter 2, experiments conducted in this facility primarily focused on the modeling and achievement of sufficiently fast supersonic mixing, and assessment of positional stability of the shock system, as these represent the minimum necessities for successful testing of the basic concept.

The two following years, discussed in Chapter 3, saw the completion and testing of the reacting facility, and, through continued development, ultimately successful proof-of-concept. The rigid schedule necessary to achieve proof-of-concept within allotted time did not allow detailed study of the recompression system prior to, or during, this period. However, because the fundamental nature of duct recompression bears directly on issues of further process refinement and especially of scaling, this dissertation includes a detailed study of this phenomenon, involving the construction of an additional facility (Chapter 4). Chapter 5 concludes with a brief discussion of issues pertaining to application of concepts presented herein to the development of a viable industrial technology and related processes.

1.8 Notes to Chapter 1

1. Adapted from Kniel, L., Winter, O., and Stork, K., *Ethylene: Keystone to the Petrochemical Industry*, Marcel Dekker, Inc., New York, NY, 1980.

2. Ross, R. H. and Steinmeyer, D., "Energy for Industry," *Scientific American*, pp. 89-98, Sept. 1990.

3. 1973 and 1978 data from Grantom, R.L. and Royer, D.J. "Ethylene," *Ullmann's Encyclopedia of Industrial Chemistry*, fifth edition, VCH Publishers, Deerfield Beach, FL, 1985, Vol. A 10, pp. 45-93. 1998 data computed from Appendix B.

4. "Newsletter," *Oil and Gas Journal*, June 30, 1997, pp. 2-4.

5. Morse, P., "Ethylene Market Softening Delayed by Outages," *Chemical and Engineering News*, Vol. 75, September 15, 1997, pp. 20.

6. "Industry Briefs," *Oil and Gas Journal*, July 28, 1997, pp. 43.

7. Adapted from Chang, T., "Worldwide Ethylene Capacity Grows in Spite of Warnings," *Oil and Gas Journal*, March 30, 1998, pp. 41-47.

8. Chang, T., "Worldwide Ethylene Capacity Grows in Spite of Warnings," *Oil and Gas Journal*, March 30, 1998, pp. 41-47.

9. Grantom, R. L. and Royer, D. J. "Ethylene," *Ullmann's Encyclopedia of Industrial Chemistry*, fifth edition, VCH Publishers, Deerfield Beach, FL, 1985, Vol. A 10, pp. 45-93.

10. Orriss, R. and Yamaguchi, H., "Idemitsu's Chiba Ethylene Plant Proves Modern Technology," *Oil and Gas Journal*, March 9, 1987, pp. 27-30.

11. Adapted from Hertzberg, A., and Glick, H. S., "Kinetic Studies in a Single-Pulse Shock Tube", *AGARDograph* No. 41, 1959, pp. 161-182.

12. Hertzberg, A., Squire, W., and Glick, H. S., "The Cal Pressure Wave Chemical Reactor," Cornell Aeronautical Laboratory Report AD-1052-A-13, January, 1956.

13. Hertzberg, A., Mattick, A. T., Russell, D. A., *Shock Controlled Reactors*, edited by Takayama, K., Shock Waves, *Proceedings of the 18th International Symposium on Shock Waves*, 1991, pp. 1289-1294.

14. Knowlen, C., Mattick, A. T., Russell, D. A., and Masse, R. K. "Petrochemical Pyrolysis with Shock Waves," AIAA Paper 95-0402, Jan. 1995.

15. Hertzberg, A., Mattick, A. T., Russell, D. A., "Apparatus for Initiating Pyrolysis Using a Shock Wave," U.S. Patent 5219530, 1992

16. Hertzberg, A., Mattick, A. T., Russell, D. A., "Method for Initiating Pyrolysis Using a Shock Wave," U.S. Patent 5300216, 1994

17. Mattick, A. T., "The Supersonic-mixing, Shock-wave Reactor: An Innovative Approach for Efficient Chemical Production," Final Report, U. S. Department of Energy contract number DE-FG06-93ER12136, 1999.

18. Schillmoller, C. M., "Use These Materials to Retrofit Ethylene Furnaces," *Hydrocarbon Processing*, September, 1985, pp. 101-104.

2. Supersonic Mixing

Unlike conventional hydrocarbon cracking techniques, shock wave pyrolysis does not involve direct heating of feedstock, but instead, the mixing of feedstock with a high energy inert. The streamwise progression of this process must be viewed as being in direct competition with the development of the boundary-layer, which, if allowed to entrain a significant fraction of the flow, serves to defeat the fundamental volumetric advantage of shock wave pyrolysis. The reactor sidewalls must be maintained below cracking temperatures in order to avoid catalytic coke formation in the nearly stagnated laminar sublayer. Hence, the sidewalls of the mixing region not only result in total pressure loss, but function as a substantial source of heat loss and, therefore, thermal inefficiency. Furthermore, the presence of boundary-layers is seen to affect a spreading of normal shock waves into extended shock trains (see Chapter 4). In the limit of large reactor cross-sectional area (such as would be the case on an industrial scale) it is intuitive that these loss mechanisms become small; however, they are a critical matter within the smaller scale of an economically feasible experiment. Thus, it is clear that while the achievement of rapid supersonic mixing is important on an industrial scale with regard to efficiency, it is essential within the laboratory.

2.1 Nozzle Arrays

Dimensional analysis reveals that the length required for turbulent shear mixing of parallel streams scales with the span of the two streams. Where rapid mixing is desired, this suggests the reduction of the relevant transverse length through the use of multi-orifice arrays in place of a single, flowfield scale injection scheme as is observed in the evolution of nozzle geometries in the development of gas dynamic lasers through increasingly fine 2-D nozzle arrays to, ultimately, screen nozzles. For the Shock Wave Reactor, the design of the nozzle array must guarantee uniform feedstock injection, acceptable total pressure losses, and rapid mixing at uniformly low temperatures; and will ultimately determine flow properties throughout the downstream pressure/temperature recovery within the reaction zone. Thus, the mixing nozzle array may be perceived as the

very heart of the Shock Wave Reactor, and analytical techniques for predicting nozzle performance the heart of Shock Wave Reactor design.

Russell[1] outlines an analytic procedure to estimate nozzle losses, based on the assumption that each nozzle emits a radial flow with boundary-layers into the upstream edge of a control volume which exits downstream uniform and parallel. (See Figure 2.1.) Mathematically this becomes the conservation set:

$$\rho_e U_e \left[\beta - \Delta\left(\frac{\delta^*}{d}\right)_e\right] = \rho_f U_f \left(\frac{A_f}{A_e}\right) \qquad 2.1a$$

$$p_e \left\{1 + \left(\frac{p_b}{p_e}\right)\left[\left(\frac{A_f}{A_e}\right) - 1\right]\right\} + \rho_e U_e^2 \left[1 - \lambda\Delta\left(\frac{\theta^*}{d}\right)_e\right] = \left[p_f + \rho_f U_f^2\right]\left(\frac{A_f}{A_e}\right) \qquad 2.1b$$

$$\rho_e U_e h_{te} \left[\beta - \Delta\left(\frac{\varepsilon^*}{d}\right)_e\right] = \rho_f U_f h_{tf} \left(\frac{A_f}{A_e}\right) \qquad 2.1c$$

Table 2.1 Geometric parameters

	Δ	β	λ
2-D Wedge	2	$\alpha/(\sin\alpha)$	$\cos\alpha$
3-D Conical	4	$2/(1+\cos\alpha)$	

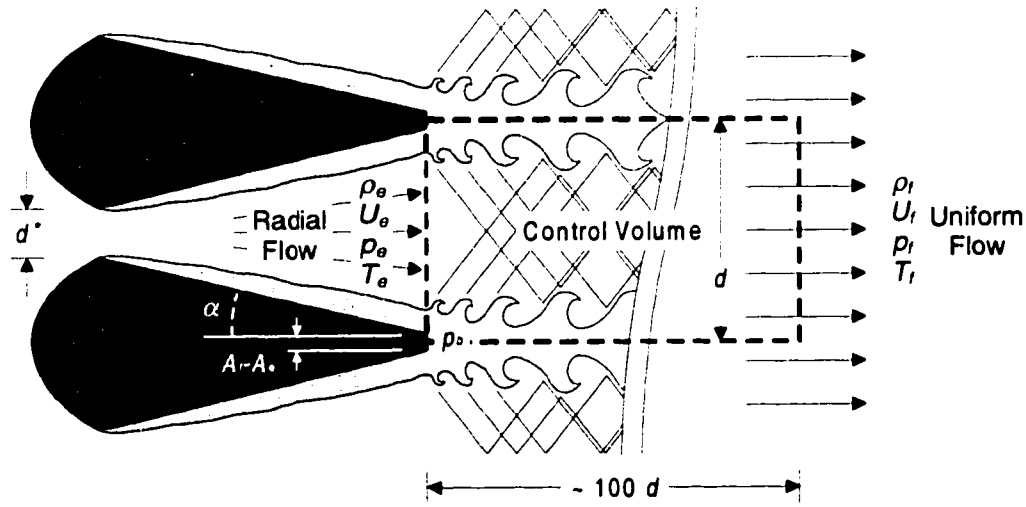

Figure 2.1 Model for determination of boundary-layer and shock losses downstream of nozzle.

Subscripts e and f denote flow exiting the nozzle and control volume, respectively, and d^* and d the nozzle throat and exit spans. The value of the base pressure, p_b, expected to be less than one, is difficult to calculate, but its effects may and should be minimized if the base area is designed to be as small as possible. Geometric parameters Δ, β, and λ are defined in Table 2.1 for both 2-D wedge and 3-D conical straight-walled nozzles. Boundary-layer thicknesses are defined as follows:

$$\left(\frac{\delta^*}{d}\right)_e \equiv \frac{1}{2}\int_0^1 \left(1 - \frac{\rho U}{\rho_e U_e}\right) d\left(\frac{y}{d}\right)_e$$

$$\left(\frac{\theta^*}{d}\right)_e \equiv \frac{1}{2}\int_0^1 \left(1 - \frac{\rho U^2}{\rho_e U_e^2}\right) d\left(\frac{y}{d}\right)_e$$

$$\left(\frac{\varepsilon^*}{d}\right)_e \equiv \frac{1}{2}\int_0^1 \left(1 - \frac{\rho U h_t}{\rho_e U_e h_{te}}\right) d\left(\frac{y}{d}\right)_e$$

But note alternatively that:

$$\left(\frac{\theta^*}{d}\right)_e = \left(\frac{\delta^*}{d}\right)_e + \left(\frac{\theta}{d}\right)_e \quad \text{and} \quad \left(\frac{\varepsilon^*}{d}\right)_e = \left(\frac{\delta^*}{d}\right)_e - \left(\frac{\varepsilon}{d}\right)_e \qquad 2.2a, b$$

Where:

$$\left(\frac{\theta}{d}\right)_e \equiv \frac{1}{2}\int_0^1 \frac{\rho U}{\rho_e U_e}\left(1 - \frac{U}{U_e}\right) d\left(\frac{y}{d}\right)_e \quad \text{and} \quad \left(\frac{\varepsilon}{h}\right)_e \equiv \frac{1}{2}\int_0^1 \frac{\rho U}{\rho_e U_e}\left(\frac{h_t}{h_{te}} - 1\right) d\left(\frac{y}{d}\right)_e$$

Initially, both blade and screen-type nozzles were considered for the Shock Wave Reactor, but, as the substantially increased shock losses and larger stagnated base area flow of the 3-D screen nozzles are undesirable[2], 2-D blade nozzles prevailed as the design choice. For simplicity, 2-D straight angle expansions of (α =) 5°, 10° and 20° were initially examined. Boundary-layer properties for use in Equations 2.1a-c were computed using compressible integral methods of Thwaits[3] based on similar solutions of Cohen and Roshotko[4], and results of a typical example (α=10°, T_t/T_w = 4.7) are displayed in Figure 2.2. The normalized boundary-layer thicknesses are multiplied by the natural

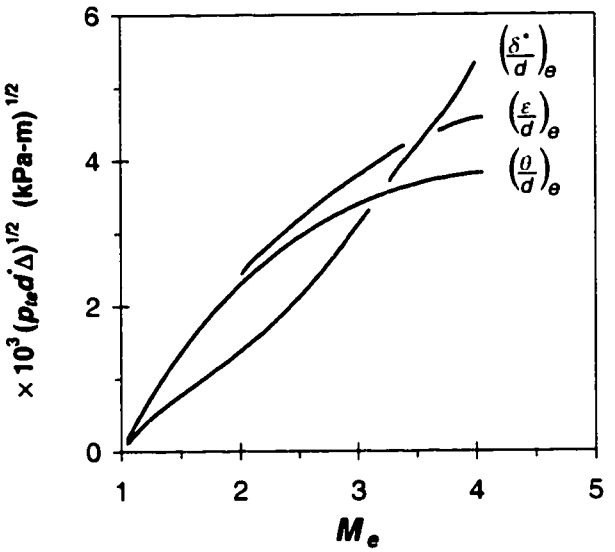

Figure 2.2 10° 2-D wedge nozzle exiting boundary-layer properties as function of exit Mach number.

parameter grouping $(p_{te}d^*\Delta)^{1/2}$ for generality, incorporating the pressure, scale, and most of the α dependence as pertaining to Equations 2.1a-c.

The resulting flow properties at the control volume exit, normalized by nominal values exiting 10° and 20° wedge nozzles with identical total-to-wall temperature ratio as the previous example, are compared to the performance of an ideal nozzle in Figure 2.3. To illustrate the significant amplification of losses by increased Mach number, cases for M_e = 2 and 4 are shown. Note that as the nozzle scale becomes increasingly small, characterized by throat diameter, d^*, recovered total properties and Mach number dramatically diminish due to rising domination of viscous losses, whereas as d^* becomes large, asymptote to what may be considered solely shock losses associated with the turning of colliding adjacent exit flows is observed. Hence, one may infer that for small nozzles minimization of the wall length (i.e., use of high divergence angle) is of greater actual importance than contour. As would therefore be suspected, further computations predict 2-D 5° wedge nozzles to have very similar performance to the ideal 2-D contour at pressure and length scales associated with the Shock Wave Reactor. (The 5° curves are omitted in Figure 2.3 for clarity.)

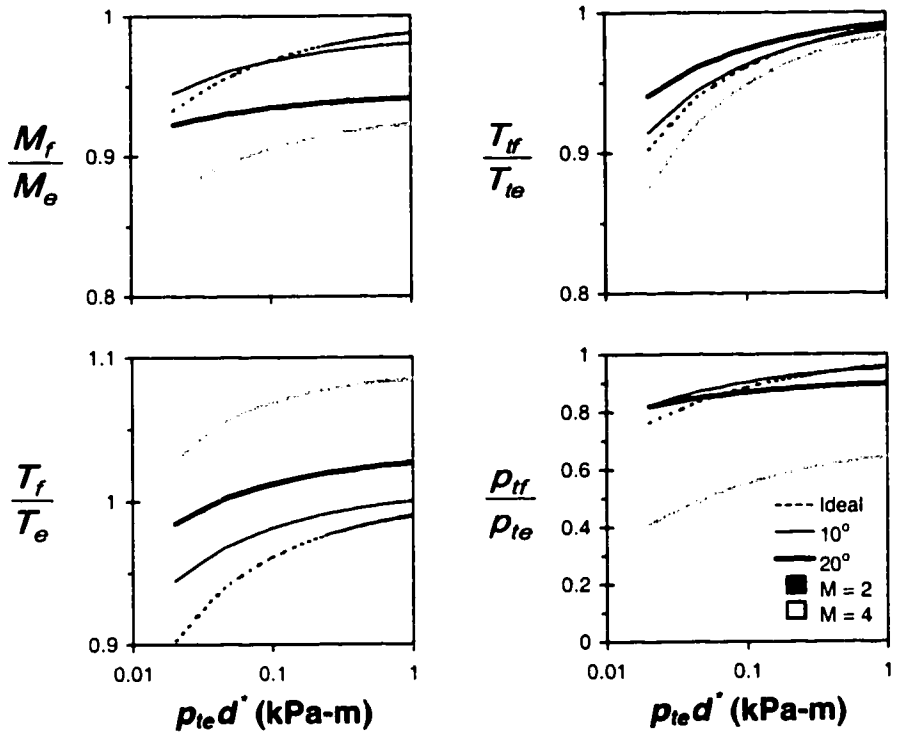

Figure 2.3 Normalized flow properties of fully-mixed fluid downstream of 2-D blade nozzle arrays.

2.2 Mixing Length

For two-dimensional turbulent shear layers, dimensional analysis reveals linear downstream growth of the mixed region at the fluid interface. Experimentally Brown[5] has demonstrated the semi-empirical model:

$$\left(\frac{\delta}{x}\right)_{temporal} = \text{constant}\,\frac{\left(1-\frac{U_2}{U_1}\right)\left(1+\sqrt{\frac{\rho_2}{\rho_1}}\right)}{1+\frac{U_2}{U_1}\sqrt{\frac{\rho_2}{\rho_1}}} \qquad 2.3$$

to characterize the influence of relative velocity and density of the two streams on the temporal (in a Galilean frame of reference fixed to convective structures in the flow, ignoring spatial variation in the mixed-layer height) growth of the thickness of the mixed fluid layer at the interface, $(\delta/x)_{temporal}$, for incompressible flows where the constants have been observed through a range of 0.25 to 0.45. In turn, Dimotakis[6-8] argues that the

above expression may be applied to spatially growing layers multiplying by the factor:

$$\left(\frac{\delta}{x}\right)_{\text{inc}} \frac{(\delta/x)_{spacial}}{(\delta/x)_{temporal}} = 1 - \frac{\left(1-\sqrt{\frac{\rho_2}{\rho_1}}\right)\left(1+\sqrt{\frac{\rho_2}{\rho_1}}\right)}{1+2.9\left(1+\frac{U_2}{U_1}\right)\left(1-\frac{U_2}{U_1}\right)} \qquad 2.4$$

to obtain:

$$\left(\frac{\delta}{x}\right)_{inc.} = \text{constant}\,\frac{\left(1-\frac{U_2}{U_1}\right)\left(1+\sqrt{\frac{\rho_2}{\rho_1}}\right)}{1+\frac{U_2}{U_1}\sqrt{\frac{\rho_2}{\rho_1}}}\left[1-\frac{\left(1-\sqrt{\frac{\rho_2}{\rho_1}}\right)\left(1+\sqrt{\frac{\rho_2}{\rho_1}}\right)}{1+2.9\left(1+\frac{U_2}{U_1}\right)\left(1-\frac{U_2}{U_1}\right)}\right] \qquad 2.5$$

where the spatial denotation has been replaced by subscript "*inc.*" to make explicit the incompressible premise of Equation 2.5 in further discussion. Important here to note is that this correlation, directly applied, is only strictly valid in describing the growth of simple shear layers of semi-infinite span (unconfined) where the mixed fluid region has no effect on the free stream velocity and density. It makes sense, however, to assume that for all shear flows, of finite span or otherwise, there is at least some streamwise length within which the mixed layer has not yet grown sufficiently large to affect the centerline flow properties of either fluid layer. (Indeed, this assumption is necessarily implicit in the very experiments from which Equation 2.5 proceeds.) For simplicity, all here subsequent treatment of mixing will, therefore, further extrapolate by dismissing all influence of flow boundedness in as much as Equation 2.5 will be applied to shear mixing even to the edge of the flowfield. Additionally, the shorthand nomer "Brown-Dimotakis mixing length" will hereafter apply to the distance required for the mixed region to grow to the flowfield edge for subsequent brevity.

For the case of the Shock Wave Reactor, boundary effects on mixing may effectively be ignored. This does not represent a gross approximation, in that walls only border the outermost of a group of alternating plenum and feedstock streams, thus may potentially be considered quite far from internal regions of the flowfield. (Recall that the mixing conditions of the Shock Wave Reactor are, in fact, specifically designed to minimize the role of the boundary-layers.) Furthermore, it should be noted that, as a

short mixing distance is desired, disinclusion of wall effects is conservative. Boundary-layers tend to enhance mixing (reduce mixing length) by generating turbulence and slowing the flow.

Therefore, for shear flows between streams of equal span, if it is assumed that the mixed layer defines the entire region of velocity and density affected flow, and that its concentration is relatively uniform, the mixing distance approximately corresponds to the Brown-Dimotakis mixing length, i.e., Equation 2.5 describes the entire downstream mixing process. Once the stream area ratio varies from unity, however, the Brown-Dimotakis mixing length is shorter than the total mixing distance, and corresponds to the length required for only the smaller of the two streams to be completely entrained by the mixing layer. (See Figure 2.4.) Thus, the Brown-Dimotakis mixing length scales with the smaller stream height.

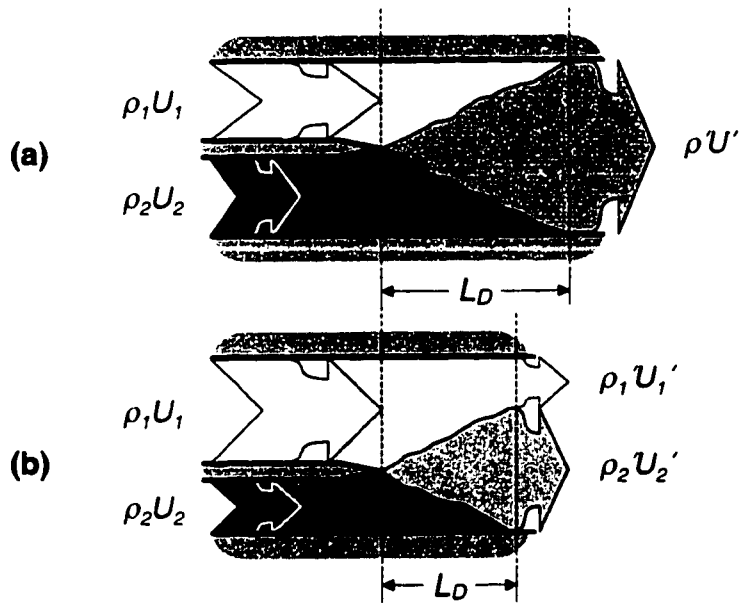

Figure 2.4 Comparison of Brown-Dimotakis mixing lengths for shear layers with equal (a) and unequal (b) heights.

This might seem to imply that Equation 2.5 is inapplicable in calculating the total mixing length for shear flows of area ratios not near unity. Assumptions already made,

however, point toward a solution strategy. It may be observed, based on the approximation that flow properties within the mixed region are uniform, that if a control volume is drawn around the region of the flowfield spanned by the Brown-Dimotakis mixing length which includes the entire smaller stream and an equal area of the larger stream, the exiting mixed flow and the flow outside the control volume once again form simple shear layer between two parallel streams. This suggests a staged calculation, where the total mixing length computed as the sum of the lengths of a series of consecutive steps as depicted in Figure 2.5.

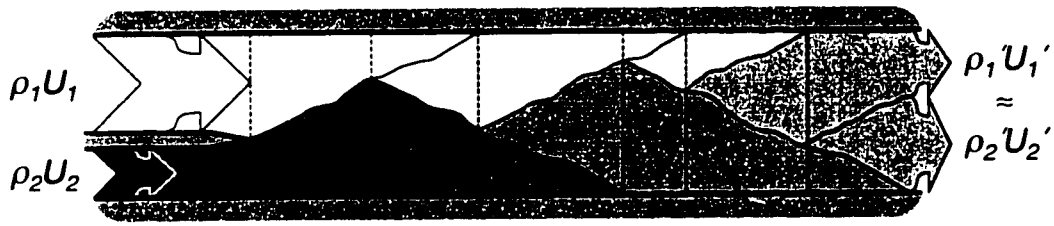

Figure 2.5 Multi-stage mixing.

Note that the Brown-Dimotakis mixing length of each stage, based on the smaller of the two stream heights is never sufficient to allow the mixed region to entrain the entire flowfield (unless, of course, for some stage the outflow heights are coincidentally equal). Flow uniformity is only asymptotically approached as the number of stages becomes large. Thus, the point at which mixing is complete must be arbitrarily defined. One possibility is to truncate the calculation at a point downstream where some span-wise integrated norm is reduced to a specified value near zero. Another option of the lowest order is to simply assign the final stage of mixing to be that following one within which the mixed region first becomes the larger of the two exiting streams (i.e., to allow the mixed layer to span each initial stream area a single time). This arbitration preserves the relative influence of stream properties on the mixing distance, but can be expected to require adjustment of the constant in Equation 2.5 to correspond to actual experimental values.

The outflow properties of each stage supply input to its successor; however,

considerable increase in complexity in the computation of these properties accompanies the substitution of the single uniform output of the symmetric case by the exit of a modified shear layer pair representing the partially complete mixing of the incoming layers. The conservation equations now become:

$$\dot{m}_1' + \dot{m}_2' = \dot{m}_1 + \dot{m}_2 \qquad 2.6a$$

$$p_1' A_1' + p_2' A_2' + \dot{m}_1' U_1' + \dot{m}_2' U_2' = p_1 A_1 + p_2 A_2 + \dot{Q}_1 + \dot{Q}_2 \qquad 2.6b$$

$$\dot{m}_1' h_{t1}' + \dot{m}_2' h_{t2}' = \dot{H}_{t1} + \dot{H}_{t2} \qquad 2.6c$$

where the incoming momentum and enthalpy fluxes, $\dot{H}_{ti}$ and $\dot{Q}_i$ respectively, are left in general notation to encompass the boundary-layer deficits entering from upstream when considering the first stage. Certainly, for all subsequent stages, $\dot{H}_{ti} = \dot{m}_i h_{ti}$ and $\dot{Q}_i = \dot{m}_i U_i$ as a consequence of the implicit approximation that flow within each stream be uniform. In practice, inclusion of the incoming boundary-layers little impacts the calculated mixing distance, and will hereafter be neglected in that context. Additionally, for simplicity, the entraining region will be assumed symmetric (which is not precisely observed experimentally), and it directly follows that the mixed fluid region, contiguous to the same wall as the narrower entering stream, will encompass twice its area, the balance unmixed.

Note that Equations 2.6a–c do not form a closed system, but that additional information is necessary to determine in what way the effluent mass, momentum, and enthalpy are distributed between the exiting flows. Of simplest design is to assume that the unmixed fluid exits completely unperturbed by the presence of the mixing layer, i.e., supplement Equations 2.6a–c with:

$$\dot{m}_u' = \frac{A_u'}{A_u} \dot{m}_u \qquad 2.7$$

$$p_u' = p_u \quad \text{or equivalently} \quad \dot{m}_u' U_u'^2 = \frac{A_u'}{A_u} \dot{Q}_u \qquad 2.8a, b$$

$$\dot{m}_u{}'h_{tu}{}' = \frac{A_u{}'}{A_u}\dot{H}_u \qquad 2.9$$

The subscript u is employed to denote that the above equation set applies to the unmixed fluid and upstream adjacent stream. (It will perhaps aid the reader to here recall that subscripts 1 and 2 denote the faster and slower streams, respectively, but either may, in turn, correspond to subscript u, as either the faster or slower stream may be of the larger area.) With the addition of an equation of state (an ideal gas will suffice here), the mixed region properties may then be explicitly solved merely by ignoring this part of the duct, effectively reducing the problem to the symmetric case.

Such a solution is problematic, however, in that the pressures across the shear layer are not matched, which must certainly be the case in actuality. Clearly the pushing of one layer against the other represents the primary mechanism by which static equilibrium across the shear layer is maintained. Thus, to bring the equation set into better approximation to reality, it is logical to replace the above momentum balance (Equation 10a or b) with the simple stipulation:

$$p_1{}' = p_2{}' \qquad 2.10$$

This is not to imply that the initial pressures are matched. Experiments, however, indicate that wave activity generated by mismatched pressure at the origin of the fluid interface interact only very weakly with the shear layer.[9] Thus, the above-described analysis will subsequently be applied equally to nozzle arrays operating on and off design.

2.3 Convective Mach Number

Feedstock must be mixed supersonically with the energy carrying plenum flow to avoid instantaneous onset of cracking in an uncontrolled manner. Recent shear layer experiments, however, indicate that flows with highly differentiated Mach numbers require substantially increased distances for mixing as compared to low differential Mach number theoretical counterparts. [8,10-12] While a precise definition of the relevant

parameter is still under debate, data indicate a steep decline in mixed layer spreading angle with an increasing "convective Mach number". Considered a measure of the speed of turbulent structures within the mixed layer relative to the outside flow on either side, a shear layer generally is characterized by two such parameters defined:

$$M_{c1} = \frac{U_1 - U_c}{a_1} \quad \text{and} \quad M_{c2} = \frac{U_c - U_2}{a_2} \qquad 2.11a, b$$

on the high and low speed sides, respectively.

Strictly speaking, the convective speed, U_c must be experimentally determined, although arguments balancing total pressure across stagnated fluid boundaries between large-scale mixing structures in the convective reference frame[6,8,10,13] yield:

$$p_1\left(1+\frac{\gamma_1-1}{2}M_{c1}^{\,2}\right)^{\gamma_1/(\gamma_1-1)} = p_2\left(1+\frac{\gamma_2-1}{2}M_{c2}^{\,2}\right)^{\gamma_2/(\gamma_2-1)} \qquad 2.12$$

Taken with the definitions of M_{c1} and M_{c2}, this forms a closed equation set and, in principle, allows computation of U_c. Note, however, that for matched specific heat ratios and static pressures, Equation 2.12 indicates identical M_{c1} and M_{c2}. This is not observed in the laboratory[14]. Nevertheless, Hall et al.,[8] observing the reasonable collapse of δ/x, normalized by $(\delta/x)_{inc.}$ as per Equation 2.5, when plotted verses M_{c1} (Figure 2.6), suggest to interpret U_c computed in this fashion as perhaps some measure of the average convective features of the flow. In few instances of study are p_1 and p_2 greatly disparate; Hall et al. point out that even for $\gamma_1 \neq \gamma_2$, generally M_{c1} and M_{c2} are quite close. Thus, characterization of compressibility effects on mixing may be approximately characterized by a single convective Mach number, as in the following curve fit proposed by Dimotakis[7] (for most cases, as evidenced by the curve superimposed in Figure 2.6):

$$\frac{(\delta/x)}{(\delta/x)_{inc}} \equiv 0.8e^{-3M_{c1}^{\,2}} + 0.2 \qquad 2.13$$

It becomes apparent that to account for compressibility effects in the staged calculation, the mixing angle within each stage must be multiplied by a locally computed

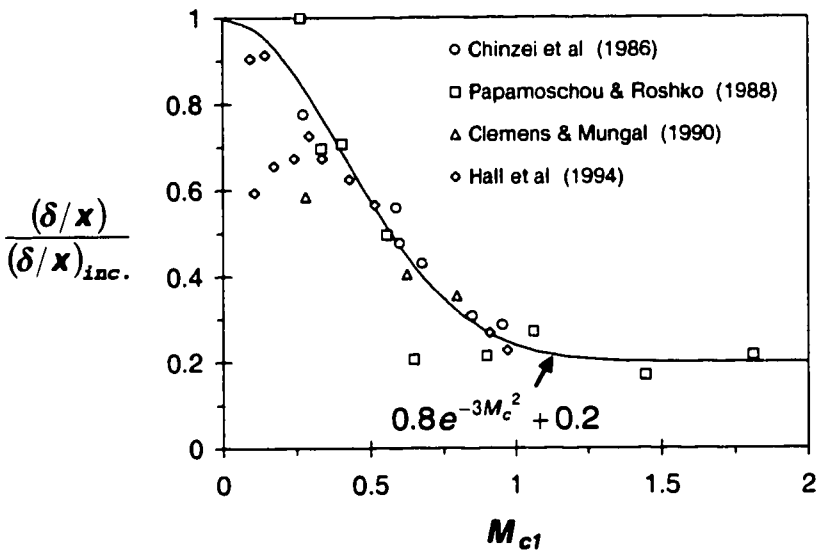

Figure 2.6 Mach number influence on mixed layer growth as reported by various experimenters. Curve fit of Dimotakis superimposed.[15]

convective Mach number factor. This is equivalent to multiplying the Brown-Dimotakis mixing length by $(\delta/x)/(\delta/x)_{inc.}$. Figure 2.7 provides a visual representation of the relative magnitude of this effect, displaying plots of the computed Brown-Dimotakis mixing

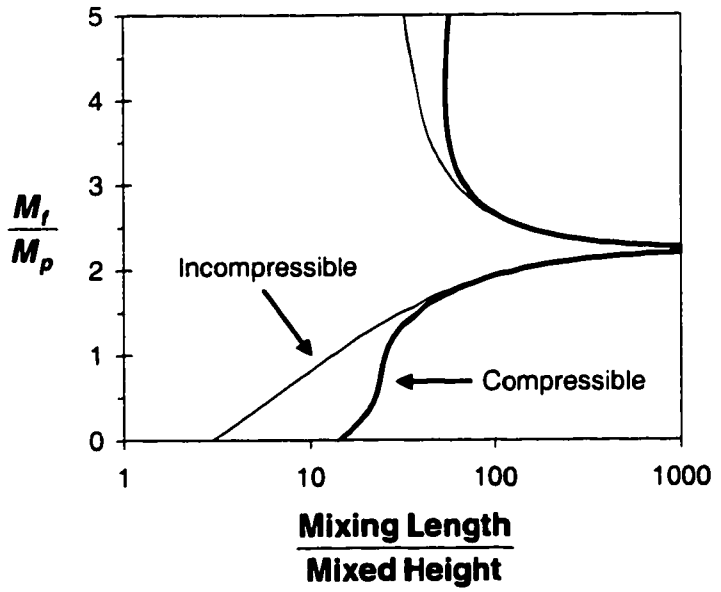

Figure 2.7 Calculated mixing distance for simple shear layers with and without compressibility correction.

length for a simple shear layer with and without the correction factor, as functions of the feed-to-plenum Mach number ratio. (Here, in deference to the ultimate objective of mixing high temperature steam plenum flow and ethane feedstock, γ_f/γ_p = 1.09/1.2, molecular weight ratio $(M.W.)_f/(M.W.)_p$ = 30/18, T_{tf}/T_{tp} = .5; and an approximate plenum flow Mach number value of 2 is assigned to M_p. Subscripts p and f denote the plenum and feed flows, respectively.) Note that the approach of the mixing distance to large values near $M_f/M_p \rightarrow 1.9$ corresponds to $\Delta U \rightarrow 0$, i.e., the point at which the streams have zero relative velocity. Below this point subscripts 1 and 2 in previous expressions correspond with f and p, respectively, and vice-versa above.)

Thus, the general expression for the total mixing length becomes:

$$L_{mix} = \sum_i F_{Ci} L_{D_i} \qquad 2.14$$

where

$$L_{D_i} = \frac{2h_i}{(\delta/x)_{inc.,i}} \quad \text{and} \quad F_{Ci} \equiv \frac{(\delta/x)_i}{(\delta/x)_{inc.,i}}$$

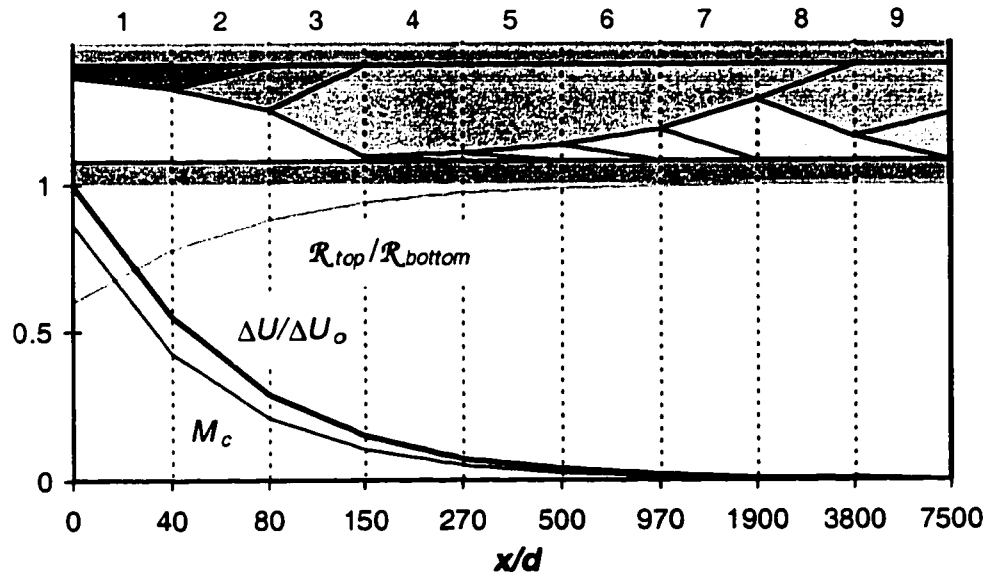

Figure 2.8 Typical set of mixing stages and corresponding flow property profiles.

for stage i. Because each stage is defined sufficiently long to allow only one of the entering streams to be fully entrained, h_i represents the smaller of the two respective heights. A typical set of stages and the corresponding asymptotic decay in the velocity difference across the fluid interface and convective Mach number, approximating the proof-of-concept experiment to be discussed in Chapter 3, is displayed in Figure 2.8 (γ_f/γ_p, $(M.W.)_f/(M.W.)_p$, and T_{tf}/T_{tp} same as above with a feedstock-to-carrier area ratio of 7.3). The ratio of ideal gas constants for the upper and lower flow regions, R_{top}/R_{bottom}, is plotted as a measure of chemical uniformity.

2.4 Implications of Solid Body Rotation on Convective Mach Number

Mixing of incompressible shear layers is observed to occur within large eddies which rotate approximately as solid bodies of uniform core composition, on the scale of the mixed layer thickness, δ. For compressible mixing, however, typically observed structures are of lesser scale. Thus, it is logical to deduce that perhaps some light may be shed upon this distinction by comparing incompressible and compressible solutions to solid body rotating flows. To begin, inserting $\underline{U} = u_\theta \underline{e}_\theta$ into the inviscid momentum equation yields:

$$\frac{\rho u_\theta^{\,2}}{r} = \frac{dp}{dr} \tag{2.15}$$

The analysis is two-dimensional and nothing varies in the θ direction, hence the use of the total derivative. Substituting $u_\theta = (r/R)U_\theta$, where capitals denote values at the edge of the eddy furnishes the result:

$$\frac{dp}{d(r/R)} = \rho U_\theta^{\,2}(r/R) \tag{2.16}$$

For the incompressible case Equation 2.16 may be immediately integrated and the constants evaluated by stipulating freestream pressure, p_o, at the eddy edge:

$$\left.\frac{p}{p_o}\right|_{inc.} = 1 - \frac{\rho U_\theta^{\,2}}{2p_o}\left[1-(r/R)^2\right] \tag{2.17}$$

To include compressibility, substituting $\rho = p/\mathcal{R}T$ from the ideal gas law and employing the energy equation (T_t is the total temperature) it is easy to show:

$$\left.\frac{dp}{p}\right|_{compr.} = \frac{(r/R)}{\frac{\mathcal{R}T_t}{U_\theta^2} - \frac{\gamma-1}{2\gamma}(r/R)^2} \qquad 2.18$$

which, employing the same boundary conditions as for the incompressible case, integrates to:

$$\left.\frac{p}{p_o}\right|_{compr.} = \left(\frac{K-1}{K-(r/R)^2}\right)^{\frac{\gamma}{\gamma-1}} \text{ where } K \equiv \frac{2}{\gamma-1}\left(\frac{1+\frac{\gamma-1}{2}M_{\theta e}^{\ 2}}{M_{\theta e}^{\ 2}}\right) \qquad 2.19$$

and $M_{\theta e}$ denotes the eddy edge Mach number.

The two cases are characteristically similar from the perspective of pressure distribution, as illustrated in Figure 2.9, where the normalized pressure for various radii throughout the rotating body are plotted versus edge velocity, normalized by the speed of sound for the compressible case. (For the compressible case, this is the edge Mach number; however, for incompressible flow the normalization is merely an arbitrary

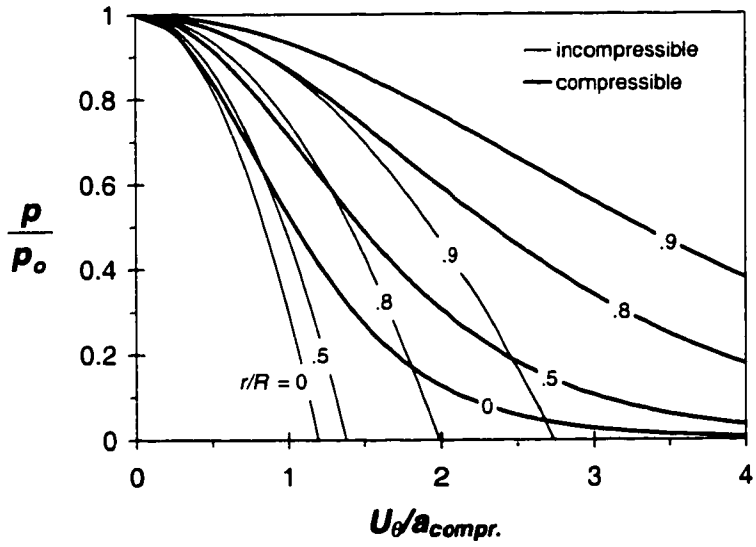

Figure 2.9 Pressure at various radii for solid body rotation vs. edge speed normalized by speed of sound for compressible case.

convenience for the purposes of comparison.) The incompressible core reaches zero pressure at finite edge velocity (cavitation must shortly precede this limiting condition, at which point the solid body model breaks down). Likewise, in the compressible case, the core is evacuated, although the introduction of a gradual transition substantially increases the actual edge velocity at which the core at a given radius may be considered essentially vacuum. Nevertheless, in as much as the pressure profiles bear resemblance, compressible radial density distributions for various Mach numbers, isentropically related to the pressure profiles displayed alongside in Figure 2.10, illustrate a key difference. In contrast to the uniform density of the incompressible rotating body, compressibility necessitates mass displacement. Eddies on the scale of δ will have edge Mach numbers which scale with the convective Mach number, that is, the relative Mach number difference between the two streams. Thus, the formation of eddies on this scale at high convective Mach number would require that the interface region be highly evacuated.

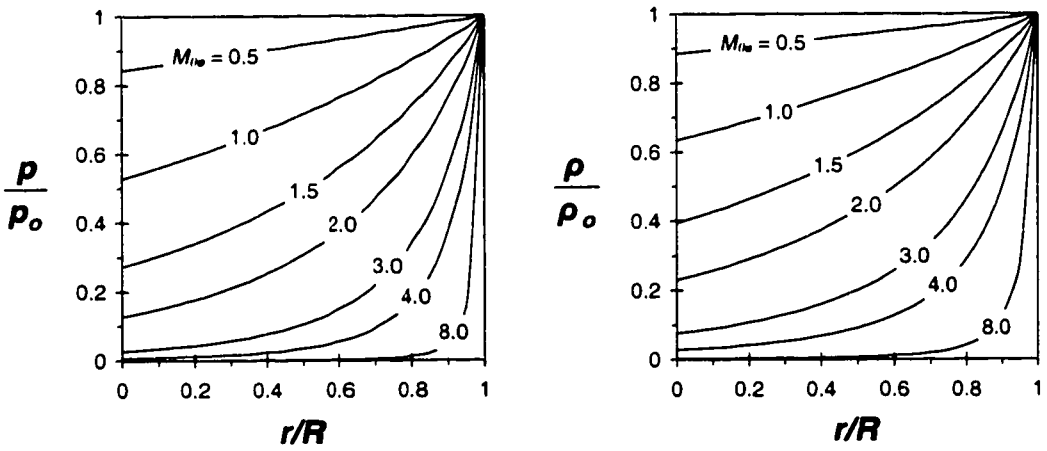

Figure 2.10 Radial pressure and density distributions for solid body rotation, normalized by edge values.

Eddies are seen to be formed by the penetration of the developing shear layer from top and bottom by reciprocal tongues of high and low speed fluid. Consideration of momentum balance in the azimuthal direction and observation of the typical eddy lifespan of about one rotation immediately allows conclusion that there is inadequate time for the establishment of such dynamic mass distribution. Rather, at high Mach number,

fluid already present within the core region at the time of penetration of an incoming tongue will respond to the induced gradients and produce a reciprocal tongue more locally. In essence, pinching of the entering fluid into eddies of smaller scale would be expected. A breakdown in the scale of turbulence is, in fact, generally observed, lending credence to predictions of Breidenthal, based on the assumption that eddies formed at a reduced scale, corresponding to a sonic edge Mach number, act as the functional machinery of entrainment.[16]

Noting the similarity in trends verses Mach number of p/p_o profiles of Figure 2.9 and the data of Figure 2.6, an alternative to Equation 2.13 is suggested based on this parameter, or rather the isentropically related density ratio. It has been above noted that structural similarity is not preserved between incompressible and highly compressible mixing, thus the mechanism of transition is not simply related to the density ratio. Nevertheless, the above arguments indicate that displacement effects surely must act to some degree on the core density of the observed small scale eddies, perhaps setting the very scale of the effective entraining structures, and, in fact, displacement associated with combustive heating of the eddy core is known to adversely affect mixing.[7] Additionally, the existence of large-scale structures is evidenced by Hall et al.[8] Thus, it is not surprising that a relatively simple fit based on the displacement ratio, ρ_c/ρ_o, at the center of a hypothetical eddy with edge Mach number equal to M_{c1}, can be obtained as follows:

$$\frac{(\delta/x)}{(\delta/x)_{inc.}} = 1 - 0.2\left\{1 - \left(\frac{\rho_c}{\rho_o}\right)^6\right\} \qquad 2.20$$

Equation 2.20, superimposed on Figure 2.6 in Figure 2.11, essentially equates $(\delta/x)/(\delta/x)_{inc.}$ to this displacement ratio to the best fit power, with an asymptote artificially inserted to enforce the experimentally observed:

$$\lim_{M_c \to \infty} \frac{(\delta/x)}{(\delta/x)_{inc.}} \approx 0.2 \qquad 2.21$$

Here the sixth power seems to provide the best correspondence, but this exponent is

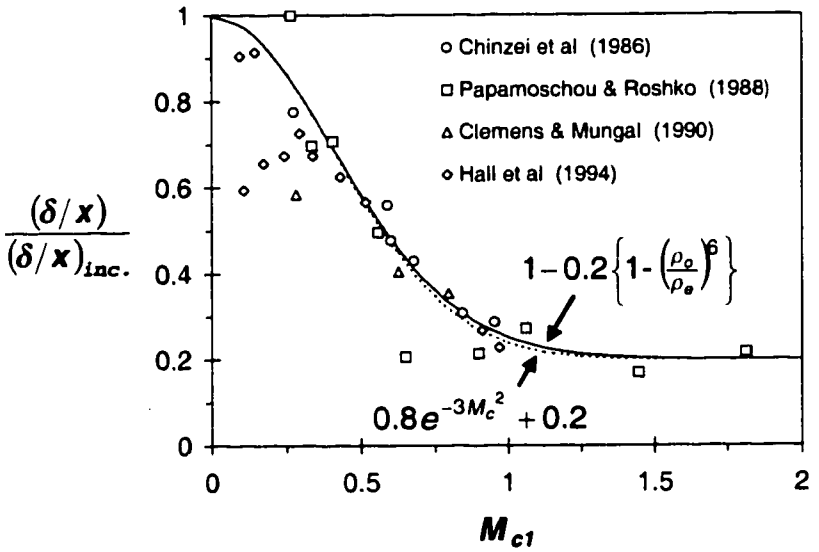

Figure 2.11 Mach number influence on mixed layer growth as reported by various experimenters. Curve fits superimposed.

likely in actuality to vary with γ, and, not to be further explored here, may provide an interesting avenue for continued research. Additionally, experimental measurement of time-averaged density distribution across the shear layer would be of value in providing a direct estimate of the significance of displacement effects.

2.5 Nozzle Design

The equations and techniques for estimating total pressure loss and mixing length of the preceding section form an almost complete package for blade mixing nozzle design. A single issue remains - the determination of the ideal number of blades in the array. Dimensional arguments demonstrate that mixing length scales with blade spacing, i.e., inversely with the number of blades. Practical considerations dictate, however, that there cannot be an infinite array of infinitely thin blades, leading one to perhaps initially surmise, based on data presented in Figure 2.3, that frictional total pressure losses might ultimately limit the fineness of nozzle scale. This would surely be the case, were not an additional consideration to intervene.

Feedstock must enter the hollow blade through either one or both of the ends, (the

next chapter will address the role of thermal expansion in this respect) and must negotiate a 90° flow turn in order to exit through the trailing edge throat and nozzle. In order to avoid excessive loss of spanwise effluent uniformity, it must necessarily be concluded that the flow at the blade inlet must be well subsonic. The internal cross sectional area of the blade must therefore be large relative to the total exiting throat area, representing a far more stringent limit on blade number than that imposed by viscous considerations.

To obtain an estimate of the maximum possible blade number, one must first gauge the maximum allowable Mach number of the feedstock flow as it enters the feed end of the blade. Note that while the spanwise internal pressure distribution may be obtained within reasonable approximation via the solution of a nonlinear ordinary differential equation, the fact that only the maximum pressure difference is of actual interest here provides great simplification. As the spanwise component of the internal flow velocity must vanish at either the far end from the feed or centerline for nozzles fed from one or both ends, respectively (see Figure 2.12), one may conclude from a momentum balance over a control volume enclosing this portion of the internal flow that the minimum and maximum of the pressure distribution occur at the spanwise extrema of this control volume. It is easy to show that the normalized pressure difference across this span will scale with the square of the inlet Mach number:

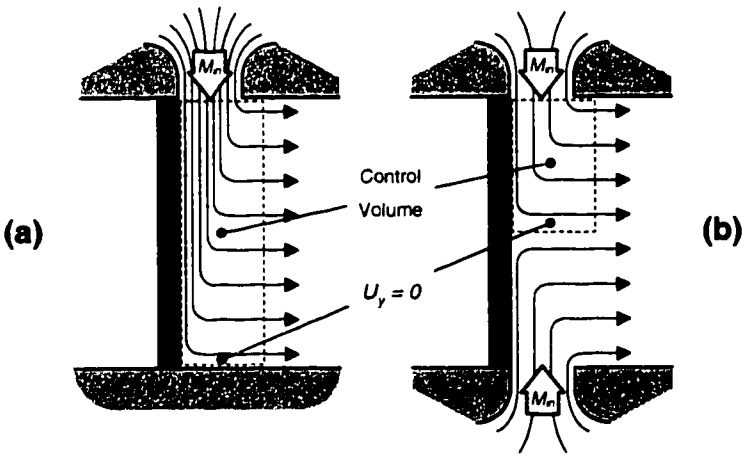

Figure 2.12 Control volume sketches for (a) singly and (b) doubly fed blade nozzles.

$$\frac{\Delta p}{p_{in}} = \gamma M_{in}^{\ 2} \qquad 2.22$$

At M_{in} = 0.2 the pressure varies by approximately 5% across the blade span. A feed Mach number of 0.3, with resulting variation approaching 10%, can be considered a practical upper limit at which the exit stream may be assumed essentially homogeneous. In turn, ignoring frictional effects, the maximum acceptable Mach number may be isentropically related to a minimum feed-to-throat area ratio, a parameter which may be considered characteristic and henceforth denoted as ω. Examination of an example nozzle pair cross-section to arrive at the straightforward geometric observations:

$$w = h_p + h_f - h_p^* = \left(\left.\frac{A}{A^*}\right|_p - 1 \right) h_p^* + \left.\frac{A}{A^*}\right|_f h_f^* \qquad 2.23$$

where variables are as diagrammed in Figure 2.13, subscripts p and f designate plenum versus feedstock, respectively, and A/A^* ratios of exit-to-throat area.

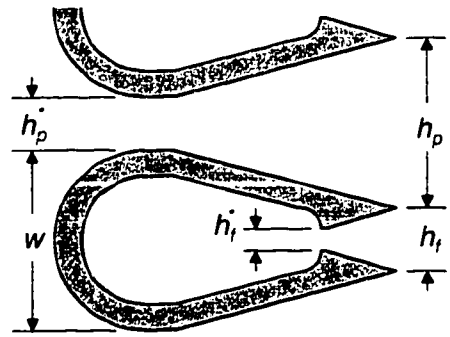

Figure 2.13 Blade nozzle characteristic cross-sectional parameters.

The analysis may further proceed by defining a shape factor, K_A, such that the nozzle blade feed area is exactly equal to K_A multiplied by the square of the external width w, i.e.,

$$K_A \equiv \frac{\text{Feed Area}}{w^2} \qquad 2.24$$

By enclosing all information on the particular blade geometry within the parameter K_A, blades of many types can be treated quite generally. Any blade of a given geometry will have a single value of K_A, regardless of scale. Increasing values of K_A designate elongation of the nozzle blade, which, while technically may lie anywhere between limits of zero and infinity, ranging from infinitely narrow to infinitely wide blades, for typical cases will fall between 1 and 3. (Additionally, it may perhaps be helpful to here direct attention to the fact that K_A will vary by a factor of two between cases where nozzle blades receive feedstock from either one or both ends; that is, K_A for a double feed nozzle will be twice that for one fed from a single end.)

Designating the blade span as H and feed-to-throat area ratio as per above, one may write:

$$\omega \equiv \frac{\text{Feed Area}}{\text{Throat Area}} = \frac{K_A w^2}{h_f^* H} = \frac{K_A\left[\left(\left.\frac{A}{A^*}\right|_p - 1\right)h_p^* + \left.\frac{A}{A^*}\right|_f h_f^*\right]^2}{h_f^* H} \qquad 2.25$$

which, when divided through by h_f^*, may be rearranged to yield:

$$\mathbf{AR}_{throat} = \frac{K_A}{\omega}\left[\left(\left.\frac{A}{A^*}\right|_p - 1\right)\frac{h_p^*}{h_f^*} + \left.\frac{A}{A^*}\right|_f\right]^2 \quad \text{where} \quad \mathbf{AR}_{throat} \equiv \frac{H}{h_f^*} \qquad 2.26$$

Having now defined the blade nozzle throat aspect ratio for the design feed-to-throat area in parameters which will later be resolved in terms of Mach numbers, the number of blades that will fit upstream of a mixing region with a given inlet width, W, and aspect ratio, $\mathbf{AR}_{inlet}$, may now be determined. Beginning again with geometric observations:

$$W = n_p h_p + n_f h_f = n_f h_f^*\left(\left.\frac{A}{A^*}\right|_p \frac{h_p^*}{h_f^*} + \left.\frac{A}{A^*}\right|_f\right) + \left(n_p - n_f\right)h_f^* \left.\frac{A}{A^*}\right|_p \frac{h_p^*}{h_f^*} \qquad 2.27$$

Here different variables, n_p and n_f, have been assigned for the number of carrier and feedstock nozzles, respectively, as they need not be identical. For instance, the array may be bounded by an extra half pair of plenum nozzles to isolate the reactants from the boundary-layer flow in the mixing region (as in the experiments presently to be discussed

in Sections 2.5-2.7 and Chapter 3 where $n_p - n_f = 1$).

Dividing through by H the above expression may be rearranged to yield:

$$n_f = \frac{\dfrac{\mathbf{AR}_{throat}}{\mathbf{AR}_{inlet}} - \left(n_p - n_f\right)\left.\frac{A}{A^*}\right|_p \frac{h_p^*}{h_f^*}}{\left.\frac{A}{A^*}\right|_p \frac{h_p^*}{h_f^*} + \left.\frac{A}{A^*}\right|_f} \quad \text{where} \quad \mathbf{AR}_{inlet} \equiv \frac{H}{W} \tag{2.28}$$

By substituting for $\mathbf{AR}_{throat}$ from Equation 2.26, the final result for the maximum possible blade number, n_{max}, is obtained:

$$n_{\max} = \frac{\dfrac{K}{\omega \mathbf{AR}_{inlet}}\left[\left(\left.\frac{A}{A^*}\right|_p - 1\right)\frac{h_p^*}{h_f^*} + \left.\frac{A}{A^*}\right|_f\right]^2 - \left(n_p - n_f\right)\left.\frac{A}{A^*}\right|_p \frac{h_p^*}{h_f^*}}{\left.\frac{A}{A^*}\right|_p \frac{h_p^*}{h_f^*} + \left.\frac{A}{A^*}\right|_f} \tag{2.29}$$

where the exit-to-throat areas may be computed via the well known 1-D isentropic relationship:

$$\left(\frac{A}{A^*}\right)^2 = \frac{1}{M^2}\left[\frac{2}{\gamma+1}\left(1 + \frac{\gamma-1}{2}M^2\right)\right]^{\frac{\gamma+1}{\gamma-1}} \tag{2.30}$$

and h_p^*/h_f^* may be shown from continuity arguments and isentropic relations to be:

$$\frac{h_p^*}{h_f^*} = \phi \frac{p_f/p_p}{\sqrt{T_{tf}/T_{tp}}} \frac{M_f}{M_p}\left[\frac{(M.W.)_f}{(M.W.)_p}\left(\frac{\gamma_f}{\gamma_p}\right)\frac{1 + \frac{\gamma_f - 1}{2}M_f^2}{1 + \frac{\gamma_p - 1}{2}M_p^2}\right]^{1/2} \tag{2.31}$$

where ϕ is the design carrier-to-feedstock mass flow ratio and, as previously, $(M.W.)$ represents molecular weight. Thus Equation 2.29 illustrates the dependence of the allowable blade number on choice of feedstock and carrier Mach numbers at the mixing region entrance, given characteristic parameters, γ_f, γ_p, ϕ, and $\mathbf{AR}_{inlet}$, as well as feedstock-to-carrier total temperature and nozzle exit static pressure ratio, T_{tf}/T_{tp} and p_f/p_p, respectively. (Here p_f/p_p has been included as a parameter, but, in order to avoid shock losses, will generally be specified at unity.)

Figure 2.14 represents a contour map of Equation 2.29 with γ_f = 1.09, γ_p = 1.2, $\mathbf{AR}_{inlet}$ = .5, ω = 3, ϕ = 6.5 (corresponding to values ultimately chosen for the Shock Wave Reactor proof-of-concept experiment). For simplicity, $n_p = n_f$. Lines of constant n_{max}/K_A are plotted vs. the feed and carrier mixing region inlet Mach numbers. One may interpret the mapping as representative of the maximum blade number for the K_A = 1 case, but may apply the contours to blades with differing values of K_A without generating an additional diagram. For that matter, because of the assignment $n_p = n_f$, contours of constant $(n_{max}\omega\mathbf{AR}_{inlet})/K_A$, might, more generally, be mapped, not done here in order that interpretation be straightforward.

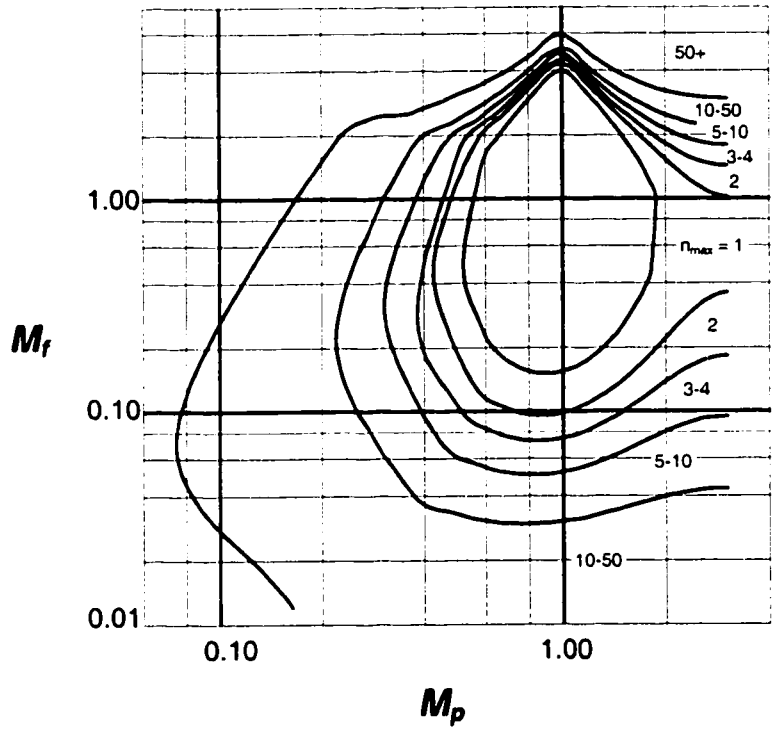

Figure 2.14 Maximum blade number as function of feed and plenum Mach numbers.

The above procedures now completely prescribe a design balance between mixing distance and total pressure losses as a function of $\mathbf{AR}_{inlet}$, K_A and feedstock and carrier Mach numbers at the mixing region inlet for any apparatus of rectangular cross section,

given feedstock and carrier composition approximately determine parameters p_{tf}, p_{tp}, T_{tf}, T_{tp}, and ϕ through thermo-chemical considerations. The above treatment may be considered as a guide for similar analysis of devices of other cross-sectional geometry, but no additional cases will be explored here.

Ultimately, design of the blade external contour proceeded more from feed considerations than concerns regarding total pressure losses. The need to maintain a high geometric feed parameter, K_A, (in order to provide sufficient cross-sectional area for adequate feed flow,) led to the selection of blades with a steeper outer nozzle wall divergence of 20° in the stead of the 10° favored by minimization of total pressure losses alone. To reclaim some of the efficiency associated with low shock losses of more shallowly angled nozzles, and to provide wall rigidity in the neighborhood of the internal throat, the nozzle wall divergence angle abruptly transitions from 20° to 10° near the trailing edge. Thus, the carrier streams encounter two 10° bends rather than endure the higher total pressure loss of a single 20° change in direction.

The purpose of this design procedure was to provide, within the specified time schedule, a functional device for implementation within the Shock Wave Weactor preliminary design and proof-of-concept experiments. Certainly development within this limited interval cannot be considered exhaustive of all possibilities and avenues for improvement, but stands as an acceptable first step in the adaptation of nozzle arrays (they have long been employed in gas dynamic lasers) to use in industrial processes, such as the Shock Wave Reactor.

2.6 Cold Flow Experiments

Because the Shock Wave Reactor's high enthalpy steam and ethane flows severely limit diagnostic capability in the proof-of-concept experiment, a blow down supersonic air tunnel of similar geometry, shown in schematic in Figure 2.15 and photograph in Figure 2.16, was constructed to investigate the relevant fluid mechanics.[9] The facility employs a stainless steel array of blade nozzles (Figure 2.17), alternating four feed and five plenum flow nozzles, across a 10 cm span at the entrance to an aluminum

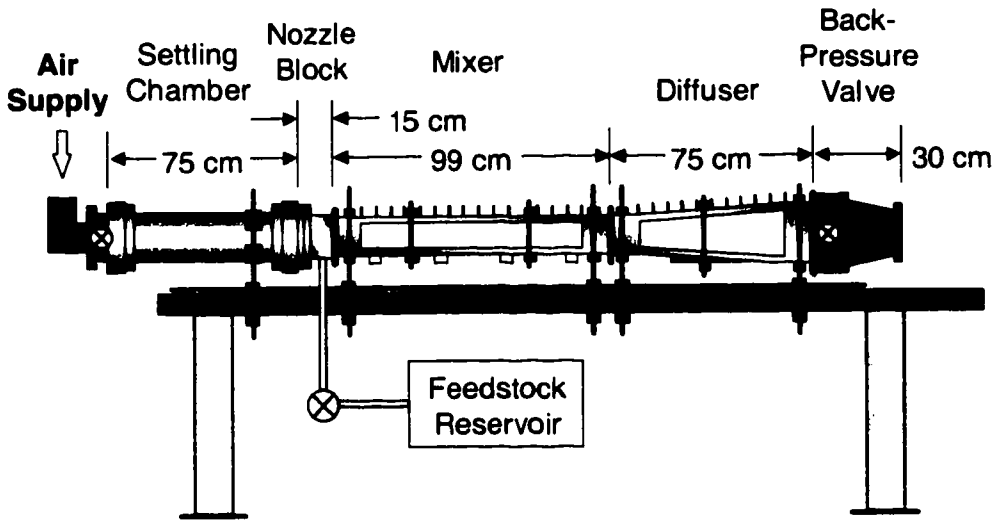

Figure 2.15 Schematic of cold flow facility

mixing channel of 5 x 10 cm cross section. Plenum and feedstock nozzle exit to throat area ratios were 2.35 and 2.05, respectively. An additional section, mimicking the flow diffusing reaction zone of the proposed proof-of-concept experiment (See Chapter 3), diverged the flow cross section from the 5 x 10 cm mixing chamber exit to 14.2 cm square over a distance of 75 cm, terminating in a 15.3 cm butterfly valve, used to control back pressure. Instrumentation included Newark Electronics model MPX-2200ASX

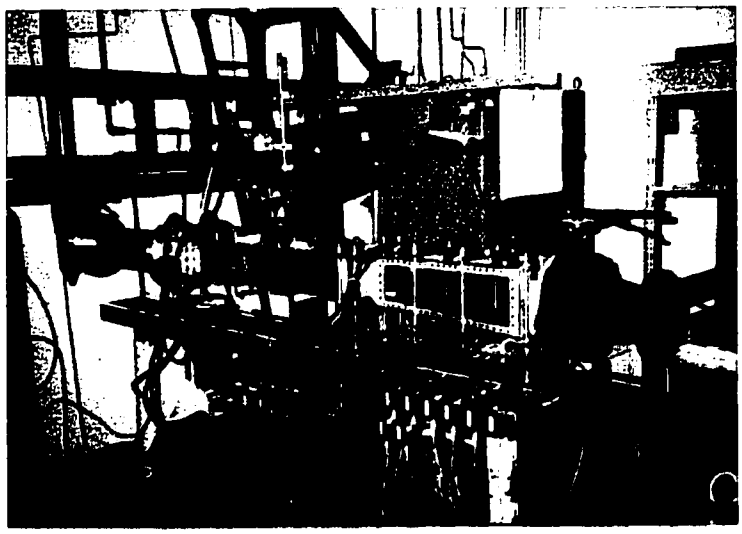

Figure 2.16 Cold flow facility.

Figure 2.17 Mixing nozzle array

pressure transducers, connected to ports spaced at 5.7 cm intervals along the centerline of the test sections' upper sidewalls, and a four-element sampling rake with adjustable spacing, which entered the flowfield through one of four evenly spaced ports on the opposite wall of the mixing section. Samples were analyzed with a SRI Instruments model 8610 gas chromatograph utilizing a single element thermal conductivity detector.

Pairs of rectangular 10 x 80 and trapezoidal 10.8-14.0 x 54 cm windows set opposite each other provided visual access for a double pass schlieren system on each of the mixing and diffusing sections, respectively. Light sources employed by the schlieren system included a 50 mW argon-ion laser and a 70 W mercury-vapor arc lamp. To circumvent limitations imposed by the narrow scope of the viewing area provided by its 20.3 cm round mirrors (as compared with the 80 cm span of the mixing section windows), the entire visualization apparatus was mounted upon casters, allowing the view area to traverse the entire section window while a video camera recorded images. Thus, provided steady flow had been established prior to the traverse, video frame capturing equipment and subsequent manual image assembly on a computer enabled the construction of complete quasi-steady images of the entire flowfield within view of the windows. Taking advantage of the high difference in index of refraction, injection of

helium "feedstock" into an air plenum flow was employed in all cases involving schlieren videography.

2.7 Results of Cold Flow Experiments

Figure 2.18 was reproduced from schlieren video scans of Mach 2.4 helium injection into an air carrier flow, also at Mach 2.4, superimposed on a plot of theoretical mixing distance normalized by the nozzle centerline spacing, *x/d*, as calculated from the procedure of Sections 2.1 and 2.2. For comparison, calculations employing both the isolated-streams and the (more accurate) pressure-matched conditions are demonstrated, i.e., either Equations 2.8 (a or b) or 2.10 are employed in the respective cases. For simplicity, mixing here is considered complete after a single traverse of the flow section by mixed fluid. Interestingly both calculations adequately predict the observed trend in mixing distance with diminishing feed-to-plenum total pressure ratio, and are, in fact, virtually indistinguishable with the exception of some 20% in magnitude. Here, to facilitate comparison, the constant in the Brown-Dimotakis mixing length is assigned the same value of 0.2, corresponding to that necessary to bring the pressure matched-curve

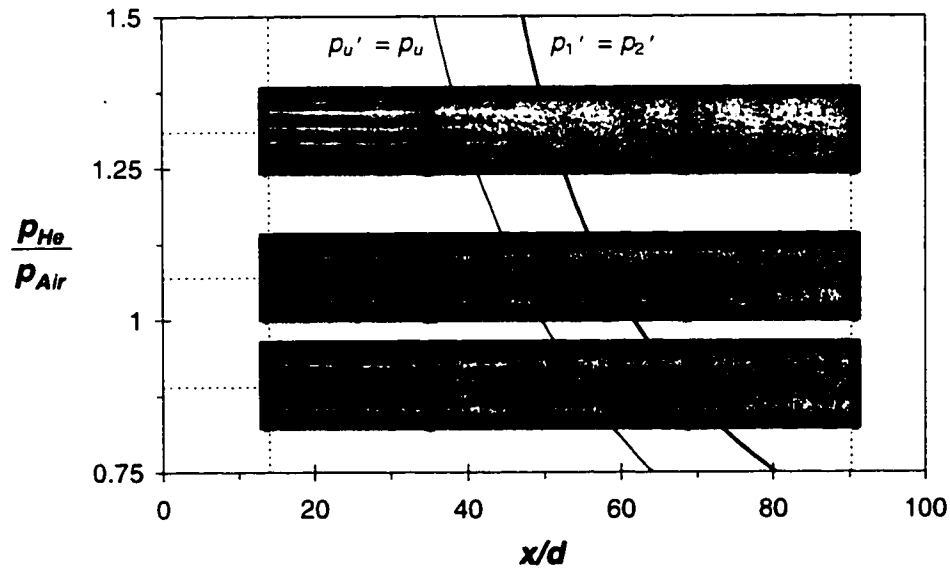

Figure 2.18 Schlieren video scans for various feed-to-plenum pressure ratios superimposed on plots of predicted mixing distance.

into agreement with the data, in both computations. With appropriate adjustment of this constant in the isolated-stream procedure, the results are essentially equivalent. This is of interest in light of the fact that the isolated-streams procedure, while not strictly physically correct, yields its solution in the form of explicit relationships. Such is not the case for the more complex equation set of the more rigorous technique.

The nozzle employed by the cold flow facility was designed of similar geometry to that which would ultimately be utilized in the proof-of-concept experiment; the throat-to-exit area ratios of adjacent nozzles were chosen so as to achieve interleaved streams at Mach 2.2 and 2.0 with plenum and feedstock flows of high temperature steam ($\gamma = 1.2$) and ethane ($\gamma = 1.09$), respectively. Substitution of plenum air and helium feedstock, while useful in evaluating the computational procedure of Sections 2.2 and 2.3, produces a substantially different mixing case, when the incipient velocity difference across the shear layer is considered. Owing to the large differences in total temperature ratio and, especially molecular weight (particularly when comparing ethane verses helium feedstock), the relatively small changes in exiting Mach number of the plenum and feedstock flows, due to differing specific heat ratios, correspond to very large differences in U_f/U_p, approximately 0.6 for the design fluids (at $T_{tf}/T_{tp} = {}^1/_2$) verses 2.6 for those actually used in the cold flow experiment ($T_{tf}/T_{tp} = 1$). Thus, experiments involving the injection of helium into air represent a very different, jet-like mixing process as compared with the wake-like process of ethane into steam. In one case the smaller of the two mixant streams has much greater velocity than the larger while for the other case the extreme opposite is true.

In subsequent cold facility experiments conducted to expand the data set to include cases more similar to injection of ethane into steam, carbon dioxide replaced helium as the feedstock. Because lack of dissimilarity between the indices of refraction of air and carbon dioxide prevented the use of schlieren photography to image mixing for these cases, an alternative visualization technique was employed. As the feedstock stream (which begins the experiment at a total temperature equal to ambient) expands to a nozzle exit Mach number of approximately 2.2, some of the carbon dioxide condenses,

allowing the stream to be viewed by simple, direct illumination of solid particles as shown in Figure 2.19a. A sampling rake, previously mentioned, with probes evenly spaced over a 2 cm span bordering the channel centerline (seen at right of figure), enabled the direct comparison of visual and sampled data. Figure 2.19b spatially resolves CO_2 mole fraction of (time-averaged) samples taken for the case shown in 4a, at x/d = 33.8.

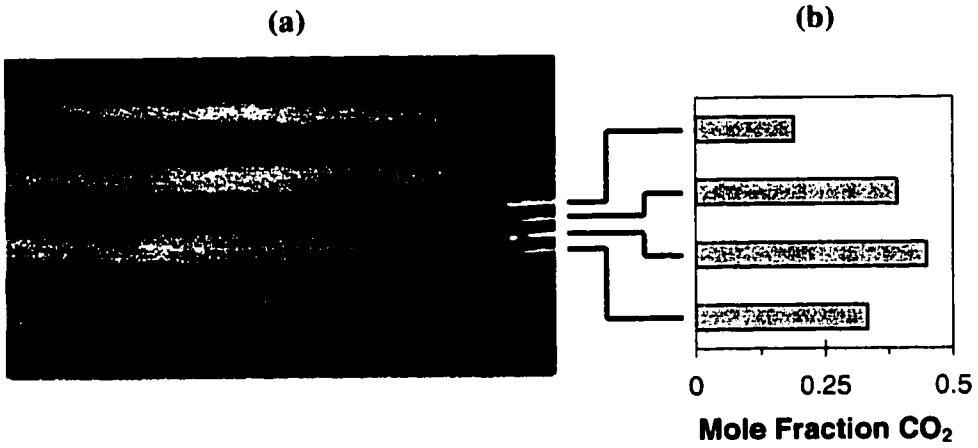

Figure 2.19 (a) Sampling probe rake with CO_2 injection in air displayed beside (b) results of analysis.

For purposes of quantitative comparison of data taken at various stations and feed-to-plenum pressure ratios, the normalized mean-square standard deviation of CO_2 mole fraction, σ, for the four probes is plotted in Figure 2.20. (For this particular probe spacing, exactly equal to the nozzle spacing, σ may vary from approximately unity to zero for the completely unmixed and mixed states, respectively.) It is observed that the rate of mixing is rapid initially, and decays downstream. This and the notable improvement in mixing efficiency as a function of increasing feed-to-plenum ratio agree well with analytic predictions of Sections 2.2 and 2.3.

Of course, the heat of sublimation is released into the flow as the CO_2 freezes, and in turn raises the temperature to limit further freezing and counter the drop in pressure. CO_2 particle visualization must therefore be considered valid only in cases where the net influence of these mutually opposing effects on Mach number is small. It may further be

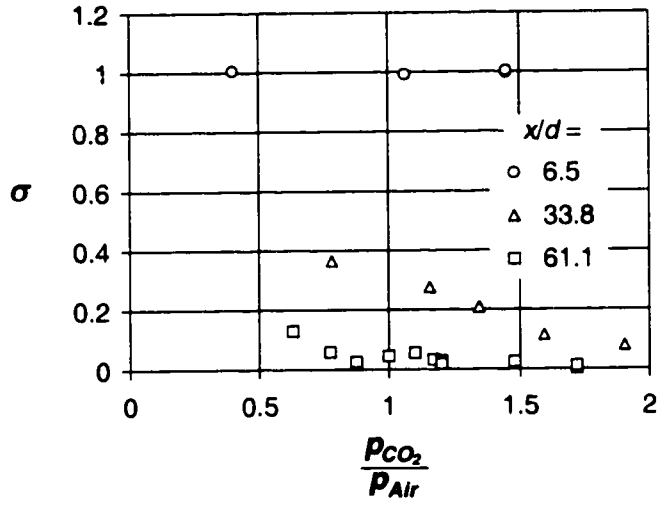

Figure 2.20 Mean-square standard deviation vs. feed-to-plenum pressure ratio for x/d = 6.5, 33.8, and 61.1.

deduced that at low concentrations, condensation levels must primarily reflect CO_2 mole fraction, while beyond a certain temperature-dependent saturation concentration, CO_2 condensation becomes solely dependent on thermodynamic properties of the flowfield. This is due to the fact that at low CO_2 levels, all of the available CO_2 will freeze, but at high concentrations, the amount of condensate will be directly a function of the energy sink available to absorb the heat of sublimation.

The sensitivity of pure CO_2 injection is expected, therefore, to be somewhat limited as an effective diagnostic for mixing. In Figure 2.21, curve fits of streamwise σ variation generated from the data of Figure 2.20 are plotted below a video image of illuminated CO_2 condensation. Visible stratification of the flowfield demonstrates clear decline throughout the early stages of mixing where σ varies from unity to 0.1, but the completion of mixing beyond this point corresponds to no obvious visual progression. While this is not of great importance for the linear mixing case of simple shear layers, it represents a critical diagnostic shortcoming in the measurement of the wake-like mixing of the Shock Wave Reactor, where the last stages of mixing comprise a much larger component of the total mixing length. The ultimate result of this inability is that variation of feed-to-plenum pressure ratio (measured to produce significant differences in mixing

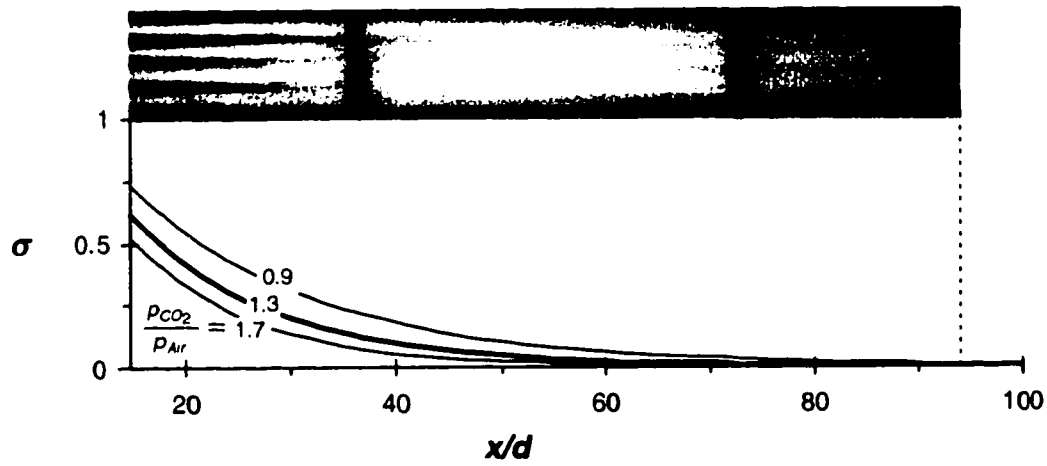

Figure 2.21 Sample mean-standard deviation streamwise variation for feed-to-plenum pressure ratios of 0.9, 1.3, and 1.7. Photograph of CO_2 condensation for 1.3 case superimposed.

length) is observed to have only subtle visual consequence. Tests with mixed gas injectant streams with CO_2 levels below saturation are recommended for the further evaluation of this technique as a tool for flow visualization, but would, in fact, be somewhat off the subject here. Note, however, that the saturated flow in the last half of the section resolves the growth of the thermal boundary-layer quite well.

2.8 Flow Visualization of Shock Structure

The shock system within the reactor is of critical importance, for it is by design the primary factor controlling temperature history. Thus, while the primary focus of preliminary cold flow experiments was supersonic mixing, initial, cursory studies of the shock wave systems within the reactor were also conducted prior to construction of the proof-of-concept experiment, to access the magnitude of shock disturbances generated by the nozzles array (particularly with respect to off-design performance) and (especially) to forecast the general character and stability of the reaction-initiating recompression system. The influence of varying the feed-to-plenum pressure ratio on the oblique shock system emanating from the nozzle array may be observed in Figure 2.18. Interestingly, the oblique shock system is seen to lengthen significantly at lower values, but appears relatively insensitive to increases beyond the design pressure ratio of one. This

presumably results as a consequence of the very different exit areas of adjacent nozzles.

Figure 2.22 presents a schlieren video scan of the normal shock train (with no feed injection) superimposed over a plot of measured streamwise static pressure distribution. (Here the abscissa has been normalized by the 10 cm mixing section height, h, rather than the nozzle half-span, in deference to the expected scaling of the recompression system.) The shock train appears to oscillate around an average position, controllable through upstream and/or back pressure adjustments. The stability of the location and length of the shock train are found to increase with the boundary-layer thickness in concurrence with other investigations[17,18].

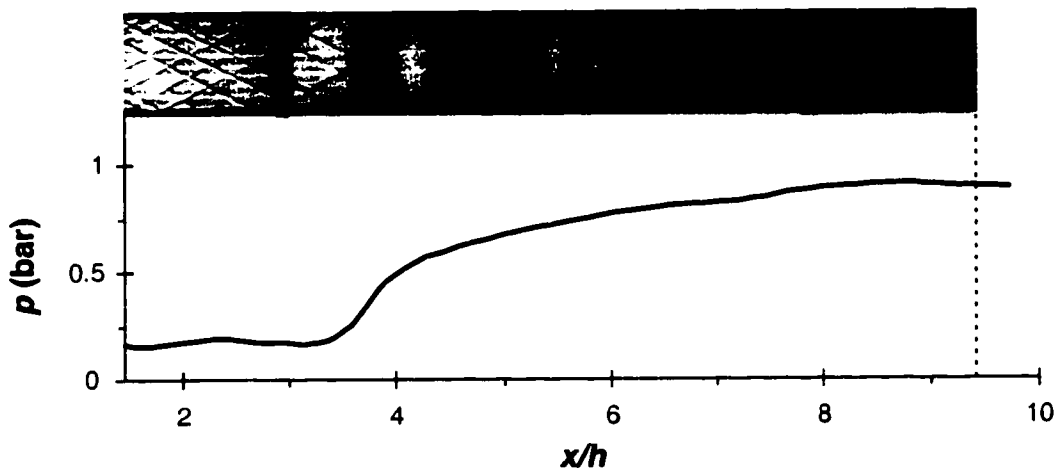

Figure 2.22 Schlieren video scan of mixing-section flow without feedstock injection, superimposed over pressure distribution.

In Figure 2.23, some of the thermal characteristics of a normal shock train are illuminated through CO_2 condensation. While previously discussed sensitivity limits permit distinct resolution of only the first lambda shock, the initial instantaneous reduction at about midsection followed by a gradual decrease in visible CO_2 indicates that the image intensity corresponds well with a temperature recovery history normally associated with the measured pressure profile. Thus, one may infer a direct relationship between condensation intensity and temperature for uniformly mixed flows.

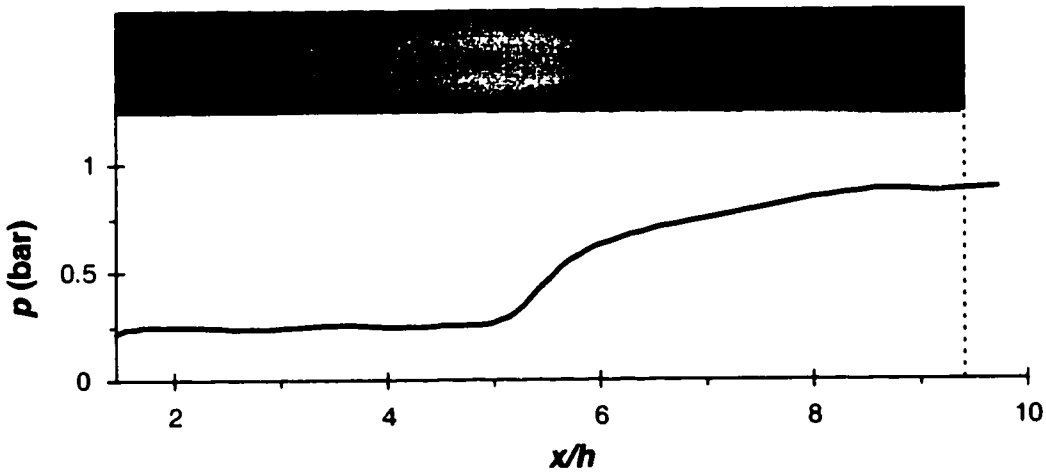

Figure 2.23 Photograph of CO_2 condensation in mixing section superimposed over pressure distribution.

2.9 Conclusion of Cold Flow Experiments

Data gathered during the approximately one year of design, construction, testing and operation of the cold flow facility proved invaluable in the development of the proof-of-concept experiment. With adequate analytical models proposed and tested, uncertainties in the fluid dynamic design considerations concerning mixing were minimized. Additionally, while adherence to a manditorally strict experimental schedule (to achieve proof-of-concept within specified deadlines) prevented detailed study of the shock structure during the initial experimental development phase, necessary assessment of shock stability was achieved. The recompression region was observed to oscillate at a half-section-width amplitude around a stable mean position, very nearly invariant throughout the approximately one minute time scale required for the proposed hot flow experiment.

2.10 Notes to Chapter 2

1. Russell, D. A., "Fluid Mechanics of High Power Grid Nozzle Lasers," AIAA Paper 74-223, January 1974.

2. Russell, D. A., Neice, S. E., and Rose, P. H., "Screen Nozzles for Gas Dynamic Lasers," *AIAA Journal*, Vol. 13, No. 5, 1975, pp. 593-599.

3. White, F. M., *Viscous Fluid Flow*, 2nd edition, McGraw-Hill Book Company, New York, NY, 1991.

4. Cohen, C. B., and Reshotko, E., "Similar Solutions for the Compressible Laminar Boundary Layer with Heat Transfer and Pressure Gradient," NACA Report 1293, 1956.

5. Brown, G. L., "The Entrainment and Large Structure in Turbulent Mixing Layers," *Proceedings of the 5th Australasian Converence on Hydraulics and Fluid Mechanics*, Univ. of Canterbury, Christchurch, New Zealand, 1974, pp. 352-359.

6. Dimotakis, P. E., "Two-Dimensional Shear-Layer Entrainment," *AIAA Journal*, Vol. 24, No. 11, 1986, pp. 1791-1796.

7. Dimotakis, P. E., "Turbulent Free Shear Layer Mixing and Combustion," *High Speed Flight Propulsion Systems*, Edited by S.N.B. Murphy and E.T. Curran, Vol.137, pp. 265-340, Progress in Aeronautics and Astronautics, AIAA, Washington, DC, 1991, Chapter 5, pp. 265-340.

8. Hall, J. L., Dimotakis, P. E., and Rosemann, H. "Experiments in Nonreacting Compressible Shear Layers," *AIAA Journal*, Vol. 31, No. 12, 1993, pp. 2247-2254.

9. Masse, R. K., Knowlen, C. Mattick, A. T., and Russell, D. A., "A Flow Visualization Study of Supersonic Mixing and Shock Structure," *Proceedings of the Seventh International Symposium on Flow Visualization*, Seattle, WA, 1995, pp 847-852.

10. Papamoshchou, D., and Roshko, A., "The Compressible Turbulent Shear Layer: An Experimental Study," *Journal of Fluid Mechanics*, Vol. 197, Dec. 1988, pp. 453-477.

11. Clemens. N. T., and Mungal, M. G., "Two- and Three-Dimensional Effects in the Supersonic Mixing Layer," AIAA Paper 90-1978, July 1990.

12. Chinzei, N., Masua, G., Komuro, T., Murasakami, A., and Kudou, K., "Spreading of Two-Stream Supersonic Turbulent Mixing Layers," *Physics of Fluids*, Vol. 29, No. 5, 1986, pp. 1345-1347.

13. Bogdanoff, D. W., "Compressibility Effects in Turbulent Shear Layers," *AIAA Journal*, Vol. 21, No. 6, 1983, pp. 926-927.

14. Papamoschou, D., "Structure of the Compressible Turbulent Shear Layer," *AIAA Journal*, Vol. 29, No. 5, 1991, pp. 680-681.

15. Adapted from Hall, J. L., Dimotakis, P. E., and Rosemann, H. "Experiments in Nonreacting Compressible Shear Layers," *AIAA Journal*, Vol. 31, No. 12, 1993, pp. 2247-2254.

16. Breidenthal, R. E., "Sonic Eddy-A Model for Compressible Turbulence," *AIAA Journal*, Vol. 30, No. 1, 1992, pp. 101-104.

17. Lukasiewicz, J., "Diffusers for Supersonic Wind Tunnels," *Journal of the Aeronautical Sciences*, Sept. 1953, pp. 617-626.

18. Chen, C. P., Sajben, M., and Kroutil, J. C., "Shock-Wave Oscillations in a Transonic Diffuser Flow," *AIAA Journal*, Vol. 17, No. 10, 1979, pp. 1076-1083.

3. Proof-of-Concept Experiment

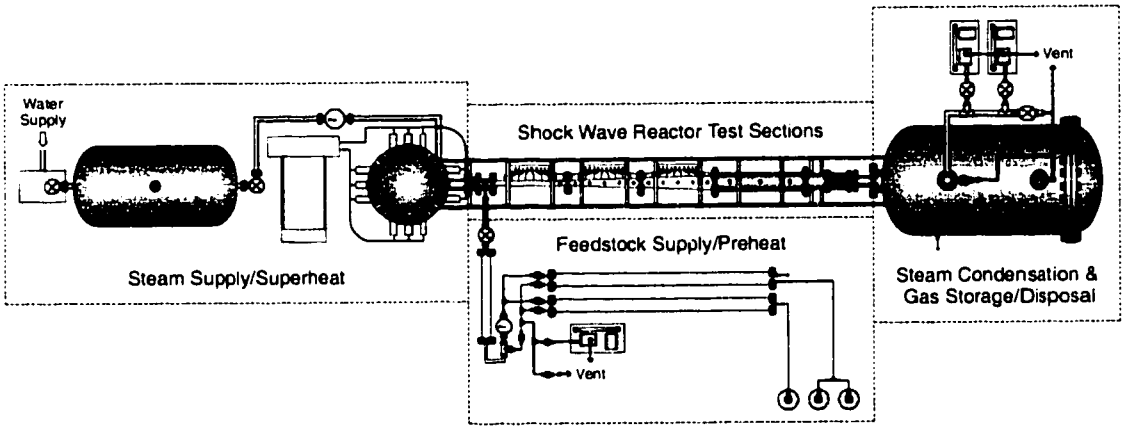

Figure 3.1 Schematic of proof-of-concept facility (top view).

In an industrial setting, a Shock Wave Reactor would represent the heart of a large facility providing a continuous supply of steam and feedstock, as well as steady channeling away of output to post-pyrolysis separations and processing. It is therefore quite natural that the proof-of-concept experiment should be comprised only in small part by the actual pyrolysis device, but rather, primarily of support equipment simulating the various surrounding plant operations. In providing a description of the proof-of-concept experimental facility it is therefore logical to begin by dividing the apparati into four

Figure 3.2 Photograph of experimental facility.

basic groupings which include, in addition to the shock wave pyrolysis device itself, three supporting systems consisting of superheated steam generation equipment, preheated feedstock supply system, and a waste gas disposal system. Each of the auxiliary components, followed by the test Shock Wave Reactor will here be briefly described. The complete assembly is shown in schematic in Figure 3.1 and photograph in Figure 3.2.

3.1 Superheated Steam Supply System

Providing an adequate supply of sufficiently superheated steam proved to rank among the most challenging of the design tasks associated with the hot flow experiment. Early on, it became apparent that the energy requirements of a system capable of sustained (steady-state) supply of the approximately half kilogram per second, ~1500 K steam required for the experiment would be unfeasible and unnecessary. In place of direct, "on the fly" heating of the carrier flow, heat transfer from an insulated, previously heated (gradually, at lower power) thermal mass was selected as the method of steam superheating. Such a capacitive heater allows heat from a relatively low power electric source to be stored over a period of several hours and then extracted at much higher transfer rates during the experimental run time of approximately one minute. As long as the capacitive bed is sufficiently large, a steady-state output temperature at exactly the bed temperature is achievable over a specified design duration due to the fact that as the fluid to be heated enters the exchange region, only the initial location of thermal contact within the bed loses heat (assuming conduction may be neglected in comparison to convection). Subsequent contact with downstream portions of the bed is ineffective, as the gas is already at temperature. Thus a wave of localized cooling is seen to propagate from inlet to outlet of the capacitive heating bed with an essentially constant output temperature until after this traverse.

With the objective of gaining the benefit of pre-existing expertise and manpower in order to save time and allow concentration on the truly experimental aspects of the Shock Wave Reactor, design of the superheated steam supply system was subcontracted

shortly after the project outset to Phoenix Solutions, Inc. (Note evaluation in Appendix C.) The delivered system, shown in schematic at the right of Figure 3.1 and enlarged in Figure 3.3, consists of a 12 kW Chromalox model CES-006AS010-205 boiler which maintains an accumulated 3 m^3 of 6.8 bar saturated steam within a connected storage tank. Separated from the tank by a 2.5 cm solenoid activated valve and a 6.5 cm Armstrong model GP-11 reducing valve (flow controller) is a capacitive heater, employing a vertically oriented 64 cm diameter, 60 cm high cylindrical bed of 12-19 mm diameter aluminum oxide spheres, electrically heated by eighteen Kanthal DS silicon carbide elements. (See schematic in Appendix D.) Flow exiting the top of the bed turns ninety degrees and passes through a nozzle (a safety feature to limit the maximum flow rate in the event of a downstream failure) to enter a tube transforming the cross sectional area from 15.2 cm diameter circular to the 5 x 10 cm aspect ratio of the blade mixing nozzle block. The pebble bed heater and transition section are instrumented at various stations with R and K-type thermocouples and Barclay model 402H2-03CA-04-3 pressure transducers.

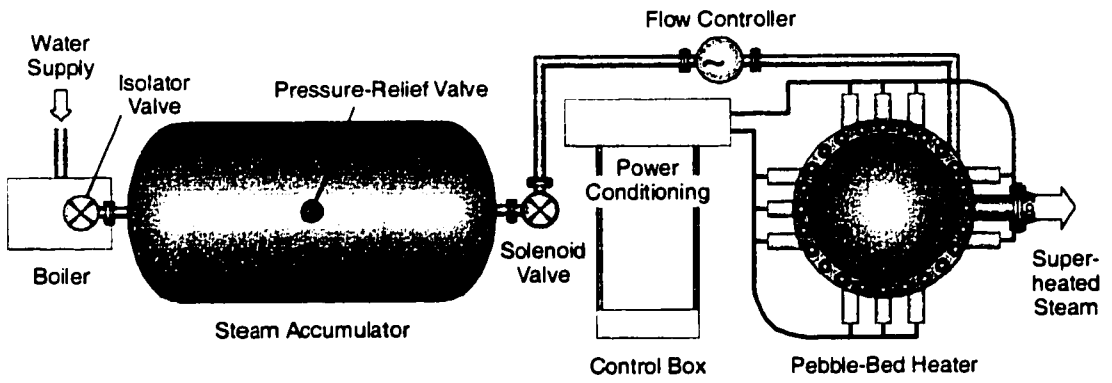

Figure 3.3 Superheated steam supply system for proof-of-concept facility.

3.2 Preheated Feedstock Supply System

For identical reasons as were the case for the steam flow, a capacitive heating scheme, illustrated at the lower center of Figure 3.1 and enlarged in Figure 3.4, was

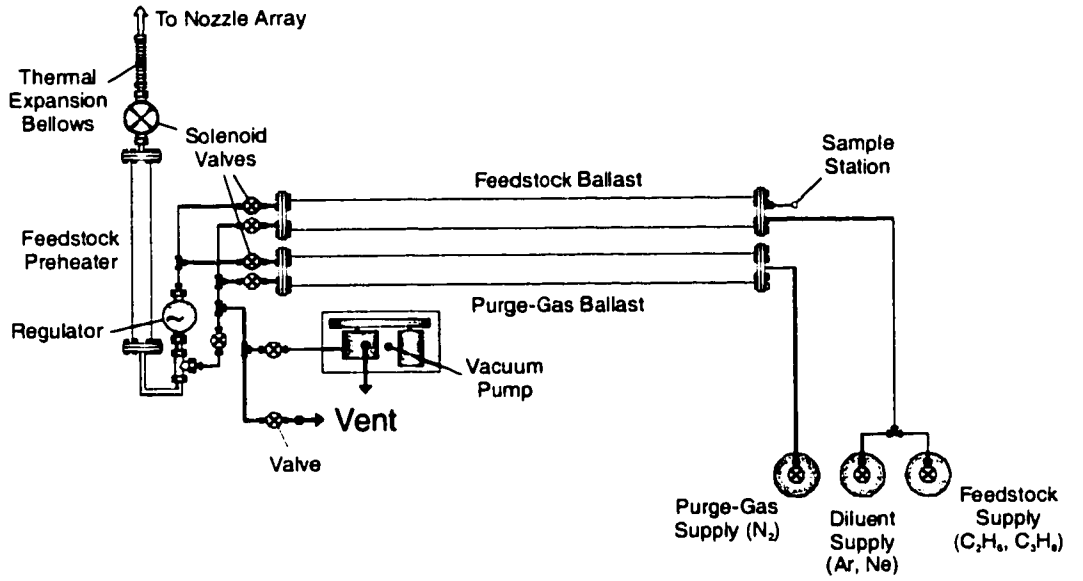

Figure 3.4 Preheated feedstock supply system for proof-of-concept facility.

chosen for the feedstock as well. Because of its lower temperature requirements and smaller scale, however, the feedstock supply system was designed and constructed on site. The apparatus consists of an aluminum 25.4 cm diameter x 3 m long cylindrical feedstock reservoir connected to a 12.7 cm (inner) diameter x 1.5 m long capacitive heat exchanger. Heat is deposited by conduction from three 750 W heating tapes underneath Kaowool refractory ceramic fiber insulation, wrapped around the exterior, through schedule 40, 318 stainless steel walls into the core, consisting of approximately 60 closely packed copper tubes (1.3 cm O.D. x 0.32 cm wall thickness x 1.5 m in length). (See schematic in Appendix D.) A steady, preset temperature is maintained by a controller accepting feedback from K-type thermocouples monitoring the outer wall temperature. The connecting line passes through a 1.3 cm solenoid valve and regulator, and a final 2.5 cm pneumatically actuated Neles-Jamesbury type BC 6/15 U valve separates the downstream end of the feedstock preheater from the nozzle block feed manifold. For added safety, an additional, identical ballast and solenoid valve parallel the feedstock pair, allowing the feedstock supply system to switch to injection of (inert) nitrogen in order to purge the system of any remaining flammable gases as well as dilute the mixture within the downstream collection tank.

3.3 Waste Gas Collection and Disposal

Figure 3.1 displays a 1.5 m diameter x 2.7 m long (8 mm wall thickness) cylindrical dump-tank immediately downstream of the Shock Wave Reactor test section, enlarged in Figure 3.5. While only seconds would be required for the ~0.5 kg/sec steam mass flow of the experiment to raise the back pressure within the empty ~4.5 m^3 volume of the tank sufficiently high to cause unstart within the Shock Wave Reactor, addition of ~250 kg of vertically aligned parallel aluminum plates alleviates this limitation.

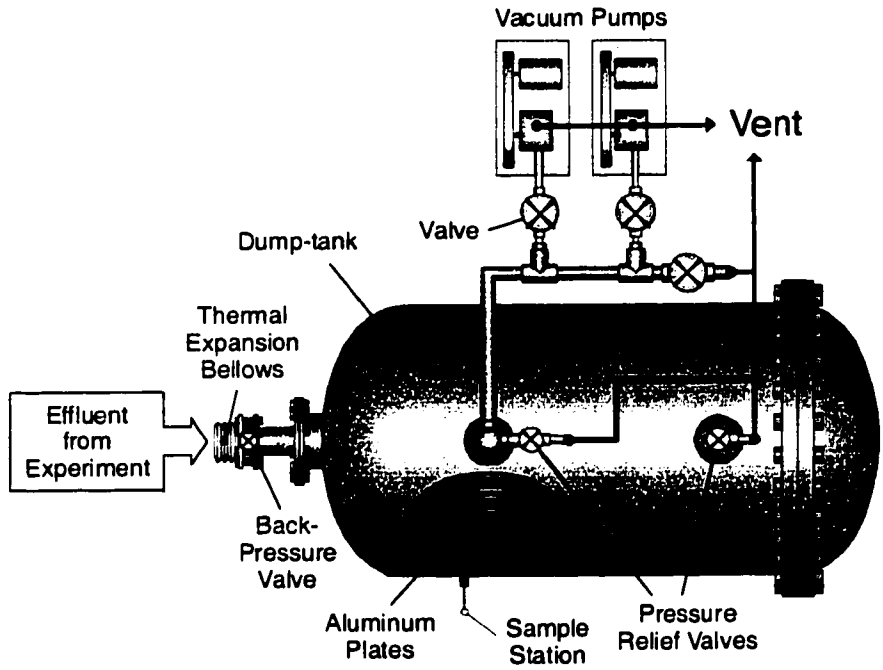

Figure 3.5 Waste gas disposal system for proof-of-concept experiment.

Sufficient surface area is provided such that as inflowing steam contacts the plates, which begin the procedure at room temperature, condensation is virtually instantaneous relative to the timescales of the flowfield. Thus, all of the steam within the Shock Wave Reactor effluent essentially vanishes as it enters the dump-tank. Pressure (instrumented by both an analog gauge and Barclay model 402H2-03CA-04-3 pressure transducer) within the vessel is seen to rise very slowly, in proportion to the accumulation of only the small fraction of the flow remaining gaseous, to levels insufficient to unchoke the back pressure

control valve immediately upstream throughout the typical ~60 sec run interval. Two Kunkle model 6010JH pressure relief valves (set to 2.0 bar release pressure) located at the top of either end of the tank insure against accidental overpressure. Two Welsch model 1397 vacuum pumps connected to the dump tank evacuate the entire system of air prior to, and diluted (with N_2) product mixture subsequent to each experiment. The pump outflow is ejected from a waste port located on the roof of the facility. A large X-Y positioner allows easy movement of the entire dump-tank/vacuum pump assembly to facilitate alignment of the ~2300 kg structure with the experiment.

3.4 Shock Wave Reactor Test Sections

The Shock Wave Reactor test device, shown in schematic at the center of Figure 3.1, and in greater detail in Figures 3.6 (top view) and 3.7 (side view with dimensions and thermocouple and sample probe labels), consists of a supersonic blade mixing nozzle array (see Section 3.6 below) bringing together the carrier and feedstock supply and injecting them in an interleaved fashion into a 5 x 10 cm cross section x 1.0 m long mixing chamber. Mixed carrier and feedstock then proceed through a multi-component reaction zone (following initiation of recompression near the end of the mixing chamber), comprised of two initial sections which linearly expand the transverse flowfield dimensions from the 5 x 10 cm at the mixing section outlet to 15.2 cm square over a distance of 2 m, followed in later experiments by a third 30.5 cm diameter x 1.2 m long cylindrical addition to increase the reaction duration. (A stainless steel insert, not shown in Figures 3.6 and 3.7, smoothly adapts the square-to-round cross sectional transition within the first 25 cm of the cylindrical section.) Further downstream, a 25 cm pneumatically positionable Neles-Jamesbury type L11CMB06PACA butterfly valve, connecting with the dump tank, sets the system back pressure. To accommodate thermal expansion, ~30.5 cm flexible stainless steel bellows of 25 and 2.5 cm diameters, respectively, connect the final reaction zone to the back pressure valve and well as the feedstock heater outlet to the nozzle block feed manifold. An automated system controls all run-time operations and data acquisition.

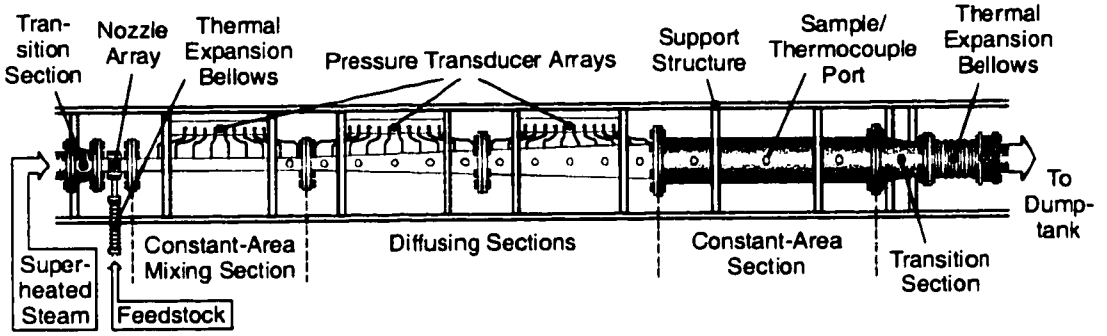

Figure 3.6 Top view of proof-of-concept facility test sections. (Wall heating equipment and insulation not shown for clarity.)

The walls of all sections are of 1.3 cm thick 304 stainless steel, save those of the final reaction zone, which are of mild steel. Following run number 43, to reduce heat loss, the walls of all sections were fitted with 750 W Watlow model SGA1J30J02 heating bars (two per section), heat tapes (at flanges), and Kaowool refractory ceramic fiber and fiberglass insulation. Wall temperatures were then monitored with K-type thermocouples at approximately 30.5 cm spacing and maintained at specified values (up to ~540 °C) by controllers similar to that employed by the feedstock preheater. One sidewall of each section, with the exception of the cylindrical addition, is instrumented with Barclay

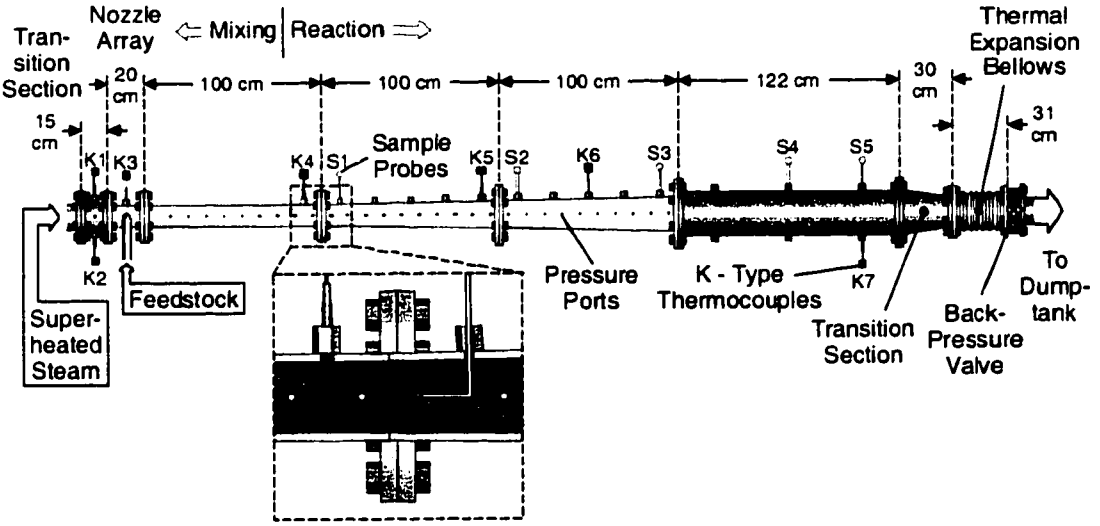

Figure 3.7 Side view of proof-of-concept facility test sections with enlarged cutaway. (Wall heating equipment, insulation and supports not shown for clarity.)

model 402H2-03CA-04-3 pressure transducers at 2.5 cm spacing. Additionally, a row of 3-4 evenly spaced ports along the top centerline of each section allows insertion of either K-type thermocouples or quartz aeroquench sampling probes (see Section 3.5 below). Each section was outfitted with at least one thermocouple and one sampling probe for a typical experimental run of the facility.

3.5 Gas Sampling and Analysis

Multi-station sampling using aeroquench probes throughout the reaction zone length provided accurate assessment of conversion and selectivity as functions of time (distance downstream) for a given set of run conditions.[1] Aeroquench sampling probes function by gas dynamically re-accelerating the gas mixture to supersonic speeds thereby depressing the static temperature sufficiently to halt any thermally sensitive reaction. (See Figure 3.8.) Heat loss to the quartz walls deprives the mixture of the energy necessary for continued chemical re-arrangement before choking ultimately occurs. Thus, influx is effectively frozen at the composition near the probe tip.

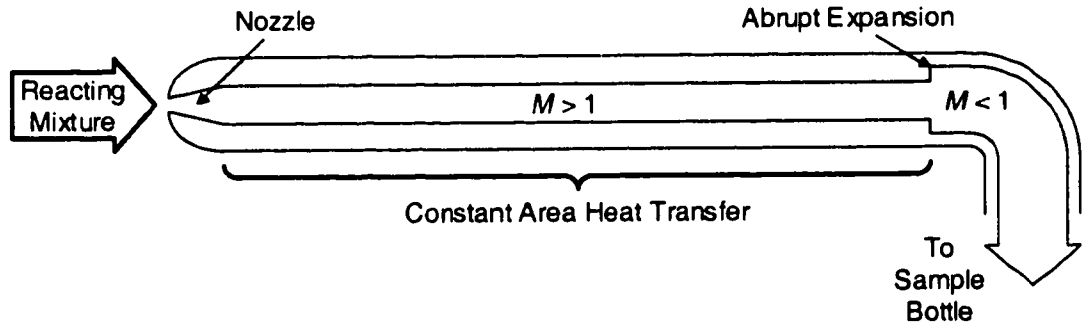

Figure 3.8 Schematic of aeroquench sampling probe.

3.2 mm stainless steel tubing connects each of the Shock Wave Reactor test facility's 5-6 aeroquench probes to solenoid activated valves and, in turn, to 75 cc sample bottles. The bottles, initially evacuated, fill over a 3 second interval during which the control system actuates the solenoids. Subsequent to each experimental run, these, and additional samples taken from the initial feedstock ballast composition and final mixture within the dump-tank, were analyzed on a SRI Instruments model 8610 dual element

(both thermal conductivity and flame ionization detectors) gas chromatograph employing an 11.0 m x 3.2 mm stainless steel 60/80 Carboxen 1000 coil.

3.6 Supersonic Blade Mixing Nozzles, Revisited

Due to the success of the supersonic blade mixing nozzle array employed in the cold gas mixing experiments, adaptation of the design to meet the needs of the proof-of-concept experiment required minimal alterations. Temperature requirements associated with the high enthalpy flows within the actual test device did stipulate need for some key changes, however.

While heat transfer to the relatively cold internal feedstock flow was expected to provide cooling to the blade walls, in response to the potentiality of accidental feedless operation, the, nozzle array was designed to withstand short duration excursions up to the maximum experimental peak steam temperature of 1500 K, somewhat above the reliable operating range of the 316 stainless steel construction of the cold flow test array. In addition to assurance of survivability, stiffness at high temperature, as well as minimal alteration of geometry through thermal expansion, were imperative to guarantee achievement of design flow conditions. Thus Hanes 230 high temperature alloy replaced the stainless steel of the cold flow nozzles for reasons of enhanced high temperature strength and reduced thermal expansivity. Because elevated temperature data corresponding to performance specifications of the Shock Wave Reactor experiment are somewhat scanty for the superalloy, blade wall thickness was augmented by 50% over that of the test model.

Despite the fairly low thermal expansion characteristics of Hanes 230, calculations indicated that welding of both ends of the blades to the channel walls would inevitably lead to buckling during the rapid, non-uniform heating at the beginning of an experimental test cycle. In an industrial setting, the availability of ample steam circumvents this limitation by allowing system heating to occur over a sufficiently slow period so as to be relatively uniform. The system expands simultaneously throughout. In the laboratory, however, the heat and gas storage capacities of the quasi-steady state

device fall vastly short of providing such a capability at any practical experimental scale. Thus, in the absence of some complex scheme to accommodate blade expansion while simultaneously maintaining necessary seals between steam and feed system, reactor and environment, this limitation constrains the system to feed the nozzle blades from a single end, leaving the opposite extremity to slide freely within a guide slot. This effective halving of the geometric feed parameter (as detailed in Section 2.5) represents a key modification of design criteria. As a result, while conceptually identical, notable differences in cross-sectional proportions, and, in turn, design feed and output specifications exist between the blade nozzle arrays employed by the cold preliminary and actual proof-of-concept apparatus. (See Figure 3.9.)

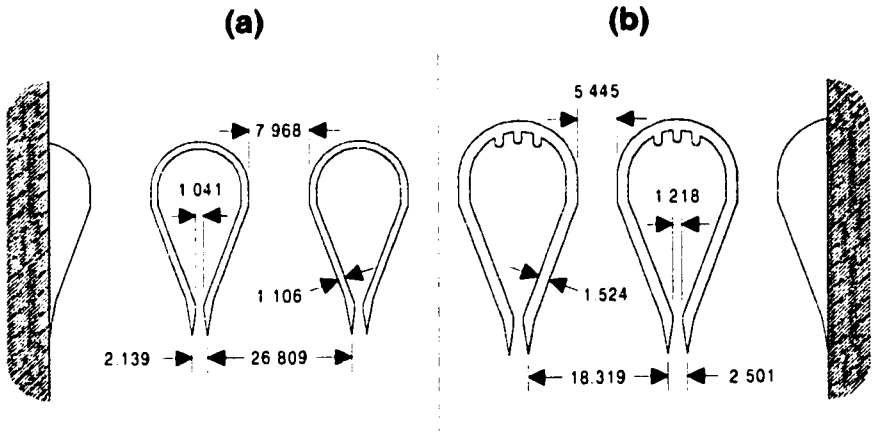

Figure 3.9 Blade nozzle cross sections for a) cold and b) hot experiments and corresponding data.

The presence of an array of three fins near the leading edge within the internal cavity noticeably presents itself as the final design modification. Placed and oriented so as to minimize turbulence generation, the fins serve to enhance heat exchange between the blade walls and cooling internal flow while providing structural reinforcement to the leading surfaces.

While the nozzle array was, in fact, designed with the potentiality of operation at 1500 K wall temperatures, due to material performance uncertainties stemming from the limited availability of data at this temperature, the experimental procedure was designed,

in turn, to rely on internal cooling of the blades by the feedstock flow to prevent exploration of this contingency. To this end a K-type thermocouple was affixed to the inner blade wall, between two cooling fins (where it was likely to at least semi-permanently remain attached) with high temperature cement. This secondary failsafe was then implemented simply by observing the characteristic rate of heating during preliminary facility tests at lower total enthalpies, and limiting pre-feedstock injection intervals to below that required to reach a designated failsafe temperature for subsequent, high enthalpy operation.

An estimate of the heat transfer rate from the external superheated steam bath to the nozzle blade wall, may be obtained by first defining a heat transfer coefficient, h_p, such that:

$$d\dot{Q} = h_p dA(T_r - T_w) \tag{3.1}$$

To obtain the overall heat transfer, the above expression must be integrated over the blade surface area. Here, for simplicity, it will be presumed that thermal conduction within the superalloy is sufficiently fast compared to heat transfer into the stainless steel supporting the ends and external convection to insure that the blade wall temperature, T_w, is essentially uniform. Alternatively, T_w might be equally regarded as some mean effective wall temperature for the nozzle blade. Note, however, that in general the recovery temperature, T_r, will not be constant over the blade surface, but will vary with freestream Mach number in the flow direction:

$$\dot{Q} = h_p \left(\int_{A_p} T_r dA - A_p T_w \right) \text{ where } T_r = T\left(1 + \tfrac{\gamma-1}{2} PrM^2\right) \tag{3.2}$$

Now since the flow area is a well defined function of dA by the nozzle geometry and isentropic relations, to a good approximation, relate the freestream Mach number to the flow area, the remaining integration in Equation 3.2 is tractable (assuming nearly constant Prandtl number, Pr). Nevertheless, here it will suffice to simply make the observation that:

$$\int_{A_p} T_r dA = \int_{A_p} \left(\frac{T_r}{T_p}\right)\left(\frac{T_p}{T_{tp}}\right) T_{tp} dA = \beta A_p T_{tp} \quad \text{where} \quad \beta \equiv \int_{A_p} \left(\frac{T_r}{T_p}\right)\left(\frac{T_p}{T_{tp}}\right) dA \tag{3.3}$$

Note β is independent of flow total properties, but varies only with nozzle geometry yielding two solutions corresponding to either started or unstarted nozzle operation. While strictly true only for the low Mach number of the unstarted flow, for simplicity, present consideration shall be limited to $T_r \cong T_{tp}$ i.e., β will be treated as unity. Indeed, the fact that the ducting connecting the steam heater to the nozzle array has sufficient length for transition to turbulent flow upstream of the nozzle array, in fact, suggests an effective Prandtl number (due to the large degree of convective transport associated with turbulent flow) near one. Thus, this approximation is quite reasonable, for this case. Substitution into Equation 3.2 then yields:

$$\dot{Q} = (hA)_p \left(\beta T_{tp} - T_w\right) \tag{3.4}$$

where $(hA)_p$ has been substituted for $h_p A_p$ as a notational convenience. The heat flux may be then equated to the rate of change of enthalpy of the blade wall as follows:

$$\dot{Q} = (hA)_p \left(\beta T_{tp} - T_w\right) = m_w C_{vw} \frac{\partial T_w}{\partial t} \tag{3.5}$$

where $m_w C_{vw}$ represents the thermal mass of the nozzle blade. Note that linear dependence upon nozzle span is implicit in both $(hA)_p$ and m_w and its presence in Equation 3.5 is thus arbitrary. Normalization by span (denoted by "^") yields:

$$(h\hat{A})_p \left(\beta T_{tp} - T_w\right) = \hat{m}_w C_{vw} \frac{\partial T_w}{\partial t} \tag{3.6}$$

(The mass per unit length of each nozzle blade employed in the proof-of-concept experiment is approximately 6.8 g/cm, while C_{vw} for Hanes 230 is tabulated as a function of temperature in Appendix E.) Choosing, an appropriate average, constant value for the specific heat of ~ 600J/kg-K, the above expression may be integrated with respect to time to obtain:

$$\frac{T_w - \beta T_{tp}}{T_{wo} - \beta T_{tp}} = e^{\frac{-(h\hat{A})_p}{\dot{m}_w C_{vw}}(t-t_o)} \qquad 3.7$$

where the subscripts "o" designate initial values.

To estimate $(h\hat{A})_p$ right hand side of Equation 3.7 may inverted and its natural log plotted verses t-t_o. The initial condition may be arbitrarily chosen at any time during the experimental run after steady plenum flow has been established, but before the initiation of feedstock injection, shown in Figure 3.10 for data obtained from Runs 63 - 68. (Here

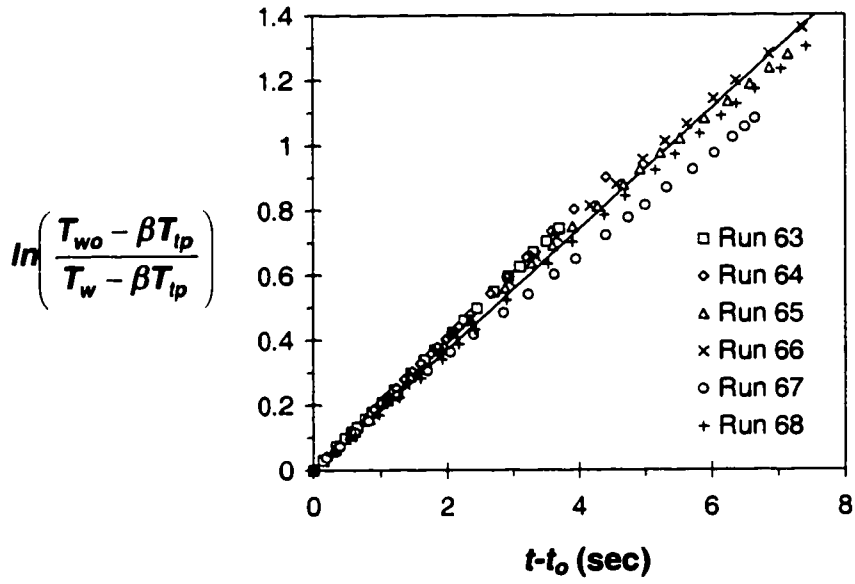

Figure 3.10 Blade nozzle heating characteristics with calculation superimposed.

the T_{tp} has been estimated at 95% of the value reported by the thermocouple upstream of the nozzle array, assuming ~5% loss in the interim distance based on general observations of system performance.) Considering the various approximations made in obtaining Equation 3.7, assignment of a value of 76 J/s-m-K to $(h\hat{A})_p$ yields striking agreement (solid line in figure).

Runs 67 and 68, representing the cases of maximum deviation, correspond well

with the trend predicted by Equation 3.7 in that they express clear linearity; however, they appear to report slightly different values for $(h\hat{A})_p/(\hat{m}_w C_{vw})$, and it is tempting to ascribe this to the fact that these two runs were conducted at about 200 °C lower average temperature than the other cases displayed. While this might, indeed, be expected to have significant influence (in light of the fair degree of variation with temperature of the superalloy specific heat, here assumed constant), their alternate relative placement, above and below the remainder of the data, point rather to some experimental inconsistency. Thus, though it is difficult to make precise comment on the seemingly poorer agreement of Runs 67 and particularly 68, it is perhaps helpful to place here a note that the transition section thermocouple needed replacement following Run 65, and the conjecture that perhaps subsequent wearing of the thermocouple or bending of its supporting post during the "breaking in" of the new sensor played a role. Such effects were observed more dynamically in thermocouples placed within faster regions of flow, where wear and, especially, bending were demonstrated to produce dramatically altered readings. Hence, it may be pure coincidence, that the brand new thermocouple of Run 65 nearly precisely matched the output of the older unit in immediately previous runs, due, perhaps, to some small difference in length, strength, etc.

For heat transfer to flow inside the blade one may begin similarly to above:

$$d\dot{Q} = h_f dA(T_r - T_w) \tag{3.8}$$

From this point, however, the analyses must diverge. Whereas the high velocity and mass flow of the external steam bath guaranteed a virtually constant freestream total temperature, the slower, smaller in quantity, and well mixed flow (slow and turbulent) within the blade over a longer path of contact requires taking into account the fact that the feedstock total temperature (and, in turn, the recovery temperature) rises as a result of the heat exchange with the blade wall. The increased complexity of the internal flow may be mitigated to some extent, nonetheless, by observing that in this case that the flow throughout is well subsonic, with only the exception of the small trailing edge nozzle region. Thus it may be asserted that $T_r \cong T_{tf}$ and:

$$d\dot{Q} = h_f dA\left(T_{tf} - T_w\right) \tag{3.9}$$

To continue, the energy balance for the feedstock flow may be expressed:

$$d\dot{Q} = d\left(\dot{m}_f C_{pf} T_{tf}\right) \tag{3.10}$$

and equated, above, to obtain:

$$d\left(\dot{m}_f C_{pf} T_{tf}\right) = h_f dA\left(T_{tf} - T_w\right) \tag{3.11}$$

Because the flowfield within the nozzle blade is complex, direct integration of Equation 3.11 is intractable; however, once again because the flow is well subsonic virtually throughout, one may approximate:

$$d\left(\dot{m}_f C_{pf} T_{tf}\right) \equiv \dot{m}_f C_{pf} dT_{tf} \tag{3.12}$$

Recalling the assumption of uniform wall temperature, Equation 3.11 may now be integrated and limits applied to yield:

$$\frac{\Delta T_{tf}}{\left(\Delta T_{tf}\right)_{\max.}} \equiv \frac{T_{tfe} - T_{tfo}}{T_w - T_{tfo}} = 1 - e^{-(hA)_f / \left(\dot{m}_f C_{pf}\right)} \tag{3.13}$$

and, noting that:

$$\dot{Q} = \dot{m}_f C_{pf}\left(T_{tfe} - T_{tfo}\right) \tag{3.14}$$

the total heat transfer from the blade wall into the feedstock flow may be written:

$$\dot{Q} = (hA)_f^*\left(T_w - T_{tfo}\right) \tag{3.15}$$

where the effective heat transfer coefficient, $(hA)_f^*$ is defined:

$$(hA)_f^* \equiv \dot{m}_f C_{pf}\left(1 - e^{-(hA)_f / \left(\dot{m}_f C_p\right)}\right) \tag{3.16}$$

Equation 3.15 and the corresponding definition for $(hA)_f^*$ demonstrate plausibility in that they predict expected behavior for the relationship of interior blade wall heat transfer to feedstock thermal-mass flow rate, $\dot{m}_f C_{pf}$. (See Figure 3.11.) In the limit of

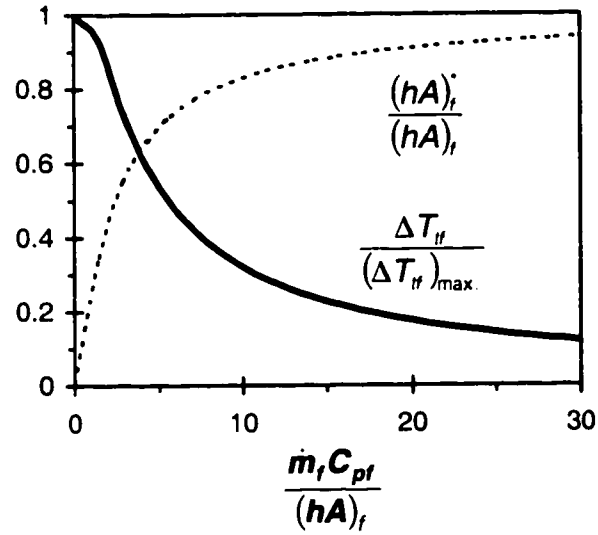

Figure 3.11 Effect of internal flow on blade nozzle heat transfer to feedstock.

low internal mass flow, the exit temperature is observed to approach the blade wall temperature and heat removal becomes simply proportional to the mass flow (ultimately approaching zero for the case of no feedstock flow), whereas for large mass flow, heating of the feedstock becomes negligible and heat transfer described by the simple coefficient $(hA)_f$, which may be expected to be of the order of $(hA)_c$, above.

Having now obtained expressions for heat transfer to both carrier and feedstock, the analysis may now be extended to consider the blade nozzle with both steady external and internal flows by modifying Equation 3.4 as follows:

$$\dot{Q} = (hA)_p\left(\beta T_{tp} - T_w\right) - (hA)_f{}^*\left(T_{tf} - T_w\right) = m_w C_{pw}\frac{\partial T_w}{\partial t} \qquad 3.17$$

which integrates to:

$$\frac{T_w - T_w{}^*}{T_{wo} - T_w{}^*} = e^{-(t-t_o)/\tau} \quad \text{where} \quad \begin{cases} \tau \equiv \dfrac{\dot{m}_w C_{pw}}{(hA)_f{}^* + (hA)_p} \\ T_w{}^* \equiv \dfrac{(hA)_f{}^* T_{tf} + (hA)_p \beta T_{tp}}{(hA)_f{}^* + (hA)_p} \end{cases} \qquad 3.18$$

and T_{wo} and T_w* are defined to be the values of wall temperature at time t_o and steady-state ($t \rightarrow \infty$), respectively. The above expression, in that it assumes constant internal mass flow, is not particularly useful in comparison to data obtained from the Shock Wave Reactor test device, however, as, in application, the characteristic heat transfer time scale, τ, proves to be quite short and of the same order as the time required to establish steady flow following initiation of feedstock injection. (See Figure 3.12.) Nevertheless, the

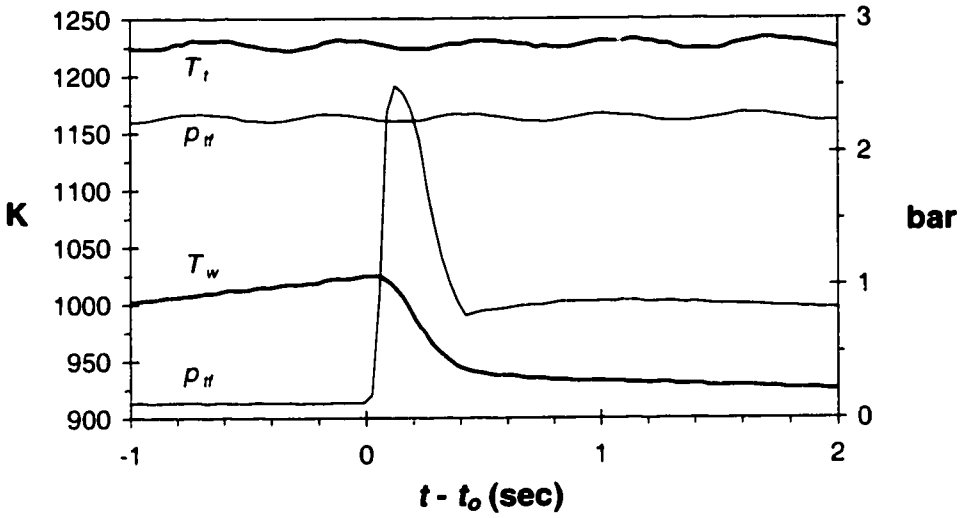

Figure 3.12 Comparison of nozzle blade temperature and feed pressure time histories. Plenum values displayed for reference (Run 65).

very same feature provides an alternative approach to estimating the blade internal heat transfer coefficient by resulting in fast approach of the system to a quasi-steady state. (The thermal data continue to drift very gradually as the system walls, representing a relatively large thermal mass, slowly rise in temperature.) Thus, rearrangement of the definition of T_w^* yields:

$$\frac{(hA)_f^*}{(hA)_f} = -\left[\frac{(hA)_p}{(hA)_f}\right]\frac{\beta T_{tp} - T_w^*}{T_{tf} - T_w^*}, \qquad 3.19$$

The superposition of $(hA)_f^*/(hA)_f$, obtained by normalizing Equation 3.16, over values determined from Equation 3.19 using experimental data (Figure 3.13) illustrates

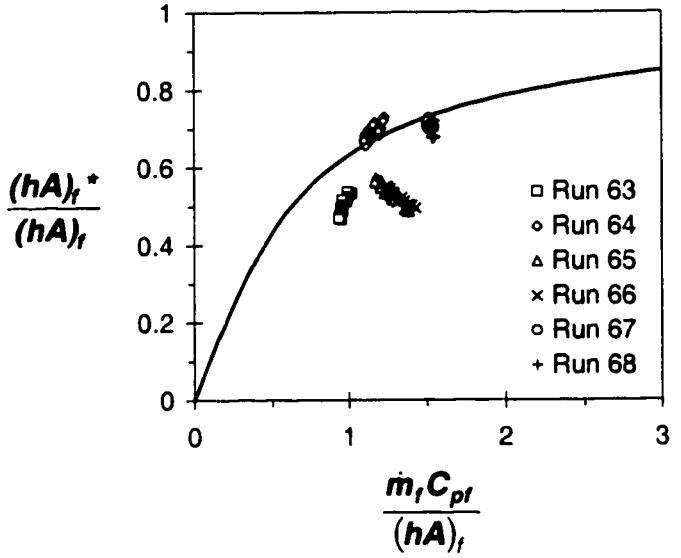

Figure 3.13 Comparison of predicted and experimentally determined normalized heat transfer coefficients.

acceptable agreement, albeit, with some scatter, demonstrating reasonable the previous assumption that $(hA)_f/(hA)_p \cong 1$. Figure 3.14 displays computed values for mean feedstock temperatures entering and exiting the nozzle blade for cases corresponding to the data of Figures 3.10 and 3.13 computed in the steady-state limit where Equation 3.13

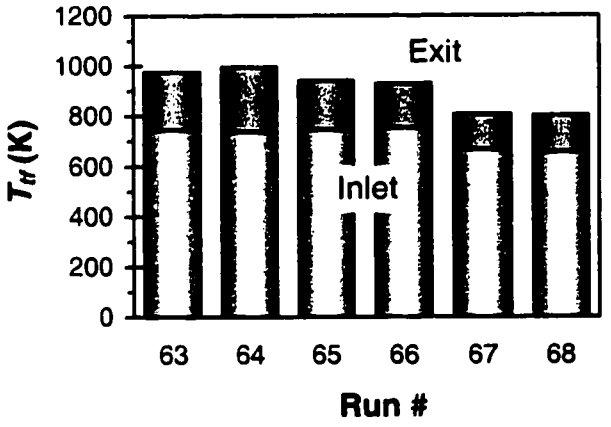

Figure 3.14 Computed feedstock temperature rise through nozzle blade.

may be reduced to:

$$T_{tfe} = T_{tfo} + \frac{(hA)_p \left(\beta T_{tp} - T_w^*\right)}{\dot{m}_f C_{pf}} \qquad 3.20$$

3.7 System Development

The experimental log summary of Table 3.1 presents a concise synopsis of run history and evolution of the Shock Wave Reactor proof-of-concept facility. Testing of the Shock Wave Reactor proof-of-concept apparatus commenced immediately following completion of construction in October of 1995 with reduced temperature trials of pure superheated steam in the absence of feedstock, and continuous improvement and adaptation of data acquisition equipment and software, and optimization of the control system, comprised an initial 32 runs. (Of particular interest was the development of pressure measurement diagnostics for superheated steam, the discussion of which would be incongruous here, but may be found in Appendix F.) Carbon dioxide mimicked the role of feedstock for the purpose of injection control system development in the latter third of the pre-pyrolysis testing phase.

3.8 Initial Pyrolysis Experiments

Runs 33-37 marked the earliest attempts to crack ethane. Yield in each case was effectively zero; the system failed to produce mixtures of sufficiently elevated temperature to achieve appreciable pyrolysis within the ~23 ms interval during which reactants moved from the initiating shock wave to the quench plates within the dump-tank, clearly a result of heat loss to the section walls. With each trial, incremental increases were made to pebble bed, feedstock, and section wall set temperatures, intended to circumvent the heat transfer limitation, exploring a range of 1127-1250, 427-625, ~120-200 °C, through Runs 33-37 for each set temperature, respectively.

The recovery temperature profiles acquired by thermocouples positioned at various stations throughout the system for Run 37 (Figure 3.15) illustrate two key features of the temperature loss. (Runs 33-36 lacked the measurement taken at 2.0 m

Table 3.1 Proof-of-concept experimental log summary.

Runs	Dates	Objectives	Feedstock (mole parts)
1-32	10/95 - 12/16/95	Apparatus and diagnostics development/testing.	None
33-38	12/17/95 - 12/22/95	Initial live feedstock tests with trace argon dilution.	C_2H_6:Ar 15.4:1
39	1/10/96		
40	1/11/96	Increased dilution with argon to lower mixture specific heat.	C_2H_6:Ar 1.2:1
41-43	1/12/96 - 1/13/96	High feedstock dilution with Argon to maximize conversion.	C_2H_6:Ar 1: 2.9
44	1/13/96		
45-52	2/5/96		
46	2/21/96		
47	2/22/96		
48-50	2/23/96- 2/29/96		
51	3/18/96		
52	6/6/96		
53-60	6/11/96- 6/24/96	Shock position varied to assess influence on pyrolysis selectivity.	C_2H_6:Ar 1:2.3
61-67	7/1/1996- 8/16/96	Feedstock dilution reduced to explore higher ethane/steam mass flow ratios.	C_2H_6:Ar 9.1:1
68	11/6/96	Obtain samples to be analyzed by independent source.	C_2H_6:Ar 1:1.8
69-71	11/7/96- 12/13/96	Neon added as tracer to feedstock mixture.	C_2H_6:Ar:Ne 2.3:2.6:1
72-73	11/20/96- 11/26/96	Alternative feedstock - Propane.	C_3H_8:Ar 1:1.5
74	12/5/96	Pure ethane feedstock.	C_2H_6
75-80	1/7/97- 2/18/97	Shock studies.	None

Dogleg removed.

Channel walls fitted with heaters and insulation.

Flanges fitted with heaters and insulation.

Reaction zone length increased by 1.2 m.

Reaction zone addition heated and insulated.

Additional insulation on walls and X-section.

Upstream X-section junction smoothed.

Reaction zone addition junction smoothed.

Additional insulation.

downstream of the nozzles.) Firstly, evidenced by the only small additional drop in temperature between the transition section, immediately upstream, and station 1, next downstream of the nozzle array, before and after injection, is the notable fact that

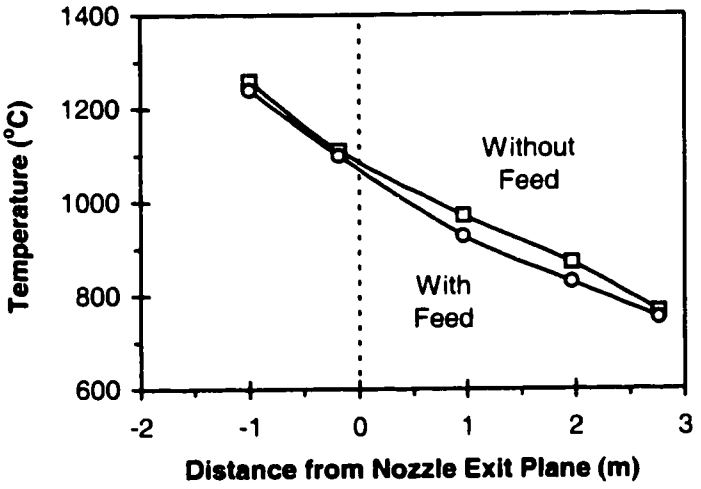

Figure 3.15 Temperature profiles for Run 37 before and after initiation of feedstock injection.

temperature reduction due to mixture of the steam with the colder feedstock comprises only about 25% that transferred to the walls in that span. Secondly apparent is that the superheated steam temperature dropped by ~150 °C in an approximately one meter long dogleg connecting the pebble bed heater to the mixing nozzle block. This component had been included as an initial fail-safe measure to shield the nozzle array from exposure to direct radiative heating from within the pebble bed while the system regenerated between

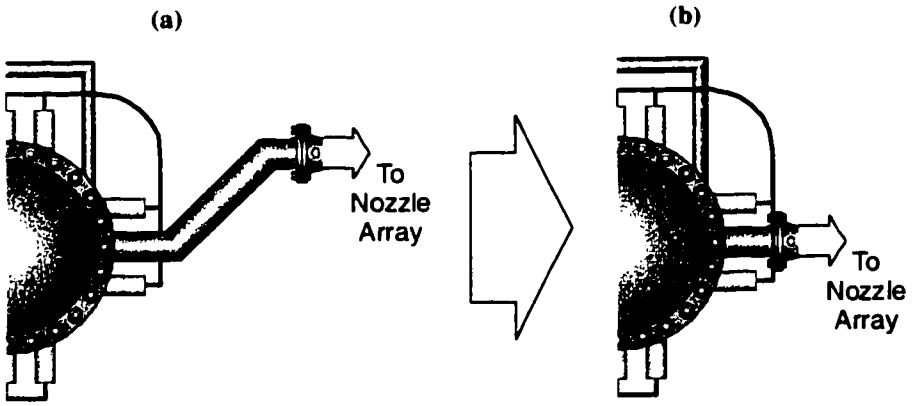

Figure 3.16 Pebble bed connection to experiment with a) original dogleg configuration and b) dogleg removed.

experiments. Re-evaluation of this conservative feature as an unnecessary source of severe heat loss ultimately dictated the system be blown down (Run 39) and retrofitted with a short, straight-in flange connection. (See Figure 3.16.)

3.9 Dilution and Additional Apparatus Modifications

The proof-of-concept device, in its fortieth run, first achieved a quantifiable ethylene yield on January 10, 1996. Despite an increase of the indicated recovery temperature (≡ total temperature) immediately upstream of the mixing array to 1148 °C, only ~1% of the ethane cracked, as the mixing and reaction zone walls remained substantial (and primary) sources of thermal loss.

Mentioned above, data indicate feedstock heating accounted for only 25% of the temperature reduction within the mixing zone. While relatively small compared to wall heat transfer, this does, in fact, represent the more easily mitigated source of temperature decrease, and diminution of the feedstock as a temperature sink was effected by increased dilution with ~1 mole part (lower specific heat) gaseous argon for Run 40 as compared to the only 1:15.4: mole parts argon (as a tracer gas; see below) to ethane for Runs 33-38. Dilution was further increased to ~ 2.9:1 mole parts argon to ethane for Runs 41-52.

Subsequent to Run 44, the simple, heat-tape wall preheating system was replaced by a more sophisticated arrangement employing feedback control, allowing section walls to safely attain preheats to ~500 °C, and continued improvement of insulation as well as the installment of and additional section lengthening the reaction zone (and thereby reaction time) marked steadily enhanced yield capability. Following Run 50, wall inserts were welded within the upstream transition section, smoothing the previously abrupt 10 cm diameter circular to 5 x 10 cm rectangular transition in order to diminish heat transport by recirculating zones within the flowfield. By running the system nearly unstarted (positioning the initial shock within the nozzle array and foregoing any pre-pyrolysis supersonic mixing) in order to maximize reaction temperature and time, a maximum conversion of 84% was obtained in Run 50. With the installment and testing, in Run 52, of an additional transition smoothing device to diminish potentially

deleterious recirculation at the 15.2 square to 30.5 cm diameter circular junction to the reaction zone addition (which was circular for economy), and further, minor improvements in wall insulation, the apparatus reached its final configuration in June of 1996.

3.10 Proof of Concept

An experimental series designed to directly ascertain the role of the shock wave in yield optimization followed completion of the final system modifications. Throughout a series of six trials (Runs 55-60), all system parameters were maintained approximately invariant with the exception of the shock position, which was adjusted through four distinct locations by increments in back pressure. At ~0 (unstarted), 40, 70, and 90% of the downstream straight-walled chamber length measured from the nozzle exit, these stations were intended to initiate the reaction within the flowfield with mixing complete to varying degrees, corresponding to totally unmixed flow, as well as ~50, 100, and 120%, respectively, of the predicted mixing length, as computed per the techniques outlined in Sections 2.2 and 2.3. (Note that the terminology "unstarted" here refers merely to the fact that the mixing takes place almost entirely subsonically. The nozzle throats for this case are, in fact, choked, but back pressure set sufficiently high so as to initiate pressure recovery within the nozzle array, ahead of the onset of mixing.)

Figure 3.17 displays static pressure measurements underneath a corresponding plot of section cross-sectional area variation over the channel length, measured from the nozzle blade trailing edge and non-dimensionalized with respect to the mixing array width of 10 cm. Data from Runs 55-58 demonstrate the typical, steady pressure rise within the straight-walled mixing section associated with viscous dissipation from a supersonic channel flow upstream of transitions to rapid pressure recovery between 4 and 5, 7 and 8, and 9 and 10 span lengths. (As the curves are quite steep, it is impossible to estimate the position of the initial pressure rise to greater accuracy than within a range equal to the pressure transducer spacing of 10 cm.) The pressure distribution upstream of the shock system is seen to be identical in each case, indicating each trial to indeed be

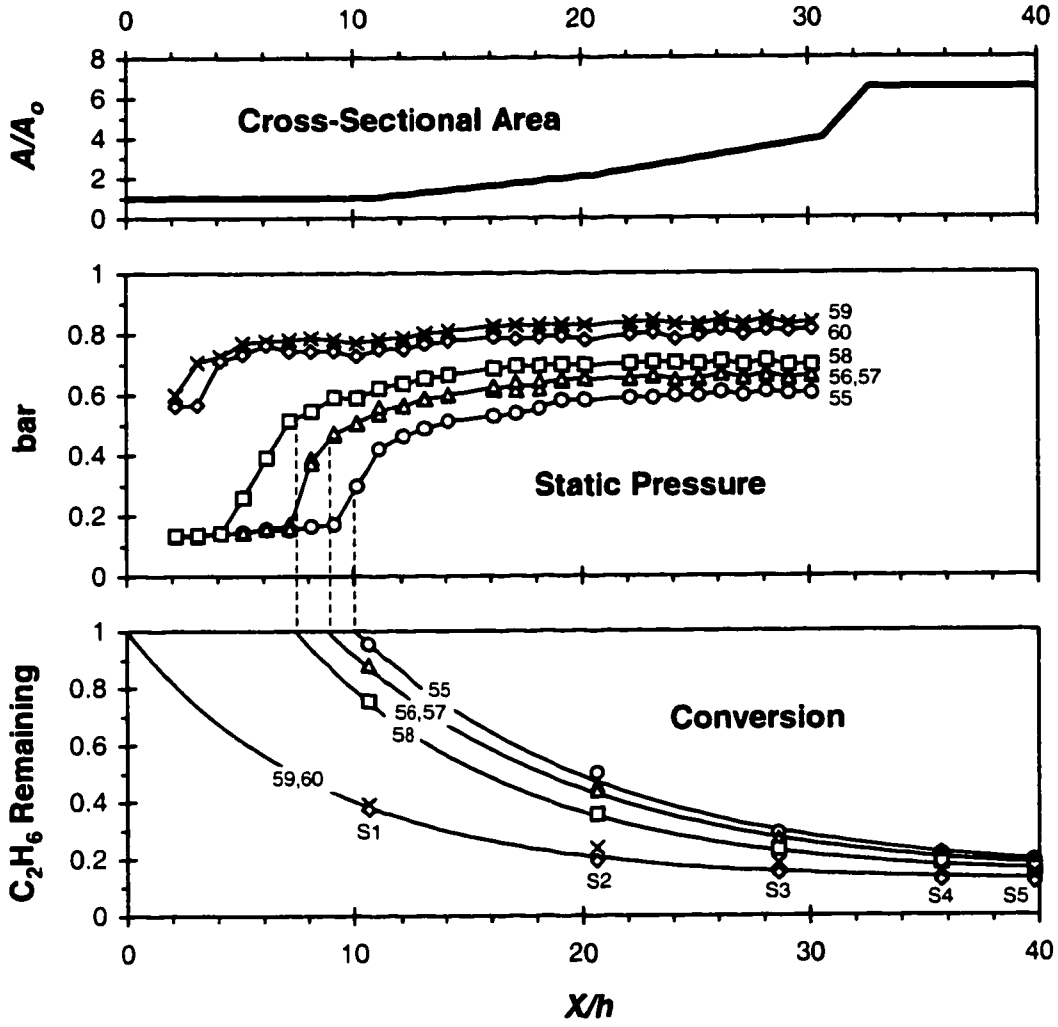

Figure 3.17 Proof-of-concept experiment cross-sectional area and static pressure contours shown alongside conversion.

similar with the exception of positioning of the shock system. In each case, the pressure recovery appears to occur over 6-7 section spans. The smaller pressure rises seen between the first and third transducer locations of Runs 59 and 60 do not represent shock structures akin to those of the preceding cases, as for this to be the case the projected distribution would necessarily intersect an identical upstream supersonic pressure history. As this is clearly not the case, these pressure jumps may be attributed to weaker shock systems propagating from separated, transonic flow emerging from the partially started

nozzles of the mixing array. In all cases, channel divergence accounts for the continuous, gradual pressure rise throughout the reaction zone.

Displayed parametric to the pressure plots at the bottom of Figure 3.17 are computed (from gas chromatography) remaining fractions of ethane for the various sample probe stations of the proof-of-concept device. Curve fits of the form of decaying exponentials $(\phi-\phi_\infty) = (\phi-\phi_\infty)_o \exp\{-\beta(x-x_o)/h\}$ provide excellent agreement with data, as might well be expected from considering the fact that the cracking history here proceeds from combined heat transfer and chemical kinetic mechanisms, each generally exponential in nature. By projecting the curves backward, to the point of intersection with unity, one may observe approximately predicted points of reaction origination in reasonable correspondence to the location of the initial pressure recovery, verifying that the upstream mixing process effects negligible or no pyrolysis and, in turn, that the device performs exactly according to its design.

Recovery temperature data acquired by thermocouples located at x/h values of −1.8 (upstream of nozzle array), 9.7, 19.7, 27.7, and 40.8 describe an essentially identical, linear profile throughout the series (Figure 3.18). Note that the high temperature and shock waves within the pressure recovery region greatly limited

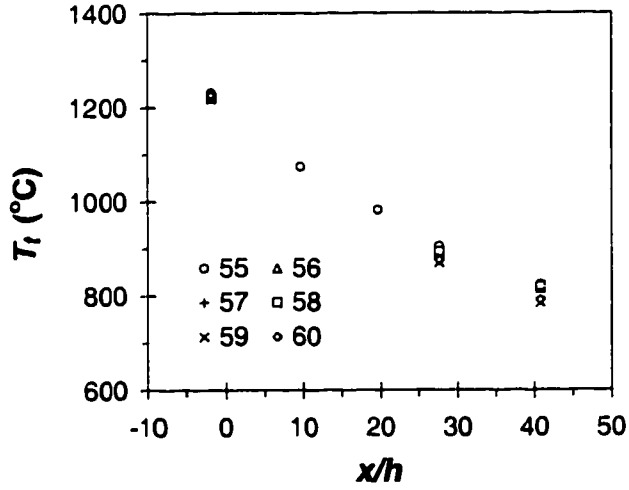

Figure 3.18 Total temperature vs. position from nozzle array normalized by section height for Runs 55-60.

thermocouple life. Thus, measurements at the first two stations downstream of the nozzle array are available here only for Run 55.) Assuming turbulent Prandtl numbers near unity, (and additionally noting that the flow is well subsonic at all but one temperature probe station), one may take recovery for total temperature, and linearly extrapolate to obtain the total temperature at the steam nozzle throat. Because the relative rate of flow of thermal mass of the feedstock is small compared to that of the steam, the fact that it is added ~20% of the way between two temperature probes introduces an error on the order of only a few °C with respect to this estimate, relatively small in comparison to inaccuracy in the reporting and calibration of the thermocouples, themselves. Referring back to Figure 3.15 one may observe an estimate of this error, magnified by the fact of the low dilution of Run 37. With the additional assertion that total pressure losses are small within the short, low speed traverse from the instrumented transition section to the nozzle blades, the steam mass flow rate can be computed using 1-D, constant specific heat ($\gamma \equiv 1.21$) choking assumptions at the known throat area.

Section 3.6 examined the change in total temperature as feedstock passes through the blade core. Noting that the overwhelming majority of the fluid-wall contact occurs within the cavity upstream of the throat, approximate equality may be assumed between internal throat and exit total temperature, determined from the feed plenum measurement and Equation 3.20. In similar fashion to the above treatment, one may proceed to compute the feedstock mass flow rate using ideal gas assumptions, where, for mixed gases (each species being of molar fraction N_i) it may shown that the effective ideal gas constant and specific heat ratio may be computed as follows:

$$\mathcal{R}_{mix} = \frac{\sum_i N_i (M.W.)_i \mathcal{R}_i}{\sum_i N_i (M.W.)_i} \quad \text{and} \quad \gamma_{mix} = \frac{\sum_i \left(\frac{N_i}{\gamma_i - 1} \right) \gamma_i}{\sum_i \left(\frac{N_i}{\gamma_i - 1} \right)_i} \qquad 3.21a, b$$

With the mass flow rates of the carrier and feedstock well approximated, Mach number and flow temperature estimates, shown in Figure 3.19, may be obtained throughout the

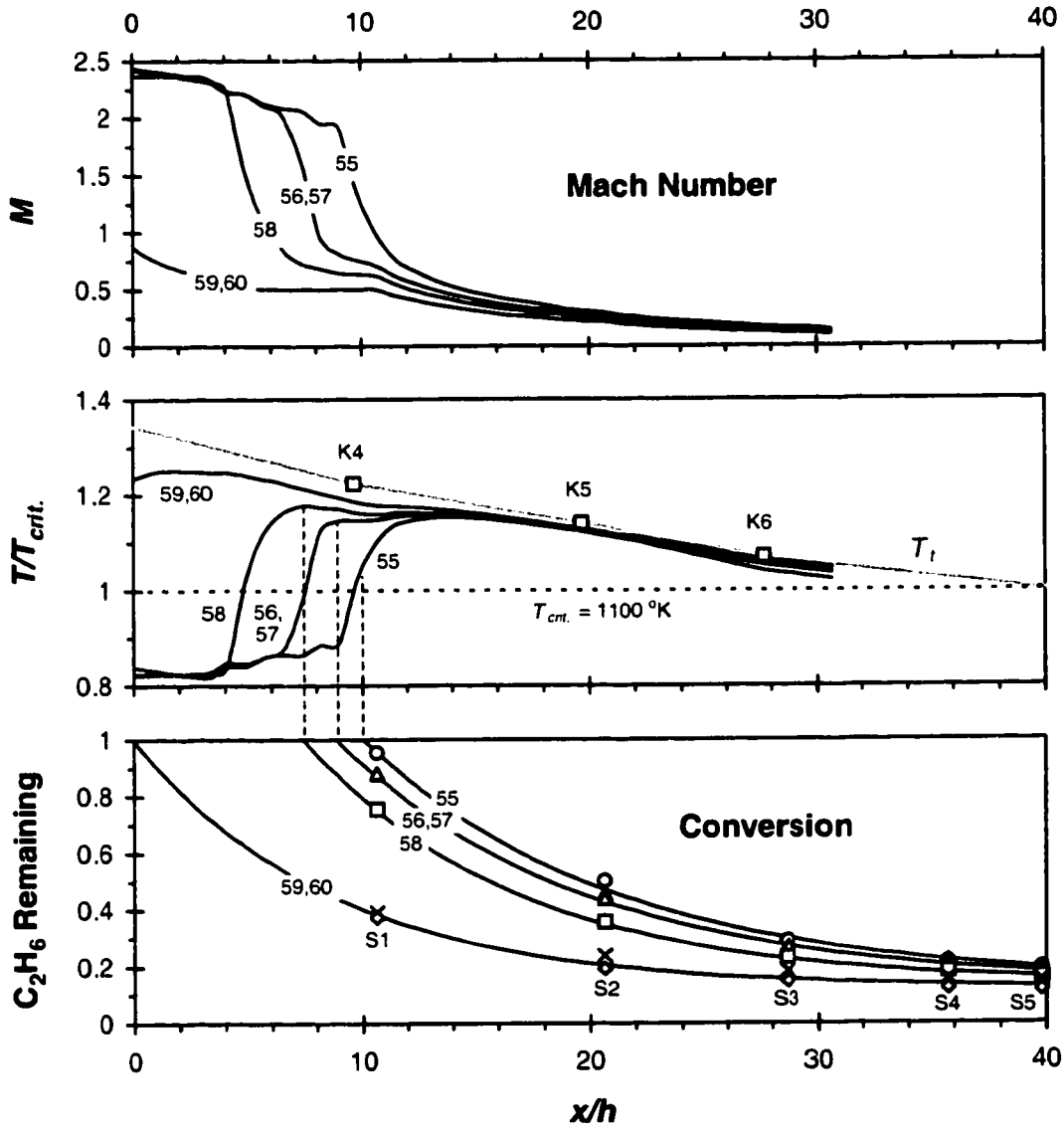

Figure 3.19 Measured total temperature and computed Mach number and static temperature profiles shown alongside conversion.

mixing and reaction processes from the pressure and recovery temperature data via the continuity equation for simple 1-D flow. (Because the flow is highly turbulent, gradients in the flowfield can be expected to be concentrated near the wall; thus the centerline properties are an acceptable estimate of the spanwise average.) While the plug flow model is not strictly correct immediately downstream of the mixing nozzle array where

fluid has not yet reached uniformity, the results of such a calculation may still be interpreted as reasonable, effective averages in light of the fact that the gradients in the flow will be periodic to the scale of the nozzle array, at a fifth of the overall scale, and will decay exponentially. Additionally, the effluent is, in fact, almost uniformly superheated steam, as the feedstock-steam mass flow ratio is quite low.

As in Figure 3.17, conversion data is displayed beneath the computed Mach number and temperature profiles for direct comparison. Here temperatures have been normalized by a reference value of 1100 K, which may be taken as an approximate value of the temperature at which the rate of the primary pyrolysis initiating reaction (where ethane breaks into two methyl radicals):

$$C_2H_6 \rightarrow \dot{C}H_3 + \dot{C}H_3 \qquad 3.22$$

becomes of the sufficient order to effect significant pyrolysis on the ~20 ms reaction timescale of the experiment. Illustrated is that for the started cases, the calculated temperature remains well below the minimum cracking temperature throughout the mixing process until initiated by the recompression at which point an initially rapid followed by gradual recovery toward the total temperature occurs. The displayed non-dimensional total temperature history is that of Run 55, but may be considered characteristically representative of all cases. Increased wall contact time due to the longer post-shock subsonic flow distances of the subsequent trials increased the temperature loss by 35 K over the measured length for the maximal case of Run 59. Mixing was initiated in the started cases at an average estimated Mach number of 2.4 (the steam and feedstock nozzles were designed using 1-D isentropic models for exit Mach numbers of 2.5 and 2.0, respectively), but within the transonic regime for the unstarted cases, as above conjectured.

Selectivity verses conversion (fraction of cracked hydrocarbon feedstock which became C_2H_4 versus fraction cracked) characteristics for Runs 55-60, plotted in Figure 3.20 with curve fits for maximal and minimal cases, demonstrate ethylene yield per amount of ethane cracked to be maximized with the initial pressure recovery near the

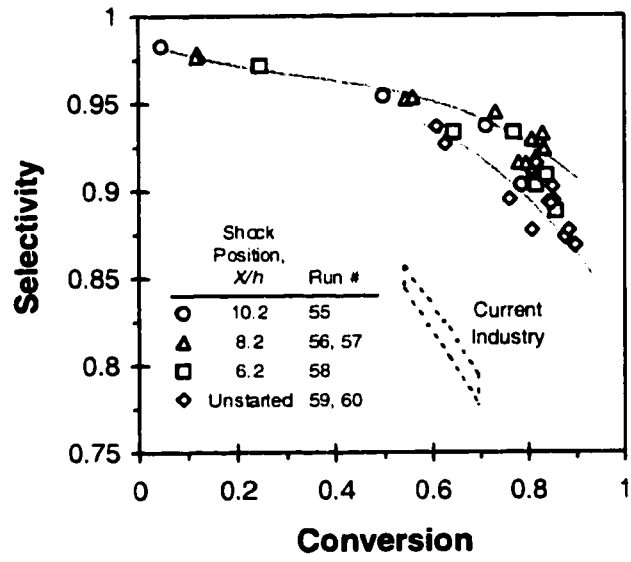

Figure 3.20 Conversion vs. selectivity for various recompression locations.

design location, immediately downstream of the predicted mixing length. Efficiency is observed to deteriorate with premature reaction initiation, reaching its minimum for the totally unstarted cases. This is a feature of key importance, as it directly affirms that shock induction of the reaction can be employed to benefit yield as compared to initiation by simple, fast mixing of feedstock with the energy supplying gas. Additionally, the late reaction initiation of Run 55 effects reduced conversion efficiency compared to the design cases as well, presumably due to the lower peak cracking temperature at the further downstream point of initial temperature recovery. The operating and yield regime of a typical modern pyrolysis furnace is designated at the lower right of the figure for comparison.[2]

3.11 Dilution

Industrial pyrolysis must be implemented at high per-pass conversions as separation of unreacted feedstock for re-processing is energy intensive. Additionally, as previously mentioned, due to much increased steam-to-feedstock ratios, the economic viability of shock wave pyrolysis is equally dependent upon effective energy recovery

from the post-reaction mixture. Indeed, the magnitude of this necessity scales directly with this parameter. Proof-of-concept had been achieved at very high dilution (approximate steam-to-ethane mass flow ratio $\dot{m}_{steam} / \dot{m}_{feed} \cong 26$) -- necessary to achieve the 85% single-pass conversions of interest within the industry given added heat transfer imposed by the limited experimental scale. With the basic principle demonstrated effective, experiments proceeded from this point in the direction of exploring performance at higher feedstock fractions, albeit at consequently lower overall conversion.

In Figure 3.21, data from experiments with feedstock dilution of 9.1 parts ethane to 1 part argon (Runs 61-65) are compared with previously shown data and trendline from higher dilution trials where the initial shock recompression is similarly positioned, within 8.15 and 9.15 section spans downstream of the mixing array exit plane (i.e., identical to within the resolution of the pressure tap spacing). The data remain generally distributed along an identical trendline, also reproduced from the preceding figure, to within the ±1% scatter observed in the high dilution cases. (Three data points in the

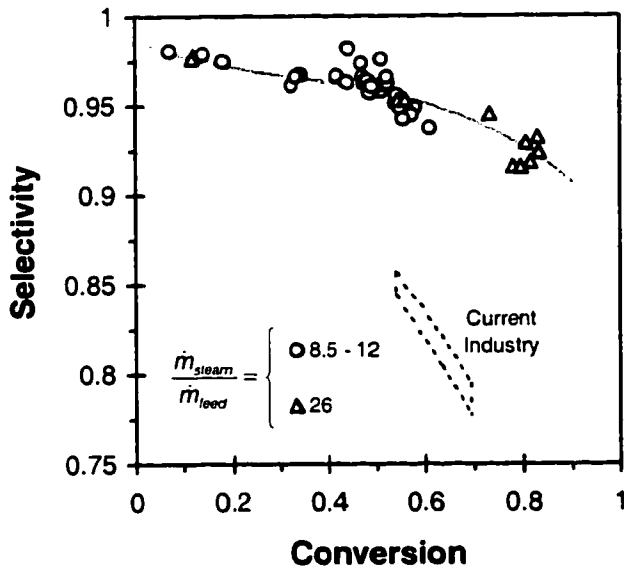

Figure 3.21 Comparison of selectivity vs. conversion for two dilution regimes.

range of 40-43% conversion exceed this trend in excess of the expected random error, but correspond to no identified, consistent parameter variation, and may perhaps be the result of some accidental, procedural deviation.)

During the course of the reduced dilution trials, the pre-feedstock injection steam run time was steadily increased in attempt to augment mixture total temperature by additional preheating of upstream channel walls and thereby incrementally enhancing conversion. The result proved to be diametric, as the altered choking conditions by total temperature increase of the steam at the nozzle throats effected steadily decreased steam mass flow, thereby yielding feedstock richer mixtures and overall lower reaction temperatures and corresponding conversions. Steam-to-ethane mass flow ratios varied from approximately 8.5 to 12 with selectivity tested to maximum conversions around 60%. The fact that these data align well with more dilute cases points to the expectation that the selectivity will continue along the same trend for higher conversions as well. In effect, the lower dilution trials do not represent departure from an effectively saturated regime where the endothermy of the reactions remains essentially negligible in the overall heat balance. However, as may be inferred by the afore mentioned decline in conversion with incremental increases in upstream total temperature, exploration of higher conversion at lower dilutions would require either replacement of the nozzle array in addition to augmentation of steam superheating, or, more desirably, reduction of heat transfer to the channel walls.

It should be noted that, short of increasing the experimental scale, little may be done to reduce the propensity of the channel thermal boundary-layers downstream of the mixing nozzle array to entrain energy from the carrier steam other than to simply further increase the wall temperature. Here the deliberate generation of vorticity to enhance mixing inevitably results in an almost instantaneously fully developed, turbulent flowfield with all associated heat transport and, after all, no fluid element within the mixing section is ever further than 2.5 cm from the wall. As catalysis by the wall surfaces is expected to increase dramatically with further increases in wall temperature, this avenue of exploration, while certainly of interest in regard to establishing upper

limits of performance, bodes substantial augmentation of deleterious coke production. Hence the problem is poignantly reduced to a simple matter of scale, and continued development of the Shock Wave Reactor concept should certainly include testing of an industrial pilot scale facility.

3.12 Tracer Gasses and Error Estimate for Gas Chromatography

Throughout the various trials of the proof-of-concept experiment, feedstock partial pressures comprised less than 10% of the ~2 bar total operating pressure. Consequently, gas chromatography of the extracted sample volumes at correspondingly low pressures proved non-trivial, and continuous technical and analytical efforts to improve the accuracy and sensitivity of sample analysis paralleled the entire Shock Wave Reactor test program. The SRI Instruments model 8610 gas chromatograph employs a single separation coil within a single oven. This represents a substantial obstacle in the analysis of mixtures of species with significantly varying molecular weights, such as the hydrocarbon chains of varying lengths of particular interest here, where long coil residence times are necessary to separate similar light species (e.g. C_2H_2, C_2H_4, and C_2H_6), but result in exponentially slower diffusion rates for heavier C_3's and C_4's. Thus, samples were only analyzed for C_2 and lighter species under the assumption that the operational temperatures and partial pressures of the proof-of-concept device would not produce significant yields of larger hydrocarbons through Run 71. (Ultimately this assumption was demonstrated reasonable in Run 74, discussed in Section 3.14.)

Periodically, the accuracy of chromatography results were verified by comparison for repeatability of multiple analyses of one or more of the sample volumes harvested upon successful completion of an experiment. The flame ionization detector (FID) proved to be the more valuable of the two gas sensors located at the carboxen column terminus, where root-mean-square standard deviation of mole fractions of the various hydrocarbon species, shown in Table 3.2 for data collected post Runs 68 and 69 varies by typically far less than a maximum of 0.3% over three or more consecutive analyses.

Because analysis by flame ionization detects only the hydrocarbon species,

Table 3.2 Average concentrations for multiple FID sample analyses and root-mean-square standard deviation.

Sample Location, x/h	CH_4		C_2H_2		C_2H_4		C_2H_6		Number of Samples	Source Run
	Average %	% R.M.S.D.	Average %	% R.M.S.D.	Average %	% R.M.S.D.	Average %	% R.M.S.D.		
Reservoir	0.0	0.00	0.0	0.00	0.4	0.01	99.6	0.01	11	68
10.6	2.1	0.02	0.4	0.01	41.6	0.20	55.9	0.23	3	68
16.6	3.0	0.03	1.9	0.01	55.3	0.24	39.9	0.24	3	68
20.6	4.6	0.04	5.1	0.04	71.0	0.12	19.3	0.14	3	68
28.6	4.6	0.06	2.9	0.03	73.3	0.06	19.2	0.05	3	69
39.8	4.6	0.02	5.2	0.01	73.5	0.04	16.7	0.02	3	69
Dumptank	5.5	0.04	7.8	0.25	72.9	0.14	13.8	0.13	3	68

however, a 4 element thermal conductivity detector (TCD), sensitive to all gases within the mixture, was employed to corroborate FID results, firstly by providing an alternative, although less accurate measure of the light hydrocarbon proportions, and, secondly, by allowing comparison of the total carbon constituency within the mixture to a non-condensable, inert tracer to access what unaccounted fraction might be ascribed to larger hydrocarbon and coke formation. While argon served as diluent and tracer throughout the Shock Wave Reactor test program, neon supplemented in the role of tracer during Runs 69-71, to circumvent difficulties distinguishing argon from nitrogen, which entered samples as a result of its residual presence in sample lines at incomplete pretrial evacuation to ~2 mm Hg and additionally through small system leaks during operation. (Because the two gases diffuse through the column at virtually identical rates at the 200 °C oven temperature employed to separate the hydrocarbon species, an additional column pass at 40 °C was necessary to resolve their relative mole ratio.)

Average concentrations and root-mean-square standard deviations for TCD analyses of identical samples to those for Run 68 in the preceding FID table are tabulated in similar fashion (Table 3.3.). (The TCD detector was amidst replacement for the

Table 3.3 Average concentrations for multiple TCD sample analyses and root-mean-square standard deviation.

Sample Location, *x/h*	CH_4		C_2H_2		C_2H_4		C_2H_6		Number of Samples	Source Run
	Average %	R.M.S.D.	Average %	R.M.S.D.	Average %	R.M.S.D.	Average %	R.M.S.D.		
Reservoir	0.0	0.00	0.0	0.00	0.0	0.00	100.0	0.00	11	68
10.6	3.1	0.20	1.0	0.00	34.6	1.50	61.3	0.38	3	68
16.6	5.7	0.43	2.6	0.00	47.8	0.29	43.8	0.61	3	68
20.6	6.4	0.22	7.6	0.36	63.2	0.42	22.8	0.70	3	68
Dumptank	6.7	0.49	13.3	0.76	61.2	0.64	18.8	0.90	2	68

following run, thus data are not available for comparison for these cases.) TCD data demonstrate acceptable repeatability for C_2 species, but very poor consistency in measurement of the methane concentration is observed, especially in samples extracted at the station first downstream of the initial temperature recovery. (The larger deviations for the sample volume extracted at x/h = 10.6 are due primarily to the large variation in the CH_4 proportion; the ratios of C_2's to each other compare well with the other cases listed.) This large error occurs as a direct result of the lower hydrocarbon sensitivity and wider utility range of the TCD, due specifically to difficulty resolving the comparatively small CH_4 constituency amidst nitrogen and, particularly, argon exiting the column prior, but inconsequential for FID analysis where the inert species effect no signal. Additionally, even neglecting CH_4 to remove this component of error, TCD measurements compared at much greater inconsistency, especially with regard to detection of sparse components, attributable to a higher signal-to-noise ratio observed relative to the FID as contrasted by the sample gas chromatograms of Figure 2.22. (In order that they may be compared, the signals have been offset by 20 seconds to avoid obscuration of one by the other.) Attempts to augment the signal by construction of an apparatus to boost sample pressures prior to analyses effected only minor improvement.

Perhaps more condemnatory than the inconsistency in the TCD measurements is

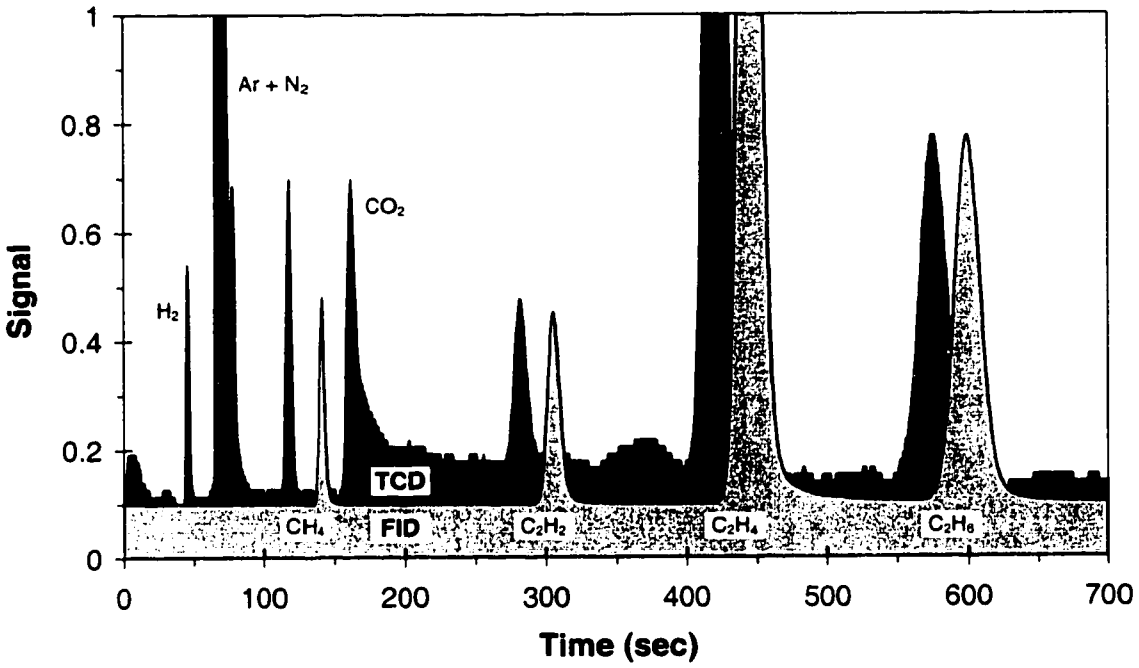

Figure 2.22 Comparison of sample gas chromatograms from FID and TCD analysis. (Run 68, x/h = 21.7)

that between the TCD and FID data, which is notably poor in comparing Tables 3.2 and 3.3. This illustrates that the random error represented by the root-mean-square standard deviation shown in Table 3.3 comprises only a small component of the total error, the majority of which is quite repeatable; indeed it might well be inferred and was, in fact, observed, that the large peaks of the inert species and overall jagged nature of the chromatogram curve consistently skew integration of CH_4 and other minor species' signals exceeding the noise level by insufficient margins. (As might therefore be expected, samples extracted from the dump-tank volume, highly diluted with the nitrogen employed to purge the upstream system following an experimental run, generally showed the least consistency. (All other samples were isolated by solenoid valves prior to the system purge.) Additionally, periodic reassessment throughout the Shock Wave Reactor program revealed calibration drift be quite large for the TCD, but, fortuitously, virtually non-existent for the FID. Thus, TCD analyses, requiring of frequent and time intensive recalibration to achieve moderate accuracy, were not always performed, in favor of

clearly more reliable FID and the role of argon relegated to that of a simple diluent for some cases.

By circumstance, the presented test data used to estimate repeatability for the TCD (which are in low abundance for the above stated reasons), depict the worst case with respect to comparison with FID results. More typically, data obtained by the two methods following recent TCD calibration agreed to approximately within 10% for the minor species, less disconcerting but still well short of the accuracy required to assess the presence of unanalyzed minor hydrocarbon constituents. In Table 3.4, the average values presented in Tables 3.2 and 3.3 for C_2H_4 and C_2H_6 have been normalized to neglect minor constituents and compare to within 4% root-mean-square standard deviation for all available data. This was typical of all trials. In summary, the high signal-to-noise ratio and steadfast consistency of the FID measurements resulted in reliance upon it as the primary diagnostic while TCD provided only a very approximate safeguard check of the relative proportions of the major products.

Table 3.4 Average relative percentages of C_2H_4 and C_2H_6 by FID and TCD analyses and root-mean-square standard deviation for Run 68.

Sample Location, *x/h*	C_2H_4 Average %	C_2H_4 % R.M.S.D.	C_2H_6 Average %	C_2H_6 % R.M.S.D.	Number of Samples	R.M.S.D.
Reservoir	0.4	0.0	99.6	100.0	11	0.19
10.6	42.6	36.2	57.4	63.8	3	3.23
16.6	58.1	52.2	41.9	47.8	3	2.95
20.6	78.6	73.5	21.4	26.5	3	2.56
Dumptank	84.1	76.4	15.9	23.6	2	3.84

3.13 Independent Corroboration of Results

The Shock Wave Reactor program has elicited a high degree of interest from

within the chemical pyrolysis industry. Nova Corporation, one of several potential industrial partners who participated in presentations/demonstrations of the technology at the University of Washington (Runs 66 and 67 were preparation for and demonstration upon the occasion of this visit.) was provided gas specimens originating from the final two sample stations of the apparatus reaction zone for independent analysis and reported good agreement with the FID data.

3.14 Effect of Argon Diluent on Selectivity/Conversion -- Final Trial

For thoroughness, to assess the unlikely possibility that argon or neon should affect the reaction kinetics in any way other than as simple diluents, a final test was performed employing undiluted ethane (99.6% pure) as the feedstock injectant. Figure 3.23 dismisses this prospect, as the data, represented by dark squares, align well with results and trendline (reproduced from Figure 2.21) of previous trials with the initial pressure recovery comparably positioned, between 8.2 and 9.2 section spans downstream of the mixing array exit plane). Additionally, extracted samples were analyzed for all components with column residence times up to one hour, allowing the fractional

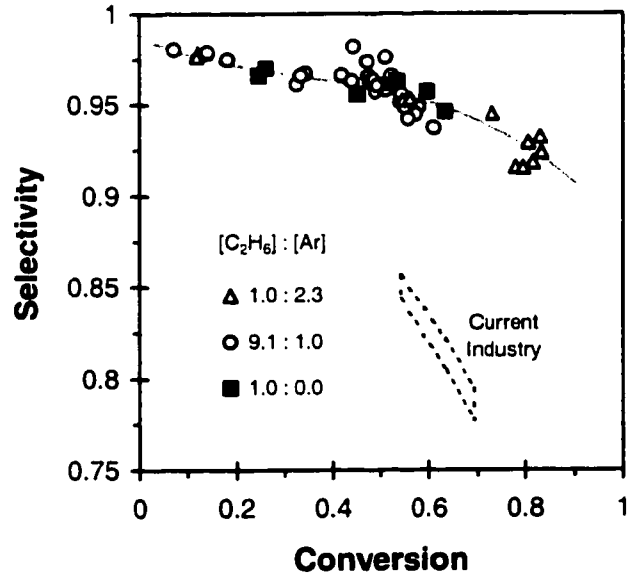

Figure 3.23 Conversion vs. selectivity for highly diluted, slightly diluted, and undiluted feedstock.

constituency of C_3 species to be measured. Mole fractions for detected hydrocarbon species are presented in Table 3.5.

Table 3.5 Hydrocarbon fractions by FID analysis for Run 74.

Sample Location, x/h	Molar Fractions, %						
	CH_4	C_2H_2	C_2H_4	C_2H_6	C_3H_4	C_3H_6	C_3H_8
Reservoir	0.0	0.0	0.4	99.6	0.00	0.00	0.00
10.6	1.1	0.1	23.6	75.1	0.00	0.03	0.08
16.6	1.0	0.1	25.1	73.7	0.00	0.02	0.09
20.6	1.9	0.8	42.6	54.6	0.00	0.06	0.12
28.6	2.1	0.7	50.8	46.2	0.00	0.05	0.09
39.8	2.4	1.2	56.4	40.0	0.00	0.03	0.07
Dumptank	2.6	1.7	59.2	36.3	0.00	0.06	0.24

3.15 Kinetic Modeling

While not specifically a topic of this dissertation, it should be mentioned that numerical chemical kinetics modeling was integral in obtaining proof of the Shock Wave Reactor concept. Employing the chemical equation set and thermodynamic reaction rate data compiled by Sundaram and Froment[3], Chemkin (Sandia Laboratories) and in-house codes employing stiff solvers provided 1-D reaction profiles necessary in the design of the proof-of-concept experiment. The Sundaram and Froment model was gradually augmented to include an additional 100 chemical equations (totaling 233) and corresponding reaction rate temperature/pressure dependencies from additional sources. Real gas effects (variable specific heats) and wall heat transfer were incoprporated into the model to more effectively simulate the reaction zone of the experiment.

The example of Figure 3.27 demonstrates good agreement between predictions and data (FID) from Run 57 (initial reaction temperature $\approx$ 1260 K) for the major hydrocarbon species. The master's thesis of Mahmood Mahmoodian[4] and the United States Department of Energy contract DE-FG06-93ER12136 Final Report[5] are recommended for supplemental information.

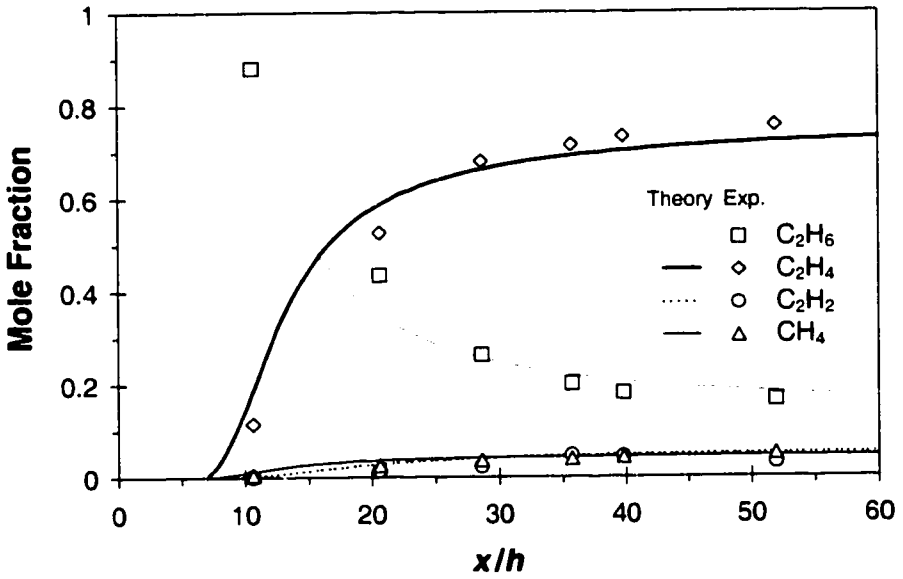

Figure 3.24 Comparison of numerical predictions and data for Run 57.

3.16 Propane Pyrolysis

Shock wave initiated pyrolysis of larger hydrocarbons was very briefly addressed experimentally. Measured temperatures and pressures, along with streamwise variation of flow properties computed in identical fashion to those of Section 3.10, are presented in Figure 3.24 for Run 73, which, with the exception of the replacement of the ethane-argon

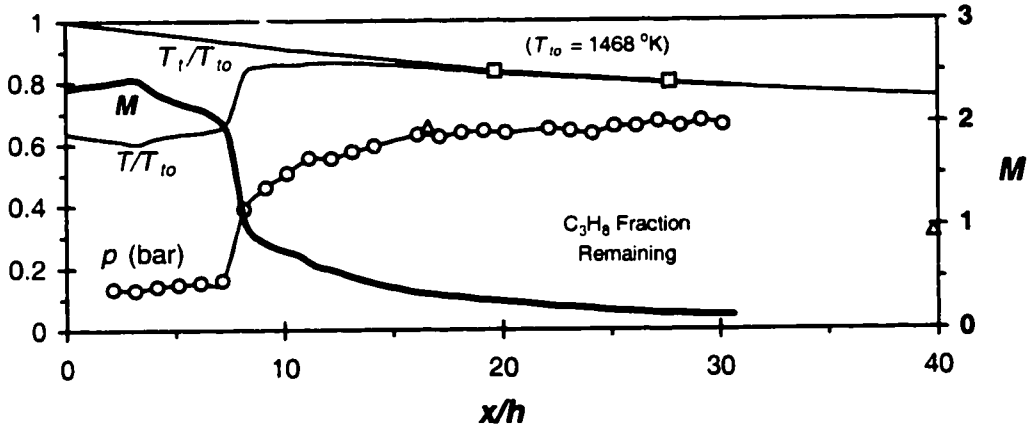

Figure 3.25 Conversion and flowfield property profiles for propane pyrolysis (Run 73).

Table 3.6 Fuel grade propane composition.

Species	Molar %
CH_4	1.06
C_2H_2	0.00
C_2H_4	0.01
C_2H_6	4.35
C_3H_4	0.00
C_3H_6	0.16
C_3H_8	94.42

mixture with fuel grade propane (Table 3.6), diluted 1:1.5 parts argon, was identical to preceding runs with the initial pressure recovery effected at $x/h \approx 7.5$. In Figure 3.25 selectivity (fraction of cracked C_2H_6 which became C_2H_4) of Run 73 and an additional datum obtained in the subsequent test, which was identical to 73 excepting a slightly earlier shock recovery to effect increased cracking, are compared to typical industry results.[2] While the maximum 79% conversion represents a 19% increase over the peak 60% for more difficult ethane pyrolysis at similar temperature and dilution, the

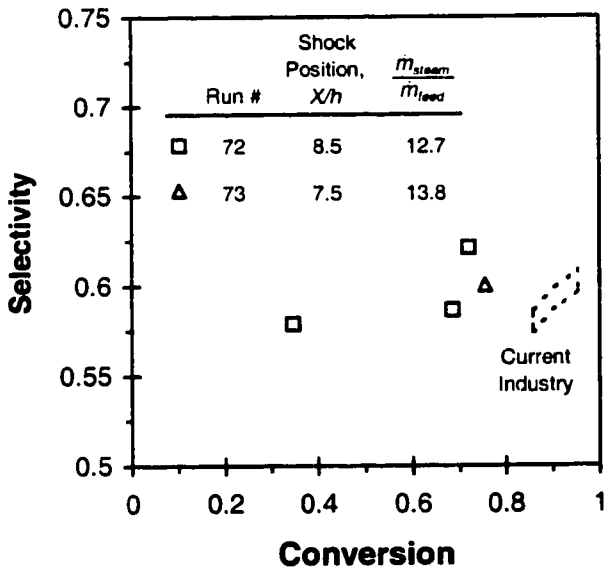

Figure 3.26 Selectivity vs. conversion for propane pyrolysis.

experimental data are difficult to compare with industrial yields[2] where propane pyrolysis processes are operated at design conversions exceeding 90% per pass. The limited data set extrapolates to comparable or perhaps slightly improved selectivity at elevated yields, however.

3.17 Conclusions for Hot Flow Experiments

The proof-of-concept apparatus demonstrates conclusively that the Shock Wave Reactor concept can be effectively employed to improve per pass ethylene yield selectivity for the pyrolysis of ethane using steam as an inert energy carrier. While the various trials of the test program employed high carrier-to-feedstock ratios in order to compensate heat transfer associated with the limited scale of a practical experiment, results showed little dependence upon this parameter through the tested range of steam-to-feedstock mass flow ratios from 7.5 to 35.0, indicating that these investigations may be interpreted as representative of an ideal, completely unsaturated regime, and that the results presented here may be extrapolated to further reduced dilutions. This is supported by numerical computations, which agree well with presented data. Additionally, fuel

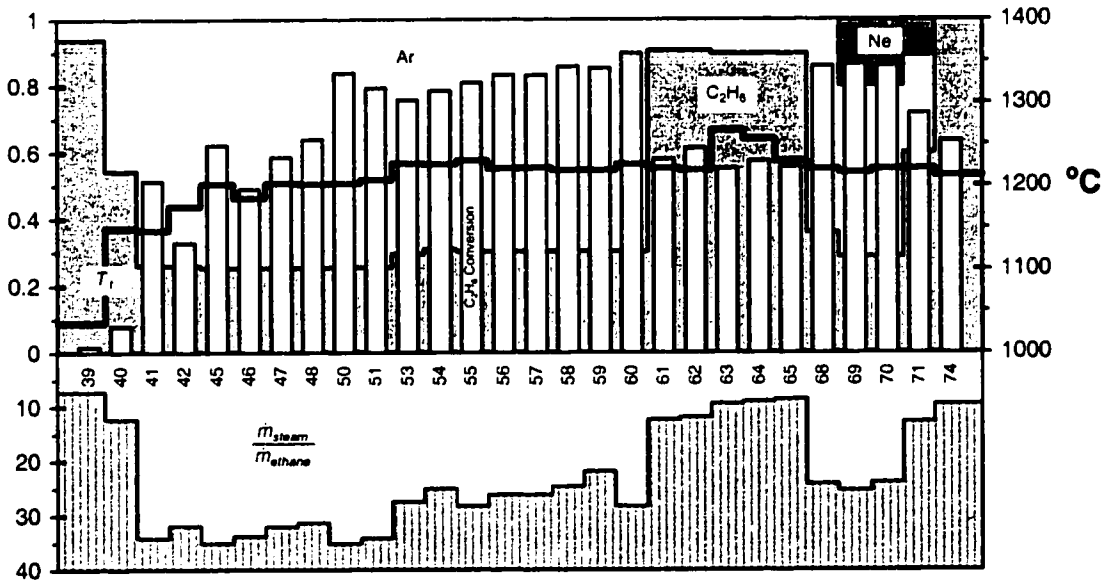

Figure 3.27 Histogram of ethane experiments.

grade propane experiments report yields indicative of comparable to industry performance. A graphical summary of feedstock composition and ratio to steam, maximum conversions, and total steam temperatures for the twenty-eight trials involving successful ethane pyrolysis through the course of the hot flow experiments is presented in the histogram of Figure 3.26. (Disincluded are runs associated with pre-cracking apparatus development, maintenance, propane pyrolysis, and reactionless demonstrations.)

3.18 Notes for Chapter 3

1. Galarza, J. Z., Design of Gas Sampling Probes for Pyrolysis Experiments, Masters Thesis, Univ. of Washington, Seattle, WA, 1995

2. Grantom, R. L. and Royer, D. J. "Ethylene," *Ullmann's Encyclopedia of Industrial Chemistry*, fifth edition, VCH Publishers, Deerfield Beach, FL, 1985, Vol. A 10, pp. 45-93.

3. Sundaram, K. M. and Froment, G. F., "Modeling of Thermal Cracking Kinetics 3: Radical Mechanisms for the Pyrolysis of Simple Paraffins, Olefins, and Their Mixtures," *Ind. Eng. Chem. Fundam.*, Vol 17, No. 3, 1978, pp 174-182

4. Mahmoodian, M., "Modeling the Pyrolysis of Ethane and Study of Boundary-Layer Growth in a Shock Wave Reactor," Masters of Science Thesis, Dept. of Aeronautics and Astronautics, University of Washington, Aug. 1994.

5. Mattick, A. T., "The Supersonic-mixing, Shock-wave Reactor: An Innovative Approach for Efficient Chemical Production," Final Report, U. S. Department of Energy contract number DE-FG06-93ER12136, 1991.

4. Shock Recompression

In the early stages of the Shock Wave Reactor development program discussed in Chapter 2, extensive effort was made to analytically and experimentally characterize the supersonic mixing process, prioritized through the necessity of accurate data and predictive capability in the design of the proof-of-concept experiment. Study of the reaction-initiating shock recompression was limited in scope to concern for spatial stability, so as to ascertain requirements to obtain consistent, repeatable operation of the experiment over approximately one minute intervals corresponding to the anticipated proof-of-concept test duration. Adherence to a necessarily strict experimental schedule prevented detailed study of the shock structure at that time.

With proof-of-concept successfully demonstrated, study of the basic concept is naturally succeeded by interest in industrial adaptation of the Shock Wave Reactor, particularly with regard to issues involving the scaling and refinement of the shock recompression. Thus, the third stage of the Shock Wave Reactor development program was comprised of studies undertaken to improve predictive capabilities via a simplified model of shock recompression within ducts, incorporating all parameter dependencies.

4.1 Shock-Boundary Layer Interaction

The heart of characterization of shock recompression within a duct rests in understanding the interaction of shock waves with subsonic regions of flow near the sidewalls. A single lambda shock (with a large normal component) and interaction are seen to transition with increasing Mach number and boundary-layer thickness to an increased number of waves and interactions with enlarging oblique components as shown in Figure 4.1. Supersonic pressure recovery within a duct is fundamentally related to the oblique waves formed near the walls; the normal components merely representing Mach reflections about the centerline.[1] This intimate relationship between pressure recovery and viscous activity within the incoming boundary-layer, implies a Reynolds number/boundary-layer dependence.

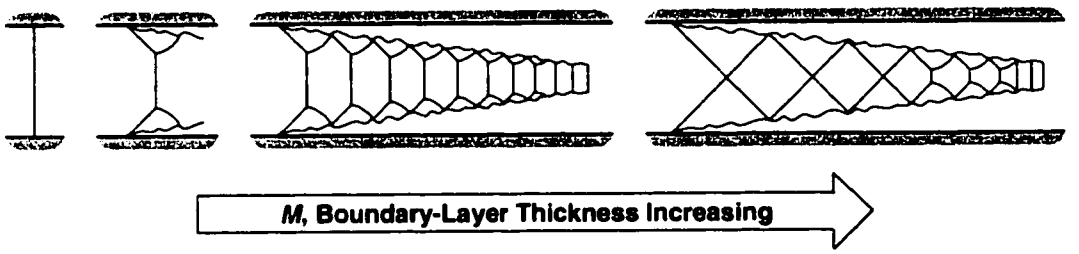

Figure 4.1 Schematic of influence of increasing Mach number and boundary-layer thickness on recompression structure.

In 1952 Donaldson and Lange proposed that shock wave induced boundary-layer separation must proceed upstream to an equilibrium point where the compression gradient exactly equals that required to detach the boundary-layer.[2] Arguing that the wall pressure gradient corresponding to the shock-boundary layer interaction must scale with the boundary-layer thickness, the following relationship for pressure across the impinging shock was predicted by dimensional arguments:

$$\frac{\Delta p_{sep}}{\rho U^2} = \frac{\text{constant}}{\text{Re}_l^{\,n}} \qquad 4.1$$

where n = $^1/_2$ for laminar layers and $^1/_5$ for turbulent. This relation was compared to experiments (Figure 4.2) which examined the separation of the boundary-layer

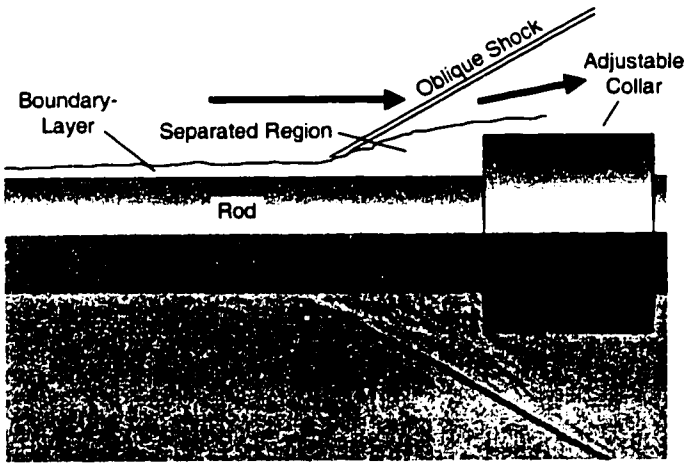

Figure 4.2 Reflected schematic and photographic half images of Donaldson and Lange experiment.

developing on a steel rod by the presence of a shock generated ahead of a collar. The growth length, and, therefore, thickness of the boundary-layer at the point of interaction could be varied by adjustment of the collar position along the rod.

The relationship may be restated for laminar flow using compressible boundary-layer equations:

$$\frac{\partial \rho u}{\partial x} + \frac{\partial \rho v}{\partial y} = 0 \qquad 4.2a$$

$$\rho u \frac{\partial u}{\partial x} + \rho v \frac{\partial v}{\partial y} = -\frac{\partial p}{\partial x} + \frac{\partial}{\partial y} \mu \frac{\partial u}{\partial y}^2 \qquad 4.2b$$

$$\rho u \frac{\partial h}{\partial x} + \rho v \frac{\partial h}{\partial y} = u \frac{\partial p}{\partial x} + \frac{\partial}{\partial y} \frac{\mu}{Pr} \frac{\partial h}{\partial y} + \mu \left(\frac{\partial u}{\partial y} \right)^2 \qquad 4.2c$$

Applying the Illingworth-Stewartson transformation[3] yields:

$$\frac{\partial \tilde{u}}{\partial \tilde{x}} + \frac{\partial \tilde{v}}{\partial \tilde{y}} = 0 \qquad 4.3a$$

$$\tilde{u} \frac{\partial \tilde{u}}{\partial \tilde{x}} + \tilde{v} \frac{\partial \tilde{v}}{\partial \tilde{y}} = \tilde{u}_1 \frac{\partial \tilde{u}_1}{\partial \tilde{x}} (1 + S) + \nu_{t1} \frac{\partial^2 \tilde{u}}{\partial \tilde{y}^2} \qquad 4.3b$$

$$\tilde{u} \frac{\partial S}{\partial \tilde{x}} + \tilde{v} \frac{\partial S}{\partial \tilde{y}} = \nu_{t1} \left[\frac{1}{Pr} \frac{\partial^2 S}{\partial \tilde{y}^2} + \frac{\mathrm{Pr} - 1}{\mathrm{Pr}} \frac{\frac{1}{2}(\gamma - 1) M_1^2}{1 + \frac{1}{2}(\gamma - 1) M_1^2} \frac{\partial^2}{\partial \tilde{y}^2} \left(\frac{\tilde{u}}{\tilde{u}_1} \right)^2 \right] \qquad 4.3c$$

where

$$\tilde{x} \equiv \int_0^x b \frac{p_1}{p_{t1}} \frac{a_1}{a_{t1}} dx ; \qquad \tilde{y} \equiv \frac{a_1}{a_{t1}} \int_0^y b \frac{\rho_1}{\rho_{t1}} dy ; \qquad 4.3d, e$$

$$b \equiv \frac{\mu / \mu_{t1}}{T / T_{t1}} ; \qquad S \equiv \frac{h + \left(u^2 / 2 \right)}{h_{t1}} - 1 \qquad 4.3f, g$$

Subscripts t and 1 denote stagnation (or total) and freestream values, respectively. Following similar solutions of Cohen and Reshotko[4] the transformed velocity profile may

be related to a shape parameter $\tilde{K} \equiv (\tilde{\theta}/\nu_{t1})(d\tilde{u}_1/d\tilde{x})$ where $\tilde{\theta}$ is the integral momentum thickness defined in transformed variables and note additionally that a specific value of $\tilde{K}(S)$ corresponds to the separation condition:

$$\tilde{K}_{sep}(S) = \frac{\tilde{\theta}^2}{\nu_{t1}} \frac{d\tilde{u}_1}{d\tilde{x}} \tag{4.4}$$

Return to physical variables may be accomplished via the identities $\tilde{\theta}/\theta = (a_1/a_{t1})(\rho_1/\rho_{t1})$ and $\tilde{u}_1 = a_{t1}M_1$:

$$\tilde{K}_{sep}(S) = \left(\frac{\theta}{l}\right)^2 \frac{Re_l}{2bM_1^2} \frac{dM_1^2}{d(x/l)} \tag{4.5}$$

where $Re_l \equiv (\rho_1 u_1 l)/\mu_1$ and l is an arbitrary length scale (which may be assigned to be the shock position for comparison to the Donaldson and Lange results). Conserving inviscid momentum in the freestream direction ($p_1 + \rho_1 u_1^2 = \text{constant}$) gives $\gamma d(M_1^2) = d(1/p)$:

$$\tilde{K}_{sep}(S) = \left(\frac{\theta}{l}\right)^2 \frac{Re_l}{2b\gamma M_1^2} \frac{d(1/p)}{d(x/l)} \tag{4.6}$$

At this point, the derivative may be discretized in analogous fashion to Donaldson and Lange ($d(\,)/dx \sim \Delta(\,)/\theta$), i.e., gradients may be assumed to scale locally with the height of the momentum boundary-layer:

$$\tilde{K}_{sep}(S) = \left(\frac{\theta}{l}\right)^2 \frac{Re_l}{2b\gamma M^2} \frac{\Delta(1/p)}{\beta(\theta/l)} \tag{4.7}$$

Here β is an arbitrary proportionality constant relating derivative and discretized quantities. Once again substituting from freestream momentum, the above expression may be rearranged to obtain:

$$\frac{\Delta p_{sep}}{\rho u_1^2}\left[\frac{1+\gamma M_1^2}{\pi(M_1)}\right] = \frac{-4\beta\tilde{K}_{sep}}{Re_L(\theta/l)} = \frac{\text{constant}}{Re_l(\theta/l)} \tag{4.8}$$

where $\pi(M)$ denotes the pressure ratio across the shock wave.

Given that $\theta/l \propto Re_l^{-1/2}$, this expression is identical to that proposed by Donaldson and Lange with the addition of a compressibility correction, subsequently denoted $K_M \equiv (1 + \gamma M_1^2)/\pi(M_1)$. In Figure 4.3, data presented by Donaldson and Lange are reproduced in original form and multiplied by K_M for comparison. Laminar data shown are reduced to a monotonic trend, with some indication of curvature appearing. As this apparent camber is based solely on the two extreme points of data, one must conclude that there is inadequate data to provide accurate assessment in this regard. Additionally, as there is no reason to assume compressibility affects should differ between laminar and turbulent flows, the correction is operated on the more plentiful turbulent data as well, yielding an intriguing result. The uncorrected data, which appeared to generally match the afore predicted $-1/5$ power Reynolds number dependence based on l (but upon closer examination appear in three distinct groupings each internally showing much reduced dependence) collapse to a single flat line, with considerably reduced scatter.

Because boundary-layers generally develop as l/Re_l^n (where l is the streamwise distance from the point of origin) Reynolds number independence generally implies a

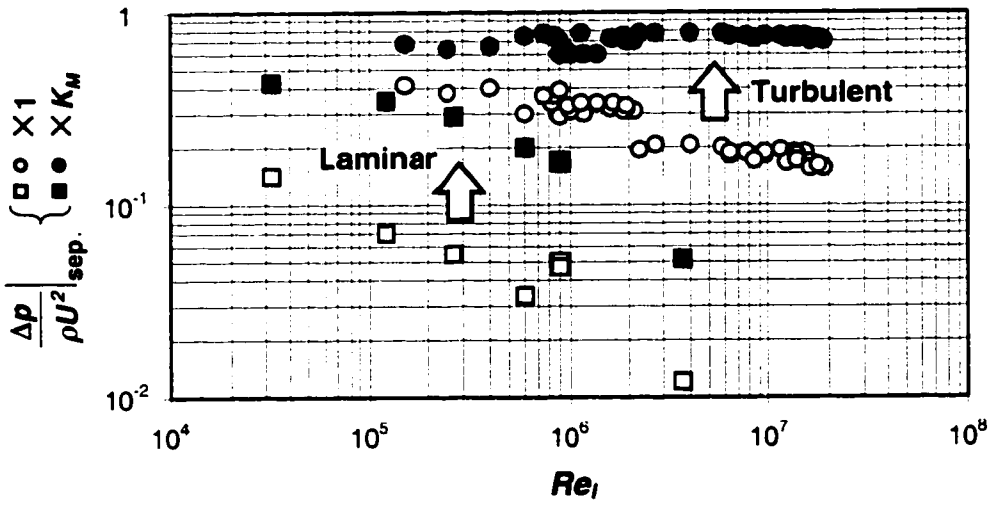

Figure 4.3 Donaldson and Lange results with and without compressibility correction factor.

nearly linear boundary-layer growth. As some of the Donaldson and Lange data shown in Figure 4.3 represent turbulent interactions with different boundary-layer thicknesses but otherwise identical flow conditions, however, the invariance demonstrated in the figure represents not only Reynolds number independence, but complete insensitivity to the collar position. This suggests that for the turbulent cases the shock interaction is simply too weak to separate the boundary-layer at all. The observed separation merely represents the boundary between the incoming boundary-layer and stagnated flow ahead of the blunt collar face which would exist with or without the presence of the wall (and boundary-layer). Further, this explanation is reinforced by comparing differences between representative, characteristic pressure profiles measured for laminar and turbulent cases, shown in Figure 4.4, and the corresponding points at which the Δp for the predicted correlation was measured. While the pressure profile and initial rise may be clearly ascribed to the boundary-layer for the laminar case, no evidence of any direct influence is observable for the case of the thinner, turbulent boundary-layer. While this renormalization does not allow definitive deduction of Reynolds number independence, the apparent elimination of this dependence by a single parameter expression in Figure 4.3 casts doubt upon these original conclusions.

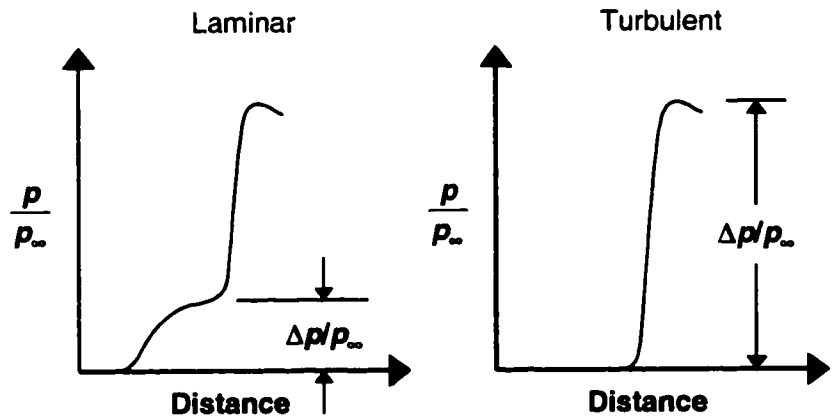

Figure 4.4 Sample pressure profiles from Donaldson and Lange experiment for laminar and turbulent cases.

4.2 Shock Recompression Experiments

The nature of interaction of the multiple-shock recompression system and turbulent boundary-layer of the Shock Wave Reactor are subject to similar inspection, and the above results suggest the possibility that, as indeed seems the case for the Donaldsdon and Lange experiment, the shock system may, in fact, be produced by the presence of a downstream-induced separation zone, vice-versa to the common interpretation of the separation being induced by a downstream-effected shock system. While offhandedly this issue may appear paramount to the semantic riddle of the chicken and the egg, the distinction is quite fundamental in that it pertains to the very nature (and therefore parameter dependence) of the recompression system, suggesting that it is the separated layer which plays the chief role in determination of the wall pressure recovery profile and relegating the shock system as a secondary, dissipative feature, analogous to wave drag on an airfoil.

A 2-D test section has been fabricated which accommodates manipulation of all flow parameters relevant to duct recompression. This apparatus (Figures 4.5 and 4.6) consists of a pair of 5.7 x 20 cm stainless steel manifolds with flexible upstream sections which, when pressed between two 2.5 cm thick glass plates, form the upper and lower walls of a blow-down wind tunnel, fed by a variable-throat-area nozzle. (Because of the contour constraints associated with variability, the nozzle expansion was designed to be gradual, rather than ideal; method-of-characteristic analysis and, ultimately, spanwise pressure measurements with a 0.3 mm diameter pitot probe confirm an approximately 2-D exit flow without significant shock losses.) More comprehensive in capability than predecessors, manipulation of feed pressure (up to 4 MPa), flow blockage dam, and appropriate positioning rods allow the variation of flow Reynolds and Mach numbers, as well as geometric features of the recompression region, including both the section height (0-2 cm, denoted h hereafter) and wall convergence/divergence (-5° to $+20^{\circ}$). Additionally, a linear array of bleed holes enables partial or complete suction of the boundary-layer. Thus, unique mapping of each of these parameter dependencies is possible; however, studies thus far have been limited to non-diverging flows without

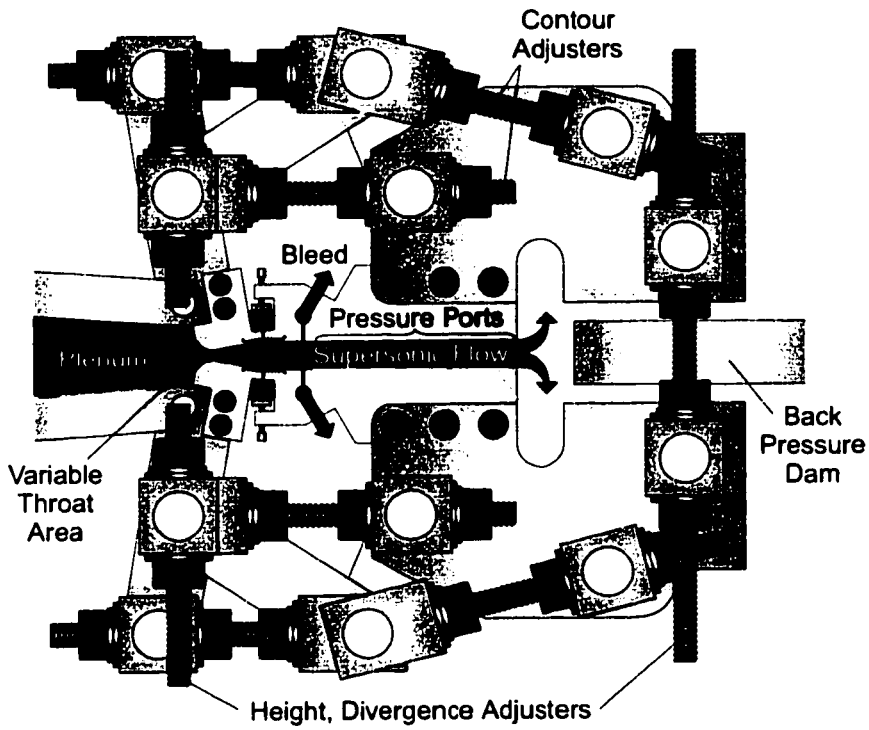

Figure 4.5 Schematic of apparatus.

boundary-layer bleed. Notable also is that, in contrast to all preceding experiments studying shock trains, the high aspect ratio of the duct enables the approximation the much simplified case of 2-D flow.

Twenty-one piezo-resistive pressure gauges (Barclay model 402H2-03CA-04-3) connect to taps spaced at 6.4 mm intervals downstream of the bleed hole-array, with additional transducers used to detect plenum and exit total pressures. All outputs are sampled and stored at 100 Hz. A 27 m^3 compressed air reservoir, chargeable to 14 MPa, provides capacity for extended operation (~1 hr); however, experiment durations of ~5 minutes were adequate to gather sufficient data on the parameters under investigation. During a run, the leading edge of the recompression shock train is positioned in the test section by varying back pressure with a rectangular dam near the duct exit while upstream conditions are maintained nearly constant.

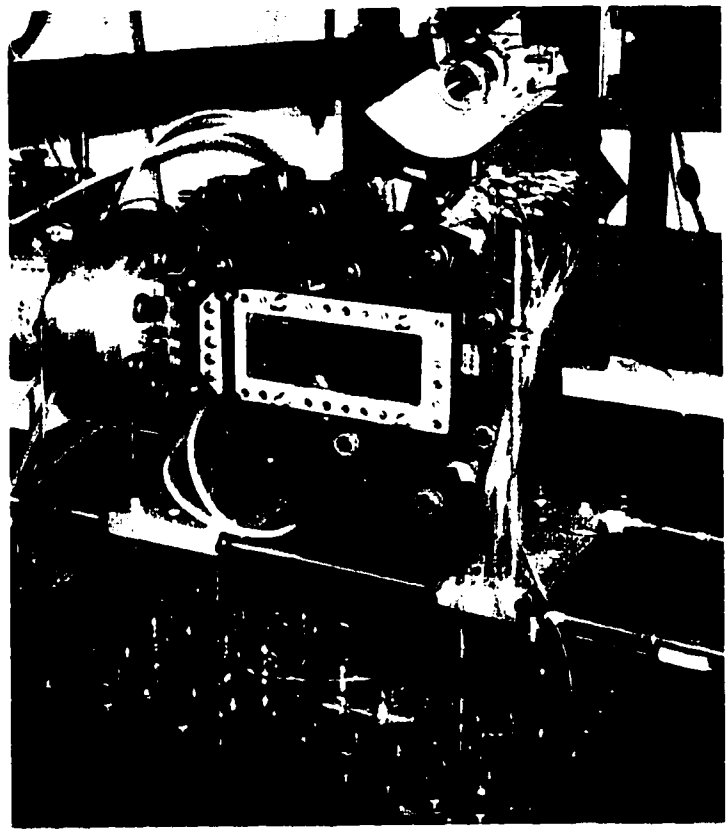

Figure 4.6 Photograph of apparatus.

4.4 Time Averaging

Low frequency oscillations in the pressure data demonstrate unsteadiness in both the recompression position and streamwise profile, in agreement with prior observations.[5] Because fluctuations appear centered around steady average values for fixed upstream and back pressure control settings, a characteristic profile may be obtained by time averaging. The pressure data of Figure 4.7 are representative of typical composites of eight instantaneous "snapshots" for profiles with nearly identical initial recompression position as well as inlet and downstream flow conditions. It should be noted that while flow parameters are relatively easy to hold invariant, such is not the case for the fundamentally oscillatory recompression position. Thus, the time profiles shown here are not necessarily composed of eight time-consecutive samples (they are in some cases), but

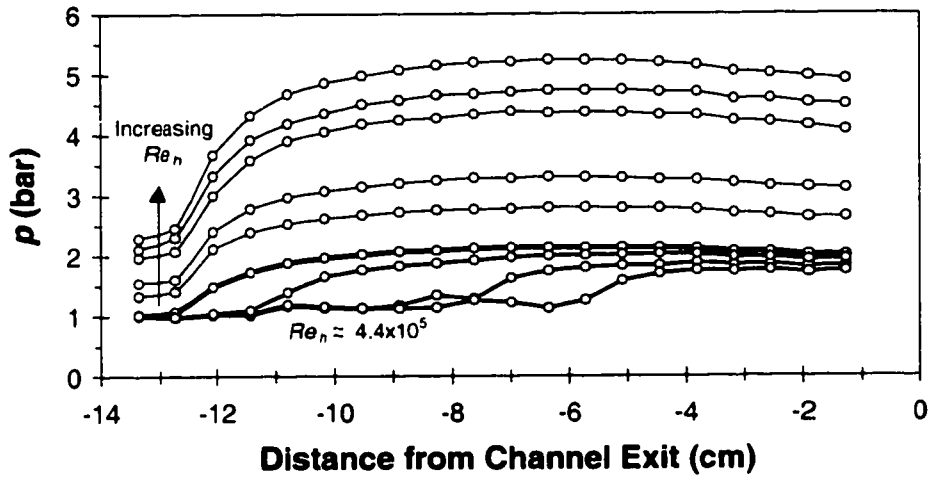

Figure 4.7 Time-averaged experimental pressure profiles at various Re_h.

rather of the eight most consecutive samples with closely matched initial pressure rise location, skipping out of phase data where necessary. This is important to avoid the "washing out" of steep pressure gradients which would occur were samples at imprecise locations combined. Note additionally that the amplitude of the pressure fluctuation was observed to increase as the shock system was moved further downstream, making these cases more susceptible to error induced in this fashion.

4.5 Shock Recompression Model

The similar and exponential appearance of the data of Figure 4.7 suggest that, as is often the case for semi-periodic phenomena, the complex, non-steady interaction of shock and compression waves with turbulence in the separated layer might be well represented by a one-dimensional (1-D), time-averaged model. The momentum equation of an ideal gas may be written in integral form:

$$\frac{d}{dx}\left[p + \rho U^2\left(1 - 2\frac{\theta^*}{h}\right)\right] = -\frac{4\tau_w}{D} \qquad 4.9$$

where τ_w is the wall shear stress, D is the hydraulic diameter, and

$$\frac{\theta^*}{h} \equiv \frac{1}{2}\int_0^1 \left(1 - \frac{\rho u^2}{\rho_1 U^2}\right) d(y/h)$$

While the static and dynamic pressures are ordinarily related via additional 1-D conservation equations, here it may be noted that transverse velocities are non-negligible. Thus, these components would have to be included in the energy balance, inherently coupling transverse momentum equations into the system, and thereby great complexity. Rather, closure must be obtained through an alternative, simpler relationship.

As per Figure 4.8, the balance of pressure forces and momentum transport on a differentially long control volume surrounding the nearly stagnant, separated flow in the vicinity of the channel wall results in:

$$\delta dp + d\left(\delta \rho_s U_s^2\right) + \rho U^2 d\delta + \tau_w dx = 0 \qquad 4.10$$

where δ represents a characteristic separation height which need not be specifically determined and subscript s denotes values within the separated region. The net momentum exchange with the core of the flowfield across the top of the control volume is assumed to time average approximately to zero. Inserting into the 1-D Momentum

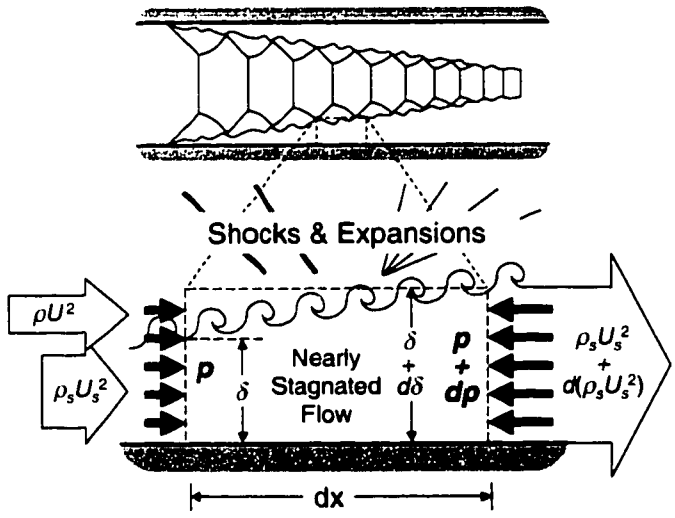

Figure 4.8 Control volume sketch

equation from above (4.9) gives:

$$\frac{d}{d\delta}\left[p+\left(1-2\frac{\theta^*}{h}\right)\left(\delta\frac{dp}{d\delta}+\frac{d}{d\delta}\left(\delta\rho_s U_s^{\,2}\right)+\frac{\tau_w}{d\delta/dx}\right)\right]=-\frac{4\tau_w}{D} \qquad 4.11$$

or, defining $L \equiv \{1\text{-}2(\theta^*/h)\}[\delta/(d\delta/dx)]$, a characteristic scale for momentum dissipation from the freestream which will be assumed approximately invariant over the shock recompression length for simplicity:

$$\frac{d}{dx}\left[p+L\frac{d\left(p+\rho_s U_s^{\,2}\right)}{dx}+\left(1-2\frac{\theta^*}{h}\right)\left(\rho_s U_s^{\,2}+\frac{\tau_w}{d\delta/dx}\right)\right]=-\frac{4\tau_w}{D} \qquad 4.12$$

At this point it may be concluded that, as the transport term corresponding to the nearly stagnated region is relatively small, its derivative may be presumed even more diminutive and thus neglected. Additionally, while one might approximate $\tau_w = (f\rho U^2)/8$, noting the near invariance of $p + \rho U^2$, plotted in Figure 4.9 for a few typical cases, it seems appropriate to neglect shear dissipation at the wall over the scale of the pressure recovery. With this final supposition (note alternatively, however, that assignment of $\tau_w = (f\rho U^2)/8$ yields an identical result with a modification of the definition of the length

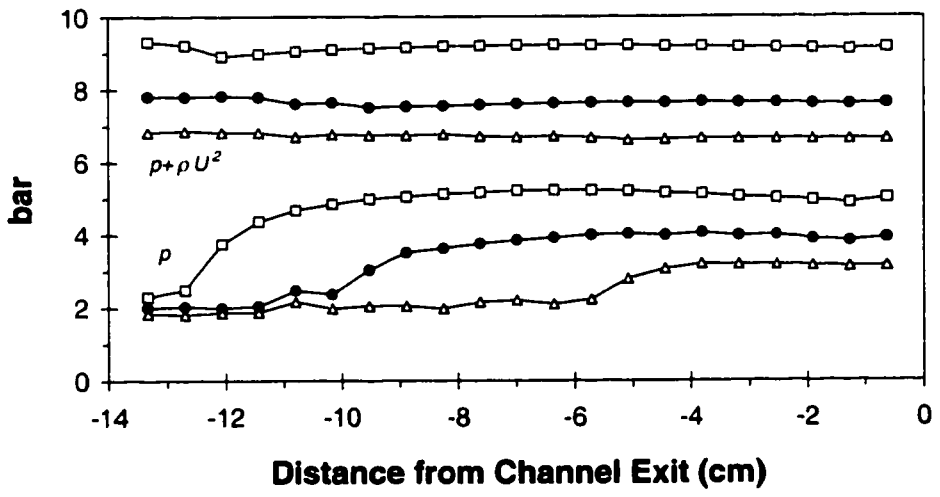

Figure 4.9 p and $p + \rho U^2$ vs. distance from channel exit.

scale, L) rearrangement results in the following:

$$\frac{d}{d(x/L)}\left(\frac{dp}{d(x/L)}\right)=\frac{dp}{d(x/L)} \tag{4.13}$$

and, after integration:

$$p-p_o=\frac{dp}{d(x/L)}\bigg|_o\left(1-e^{-\frac{x-x_o}{L}}\right) \tag{4.14}$$

where the constants of integration are expressed in terms of the initial pressure, initial pressure rise position, x_o and recovery slope.

Note $[dp/d(x/L)]_o = \Delta p_\infty \equiv p_e - p_o$, the maximum pressure recovery. Substituting this identity into the momentum balance across the stagnated layer (Equation 4.10) evaluated at the initial recompression position (with shear neglected) gives:

$$p_o+\left(1-2\frac{\theta_o^*}{h}\right)\rho_o U_o^{\,2}=p_e+\left(1-2\frac{\theta_o^*}{h}\right)\rho_s U_s^{\,2} \tag{4.15}$$

Comparing this with the overall momentum balance:

$$p_o+\left(1-2\frac{\theta_o^*}{h}\right)\rho_o U_o^{\,2}=p_e+\left(1-2\frac{\theta_e^*}{h}\right)\rho_e U_e^{\,2} \tag{4.16}$$

it becomes apparent that the two expressions would be equivalent, provided:

$$\left(1-2\frac{\theta_e^*}{h}\right)\rho_e U_e^{\,2}=\left(1-2\frac{\theta_o^*}{h}\right)\rho_s U_s^{\,2} \tag{4.17}$$

Note, however, that in light of the fact that the nearly stagnant, separated layer, ultimately entrains the entire flowfield to become the entirety of the exiting flow, strictly speaking, ρ_e, U_e, ρ_s, and U_s should be respectively equivalent. Thus, the presence of θ_o^* in the place of θ_e^* on the right hand side of Equation 4.17 indicates the expression not be considered a true equality, but allows estimation that the above approximation (that $d(\rho_s U_s^{\,2})/dx$ be neglected) introduces a relative error on the order of $(\theta_e^* - \theta_o^*)/h$, small granted sufficiently elevated Reynolds number.

The above result suggests that $(p_\infty - p_o)/\Delta p_\infty$ data should collapse onto a single curve when plotted verses $(x - x_o)/L$. Striking agreement is demonstrated by data plotted in this fashion (Figure 4.10) where the characteristic parameters are computed via least squares fits. The closely packed data, almost completely obscure lines representing the function $1 - \exp\{(x-x_o)/L\}$. Here the least of only the error in p squares was fit, as the relative streamwise position of each measurement is exactly known. Note here also that p_∞ seldom and only coincidentally ever coincides with the final pressure at the end of the channel section as this necessarily implies the shock system terminate exactly at the section outlet and flow exit smoothly, (i.e., no back pressure dam be present). More generally recompression either terminates abruptly in interaction with the dam or the pressure continues to vary in a region of transonic flow exiting the recompression due to viscous losses and subsonic pressure recovery as the flow stagnates against the back pressure dam. Data corresponding to these regions, as well as upstream data are omitted here for clarity.

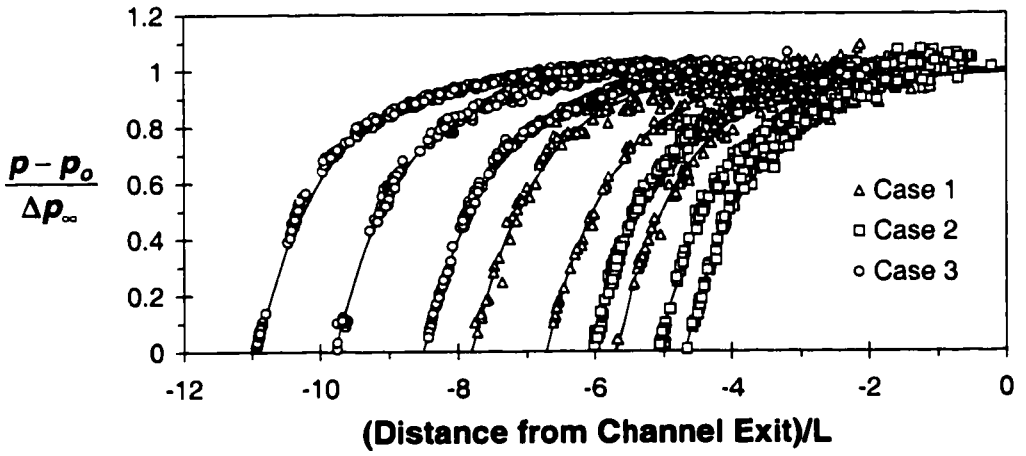

Figure 4.10 Normalized pressure profiles.

The 179 time-averaged pressure profiles displayed, represent a small sample of numerous data demonstrating unanimous behavior for various Reynolds numbers at multiple locations within the duct. The profiles have been offset by the initial pressure rise location to accommodate a larger quantity of data, but collapse to a single profile

when displaced to a common origin. Three distinct geometries are represented, the features of which may be found in Table 4.1. Ideal test section-flow Mach number, M_{ideal}, is computed from the area ratio. A more accurate Mach number, $M_{cont.}$, is based on pressure measured at x_0 and the 1-D continuity and adiabatic energy equations. Note that the variation in the actual Mach numbers reported here is primarily with streamwise position of the recompression affected by weak oblique waves emanating from upstream of the pressure ports. These were found to primarily result from the row of boundary-layer bleed holes, plugged with wax subsequent to case 2. Thus, case 3 reports a much narrowed range of Mach numbers, generally within 15% (10% at elevated *Re*) of the isentropic limit, indicating that the adjustable nozzle indeed performs in reasonable approximation to ideal in spite of the small viscous losses. Because neglect of the displacement layer will cause the core flow Mach number to be underestimated, an

Table 4.1 Test section geometry and Mach number.

Case	A/A^*	h (mm.)	M_{ideal}	$M_{cont.}$	$M_{isen.}$	$Re_h \times 10^{-5}$
1	2.14	7.87	2.3	1.3-2.0	1.7-2.1	1.7-4.6
2	1.68	11.63	2	1.2-1.8	1.6-1.9	2.3-8.2
3	1.28	10.69	1.6	1.1-1.5	1.3-1.6	2.2-11.0

additional term, $M_{isen.}$, computed from local pressure while assuming isentropic expansion, is shown for comparison, as the actual value should reside between these extrema. Mach number dependence upon Reynolds number at a fixed downstream location is, in all cases, observed to be quite minor. The relatively weak waves impinging upon the recompression from upstream for cases 1 and 2 are observed here, and previously[6], to have no significant effect on the recompression structure other than the obvious depression of the entering Mach number.

4.6 Reynolds Number Independence

It is apparent that these recompressions can be characterized by two key parameters. By compiling data for a single geometry where the initial pressure rise

position is nearly identical, streamwise variations may be eliminated from the comparison. Additionally, because at each fixed location Mach number varies only weakly with, and the boundary-layer thickness only as a unique function of the various Reynolds numbers tested, sorting of data in this fashion essentially isolates the Reynolds number dependence. Plots of Δp_∞ verses dynamic pressure for sundry initial pressure rise positions (Figure 4.11a) illustrate remarkable linearity, with the slope declining with increasing x_o. (Here dynamic pressure has been used in accord with the preceding derivation and Donaldson and Lange results; total pressure would equally suffice. Due to the only small variation in Mach number, for each data set they are essentially proportional.) While plots for only a single case (3) are here presented for simplicity, the above data may be regarded as exemplary of identical trends observed for all geometries thus far studied. No perceptible Reynolds number dependence is indicated, reinforced by the horizontal trends of Figure 4.11b where the same data, non-dimensionalized by dynamic pressure are replotted with respect to Reynolds number based on section height.

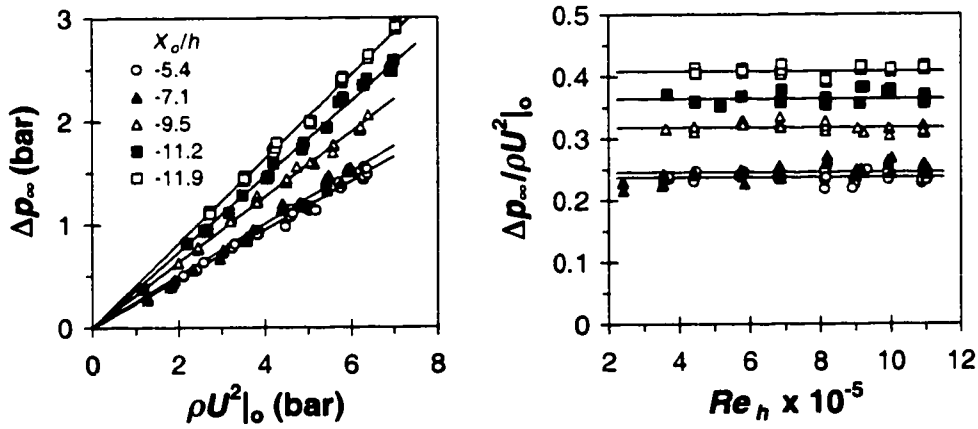

Figure 4.11 a) Initial pressure recovery slope (= Δp_∞) vs. upstream dynamic pressure at various shock positions; b) normalized initial pressure recovery slope vs. Re_h.

Logically L must scale with the section height; L/h is seen to range from 0.3 to 3, generally declining as the recompression is moved downstream. For reasons previously discussed, and, additionally, because error in the curve fits is less sensitive to L in that

while $[dp/d(x/L)]_o$, determines both the initial slope and total pressure rise (relatively easy to measure), L defines only the overall contour, scatter is much amplified in similar plots of L/h verses Re_h, in particular as the recompression moves downstream. (±15% immediately downstream of nozzle, degrading to ±40% at approximately halfway down test section.) In each case, however, the increased scatter does not prevent discernment of a general insensitivity of L to Reynolds number from relatively steady cases where the recompression is positioned close to the nozzle exit, displayed in Figure 4.12.

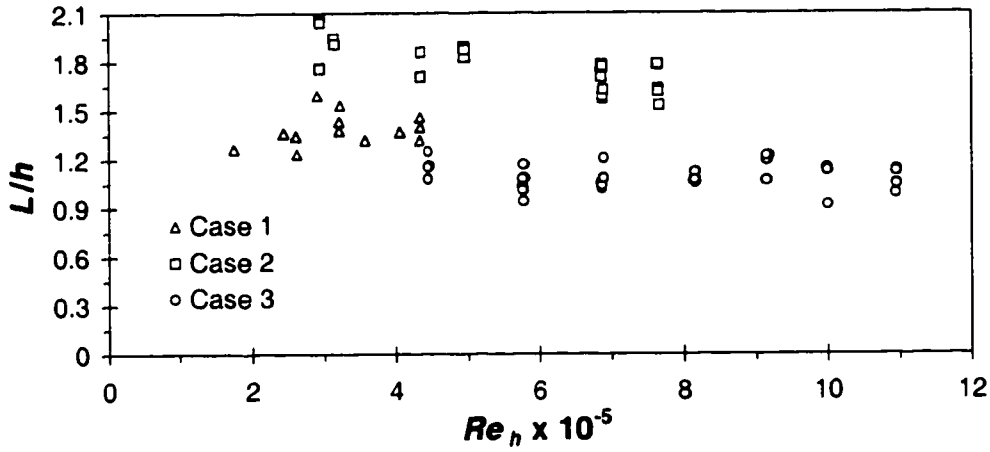

Figure 4.12 Characteristic length scale normalized by h vs. Re_h.

4.7 Maximum Pressure Rise

In treatment of duct recompression, researchers have noted generally lower pressure recovery except at low Mach numbers where greater recompression has, in fact, been observed, accompanied in all cases by larger total pressure losses, and identical trends are observed in these experiments. Shock trains are often compared, in terms of maximum pressure recovery, to normal shock waves with the same incident freestream conditions. This form of comparison, however, is somewhat misleading in its implication that the shock train internal structure plays a deterministic role. Here it is efficacious to analyze a control volume surrounding the entire shock system for 2-D flow, shown in Figure 4.13 and corresponding integral conservation equations:

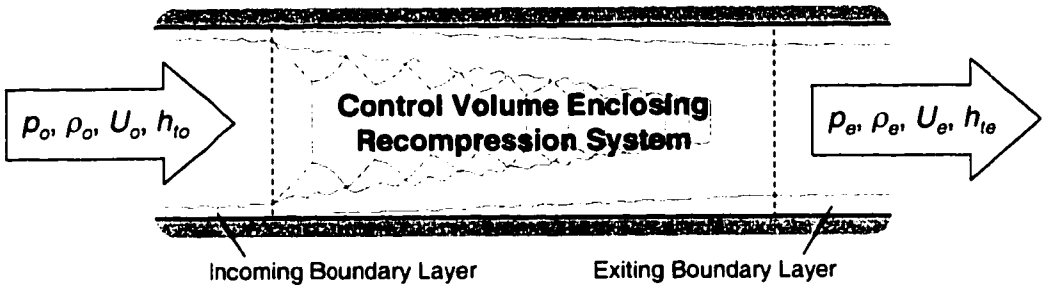

Figure 4.13 Sketch of control volume enclosing recompression system.

$$\rho_o U_o\left(1-2\frac{\delta_o^*}{h}\right)=\rho_e U_e\left(1-2\frac{\delta_e^*}{h}\right) \tag{4.18a}$$

$$p_o+\rho_o U_o^2\left(1-2\frac{\theta_o^*}{h}\right)=p_e+\rho_e U_e^2\left(1-2\frac{\theta_e^*}{h}\right) \tag{4.18b}$$

$$\rho_o U_o h_{to}\left(1-2\frac{\varepsilon_o^*}{h}\right)=\rho_e U_e h_{te}\left(1-2\frac{\varepsilon_e^*}{h}\right) \tag{4.18c}$$

Where three integral boundary-layer thicknesses are defined:

$$\frac{\delta_i^*}{h}\equiv\frac{1}{2}\int_0^1\left(1-\frac{\rho U}{\rho_i U_i}\right)d(y/h)$$

$$\frac{\theta_i^*}{h}\equiv\frac{1}{2}\int_0^1\left(1-\frac{\rho U^2}{\rho_i U_i^2}\right)d(y/h)$$

$$\frac{\varepsilon_i^*}{h}\equiv\frac{1}{2}\int_0^1\left(1-\frac{\rho U h}{\rho_i U_i h_i}\right)d(y/h)$$

Note here that the structure within the control volume is of no consequence with the exception of with respect to the wall shear term, which, in keeping with previous observations, may be assumed small provided the control volume length is not excessive. (As alluded to previously, wall shear could be included by relation to the centerline dynamic pressure obtained from the 1-D model.) Ignoring wall shear and assuming an ideal gas, the entering and exiting Mach numbers are related by the effective duct heights

for momentum entry and exit, $h_i^* \equiv 1 - 2\theta_i^*$, respectively, and a ratio of parameter groups, Γ:

$$\left\{\frac{\Gamma_o}{\Gamma_e}\right\}\frac{\left[\left(\frac{1}{(h_o^*/h)}\right)+\gamma M_o^{\,2}\right]^2}{M_o^{\,2}\left(1+\frac{\gamma-1}{2}M_o^{\,2}\right)}=\frac{\left[\left(\frac{1}{(h_e^*/h)}\right)+\gamma M_e^{\,2}\right]^2}{M_e^{\,2}\left(1+\frac{\gamma-1}{2}M_e^{\,2}\right)} \qquad 4.19$$

where

$$\Gamma_i \equiv \frac{\left(1-2\frac{\theta_i^*}{h}\right)^2}{\left(1-2\frac{\delta_i^*}{h}\right)\left(1-2\frac{\varepsilon_i^*}{h}\right)}$$

Thus, it is apparent that the maximum pressure rise has very little to do with the shock structure and virtually everything to do with the incoming and exiting boundary-layer thicknesses.

The exiting boundary-layer grows within highly mixed, turbulent, separated regions near the sidewall which ultimately entrain or merge with the entire flowfield. It is logical to assume that flow exiting the recompression system is fully developed, or rather stipulate this conjuncture as defining the point at which the recompression terminates, a proviso which gives closure to the system of equations, assuming all upstream conditions are known. In Figure 4.14 plots of $\Delta p_{ss}/\rho U^2$, computed by inserting the results of Equation 4.19 back into the integral momentum equation (4.18b), are displayed for various values of θ_o^*/h, alongside data from Case 3. As the fully-developed exiting thickness should vary little with upstream properties for a fixed flow geometry, a value of 0.05 for θ_e^*/h is considered a reasonable estimate for all cases. Setting $\Gamma_o/\Gamma_e = 1.07$ (it should generally be near unity) provides an adequate match to the majority of the data, which, for the most part, represent fully developed incoming flow (as will be demonstrated later), hence conform well with a single θ_o^*/h = constant contour. The fact that data on the very right of the plot, corresponding to recompression initiated ahead of the point at which the boundary-layer becomes fully developed, fall outside of

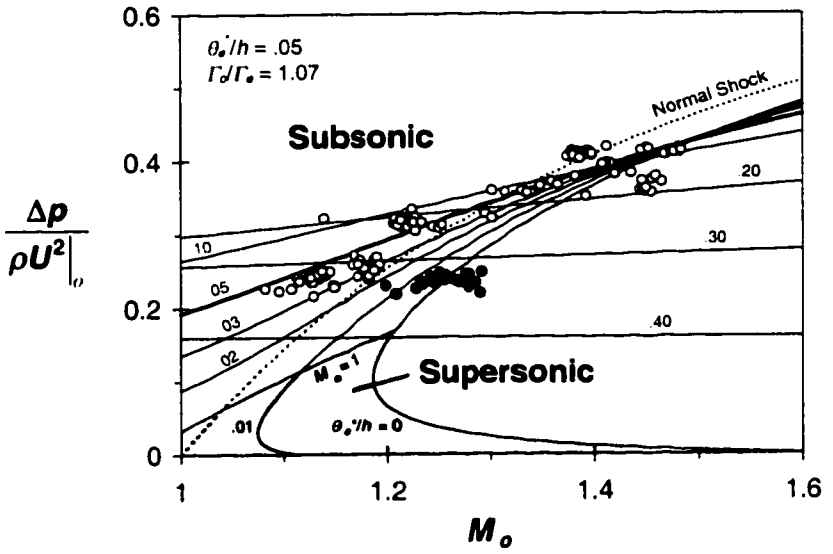

Figure 4.14 Normalized recompression maximum pressure rise for various incoming momentum thicknesses. Data and normal shock solution superimposed.

the converging θ_o^*/h contours suggests variation in Γ_o with boundary-layer growth.

Note that data clustered between Mach 1.2 and 1.3, which fall below the general trend (darkened), represent the furthest downstream shock position and illustrate an important observation. For cases where the shock system extends beyond the duct terminus, interaction with the source of backpressure is noticed to affect the wall pressure profile within several section heights of the exit plane. This occurs both for cases of free atmospheric exit and where the backpressure is applied by a dam. Thus, the cases represented by these data must be considered non-simple and should be expected to deviate from the general trend. As an aside, it should be here mentioned that an unfortunate consequence of this feature is that the profiles of Waltrup and Billig[1], representing recoveries which, for the most part, are quite near the source of back pressure, must be regarded as non-simple, and may not be directly compared with the results reported here. The fact that the pressure profiles within those experiments, show significant, continuous rise throughout the measured test section confirms that they occur very much within the backpressure near-field.

Figure 4.14 conclusively confirms observations (present work, Waltrup and Billig[1]) that at low Mach number with sufficiently developed θ_o^*/h, the pressure recovery may exceed that of a normal shock at identical freestream conditions, denoted by a dashed line, but that at higher Mach numbers the recovery is always lower than that of the normal shock. At low Mach number, the pressure recovery is seen to increase with the upstream momentum thickness, reaching a maximum near $\theta_o^*/h \approx 0.2$, beyond which further increases result in reduced recovery, vanishing as θ_o^*/h reaches 0.5, i.e. a condition at which there no momentum flow remains. Naturally, such thick momentum boundary-layers could only exist under artificial circumstances, but are of academic interest in that $\Delta p_\infty/\rho U^2$ is predicted to become independent of upstream Mach number in this limit. Conversely, at higher Mach number, the pressure recovery monotonically diminishes with increasing θ_o^*/h. Additionally, the figure illustrates that the inclusion of boundary-layers leads to two non-trivial $\Delta p_\infty/\rho U^2$ solutions for a given incoming Mach number. While generally one solution represents a subsonic exiting condition, cases near the minimum Mach number along each contour are double valued within the supersonic domain. All thus far observed cases seem to correspond to the lower speed, higher entropy rise solutions and whether or not the alternate solution may be physically realized is unknown at this time.

To illustrate the effect of varying Γ_o/Γ_e, essentially a ratio of shape parameters which may be used to characterize the incoming boundary-layer (but different than the $\tilde{K}$ defined in section 4.1), the data are re-superimposed over solution contours for various values of this "shape parameter ratio" in Figure 4.15. Here, θ_o^*/h and θ_e^*/h are set to 0.05, in deference to the apparent match in Figure 4.14. Note that Γ_o/Γ_e is completely determined by the incoming flow and downstream fully developed condition. High sensitivity is observed in this Mach number range, where an increase of only 4% in Γ_o/Γ_e, affects an almost two-fold increase in $\Delta p_\infty/\rho U^2$.

While, in principle, the maximum pressure recovery may be solved in this fashion, sensitivity is observed to the integral thickness θ^*/h and, especially, the shape

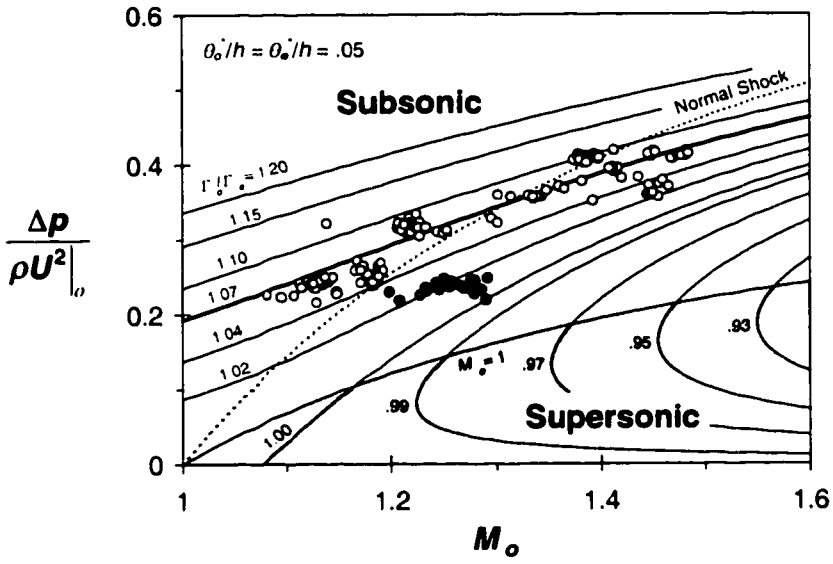

Figure 4.15 Normalized recompression maximum pressure rise for various shape parameter ratios. Data and normal shock solution superimposed.

parameter ratio Γ_o/Γ_e, both typically difficult to computationally or even experimentally resolve to the necessary level of accuracy within this regime. Thus, it would be fruitless to here follow with estimates of the turbulent boundary-layers growing within the test section based on correlations or measurements. One may note, however, extending the field of view to Mach 3 (Figures 4.16 and 4.17), that the contours representing the subsonic solution all cross, very nearly at a single point, where the recovery is approximately independent of θ_o^*/h and θ_e^*/h. Beyond this critical region, the solution demonstrates much reduced sensitivity; a relatively accurate estimate of the pressure recovery may be obtained with only crude estimates of θ_o^*/h, θ_e^*/h, and Γ_o/Γ_e. Moreover, this point of near crossing of all solutions varies only weakly over the expected gamut of the shape parameter ratio, where the transition Mach number increases from approximately 1.5 to 2.0 for Γ_o/Γ_e decreasing from 10% above to 10% below unity. Thus, Mach 2.0 may be safely regarded, as a general rule of thumb, as an effective upper bound for the sensitive regime. Finally, one may note further reduced significance of the shape parameter ratio with increasing Mach number as it is easy to show that subsonic

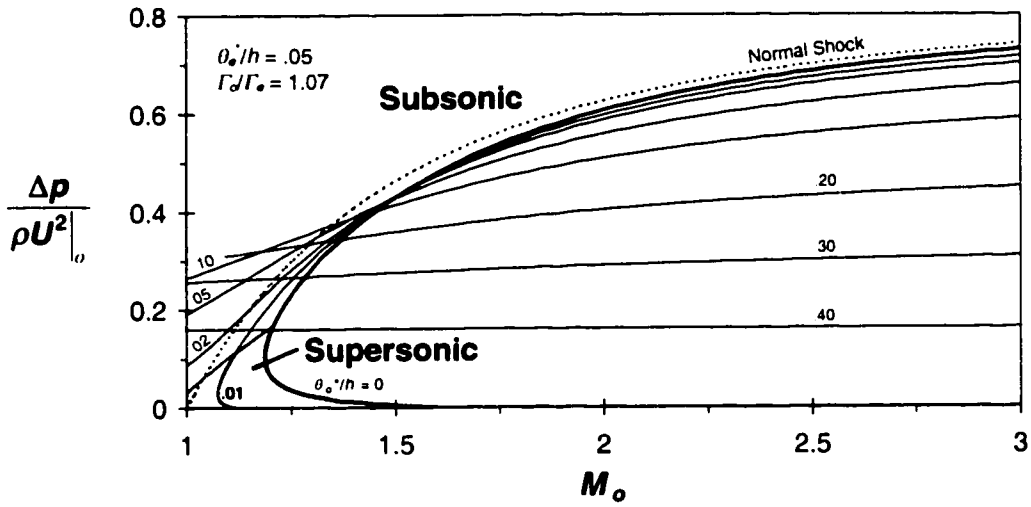

Figure 4.16 Normalized recompression maximum pressure rise for various incoming momentum thicknesses, $1 < M_o < 3$.

solutions steadily converge approximately to:

$$\lim_{M_o \to \infty} M_e^{\,2} \approx \frac{\gamma - 1}{2\gamma}\left[\frac{1}{\gamma\{\Gamma_d/\Gamma_e\}(h_e'/h) + (\gamma - 1)}\right] \qquad 4.20$$

Hence:

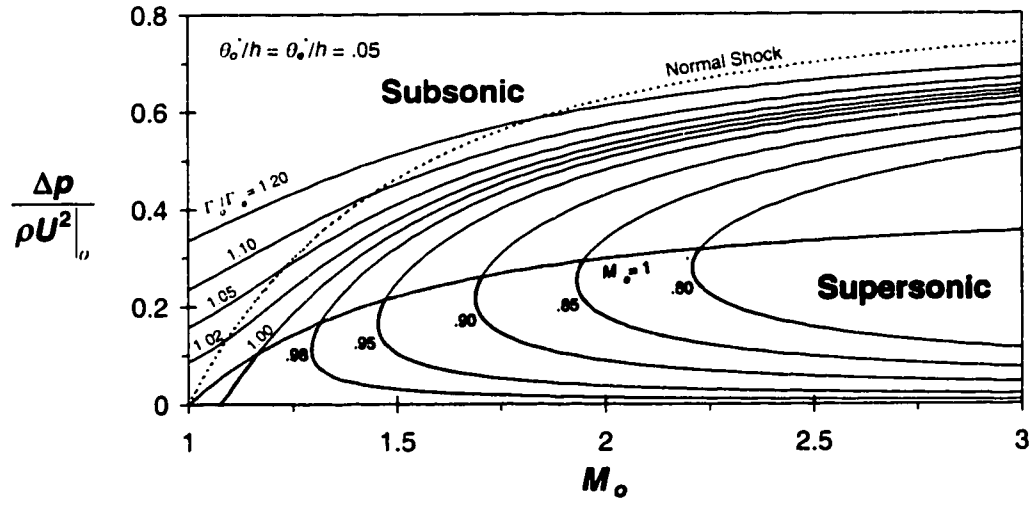

Figure 4.17 Normalized recompression maximum pressure rise for various shape parameter ratios, $1 < M_o < 3$.

$$\lim_{M_o \to \infty} \frac{\Delta p}{\rho U^2} \approx \frac{\left(h_o^*/h\right)}{1 + \frac{1}{2}\frac{\left(h_e^*/h\right)\left(\gamma - 1\right)}{\gamma \left\{\Gamma_o/\Gamma_e\right\}\left(h_e^*/h\right) + \left(\gamma - 1\right)}} \qquad 4.21$$

and, noticing the denominator to exceed unity only by a small degree, Equation 4.21 may be further reduced:

$$\lim_{M_o \to \infty} \frac{\Delta p}{\rho U^2} < \left(h_o^*/h\right) \approx \left(h_o^*/h\right) \qquad 4.22$$

In light of this last result, it is not surprising therefore to observe the asymptote of the $\theta_o^*/h = 0$ contour in Figure 4.16 toward the normal shock solution, despite non-zero exiting boundary-layer thickness and shape parameter ratio not equal to one.

4.8 Characteristic Length Scale

The pressure rise of shock recompression normalized by dynamic pressure ($\Delta p_\infty/\rho U^2$) is plotted verses initial recompression location (measured from the nozzle throat, x^*, representing the approximate origin of the boundary-layer) in Figure 4.18. Normalization of x_o-x^* by L is observed to collapse the data much more effectively than by the section height suggesting that Δp_∞ and L/h are inter-related or co-dependent. The

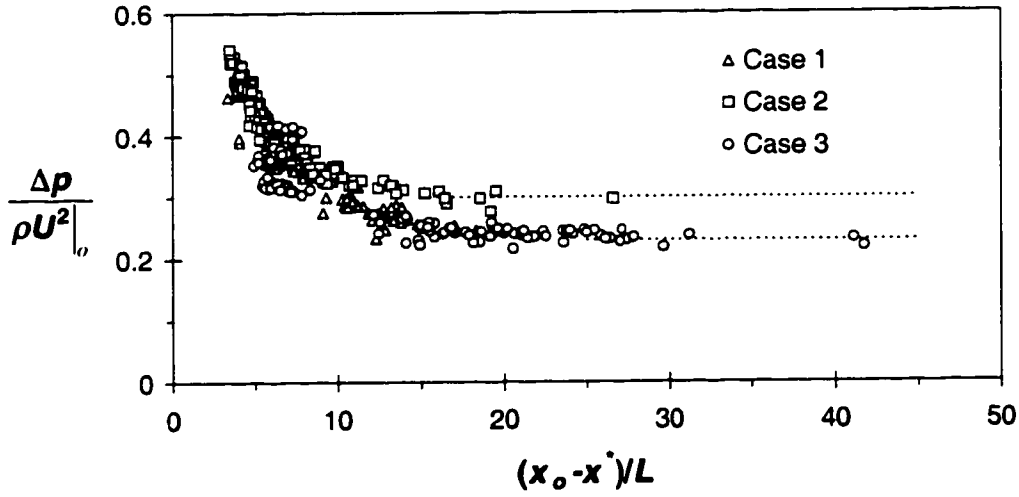

Figure 4.18 Normalized recompression maximum pressure rise vs. distance downstream of throat normalized by characteristic length scale.

data support an inverse relationship to a boundary-layer thickness which grows essentially linearly (because of the Re_h independence) through the test section in good agreement with literature, although Mach number variation throughout the test section must also play a role. The apparent non-zero asymptotes indicate that the boundary-layer becomes fully developed within the channel for these cases.

Because previously mentioned scatter only serves to complicate discernment of overall trends, and because apparent Reynolds number independence implies that it should be approximately constant at each recompression position, only the data-averaged value of L/h at each shock system location is plotted for the three cases in Figure 4.19.

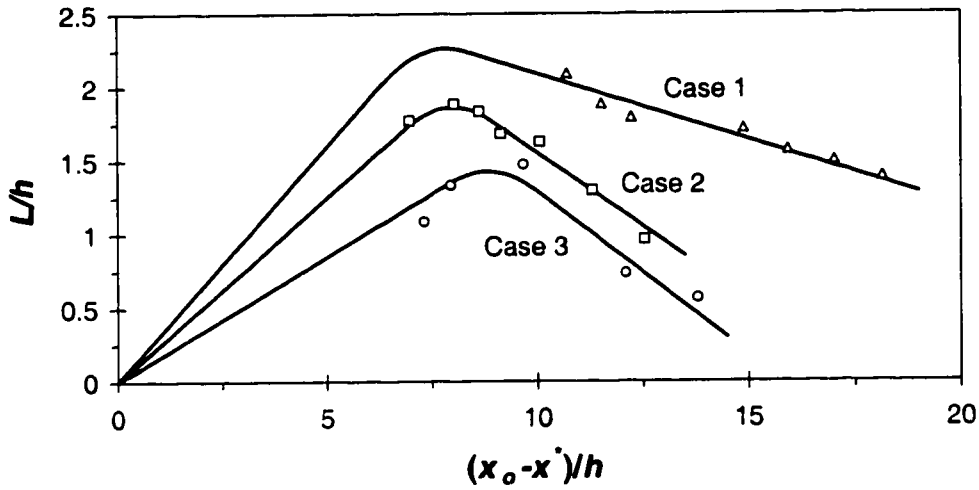

Figure 4.19 Characteristic length scale vs. distance of initial pressure rise downstream of throat, both normalized by section height.

While L/h decreases monotonically for case 1, initial increase is apparent for the lower Mach number cases, followed by similar decline. This confirms similar observations by Merkli[7] (recording the overall shock system length which naturally scales with L), who demonstrated that this reversal corresponds to transition to fully developed flow. (Note however, that while clearly Δp_∞ must approach the normal shock limit as the boundary-layer becomes thin, the analysis and data presented here and by Waltrup and Billig contrast with correlations by Merkli which assert that Δp_∞ should descend linearly from

the normal shock pressure rise with increasing displacement layer thickness. Here, predictions and data indicate pressure recoveries in excess of the normal shock limit at low Mach number.) From Figures 4.18 and 4.19, one can infer, then, that the boundary-layer reaches full development at eight to ten section heights downstream of the throat, and may construct an approximate profile for θ^*/h by assuming linear growth from the throat to this point. θ^*/h may be assumed approximately constant thereafter, where the fully developed thickness may be estimated by comparing measured values for $\Delta p_\infty/\rho U^2$ to predicted contours as in the previous example.

The apparent match of exponential profiles indicates that $L = \Delta p_\infty/(dp/dx)_0$. Indeed, it is quite logical that the length of the recompression should scale with the maximum pressure rise divided by some measurement of the rate of that rise, and, in particular, since downstream conditions ensue directly from those upstream, the initial rate, $(dp/dx)_0$. In turn, as the initial pressure slope is generally observed (as exemplified earlier by arguments of Donaldson and Lange) to scale with the boundary-layer thickness, and, additionally, that the characteristic length must approach zero in the normal shock limit, i.e., zero boundary-layer thickness, in the absence of a rigorous analytical venue, it makes sense to attempt to correlate L to $\Delta p_\infty/\rho U^2$ and θ^*/h. An acceptable, approximately linear relationship is observed when the square of the normalized pressure rise is plotted against $(L/\theta^*)/(\theta^*/h)$ (or $(L/h)/\{(\theta^*/h)^2\}$, as in Figure 4.20a. Here, the fully developed value of $\theta^*/h|_{max} = 0.050$ obtained from the fit of Figure 4.14 is employed for case 3. Assignments for cases one and two of 0.050 and 0.043, respectively, are based on best fit; data for these cases exhibit either too narrow a range (case 1) or too much scatter (case 2) to allow similar, a priori, determination for these cases, but are consistent with these estimates. Because the numerous data exhibit a fair degree of scatter, the correspondence is redisplayed in Figure 4.20b with all data corresponding to nearly identical recompression positions averaged in the same fashion as Figure 4.19. Computing the slope of the best fit yields:

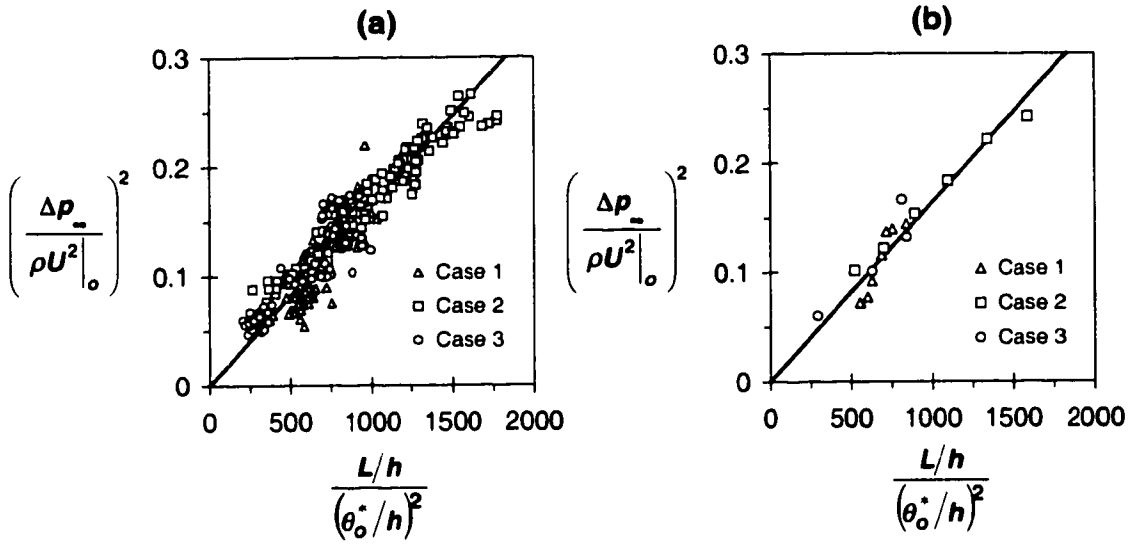

Figure 4.20 Correlation of $\Delta p/(\rho U^2)$, θ^*/h and L/h for a) all data from cases 1–3 and b) averages of data at nearly identical recompression position.

$$\frac{L}{h} \equiv \left(78 \frac{\Delta p_\infty}{\rho U^2} \frac{\theta_o^*}{h} \right)^2 \qquad 4.23$$

The above correlation, of utility in that it appears to incorporate expected behavior including appropriate limits, specifically that L approaches zero as either θ_o^*/h or Δp_∞ become small, is presented as a practical but approximate tool based on the above simple arguments and experimentation without further analysis. Note that the expression indicates that with increasing Mach number, L/h asymptotes to a maximum value at a given θ_o^*/h, in accordance with $\Delta p_\infty/\rho U^2$. This is expected and predicted by other entrainment models such as the diffusion model by Crocco[8], and a refinement by Ikui et al.[9], which do not yield accurate wall pressure profiles (they do not account for the boundary-layer), but do predict the overall recovery length in approximate conformity with experiments.

Since the linear fits of Figure 4.20a and b derive from very crude assignment of θ^*/h profiles, it is sensible to rearrange Equation 4.23:

$$\frac{1}{78}\frac{\rho U^2\big|_o}{\Delta p_\infty}\sqrt{\frac{L}{h}} \cong \frac{\theta_o^*}{h} \qquad 4.24$$

and plot verses $(x_o\text{-}x^*)/h$ (Figure 4.21) to ascertain whether or not this reconstructs a plausible boundary-layer profile. The data adequately match lines representing transition from linearly growing to constant θ_o^*/h at around $(x_o\text{-}x^*)/h \approx 9$, and the apparent asymptotes correspond well with previous estimates. Only in exception are the two most downstream points of case 1, which probably represent either influence of the backpressure dam, or three-dimensional effects to be discussed in the next section.

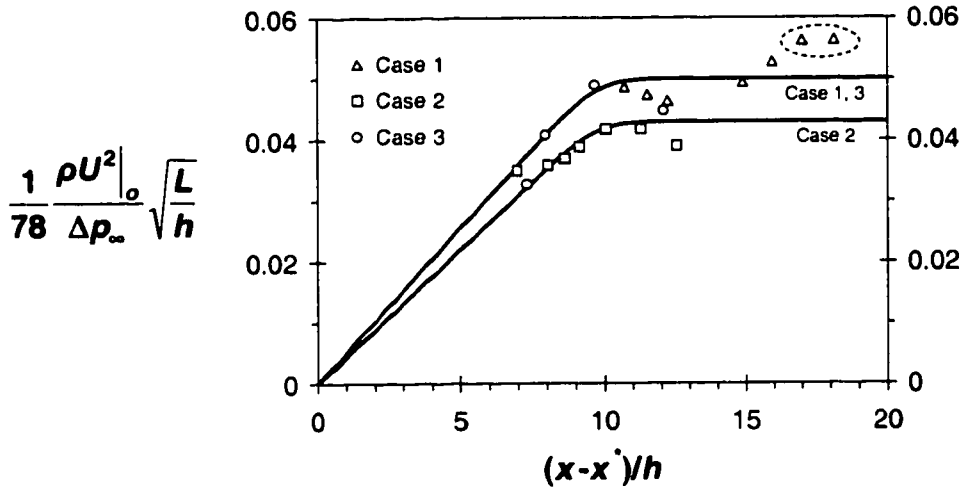

Figure 4.21 Recovery of estimates of momentum boundary-layer growth profiles by inversion of correlation.

An additional point of interest is that for non-zero θ_o^*/h the characteristic length does not vanish in Equation 4.23 as the Mach number diminishes toward unity (Δp_∞ does not vanish, see Figures 4.14–4.17), which will momentarily to draw attention upon a regime slightly removed from, but similar to, the topic of supersonic recompression. The proposed model implies that the wall pressure recovery observed in supersonic recompression occurs as a result of entrainment of the free flow by the separated layer, and that the observed shock structures and centerline pressure oscillation are secondary, induced compressibility effects. Thus, the only obvious intrinsic difference - the stronger

transverse pressure gradients associated with wave activity in the core flow are not fundamental, and, in fact, dissipate at the subsonic/supersonic flow boundary, away from at least one pair of walls. Note, however, that in no way does the primary mechanism actually require that the upstream core flow be supersonic, i.e., there is no difference in basic mechanism between subsonic and supersonic entrainment of a separated boundary-layer, and similar behavior at lower Mach number is implied. As the topic of the present discourse is supersonic recompression, Figures 4.14–4.17 were truncated to only include solutions corresponding to inlet Mach numbers in excess of one; however, one might certainly equivalently evaluate the subsonic incoming-flow regime, provided the stipulation that only the solutions corresponding to entropy gain be considered. Naturally, much reduced length scales are expected; but such are predicted by Equation 4.23, and it would be intriguing to experimentally ascertain its validity in this regime. Lastly, however, one should also note that adverse pressure gradients sufficiently strong to separate the boundary-layer are seldom found in subsonic flows in the absence of duct area expansion, which will contribute an additional term to the momentum equation. Thus, extension of the derivation to include the effects of non-constant duct area, to be briefly discussed in conclusion, is indicated prior to this embarkation.

4.9 Higher Mach Numbers, Aspect Ratios

Increases in the duct aspect ratio (by reducing h below ~0.5 cm) result in convoluted pressure recovery profiles (Figure 4.22) having notable dips (up to two have been observed in a single profile.) that are intensified by increasing Mach number, but wane with increased Re_h. Pitot traverses verify the incoming flow to be spanwise uniform. One likely explanation for this curious behavior, consistent with the above parameter trends, stems from the observation for the preceding cases that the top and bottom boundary-layers become fully developed quite early, while those of the sidewalls continue to thicken, unconstrained. Thus, the shock initiating flow detachment originates upon the sidewall, well ahead of where the thinner top and bottom layers would ordinarily separate. This implies a fundamentally three dimensional interaction of two distinct transverse length scales, sketched in Figure 4.23, where the dips in Figure 4.22

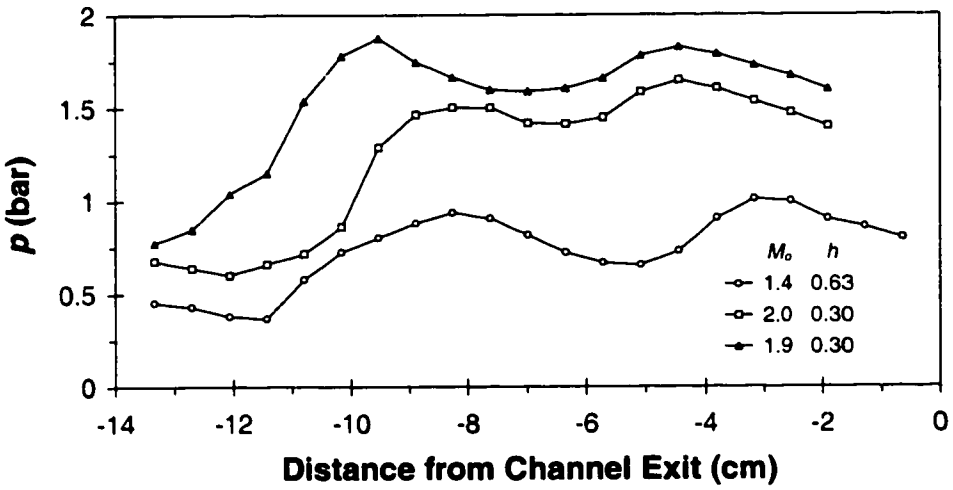

Figure 4.22 Sample pressure profiles for high aspect ratio test geometry.

correspond to oblique wave structure along the longer transverse direction.

Flow may be considered approximately two dimensional only for cases where either wave activity in one lateral direction is negligible (i.e., shock structures viewed in this plane have large normal components), or one of the two transverse lengths is either large or small compared with the scale of concern. For this condition to be satisfied necessarily implies a limiting relationship between the sidewall to floor/ceiling boundary-layer thickness ratio, Mach number, and Reynolds number; or, more specifically, some characteristic grouping of these parameters. While the previously derived exponential

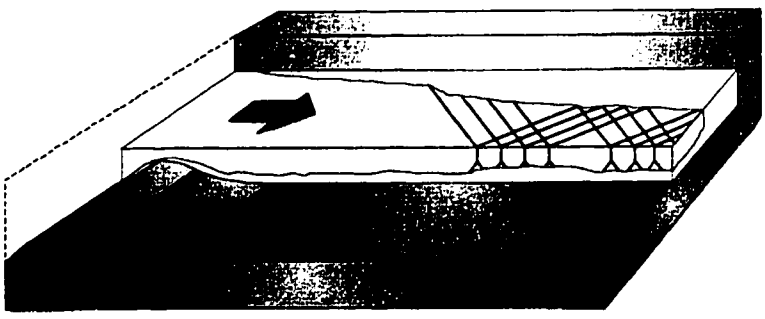

Figure 4.23 Sketch of flowfield quadrant showing boundary-layer and 3-D shock structure intersections with center-planes.

function will not predict periodicity associated with the shorter length scale without modification, it should remain applicable to the overall pressure recovery profile, and hence correspond well to the monotonically increasing pressure distribution expected along the shorter wall, representing the largest length scale of the recovery. At present, however, these walls, formed by the plate glass of the windows, are uninstrumented. It is interesting to note here that the axisymmetric cases of Waltrup and Billig, in constraining the transverse lengths to be identical, actually represent the simplest case study. In general, L must incorporate both transverse scales, disparate but of the same order.

While incorporation of three dimensionality into the length scale correlation is likely to be quite complex, extension of the analysis to obtain the maximum pressure rise is quite trivial, where Equations 18a–c may be modified to read:

$$\rho_o U_o \Delta_o^* = \rho_e U_e \Delta_e^* \qquad 4.25a$$

$$p_o + \rho_o U_o^2 \Theta_o^* = p_e + \rho_e U_e^2 \Theta_e^* \qquad 4.25b$$

$$\rho_o U_o h_o \mathrm{E}_o^* = \rho_e U_e h_e \mathrm{E}_e^* \qquad 4.25c$$

where Δ_i^*, Θ_i^*, and E_i^*, defined as occlusion factors, represent 1-2(δ_i^*/h), 1-2(θ_i^*/h), and 1-2(ε_i^*/h), respectively, in the original 2-D analysis. For a 3-D, symmetric, rectangular duct where boundary-layer thicknesses are assumed constant along the transverse span of their respective walls, h, w, it is easy to show that:

$$\Delta_i^* \equiv \left(1 - 2\frac{\delta_{h,i}^*}{h}\right)\left(1 - 2\frac{\delta_{w,i}^*}{w}\right)$$

$$\Theta_i^* \equiv \left(1 - 2\frac{\theta_{h,i}^*}{h}\right)\left(1 - 2\frac{\theta_{w,i}^*}{w}\right)$$

$$\mathrm{E}_i^* \equiv \left(1 - 2\frac{\varepsilon_{h,i}^*}{h}\right)\left(1 - 2\frac{\varepsilon_{w,i}^*}{w}\right)$$

Thus, the plots of Figures 4.14–4.17 may equally be applied to the 3-D case simply by re-interpretation of $\theta_i^*/h = (1 - \Theta_i^*)/2$ and $\Gamma_i \equiv (\Theta_i^*)^2/(\Delta_i^* \mathrm{E}_i^*)$.

4.10 Shock position and Hybridization of Model with Fanno Flow

With the exponential recovery profile and characteristic parameters Δp_∞ and L, adequately prescribed, the complete wall pressure history may be determined to the first order simply by replacing the ideal shock wave. In principle, as flow properties upstream can be determined as some function of distance along the duct, within the recompression system as a function of incoming properties, and downstream (if necessary) as the continued evolution of fully developed flow exiting the shock system, a unique location of recompression initiation should satisfy boundary conditions. Generally speaking, both viscous dissipation from the core flow and boundary-layer thickness determine the exact recompression location; however, the significance of these two competing factors varies with the degree to which the flow is developed. Where the boundary-layers are still developing, the streamwise variation in its thickness will play the key determining role, as viscous dissipation from the core flow will be minimal. Once the flow is fully developed, the boundary-layer thicknesses will be relatively constant (varying only with their Mach number dependence), and viscous dissipation then represents the only appreciable mechanism streamwise-altering incoming flow conditions, the hypothetical shock structure at each location, and therefore the position required to satisfy boundary conditions.

Depending upon the given set of boundary conditions, the duct exit pressure may be at some intermediate point within a recompression extending beyond the duct exit, as in the experiments of Waltrup and Billig, or reached by post-recompression Fanno-type dissipation, as observed in the experiments of Merkli where backpressure was varied by interchanging long (relative to the recompression scale) duct extensions of varying lengths. (The experiments of the current study vary from one regime to the other, based on the section height, characteristic length, and recompression position for a given case.) Under special circumstances, at relatively low incoming Mach number such that viscous dissipation ahead of the shock system is of the same order as behind it, hysteresis may be expected between two possible solutions. Typically, however, viscous dissipation behind the shock system is at least an order of magnitude smaller than total pressure losses

upstream of and through the recompression system, thus may be ignored.

Conversely, in cases where post-recompression frictional effects are non-negligible, seldom is the finite length of the shock recompression, generally small compared to subsonic dissipative scales, significant, and under most circumstances may be treated as simple Fanno flow. Thus, instances where hybridization of the recompression model with downstream viscous flow is necessary are rare. Nevertheless, for the sake of generality, this possibility may be addressed by noting that to perform such a graft one need only determine where to consider recompression complete, i.e., where to switch from the exponentially decaying pressure rise, $dp/dx = (dp/dx)_0 e^{-(x-x_0)/L}$, of the model to Fanno flow. Because of the apparent universal collapse of data by the single expression, it is natural to assume that, to the first order, this transition should occur at a single value of $(x-x_0)/L$ for all cases. While only the recompression profiles of case 3 demonstrate clear transition within the span of the test section, that an average total recompression length of $(x-x_0)/L = 6.0$ with a root-mean-square-standard-deviation of 10% is observed shall here be reported, for these data, as exemplary and expected approximately universal.

4.11 Conclusion of Shock Studies

Analysis of previous and present studies indicates single and multiple shock-boundary layer interactions to be essentially Reynolds number independent for turbulent flow. Assuming momentum entrainment by the separated layer to be the mechanism balancing pressure rise along the wall, a one-dimensional model predicts an exponential pressure profile that is in excellent agreement with data, and allows characterization by two key parameters, the maximum pressure recovery, Δp_∞ (or the initial slope of the wall-pressure profile $dp/d(x/L)$), and a characteristic length scale, L. This indicates that boundary-layers enact a fundamental transformation of duct recompression at the macroscopic level from the simple static discontinuity of a normal shock, to one in the mechanism of momentum transfer into subsonic regions of the flow. Ostensibly, a discontinuity in spatial derivatives of static properties is observed, rather than in the

properties themselves. While it is shown that, in principle, Δp_∞ can be derived from entering conditions by assuming fully developed exiting flow, L is obtained from more approximate arguments and experimental correlation. For easy reference, the following summary is provided:

$$p - p_o = \Delta p_\infty \left(1 - e^{-\frac{x - x_o}{L}} \right) \tag{4.26}$$

$$\frac{\Delta p_\infty}{\rho_o U_o^2} = \frac{\Theta_o^* - \left(\frac{M_e}{M_o}\right)^2 \Theta_e^*}{1 + \gamma M_e^2 \Theta_e^*} \tag{4.27a}$$

$$\left\{ \frac{\Gamma_o}{\Gamma_e} \right\} \frac{\left[\frac{1}{\Theta_o^*} + \gamma M_o^2 \right]^2}{M_o^2 \left(1 + \frac{\gamma - 1}{2} M_o^2 \right)} = \frac{\left[\frac{1}{\Theta_e^*} + \gamma M_e^2 \right]^2}{M_e^2 \left(1 + \frac{\gamma - 1}{2} M_e^2 \right)}; \qquad \Gamma_i \equiv \frac{\left(\Theta_i^*\right)^2}{\Delta_i^* \mathrm{E}_i^*} \tag{4.27b}$$

$$\Delta_i^* \equiv \prod_{j=1}^{n} \left(1 - 2 \frac{\delta_{h_j}^*}{h_j} \right); \quad \Theta_i^* \equiv \prod_{j=1}^{n} \left(1 - 2 \frac{\theta_{h_j}^*}{h_j} \right); \quad \mathrm{E}_i^* \equiv \prod_{j=1}^{n} \left(1 - 2 \frac{\varepsilon_{h_j}^*}{h_j} \right)$$

where i denotes either o or e and n signifies cross section dimension (1 for a 2-D duct and 2 for 3-D).

$$\frac{L}{h} = 0.024 \left(\frac{\Delta p_\infty}{\rho U^2} \frac{\theta_o^*}{h} \right)^2 \tag{4.28}$$

Note that while the formulation of Δp_∞ is quite general, the correlation for L/h corresponds to solutions believed to be essentially 2-D. When the duct aspect ratio is significantly far from unity, the shock initiating flow-detachment originates on the sidewall, well ahead of where the thinner top and bottom layers would ordinarily separate, initiating complex, three dimensional interactions.

Equations 4.26-4.28 establish the characteristic recovery profile as a function of two flow parameters which, in turn, are related to features of the flow. This accomplished, chemical-kinetic models (see Section 3.15) allow determination of yield optimizing temperature profiles. Assuming that the boundary-layer be determined, either

numerically or by correlation, tunnel geometry can then be tailored to achieve the desired parameters, or a compromise may be attained in the familiar, iterative fashion characteristic of all design processes.

4.12 Suggestions for Future Work

The exponential model provides an excellent framework from which to build and compare future investigations. The apparatus employed in these experiments has been used to a mere fraction of its potential; some areas for follow-on work are suggested below:

1. Higher Reynolds and Mach Numbers

While designed to a maximum safe internal operating pressure of 40 bar, the device has been operated only to a 10 bar maximum to the present, due to structural limitations in the gas supply system. Extension of the current data set, particularly through further elevation of Reynolds and Mach numbers should be of high priority, as this shortcoming is relatively simple and inexpensive to remedy, and will extend the range of all subsequent studies.

2. Section Divergence, Boundary-Layer Bleed and Flow Visualization

Examination of the effects of section divergence and use of suction to bleed the boundary-layer should also be considered integral to a continued program of operation, as these yet unexplored avenues of research represent capabilities of the apparatus in its current state. Additionally, the sidewalls of the test section were constructed of glass to take advantage of the Schlieren visualization system constructed in the first part of the Shock Wave Reactor program, but, because of the oscillatory nature of the recompression system, videography is of limited value. Installation of a high speed camera (~0.1 to 1 millisecond exposures should be adequate, however, due to limited light available from the schlieren source, a photomultiplier may be necessary) will allow photography of a panoply of recompressions of varying Mach and Reynolds number, section height and divergence, and boundary-layer thicknesses.

3. Pressure Measurement along Sidewalls

At elevated aspect ratios, the pressure along the centerline of the bottom and top walls is not monotonically increasing, but rather increase as a damped oscillation down the test section. As it is here conjectured that this is due to the fact that the pressure waves originate from the separation of sidewall boundary-layers, it is expected that the observed dips in the pressure profile represent oblique waves which do not extend into the thick, subsonic separated region along the sidewall. Pressure measurement of the sidewall, by replacement of one glass window with a ported and instrumented aluminum plate would elucidate the validity of this speculation, and allow measurement and assessment of the dependency of this lateral length scale.

4. Construction of Conjugate Devices

While the current apparatus allows the spacing between the upper and lower walls to be to arbitrarily small dimension, flow visualization through the larger transverse plane is not possible. Nevertheless, this view of the flowfield is of interest in the limit of very large aspect ratios, where one transverse scale is miniscule compared to the other. In the limit of large aspect ratio, interaction of shock waves with the thinner boundary-layer will occur over negligible distances compared with at the sidewall. The length scales should become effectively decoupled, the boundary-layer corresponding to the thinner dimension acting merely as a source of dissipation, but contributing no macroscopic structure to flow viewed in the transverse plane. While this additional friction will fundamentally alter the overall length scales, it is also observed to stabilize, and, if sufficiently strong, virtually eliminate the recompression temporal oscillation. Thus recompressions within a facility of this type should be essentially steady, therefore observable over extended intervals and requiring no high speed techniques for visualization. Naturally, such a facility must tolerate high total pressures to overcome losses.

Additionally, because the back pressure dam is observed to affect flow in its upstream vicinity, an experiment analogous to those performed by Merkli, where 3 to 5 different area ratio nozzles could be fitted to each of 3 to 5 different diameter flow

sections, each, in turn, outfitable with 3 to 5 downstream extensions to provide backpressure, would be of particular benefit in providing additional data regarding the fundamental length scale, L, and overall length scale (estimated to be ~$6L$ in Section 4.10). Nozzles and extensions should be sufficiently diverse to encompass a wide range of Mach and Reynolds numbers. Unlike the experiments of Merkli, however, as noted in section 4.9, the ducts should be axisymmetric, providing a single transverse scale, thereby representing the simplest of cases.

5. Separation and Entrainment of Boundary-Layers in Subsonic Flow

As the underlying mechanism governing supersonic recompression appears to be entrainment by the separated layer, a continuum of behavior should be observed above and below Mach one, with the subsonic/supersonic transition merely demarked by the gradual appearance of compressibility affects with Mach number increasing beyond unity, much as is observed for turbulent mixing. Section 4.8 suggests that the same analytical and empirical techniques, summarized above, may be equally applied in both sub- and supersonic flows, as the derivation of Δp_∞ is rigorous, and the correlation for L, in that it incorporates Δp_∞ , appears to include compressibility effects. While the apparatus in an unmodified state can accommodate relevant studies, because section divergence will be required to produce sufficient pressure gradients to separate the boundary-layer in subsonic flow, study of the effects of divergence upon supersonic cases is necessary to allow direct comparison.

4.13 Notes to Chapter 4

1. Waltrup, P. J. and Billig, F. S., "Structure of Shock Waves in Cylindrical Ducts," *AIAA Journal*, Vol. 11, No. 10, 1973, pp. 1404-1408.

2. Donaldson, C. duP. and Lange, R. H., "Study of the Pressure Rise Across Shock Waves Required to Separate Laminar and Turbulent Boundary Layers," NACA Technical Note 2770, 1952.

3. White, F. M., *Viscous Fluid Flow*, 2nd edition, McGraw-Hill Book Company, New York, NY, 1991.

4. Cohen, C. B., and Reshotko, E., "Similar Solutions for the Compressible Laminar Boundary Layer with Heat Transfer and Pressure Gradient," NACA Report 1293, 1956.

5. Chen, C. P., Sajben, M., and Kroutil, J. C., "Shock-Wave Oscillations in a Transonic Diffuser Flow," *AIAA Journal*, Vol. 17, No. 10, 1979, pp. 1076-1083.

6. Masse, R. K., Knowlen, C. Mattick, A. T., and Russell, D.A., "A Flow Visualization Study of Supersonic Mixing and Shock Structure," *Proceedings of the Seventh International Symposium on Flow Visualization*, University of Washington, Seattle, WA, 1995, pp. 847-852.

7. Merkli, P. E., "Pressure Recovery in Rectangular Constant Area Supersonic Diffusers," *AIAA Journal*, Vol. 14, No. 2, 1976, pp. 168-172.

8. Crocco, L., *High Speed Aerodynamics and Jet Propulsion*, Vol. III, Princeton University Press, Princeton, NJ, 1958.

9. Ikui, T., Matsuo, K., and Nagai, M., "The Mechanism of Pseudo-Shock Waves," *Bulletin of the JSME*, Vol. 17, June 1974, pp. 731-739.

5. Conclusion and Future Considerations

The Shock Wave Reactor proof-of-concept commenced with the study of supersonic mixing. Flow visualization and chemical sampling of the wake and jet-like mixing of blade nozzle arrays confirm established semi-empirical models to be extensible to 2-D wake and jet-like mixing processes by approximating such processes as a series of stages, each locally approximating simple shear layer mixing. Subsequent development and operation of a test apparatus conclusively demonstrates the Shock Wave Reactor concept effective in the improvement of per-pass pyrolysis yield selectivity, and results are corroborated by independent analysis and numerical chemical-kinetic investigations. High steam-to-feedstock mass flow ratios have been employed to offset heat transfer associated with the limited scale of these experiments, but insensitivity to this parameter over the studied range (7.5-35.0) indicates that results may be extrapolated to lower dilutions. Additionally, a 1-D model for ducted recompression has been developed, characterizing the wall pressure by a maximum pressure recovery and a characteristic length scale. While the maximum pressure recovery may be, in principle, analytically obtained, the length is shown by correlation to scale with the square of the normalized (by dynamic pressure) pressure recovery and momentum boundary-layer thickness, but inversely with duct height for approximately 2-D flows. Fundamental three-dimensionality is observed for the most general cases of ducted recompression, however.

5.1 Future Considerations

The preceding chapters provide the tools necessary for effective conceptual evaluation and design of practical steady-state devices for olefin manufacture advantageously exploiting gas dynamic processes. The results of Chapter 3, indicating high commercial potential for the Shock Wave Reactor concept, merit additional study with the specific goal of taking of the next step toward industrial application - the construction of a pilot scale facility. While this treatment has focused specifically on the features where shock wave pyrolysis fundamentally differs from conventional techniques, one additional, practical distinction concerning waste heat recovery needs be addressed in

regard to the above stated purpose.

5.2 Quenching

Although conventional quenching methods are applicable in that they are downstream of, and have no direct effect on the processes under analysis in this dissertation, the large difference in the feedstock-to-steam ratios of a traditional furnace (~3:1) and Shock Wave Reactor (~1:4, hypothetical best case) indicate substantial effort be made to recover heat remaining in waste steam, in direct contrast to current practices where the waste steam is often simply condensed and discarded as an insignificant loss. The familiar dichotomy between rapid and efficient heat transfer make design of this component as challenging is it is critical for the success of shock wave pyrolysis.

Design of a conventional heat exchange device which will couple with the Shock Wave Reactor to produce an economically viable composite is indeed feasible. However, resorting to gas dynamic processes to again decouple the thermochemistry from heat transfer, presents an avenue potentially more advantageous. Much after the fashion by which aeroquench sampling probes function (Section 3.5), thermal cracking may first be arrested by re-expansion of the flow prior to heat transfer initiated while the mixture remains supersonic. Thus, excess energy may be extracted more gradually across smaller temperature gradients, allowing more efficient recovery. Even should shock wave pyrolysis find industrial application using conventional quenching strategies, the potential of this additional technology should not be overlooked in continued research.

5.3 Combustion-Augmented Pyrolysis

Ultimately, the very need for efficient post-pyrolysis heat transfer may be mitigated through diminution of the total waste heat via reduction of the steam-to-feedstock mass flow ratio. This may be affected only by increasing the effective amount of energy stored in the carrier gas per unit mass in excess of that associated with achieving the critical reaction initiating temperature. While further heating of the steam is limited by metallurgy, the energy density may be effectively augmented through partial combustion of the feedstock, or combustion of a different fuel immediately prior to

feedstock injection. In this fashion, the plenum flow may be volumetrically heated while maintaining confinement structures within material limits. The elevated temperatures potentially afforded through combustion-augmented pyrolysis are of particular interest in regard to the possible use of methane feedstock.

5.4 Alternate Applications

As with the actors themselves, technologies - mere props, if at all, play but brief roles in the human drama. Thus, while data and analyses of the preceding chapters have been chiefly motivated by their association with the Shock Wave Reactor concept, it should be noted that the treatments are quite general, in order that they might be applied to the host of problems involving similar features. The blade nozzle mixing concepts of Chapters 2 and 3 have been borrowed from, and contributions within these chapters may be directly re-applied to, gas dynamic lasers. The study of recompression in Chapter 4 finds its foundations in hypersonics research, particularly associated with the advancement toward supersonic combustion ram jets, and the model there developed is intended for use in continuing efforts.

BIBLIOGRAPHY

1. "Industry Briefs," *Oil and Gas Journal*, July 28, 1997, pp. 43.

2. "Newsletter," *Oil and Gas Journal*, June 30, 1997, pp. 2-4.

3. Bogdanoff, D. W., "Compressibility Effects in Turbulent Shear Layers," *AIAA Journal*, Vol. 21, No. 6, 1983, pp. 926-927.

4. Breidenthal, R. E., "Sonic Eddy-A Model for Compressible Turbulence," *AIAA Journal*, Vol. 30, No. 1, 1992, pp. 101-104.

5. Brown, G. L., "The Entrainment and Large Structure in Turbulent Mixing Layers," *Proceedings of the 5th Australasian Converence on Hydraulics and Fluid Mechanics*, Univ. of Canterbury, Christchurch, New Zealand, 1974, pp. 352-359.

6. Chang, T., "Worldwide Ethylene Capacity Grows in Spite of Warnings," *Oil and Gas Journal*, March 30, 1998, pp. 41-47.

7. Chen, C. P., Sajben, M., and Kroutil, J. C., "Shock-Wave Oscillations in a Transonic Diffuser Flow," *AIAA Journal*, Vol. 17, No. 10, 1979, pp. 1076-1083.

8. Chinzei, N., Masua, G., Komuro, T., Murasakami, A., and Kudou, K., "Spreading of Two-Stream Supersonic Turbulent Mixing Layers," *Physics of Fluids*, Vol. 29, No. 5, 1986, pp. 1345-1347.

9. Clemens. N. T., and Mungal, M. G., "Two- and Three-Dimensional Effects in the Supersonic Mixing Layer," AIAA Paper 90-1978, July 1990.

10. Cohen, C. B., and Reshotko, E., "Similar Solutions for the Compressible Laminar Boundary Layer with Heat Transfer and Pressure Gradient," NACA Report 1293, 1956.

11. Crocco, L., *High Speed Aerodynamics and Jet Propulsion*, Vol. III, Princeton University Press, Princeton, NJ, 1958.

12. Dimotakis, P. E., "Turbulent Free Shear Layer Mixing and Combustion," *High Speed Flight Propulsion Systems*, Edited by S.N.B. Murphy and E.T. Curran, Vol.137, pp. 265-340, Progress in Aeronautics and Astronautics, AIAA, Washington, DC, 1991, Chapter 5, pp. 265-340.

13. Dimotakis, P. E., "Two-Dimensional Shear-Layer Entrainment," *AIAA Journal*, Vol. 24, No. 11, 1986, pp. 1791-1796.

14. Donaldson, C. duP. and Lange, R. H., "Study of the Pressure Rise Across Shock Waves Required to Separate Laminar and Turbulent Boundary Layers," NACA Technical Note 2770, 1952.

15. Galarza, J. Z., Design of Gas Sampling Probes for Pyrolysis Experiments, Masters Thesis, Univ. of Washington, Seattle, WA, 1995

16. Grantom, R.L. and Royer, D.J. "Ethylene," *Ullmann's Encyclopedia of Industrial Chemistry*, fifth edition, VCH Publishers, Deerfield Beach, FL, 1985, Vol. A 10, pp. 45-93.

17. Hall, J. L., Dimotakis, P. E., and Rosemann, H. "Experiments in Nonreacting Compressible Shear Layers," *AIAA Journal*, Vol. 31, No. 12, 1993, pp. 2247-2254.

18. Hertzberg, A., and Glick, H. S., "Kinetic Studies in a Single-Pulse Shock Tube", *AGARDograph* No. 41, 1959, pp. 161-182.

19. Hertzberg, A., Mattick, A. T., Russell, D. A., "Apparatus for Initiating Pyrolysis Using a Shock Wave," U.S. Patent 5219530, 1992

20. Hertzberg, A., Mattick, A. T., Russell, D. A., "Method for Initiating Pyrolysis Using a Shock Wave," U.S. Patent 5300216, 1994

21. Hertzberg, A., Mattick, A. T., Russell, D. A., *Shock Controlled Reactors*, edited by Takayama, K., Shock Waves, *Proceedings of the 18th International Symposium on Shock Waves*, 1991, pp. 1289-1294.

22. Hertzberg, A., Squire, W., and Glick, H. S., "The Cal Pressure Wave Chemical Reactor," Cornell Aeronautical Laboratory Report AD-1052-A-13, January, 1956.

23. Ikui, T., Matsuo, K., and Nagai, M., "The Mechanism of Pseudo-Shock Waves," *Bulletin of the JSME*, Vol. 17, June 1974, pp. 731-739.

24. Kniel, L., Winter, O., and Stork, K., *Ethylene: Keystone to the Petrochemical Industry*, Marcel Dekker, Inc., New York, NY, 1980.

25. Knowlen, C., Mattick, A. T., Russell, D. A., and Masse, R. K. "Petrochemical Pyrolysis with Shock Waves," AIAA Paper 95-0402, Jan. 1995.

26. Lukasiewicz, J., "Diffusers for Supersonic Wind Tunnels," *Journal of the Aeronautical Sciences*, Sept. 1953, pp. 617-626.

27. Mahmoodian, M., "Modeling the Pyrolysis of Ethane and Study of Boundary-Layer Growth in a Shock Wave Reactor," Masters of Science Thesis, Dept. of Aeronautics and Astronautics, University of Washington, Aug. 1994.

28. Masse, R. K., Knowlen, C. Mattick, A. T., and Russell, D.A., "A Flow Visualization Study of Supersonic Mixing and Shock Structure," *Proceedings of the Seventh International Symposium on Flow Visualization*, University of Washington, Seattle, WA, 1995, pp. 847-852.

29. Mattick, A. T., "The Supersonic-mixing, Shock-wave Reactor: An Innovative Approach for Efficient Chemical Production," Final Report, U. S. Department of Energy contract number DE-FG06-93ER12136, 1999.

30. Merkli, P. E., "Pressure Recovery in Rectangular Constant Area Supersonic Diffusers," *AIAA Journal*, Vol. 14, No. 2, 1976, pp. 168-172.

31. Morse, P., "Ethylene Market Softening Delayed by Outages," *Chemical and Engineering News*, Vol. 75, September 15, 1997, pp. 20.

32. Orriss, R. and Yamaguchi, H., "Idemitsu's Chiba Ethylene Plant Proves Modern Technology," *Oil and Gas Journal*, March 9, 1987, pp. 27-30.

33. Papamoschou, D., "Structure of the Compressible Turbulent Shear Layer," *AIAA Journal*, Vol. 29, No. 5, 1991, pp. 680-681.

34. Papamoshchou, D., and Roshko, A., "The Compressible Turbulent Shear Layer: An Experimental Study," *Journal of Fluid Mechanics*, Vol. 197, Dec. 1988, pp. 453-477.

35. Ross, R. H. and Steinmeyer, D., "Energy for Industry," *Scientific American*, pp. 89-98, Sept. 1990.

36. Russell, D. A., "Fluid Mechanics of High Power Grid Nozzle Lasers," AIAA Paper 74-223, January 1974.

37. Russell, D. A., Neice, S. E., and Rose, P. H., "Screen Nozzles for Gas Dynamic Lasers," *AIAA Journal*, Vol. 13, No. 5, 1975, pp. 593-599.

38. Schillmoller C.M., "Use These Materials to Retrofit Ethylene Furnaces," *Hydrocarbon Processing*, September, 1985, pp. 101-104.

39. Sundaram, K. M. and Froment, G. F., "Modeling of Thermal Cracking Kinetics 3: Radical Mechanisms for the Pyrolysis of Simple Paraffins, Olefins, and Their Mixtures," *Ind. Eng. Chem. Fundam.*, Vol 17, No. 3, 1978, pp 174-182

40. Waltrup, P. J. and Billig, F. S., "Structure of Shock Waves in Cylindrical Ducts," *AIAA Journal*, Vol. 11, No. 10, 1973, pp. 1404-1408.

41. White, F. M., *Viscous Fluid Flow*, 2nd edition, McGraw-Hill Book Company, New York, NY, 1991.

Appendix A. Major Ethylene Derivatives and Uses*

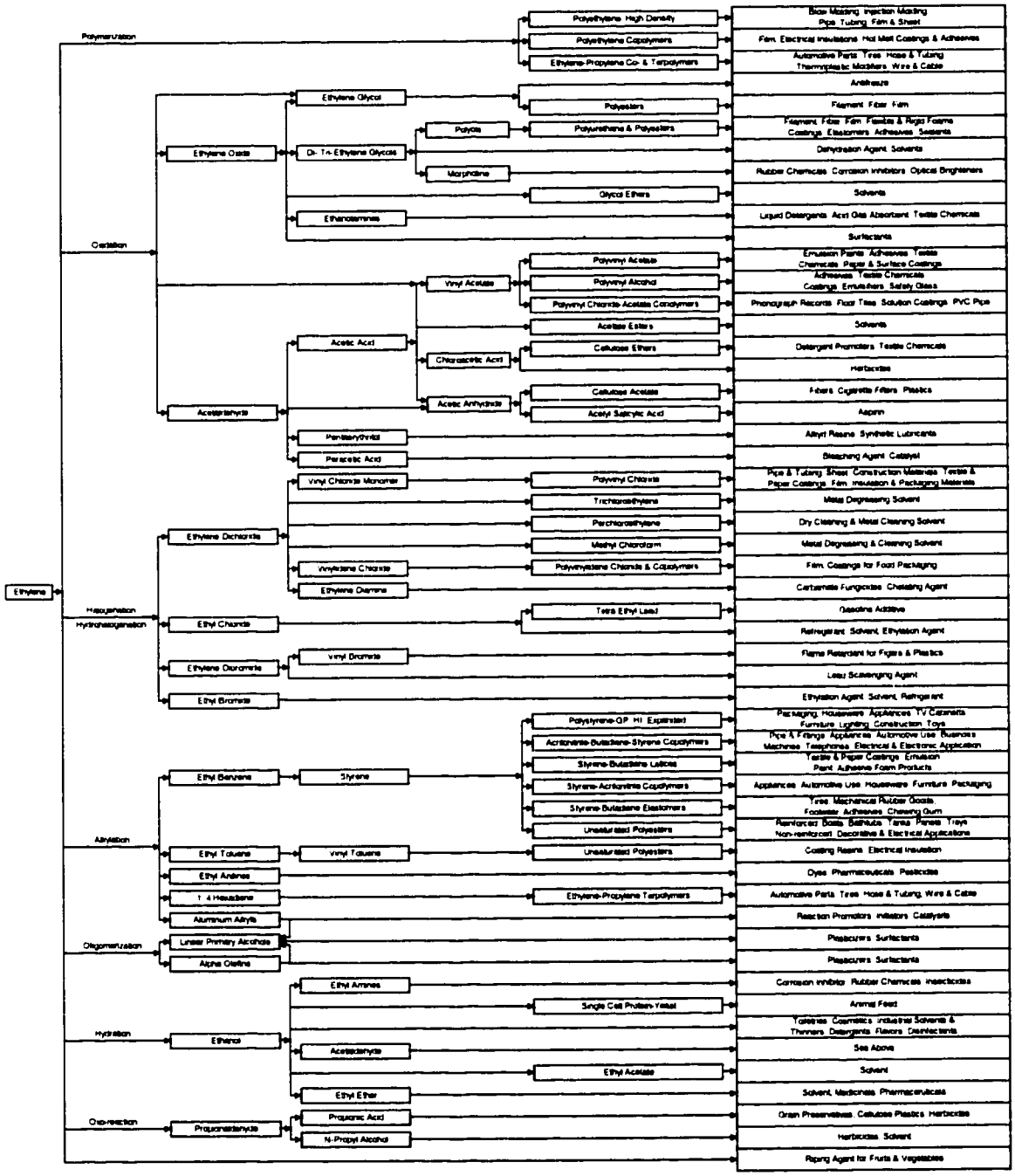

* Adapted from Schillmoller, C. M., "Use These Materials to Retrofit Ethylene Furnaces," *Hydrocarbon Processing*, September, 1985, pp. 101-104.

Appendix B. 1998 World Ethylene Production†

Company	Location	Total nameplate capacity, mty	Typical feedstock or feedstock mixture on which listed capacity is based, %					
			Ethane	Propane	Butane	Naptha	Gas oil	Other
Algeria								
Sonatrach	Arzew	132,860						LNG
Total Algeria		**132,860**						
Argentina								
ICI Argentina SAIC	San Lorenzo	20,000		25		75		
Ipako	Ensenada	15,000						Ref. gas - 100
Pasa SA	San Lorenzo	28,000		100				
Petroquimica Bahia Blanca (Govt.-51%/Ipako-21 2%)	Bahia Blanca	245,000	100					
Total Argentina		**308,000**						
Australia								
Huntsman Chemical Co. Australia Ltd.	Melbourne, Vic.	31,700	95	5				
Kemcor Australia Ltd.	Altona, Vic.	210,000	55				45	
Orica	Sydney, NSW	250,000	100					
Total Australia		**491,700**						
Austria								
OMV AG	Schwechat	345,000	12	2	18	60	8	
Total Austria		**345,000**						
Belgium								
BASF Antwerpen N.V.	Antwerp	670,000				100		
Fina Antwerp Olefins N.V. (Petrofina-65%/Exxon Chemicals-35%)	Antwerp	230,000				100		
Fina Antwerp Olefins N.V (Petrofina-65%/Exxon Chemicals-35%)	Antwerp	340,000				100		
Fina Antwerp Olefins N.V. (Petrofina-65%/Exxon Chemicals-35%)	Antwerp	490,000				100		
Total Belgium		**1,730,000**						
Brazil								
Companhia Brasileira De Estireno	Cubatao, AP	4,800						Ethanol
Copene	Camacan, Bahia	530,000				100		
Copene	Camacan, Bahia	670,000				100		
Copesul	Triunfo, RS	685,000				100		
Petroquimica Uniao SA (Unipar-30%/Union Carbide-13%)	Santo Andre, SP	500,000				100		
Total Brazil		**2,389,800**						
Bulgaria								
Neftochim	Burgas	250,000				100		
Neftochim	Burgas	150,000				100		
Total Bulgaria		**400,000**						
Canada								
Dow Chemical	Ft. Sask., Alta.	544,218	100					
Imperial Oil Products and Chemicals	Sarnia, Ont.	255,000	65	22	2			Ref. gas - 11
Nova Chemicals	Joffre, Alta	1,541,950	100					
Nova Chemicals	Corunna, Ont.	680,000	17	10	22	40	11	
Petromont	Varennes, Que.	283,000		10	35	40	5	Ref. gas - 10
Total Canada		**3,304,168**						
Chile								
Petrox SA	Concepcion	60,000	8		16	76		
Total Chile		**60,000**						
China								
	Dushanzi	140,000						
	Maoming	300,000						
	Tianjin	140,000						
	Zhongyan	140,000						
China Petrochemical Industrial Corp.	Daqing	320,000						
Dalian Petrochemical Co.	Dalian	4,000						
Fushan Petrochemical Complex	Fushun	115,000						
Gaoqiao Petrochemical Co.	Gaoqiao	14,000						
Guangzhou Petrochemical Co.	Guangzhou	150,000						
Jilin Chemical Co.	Jilin	300,000						
Lanzou Chemical Industrial Co.	Lanzhou	160,000						
Panjin Gas Processing Plant	Panjin	130,000						

Company	Location	Total nameplate capacity, mty	Typical feedstock or feedstock mixture on which listed capacity is based, %					
			Ethane	Propane	Butane	Naptha	Gas oil	Other
Sinopec	Beijing	500,000						
Sinopec	Liaoyang	90,000						
Sinopec	Qilu	330,000						
Sinopec	Shanghai	145,000						
Sinopec	Shanghai	320,000						
Sinopec	Yangtze	400,000						
Total China		**3,698,000**						
China, Taiwan								
Chinese Petroleum Corp.	Linyuan	230,000				100		
Chinese Petroleum Corp.	Linyuan	385,000				45.22	54.78	
Chinese Petroleum Corp.	Tsoying	400,000				49.99	50.01	
Total China, Taiwan		**1,015,000**						
Colombia								
Empresa Colombiana de Petroleos	Barrancabermeja	100,000	80	20				
Total Colombia		**100,000**						
Croatia								
Petrokemija	Zagreb	90,000	100					
Ina-Oki Ltd.	Zagreb	20,000						
Total Croatia		**110,000**						
Czech Republic								
Chemopetrol A.S.	Litvinov	441,000			3	48	49	
Total Czech Republic		**441,000**						
Egypt								
Egyptian Petrochemical Co.		200,000						
Total Egypt		**200,000**						
Finland								
Borealis	Porvoo	290,000				100		
Total Finland		**290,000**						
Former Soviet Union								
Azerbaijan								
Azenchem	Sumgait	30,000						
Azenchem	Sumgait	300,000						
Belarus								
Polimir	Novopolotsk	73,000						
Polimir	Novopolotsk	60,000						
Kazakhstan								
Government	Guryev	30,000						
Russia								
Angarskneftorgsintez	Angarsk, Siberia	150,000						
Angarskneftorgsintez	Angarsk, Siberia	300,000						
Bashneftechim	Ufa	60,000						
Gorkneftorgsintez	Nizhniy Novgorod	300,000						
Government	Groznyi	30,000						
Government	Orsk	30,000						
Kubishevneftorgsintez	Novokuybyshevsk	300,000						
Kubishevneftorgsintez	Novokuybyshevsk	60,000						
Nitron	Saratov	30,000						
Nizhnekamskneftekhi	Nizhnekamsk	525,000						
Omskneftorgsintez	Omsk, Siberia	105,000						
Omskneftorgsintez	Omsk, Siberia	35,000						
Orgsintez	Kazan	200,000						
Orgsintez	Kazan	120,000						
Orgsintez	Kazan	260,000						
Permneftorgsintez	Perm	60,000						
Salavatneftorgsintez	Salavat	300,000						
Salavatneftorgsintez	Salavat	100,000						
Stavropolpolymer	Budennovsk	350,000						
Sterlitamak	Sterlitamak	100,000						
Tomsk PCC	Tomsk	300,000						
Ukraine								
Chlorvinyl	Kalush	250,000						
Lisichansk Refinery	Lisichansk	300,000						
Shevchenko	Shevchenkovo	110,000						
Total FSU		**4,868,000**						
France								

Company	Location	Total nameplate capacity, mty	Typical feedstock or feedstock mixture on which listed capacity is based, %					
			Ethane	Propane	Butane	Naptha	Gas oil	Other
Copenor (Union Carbide-50%)	Dunkerque	310,000		0-12	0-8	40-100	40-100	
Elf Atochem	Gonfreville l'Orcher	480,000			10	80		10
Elf Atochem	Feyzin	240,000				100		
Elf Atochem	Lacq (Snea plant)	75,000	100					
Elf Atochem	Carling-St. Avold-Manenau	480,000				84	1	15
Enichem	Dunkerque	330,000		10	10	80		
Naftachimie (Elf Atachem-50%/BP Chemicals-50%)	Lavera	700,000			8	87		5
Shell Chimie	Berre l'Etang	420,000						
Societe Francaise Exxon Chemical	Notre Dame de Gravenchon	400,000						
Total France		**3,435,000**						
Germany								
BASF AG	Ludwigshafen	610,000						
DEA Mineroloel AG	Heide	85,000	6			94		
DEA Mineroloel AG	Wesseling	480,000			1	73	26	
Dow Chemical AG	Bohlen	450,000						
EC Erdoelchemie GmbH (BP Chemicals-50%/Bayer-50%)	Dormagan	360,000	40			60		
EC Erdoelchemie GmbH (BP Chemicals-50%/Bayer-50%)	Dormagen	380,000	40			60		
OMV Deutschland GmbH	Burghausen, Bavana	320,000	3	5	12	79	1	
Rheinische Olefinwerke GmbH-50%/								
Rheinische Olefinwerke GmbH-50%/BASF AG-50%	Wesseling	240,000					100	
Rheinische Olefinwerke GmbH-50%/BASF AG-50%	Wesseling	560,000		2	5	84	9	
Veba Oel/Ruhr Oel GmbH-50%/Pdvsa-50%	Gelsenkirchen	440,000		2	6	82	10	
Veba Oel/Ruhr Oel GmbH-50%/Pdvsa-50%	Gelsenkirchen	440,000		3	8	89		
Veba Oel/Ruhr Oel GmbH-50%/Pdvsa-50%	Munchsmunster	280,000	12	6	20	62		
Total Germany		**4,645,000**						
Greece								
Eko Chemicals Co. AE	Thessaloniki	15,000				65		
Total Greece		**15,000**						
Hungary								
Tiszai Vegyi Kombinat Ltd.	Tiszaujvaros	290,000			7	78	15	
Total Hungary		**290,000**						
India								
Chemplast Sanmar Ltd.	Mettur Dam, Tamil Nadu	16,000						Ethyl alcohol - 100
Indian Petrochemicals Corp. Ltd.	Nagothane	400,000						
Indian Petrochemicals Corp. Ltd.	Nagothane	300,000	80	20				
Indian Petrochemicals Corp. Ltd.	Vadodara	132,000				100		
National Organic Chemical Industries Ltd.	Thane, Maharashtra	75,000				100		
Oswal Agro Mills Ltd.	Bombay	22,000						
Reliance Industries	Hazira, Gugarat	750,000				100		
Total India		**1,695,000**						
Indonesia								
Pt Chandra Asri	Cilegon, West Java	550,000						
Total Indonesia		**550,000**						
Iran								
National Petrochemical Co.	Arak	247,000				100		
National Petrochemical Co.	Bandar Imam	311,000	19				81	
National Petrochemical Co.	Tabanz	136,000				100		
Total Iran		**694,000**						
Iraq								
Present Status Unknown		---						
Total Iraq		---						
Israel								
Carmel Olefins Ltd.	Haifa	200,000	5	5	5	85		
Total Israel		**200,000**						
Italy								
Enichem/Union Carbide-50%	Brindisi	400,000				100		
Enichem	Gela	250,000	30			60	10	
Enichem	Priolo	740,000				50	50	
Enichem	Porto Torres	250,000				20	80	
Enichem	Porto Marghera	460,000				90	10	
Total Italy		**2,100,000**						

Company	Location	Total nameplate capacity, mty	Typical feedstock or feedstock mixture on which listed capacity is based, %					
			Ethane	Propane	Butane	Naptha	Gas oil	Other
Japan								
Idemitsu Petrochemical Co. Ltd.	Tokuyama	485,000				•		
Idemitsu Petrochemical Co. Ltd.	Chiba	377,000						
Keiyo Ethylene	Ichihara, Chiba	600,000						
Keiyo Ethylene	Goi	525,000						
Mitsubishi Chemical Corp.	Kashima	828,000		10	20	55		HNGL - 15
Mitsubishi Chemical Corp.	Mizushima	450,000		5	5	80		HNGL - 10
Mitsubishi Chemical Corp.	Yokkaichi	272,000			10	90		
Osaki Petrochemical Industries Ltd.	Takaishi City, Osaka	387,000			•	•		
Sanyo Petrochemical Co. Ltd.	Kurasiki, Okayama	464,000				100		
Showa Denko KK	Oita	228,000				100		
Showa Denko KK	Oita	507,000				100		
Sumitomo Chemical Co. Ltd.	Chiba	415,000				•		LPG
Tonen Chemical Corp.	Kawasaki	463,000				100		
Tosoh Corp.	Yokkaichi, Mie	425,000				•		LPG
Ukishima Petrochemicals Co. Ltd.	Chiba	612,000						
Ukishima Petrochemicals Co. Ltd.	Kawasaki	435,000						
Total Japan		**7,473,000**						
Kuwait								
Equate Petrochemical Co.	Shuaiba	650,000						
Total Kuwait		**650,000**						
Libya								
Ras Lanuf Oil & Gas	Ras Lanuf	350,000						
Total Libya		**350,000**						
Malaysia								
Ethylene Malaysia Sdn. Bhd.	Kertih	400,000	100					
Titan Petrochemicals (Malaysia) Sdn. Bhd.	Pasir Gudang, Johor	230,000				100		
Total Malaysia		**630,000**						
Mexico								
Petroleos Mexicanos	La Cangrejera, Veracruz	500,000	100					
Petroleos Mexicanos	Morelos, Veracruz	500,000	100					
Petroleos Mexicanos	Pajaritos, Veracruz	182,000	100					
Petroleos Mexicanos	Poza Rica, Veracruz	182,000	100					
Petroleos Mexicanos	Reynosa, Tamaulipas	27,000	100					
Total Mexico		**1,391,000**						
Netherlands								
Dow Chemical Europe	Terneuzen	607,710	•	•	•	•		
DSM NV	Geleen	1,100,000				•	•	
Shell Nederland Chemie BV	Moerdijk	600,000						
Total Netherlands		**2,307,710**						
North Korea								
Government	Pyongyang	60,000						
Total North Korea		**60,000**						
Norway								
Norsk Hydro-51%/Borealis-49%	Rafnes, Bamble	410,000	30	45	25			
Total Norway		**410,000**						
Poland								
Petrochemia	Plock	395,000						
Total Poland		**395,000**						
Portugal								
Borealis	Sines	330,000				100		
Total Portugal		**330,000**						
Qatar								
Qatar Petrochemical Co. Ltd.	Mesaieed	525,000	100					
Total Qatar		**525,000**						
Romania								
Arpechim	Pitesti I	100,000						
Arpechim	Pitesti II	200,000						
Petrotel SA	Teleajen	220,000						
Petromidia SA	Midia	224,000	5.9	7.2	5.8	32.7		48.4
Total Romania		**744,000**						
Saudi Arabia								
Arabian Petrochemical Co.	Al-Jubail	650,000	100					
Arabian Petrochemical Co.	Al-Jubail	800,000				100		

Company	Location	Total nameplate capacity, mty	Typical feedstock or feedstock mixture on which listed capacity is based, %					
			Ethane	Propane	Butane	Naptha	Gas oil	Other
Saudi Petrochemical Co.	Al-Jubail	1,100,000	100					
Yanbu Petrochemical Co. (Mobil-50%)	Yanbu	800,000	100					
Total Saudi Arabia		**3,350,000**						
Singapore								
Petrochemical Corp. of Singapore Pte. Ltd.	Pulau Ayer Merbau	450,000			1	99		
Petrochemical Corp. of Singapore Pte. Ltd.	Pulau Ayer Merbau	515,000			1	99		
Total Singapore		**965,000**						
Slovakia								
Slovnaft Joint Stock Co.	Bratislava	205,000	5		15	80		
Novaky	Novaky	25,000						
Total Slovakia		**230,000**						
South Africa								
Sasol	Sasolburg	100,000						
Sasol	Secunda	320,000						
Total South Africa		**420,000**						
South Korea								
Daelim Industrial Co. Ltd.	Yeochun	420,000				100		
Daelim Industrial Co. Ltd.	Yeochun	310,000				100		
Hanwha Chemical Corp	Yeochun	465,000				100		
Honam Petrochemical	Yeochun	400,000				100		
Hyundai Petrochemical	Daesan	950,000				100		
Korea Petrochemical Industries Co. Ltd.	Ulsan	300,000				100		
LG Petrochemical Co. Ltd.	Yeochun	640,000				100		
Samsung General Chemicals	Daesan	500,000				100		
Yukong Ltd.	Ulsan	10,000				100		
Yukong Ltd.	Ulsan	530,000				100		
Total South Korea		**4,525,000**						
Spain								
Dow Chemical	Tarragona	462,585	•	•	•	•		
Repsol Petroleo SA	Puertollano	280,000				•		Ref. streams
Repsol Petroleo SA	Tarrogona	500,000						
Total Spain		**1,242,585**						
Sweden								
Borealis	Stenungsund	400,000				100		
Total Sweden		**400,000**						
Switzerland								
Lonza AG	Visp	31,000		20	50	30		
Total Switzerland		**31,000**						
Thailand								
National Petrochemical Corp.	Map Ta Phut	401,000						
Thai Olefins	Map Ta Phut	385,000						
Total Thailand		**786,000**						
Turkey								
Petkim Petrochemicals Holding Co.	Aliaga, Izmir	400,000				100		
Total Turkey		**400,000**						
United Kingdom								
BP Chemicals Ltd.	Grangemouth	700,000				50		E/LPG mix - 50
Exxon Chemical Co.	Fawley	120,000						
Exxon Chemical Co.	Mossmorran Fife	730,000						
Emperial Chemical Industries Ltd. (BP-20%)	Wilton	850,000				100		
Total United Kingdom		**2,400,000**						
United States								
Amoco Chemical Co.	Chocolate Bayou, Tex.	1,451,247	50	35		15		
Chevron Chemical Co.	Cedar Bayoou, Tex.	680,272	36	11	25	28		
Chevron Chemical Co.	Port Arthur, Tex.	784,580	79	21				
Condea Vista Co.	Lake Charles, La.	430,839	100					
Dow Chemical	Freeport, Tex.	1,224,500	50	50				
Dow Chemical	Plaquemine, La.	1,102,041						
DuPont	Orange, Tex.	589,569	100					
Eastman Chemical Co.	Longview, Tex.	675,737	25	67	7	1		
Equistar Chemicals LP (Lyondell-57%/Millenium-43%)	Channelview, Tex.	873,016	•	•	•	•	•	
Equistar Chemicals LP (Lyondell-57%/Millenium-43%)	Channelview, Tex.	873,016	•	•	•	•	•	

Company	Location	Total nameplate capacity, mty	Typical feedstock or feedstock mixture on which listed capacity is based, %					
			Ethane	Propane	Butane	Naptha	Gas oil	Other
Equistar Chemicals LP (Lyondell-57%/Millenium-43%)	Clinton, Iowa	435,374	95	5				
Equistar Chemicals LP (Lyondell-57%/Millenium-43%)	LaPorte, Tex.	789,116	80	20				
Equistar Chemicals LP (Lyondell-57%/Millenium-43%)	Morris, Ill.	512,472	90	10				
Exxon Chemical Co.	Baton Rouge, La.	882,000						
Exxon Chemical Co.	Baytown, Tex.	1,890,000						
Formosa Plastics Corp. USA	Point Comfort, Tex.	714,286	45	25		15	15	
Huntsman Corp.	Port Arthur, Tex.	551,364				60		LPG - 40
Huntsman Corp.	Port Neches, Tex.	136,364						Ref. gas/EP mix
Javelina Co.	Corpus Christi, Tex.	108,844						Ref. gas
Mobil Chemical Co.	Veaumont, Tex.	566,893	60	10	20	10		
Mobil Chemical Co.	Houston, Tex.	342,403	90	10				
Occidental Chemical Corp.	Chocolate Bayou, Tex.	500,000				75	25	
Occidental Chemical Corp.	Corpus Christi, Tex.	772,727	15	30		35	20	
Occidental Chemical Corp.	Lake Charles, La.	363,636	50	50				
Phillips Petroleum Co.	Sweeny, Tex.	2,040,816	*	*	*			
Rexene Products Co.	Odessa, Tex.	230,000						
Shell Chemicals Ltd.	Deer Park, Tex.	952,381	15		5	50	30	
Shell Chemicals Ltd.	Norco, La.	535,147	40	5	5	50		
Shell Chemicals Ltd.	Norco, La.	793,651	5			60	35	
Sun Co. Inc	Brandenburg, Ky.	45,351	*	*				
Sun Co. Inc	marcus Hook, Pa.	102,041	*	*				
Union Carbide Corp.	Seadrift, Tex.	414,966	60-80	20-40				
Union Carbide Corp.	Taft, La.	680,272	0-30	0-50		50-100		
Union Carbide Corp.	Texas City, Tex.	680,272	60-80	20-40				
Union Texas Petrochemicals-42%/GE Petrochemicals-16%/BASF Corp-42%	Geismar, La.	544,218	88	15				
Westlake Polymers Corp.	Calvert City, Ky.	170,068		100				
Westlake Polymers Corp.	Sulpher, La.	1,043,084	80	20				
Total United States		25,482,563						
Venezuela								
Pequiven-Petroquimica de Venezuela SA	El Tablazo, Zulia	250,000	30	70				
Pequiven-Petroquimica de Venezuela SA	El Tablazo, Zulia	350,000	100					
Total Venezuela		600,000						
Total World		89,605,386						

* Percentage not given.

† Adapted from Chang, T., "Worldwide Ethylene Capacity Grows in Spite of Warnings," *Oil & Gas Journal*, March 30 1998, pp. 41-47.

Appendix C. Evaluation of Subcontracted Equipment

The steam supply system employed in the proof-of-concept experiment represented a significant challenge to the contractor, Phoenix Solutions, Inc., in that the desired operating range was somewhat beyond that within which the bulk of typical industry experience lies, and this is here noted for the benefit of any reader who may be guided to this source in the construction of similar equipment. The equipment, as delivered (over six months late), was effective but highly problematic. The most basic errors are typified by installation of a circulating pump (which is not designed to increase pressure) instead of pressure developing pump to supply 7 bar water to the boiler and insulation of heating element aluminum leads, contrary to specifications of the element manufacturer.

Use of the silicon carbide elements in the horizontal configuration chosen, greatly limited their service life, requiring frequent replacement at substantial cost, both monetary and in time. Additionally, the silicon carbide well tubes chosen to house the elements out-gassed vaporous silicon, resulting in glass deposition upon condensation at the relatively cold point where the element emerges from its refractory sleeve. Ultimately, fusion of the element to the sleeve at this junction consistently culminated in failure when this prevented normal expansion and contraction with the thermocycling represented by operation of the experiment. Substantial modifications were necessary to diagnose and alleviate this problem, as the original heating element lead housings made element maintenance expensive and extremely tedious.

The equipment did ultimately facilitate proof-of-concept and such should be recognized. However, the author, while intending no extrapolation of the above discussion be applied to projects of Phoenix Solutions, Inc. more within its typical forte, to avoid misleading the reader must here dis-recommend the device as designed, and the experience of its operation/maintenance.

Appendix D. Supplemental Schematics of Feedstock and Steam Heating Apparati

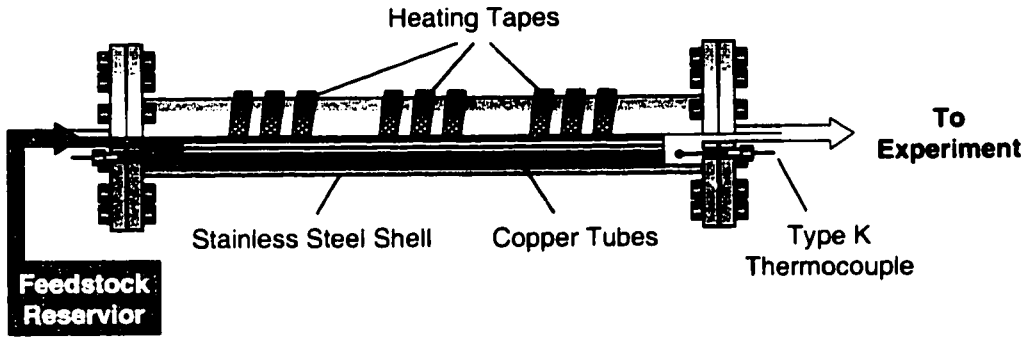

Figure D.1 Ethane preheater with insulation removed and 50% cutaway.

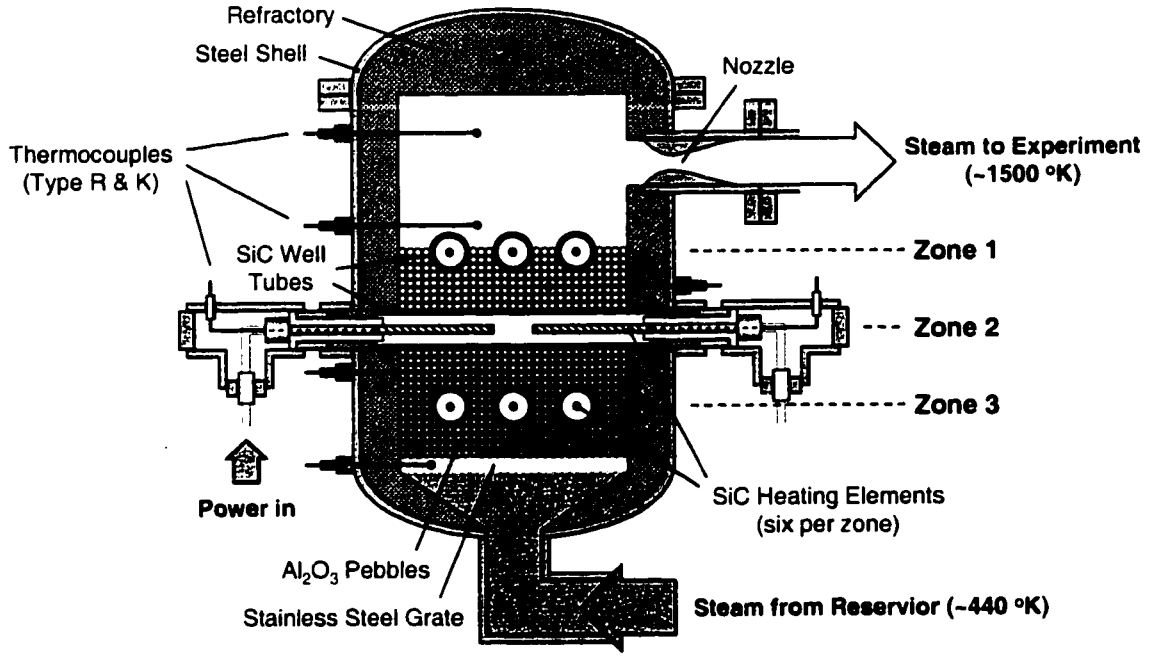

Figure D.2 Proof-of-concept experiment pebble bed steam superheater.

Appendix E. Selected Data on Haynes Alloy 230[†]

Table E.1 Haynes 230 typical physical properties vs. temperature.

Temperature (°C)	Electrical Resistivity (μΩ-cm)	Thermal Diffusivity (mm^2/sec)	Thermal Conductivity (W/m-°K)	Specific Heat (J/Kg-°K)	Coefficient of Thermal Expansion (J/Kg-°K)*	Dynamic Modulus of Elasticity (Gpa)
25	125.0	2.42	8.9	397	0.0	211
100	125.8	2.68	10.4	419	12.7	207
200	126.5	2.99	12.4	435	13.0	202
300	127.3	3.29	14.4	448	13.3	196
400	128.4	3.57	16.4	465	13.7	190
500	130.2	3.85	18.4	473	14.0	184
600	131.2	4.19	20.4	486	14.4	177
700	130.7	4.30	22.4	574	14.8	171
800	129.1	4.32	24.4	595	15.2	164
900	127.1	4.44	26.4	609	15.7	157
1000	125.0	4.82	28.4	617	16.1	150

* Data represent averaged values from 25 °C to specified temperature.

Table E.2 Haynes 230 typical tensile properties vs. temperature.

Temp. (°C)	Tensile Strength (Mpa)					
	Cold-Rolled Sheet		Hot-Rolled Plate		Cast	
	0.2% Yield	Ultimate	0.2% Yield	Ultimate	0.2% Yield	Ultimate
25	390	860	395	865	325	615
540	275	710	280	705	230	450
650	270	670	270	675	225	480
760	285	585	295	605	225	385
870	225	400	255	435	185	285
980	120	225	145	245	170	205
1095	57	120	75	135	87	89
1150	39	79	47	91	-	-
1205	26	55	30	65	-	-

[†] Data provided by Hanes International, Inc., 1020 West Park Avenue, P.O. Box 9013, Kokomo, Indiana 46904-9013.

Table E.3 Haynes 230 typical creep properties vs. temperature.

Temp. (°C)	Creep (%)	Approximate Initial Stress (Mpa) to Produce Specified Creep in: Sheet 10 hrs	Sheet 10^2 hrs	Sheet 10^3 hrs	Sheet 10^4 hrs [a]	Plate and Bar 10 hrs	Plate and Bar 10^2 hrs	Plate and Bar 10^3 hrs	Plate and Bar 10^4 hrs	Cast 10 hrs	Cast 10^2 hrs	Cast 10^3 hrs	Cast 10^4 hrs [a] hrs
650	0.5	330	220	150	-	405	235	160	-	-	-	-	-
	1	350	250	170	-	415	270	180	120	-	-	-	-
	Rupture	460	330	250	185	-	385	295	200	-	-	-	-
705	0.5	215	145	100	-	205	140	105	-	-	-	-	-
	1	235	165	115	-	240	160	125	85	-	-	-	-
	Rupture	325	235	170	130	360	270	200	145	-	-	-	-
760	0.5	120	95	75	-	130	97	76	-	-	-	-	-
	1	140	100	81	-	150	110	79	55	-	-	-	-
	Rupture	220	170	125	91	255	185	140	98	220	165	125	96
815	0.5	90	71	54	-	92	73	57	-	-	-	-	-
	1	97	77	59	-	105	83	63	45	-	-	-	-
	Rupture	160	120	86	58	180	130	97	68	160	120	90	68
870	0.5	69	52	38	-	71	55	39	-	-	-	-	-
	1	76	58	40	-	81	62	41	30	-	-	-	-
	Rupture	115	83	57	39	130	95	66	43	115	86	64	46
925	0.5	52	37	23	-	54	38	23	-	-	-	-	-
	1	57	39	25	-	61	43	28	18	-	-	-	-
	Rupture	83	55	34	22	92	65	41	24	86	62	44	31
980	0.5	37	23	12	-	38	23	11	-	-	-	-	-
	1	39	25	13	-	43	26	14	7.6	-	-	-	-
	Rupture	55	34	18	7.6	65	41	21	11	62	44	30	20
1040	0.5	-	-	-	-	-	-	-	-	-	-	-	-
	1	-	-	-	-	30[b]	14[b]	6.2[b]	-	-	-	-	-
	Rupture	52	24	11	-	48[b]	24[b]	12[b]	-	45	31	20	12
1095	0.5	-	-	-	-	-	-	-	-	-	-	-	-
	1	-	-	-	-	16[b]	5.5[b]	-	-	-	-	-	-
	Rupture	-	-	-	-	29[b]	14[b]	6.9[b]	-	32	21	12	-
1150	0.5	-	-	-	-	-	-	-	-	-	-	-	-
	1	-	-	-	-	7.6[b]	2.8[b]	-	-	-	-	-	-
	Rupture	-	-	-	-	16[b]	8.3[b]	4.1[b]	-	22	13	06.2	-

[a] Significant extrapolation of data.

[b] Based upon limited data.

Appendix F. Comments on Steam Pressure Measurement

It will, perhaps, be of aid to those engaged in similar pursuits to here mention some special considerations to be taken into account in the pressure measurement of substances which are gaseous only at elevated temperatures, but condense at typical ambient conditions, such as the steam/water employed in the proof-of-concept experiment. Because condensation requires only one or two molecular collisions, it is, in fact, quite possible to maintain a substantial pressure gradient across a tube whose wall temperature resides below that required to condense the internal gas until all regions adjacent to these walls are filled by condensate. (Indeed, high vacuum pumps exploit this principle through continuous removal of the condensate.) It is, therefore, impossible to accurately measure pressure through tubes connecting ports to measuring devices unless the measurement volume is heated, or the experiment is either of sufficient duration to fill the cold volume in question or the volume is pre-filled.

The necessarily high sampling rate of the proof-of-concept experiment stipulated automation, and, in turn, required use of piezo-resistive pressure transducers. However such instruments with elevated operational temperatures are unusual and expensive. As narrow pressure ports do not provide sufficient flow to fill the ballast volume of all available transducers within the approximately one minute experiment duration, the transducers were oriented to allow pre-filling. Fomblin Y-16 vacuum oil was selected as a ballast fluid as its low vapor pressure and high specific gravity (~2) prevent appreciable evaporation under vacuum or displacement by water during system operation. The connecting lines, impractical to pre-fill with heavy fluid, but of sufficiently small volume such that they should fill with condensate quickly, were electro-resistively heated above the condensation temperature as an extra precaution.

Appendix G. Proof-of-Concept Experiment Flow Property Data with Approximate Mass Flow Ratios

The following table contains samples of all pertinent temperature and pressure measurements from the proof-of-concept experiment, taken during the feedstock injection interval. Pressure ports were located along the centerline of the sidewall, corresponding to the 10 cm span of the mixing section. Thermocouples were positioned at the flow centerline by 1.6 mm stainless steel tubing extending from the top or bottom faces of the flow sections, at 90° to the ported walls. The K-type thermocouples employed demonstrate limited life when immersed in the involved high temperature, reacting flows. Thus temperature data acquisition becomes more problematic, hence the data increasingly scant, as the probes move upstream toward the higher temperature and velocity regions of flow. This is particularly noticeable for the thermocouple located 96.5 cm downstream of the nozzle array exit, which, in fact, resided within the shock recompression region.

Approximate steam-to-feedstock ratios are tabulated for reference assuming ideal, choked flow at the corresponding throats, where the nozzle manifold and transition section pressures are taken for the respective total pressures and the total temperatures computed as outlined in Chapter 3. Two values are listed, one representing the total feedstock mass flow and the second (graphically presented in Figure 3.26) only the hydrocarbon constituents, i.e., neglecting inert constituents.

	Location		Run 35	36	37	38	39	40	41	42
Temperature, °C	Top of Pebble Bed		1205	1218	1240	732	1050	1153	1187	1151
	Ethane Heater Exit		537	590	580	60	469	556	603	584
	Transition Section	(Near wall))	-	-	-	-	1025	1137	1193	1188
		(Centerline)	1087	1085	1099	673	1035	1148	1146	1175
	Feed Line		-	-	500	41	434	494	515	511
	Nozzle Feed Manifold		362	415	402	122	358	406	400	397
	Nozzle Wall (peak)		841	858	845	418	761	859	936	934
	X (cm) =	96.5	891	897	927	601	751	964	939	1042
		196.5	-	-	830	517	759	834	877	892
		276.5			753	468	695	756	810	819
		296.5	712	727	-	-	-	-	-	-
		408.1	-	-	-	-	-	-	-	-
Pressure, bar	Top of Pebble Bed		2.283	2.249	2.235	2.232	2.247	2.251	2.266	2.243
	Nozzle Manifold		0.670	0.580	0.626	0.077	0.848	0.945	0.761	0.798
	X section		2.270	2.235	2.223	2.221	2.229	2.236	2.246	2.232
	X (cm) =	21.5	0.130	0.128	0.128	0.088	0.133	0.138	0.452	0.137
		31.5	0.153	0.150	0.150	0.130	0.160	0.160	0.493	0.156
		41.5	0.147	0.144	0.142	0.108	0.148	0.152	0.618	0.152
		51.5	0.140	0.138	0.137	0.135	0.143	0.145	0.681	0.145
		61.5	0.153	0.150	0.150	0.113	0.158	0.161	0.714	0.159
		71.5	0.146	0.146	0.144	0.102	0.152	0.155	0.711	0.154
		81.5	0.170	0.176	0.164	0.126	0.176	0.182	0.721	0.183
		91.5	0.155	0.411	0.370	0.109	0.337	0.162	0.706	0.269
		101.5	0.355	0.481	0.482	0.118	0.472	0.257	0.715	0.429
		111.5	0.485	0.502	0.516	0.229	0.542	0.403	0.729	0.524
		121.5	0.530	0.568	0.568	0.298	0.557	0.497	0.756	0.545
		131.5	0.582	0.607	0.582	0.355	0.591	0.539	0.761	0.571
		141.5	0.582	0.620	0.611	0.390	0.627	0.571	0.759	0.598
		161.5	0.615	0.595	0.626	0.448	0.654	0.609	0.765	0.634
		171.5	0.654	0.667	0.684	0.486	0.666	0.649	0.782	0.621
		181.5	0.643	0.687	0.656	0.515	0.665	0.650	0.785	0.683
		191.5	0.664	0.685	0.666	0.530	0.678	0.644	0.785	0.660
		201.5	0.670	0.693	0.683	0.545	0.697	0.658	0.806	0.673
		221.5	0.662	0.690	0.674	0.541	0.691	0.652	0.796	0.669
		231.5	0.672	0.699	0.701	0.559	0.700	0.662	0.797	0.686
		241.5	0.648	0.670	0.663	0.596	0.676	0.637	0.774	0.654
		251.5	0.642	0.683	0.676	0.539	0.694	0.671	0.794	0.678
		261.5	0.687	0.713	0.702	0.558	0.704	0.681	0.816	0.692
		271.5	0.651	0.678	0.669	0.560	0.692	0.644	0.773	0.661
		281.5	0.669	0.688	0.683	0.570	0.699	0.658	0.798	0.674
		291.5	0.650	0.663	0.650	0.539	0.690	0.634	0.766	0.637
		301.5	0.673	0.693	0.685	0.546	0.707	0.667	0.804	0.676
	Dump-tank		0.145	0.138	0.106	0.098	0.136	0.130	0.116	0.112
m_{st}/m_{feed}		(Total)	8.6	9.3	9.4	71.2	6.7	5.8	7.1	6.7
		(Hydrocarbon Only)	9.4	0.0	10.3	0.0	7.2	12.2	34.1	31.9

	Location		Run 43	44	45	46	47	48	49	50
Temperature, °C	Top of Pebble Bed		-	-	-	-	-	-	-	1296
	Ethane Heater Exit		40	563	598	599	603	605	798	589
	Transition	(Near wall))	474	1176	1189	266	264	1239	1223	1233
	Section	(Centerline)	481	1186	1202	1185	1202	1202	1189	1202
	Feed Line		60	511	536	532	521	545	190	531
	Nozzle Feed Manifold		79	411	429	439	425	447	166	445
	Nozzle Wall (peak)		401	929	949	930	941	949	992	955
	X (cm) =	96.5	458	1023	1019	1013	1018	1009	1062	-
		196.5	376	921	931	922	930	930	970	933
		276.5	355	855	858	838	851	852	893	868
		296.5	-	-	-	-	-	-	-	-
		408.1	-	-	-	748	752	755	798	771
Pressure, bar	Top of Pebble Bed		0.359	2.272	2.249	2.261	2.237	2.277	2.255	2.282
	Nozzle Manifold		0.104	0.845	0.770	0.806	0.828	0.871	0.121	0.779
	X section		2.222	2.262	2.239	2.247	2.222	2.264	2.241	2.267
	X (cm) =	21.5	0.101	0.138	0.138	0.138	0.136	0.142	2.255	0.582
		31.5	0.148	0.161	0.160	0.157	0.155	0.160	2.241	0.707
		41.5	0.123	0.155	0.153	0.154	0.153	0.155	0.119	0.718
		51.5	0.132	0.150	0.146	0.147	0.147	0.149	0.155	0.759
		61.5	0.123	0.170	0.162	0.166	0.170	0.176	0.128	0.732
		71.5	0.128	0.272	0.353	0.158	0.157	0.185	0.141	0.778
		81.5	0.138	0.439	0.490	0.186	0.238	0.424	0.138	0.785
		91.5	0.291	0.513	0.529	0.364	0.413	0.491	0.138	0.779
		101.5	0.400	0.560	0.550	0.473	0.487	0.531	0.162	0.767
		111.5	0.470	0.575	0.586	0.529	0.526	0.589	0.185	0.777
		121.5	0.493	0.618	0.596	0.552	0.559	0.602	0.381	0.794
		131.5	0.529	0.638	0.626	0.566	0.589	0.634	0.426	0.800
		141.5	0.565	0.660	0.649	0.575	0.582	0.652	0.468	0.845
		161.5	-0.452	0.684	0.669	0.642	0.644	0.662	0.524	0.820
		171.5	0.616	0.708	0.678	0.598	0.637	0.665		0.825
		181.5	0.634	0.705	0.687	0.640	0.671	0.693	0.542	0.845
		191.5	0.646	0.702	0.675	0.648	0.649	0.683	0.624	0.830
		201.5	0.648	0.722	0.702	0.658	0.663	0.706	0.615	0.848
		221.5	0.654	0.727	0.700	0.655	0.661	0.696	0.589	0.836
		231.5	0.653	0.735	0.712	0.669	0.676	0.712	0.626	0.859
		241.5	0.667	0.729	0.691	0.653	0.662	0.676	0.603	0.792
		251.5	0.707	0.697	0.681	0.641	0.648	0.680	0.628	0.798
		261.5	0.642	0.743	0.727	0.685	0.686	0.729	0.582	0.868
		271.5	0.665	0.701	0.672	0.642	0.649	0.663	0.582	0.780
		281.5	0.665	0.722	0.710	0.661	0.666	0.700	0.644	0.844
		291.5	0.677	0.672	0.654	0.621	0.626	0.646	0.573	0.753
		301.5	0.636	0.702	0.690	0.655	0.657	0.692	0.610	0.823
	Dump-tank		0.643	0.148	0.166	0.116	0.158	0.161	0.552	0.141
m_{st}/m_{feed}		(Total)	51.0	6.4	7.1	6.9	6.5	6.4	44.8	7.2
		(Hydrocarbon Only)	0.0	31.5	35.0	33.7	31.9	31.3	0.0	35.2

	Location		Run 51	52	53	54	55	56	57	58
Temperature, °C	Top of Pebble Bed		1199	-	1222	1247	1183	1183	1182	1165
	Ethane Heater Exit		602	302	642	636	632	636	640	624
	Transition	(Near wall))	1065	-	1070	1069	1080	1081	1081	1097
	Section	(Centerline)	1207	1071	1226	1226	1230	1220	1221	1218
	Feed Line		531	125	558	555	556	551	557	547
	Nozzle Feed Manifold		434	174	455	456	460	458	464	456
	Nozzle Wall (peak)		939	1002	915	924	936	924	933	929
	X (cm) =	96.5	-	-	1072	1062	1074	-	-	-
		196.5	921	903	-	-	982	-	-	-
		276.5	868	847	892	888	904	891	894	887
		296.5	-	-	-	-	-	-	-	-
		408.1	773	784	816	-	822	814	819	805
Pressure, bar	Top of Pebble Bed		2.267	2.294	2.290	2.273	2.276	2.271	2.284	2.251
	Nozzle Manifold		0.785	0.054	0.833	0.860	0.792	0.848	0.853	0.885
	X section		2.245	2.263	2.220	2.205	2.205	2.201	2.211	2.182
	X (cm) =	21.5	0.557	0.116	0.133	0.132	0.132	0.133	0.134	0.134
		31.5	0.615	0.155	0.135	0.135	0.134	0.132	0.134	0.135
		41.5	0.726	0.131	0.145	0.144	0.144	0.143	0.144	0.142
		51.5	0.740	0.140	0.145	0.145	0.144	0.145	0.146	0.260
		61.5	0.737	0.140	0.157	0.163	0.155	0.158	0.159	0.393
		71.5	0.774	0.148	0.154	0.154	0.153	0.174	0.158	0.515
		81.5	0.811	0.163	0.168	0.169	0.166	0.391	0.374	0.546
		91.5	0.779	0.322	0.172	0.173	0.171	0.468	0.476	0.592
		101.5	0.779	0.386	0.313	0.374	0.298	0.508	0.505	0.590
		111.5	0.783	0.466	0.437	0.459	0.421	0.537	0.559	0.621
		121.5	0.800	0.474	0.468	0.487	0.463	0.565	0.562	0.637
		131.5	0.796	0.507	0.502	0.510	0.488	0.586	0.585	0.653
		141.5	0.840	0.483	0.522	0.520	0.512	0.597	0.601	0.665
		161.5	0.825	0.537	0.552	0.547	0.528	0.615	0.627	0.685
		171.5	0.839	0.542	0.560	0.571	0.538	0.614	0.640	0.695
		181.5	0.846	0.654	0.555	0.563	0.553	0.618	0.645	0.695
		191.5	0.840	0.572	0.597	0.587	0.581	0.645	0.651	0.697
		201.5	0.858	0.602	0.592	0.600	0.581	0.652	0.652	0.696
		221.5	0.841	0.600	0.606	0.606	0.589	0.651	0.653	0.704
		231.5	0.863	0.623	0.609	0.608	0.590	0.658	0.663	0.706
		241.5	0.793	0.528	0.604	0.602	0.597	0.650	0.649	0.705
		251.5	0.813	0.582	0.605	0.608	0.596	0.649	0.652	0.700
		261.5	0.897	0.648	0.607	0.614	0.607	0.671	0.665	0.709
		271.5	0.766	0.545	0.611	0.605	0.597	0.660	0.652	0.698
		281.5	0.828	0.586	0.612	0.614	0.610	0.672	0.662	0.711
		291.5	0.742	0.536	0.613	0.603	0.604	0.658	0.651	0.697
		301.5	0.832	0.631	0.621	0.618	0.603	0.660	0.664	0.696
	Dump-tank		0.169	0.007	0.154	0.007	0.183	0.006	0.006	0.005
m_{st}/m_{feed}		(Total)	7.0	103.9	6.6	6.3	6.9	6.4	6.4	6.1
		(Hydrocarbon Only)	34.2	0.0	27.4	25.0	28.2	26.1	26.2	24.6

	Location		Run 59	60	61	62	63	64	65	66
Temperature, °C	Top of Pebble Bed		-	-	-	-	-	-	-	-
	Ethane Heater Exit		639	630	648	651	635	639	650	459
	Transition	(Near wall))	1080	1089	1090	1090	1096	1103	1093	894
	Section	(Centerline)	1218	1225	1220	1218	1267	1256	1229	976
	Feed Line		554	549	558	561	544	551	561	433
	Nozzle Feed Manifold		463	454	465	470	460	470	476	390
	Nozzle Wall (peak)		940	945	912	952	935	1020	1022	786
	X (cm) =	96.5	-	-	-	-	-	-	-	-
		196.5	-	-	930	931	915	919	918	789
		276.5	870	876	863	866	852	858	855	760
		296.5	-	-	-	-	-	-	-	-
		408.1	785	791	790	796	781	787	784	705
Pressure, bar	Top of Pebble Bed		2.250	2.248	2.256	2.255	-	-	2.264	2.147
	Nozzle Manifold		0.990	0.780	0.551	0.574	0.712	0.748	0.793	0.829
	X section		2.180	2.180	2.188	2.187	2.195	2.201	2.195	2.035
	X (cm) =	21.5	0.598	0.562	0.123	0.123	0.126	0.127	0.127	0.129
		31.5	0.707	0.567	0.125	0.126	0.125	0.127	0.127	0.121
		41.5	0.725	0.713	0.135	0.135	0.136	0.138	0.137	0.174
		51.5	0.770	0.733	0.136	0.135	0.137	0.137	0.139	0.351
		61.5	0.778	0.764	0.144	0.144	0.147	0.150	0.150	0.457
		71.5	0.781	0.745	0.149	0.147	0.160	0.173	0.151	0.503
		81.5	0.787	0.743	0.319	0.357	0.374	0.375	0.360	0.562
		91.5	0.780	0.744	0.442	0.450	0.448	0.452	0.458	0.570
		101.5	0.771	0.728	0.456	0.469	0.486	0.492	0.470	0.581
		111.5	0.784	0.751	0.497	0.515	0.513	0.544	0.524	0.622
		121.5	0.788	0.749	0.531	0.534	0.537	0.549	0.559	0.605
		131.5	0.803	0.767	0.548	0.554	0.575	0.566	0.565	0.632
		141.5	0.810	0.777	0.558	0.570	0.581	0.595	0.580	0.640
		161.5	0.826	0.790	0.572	0.595	0.604	0.619	0.615	0.658
		171.5	0.828	0.784	0.572	0.583	0.638	0.623	0.566	0.657
		181.5	0.829	0.789	0.592	0.623	0.630	0.632	0.613	0.656
		191.5	0.831	0.793	0.617	0.625	0.639	0.645	0.635	0.667
		201.5	0.829	0.780	0.618	0.623	0.634	0.640	0.629	0.655
		221.5	0.837	0.798	0.622	0.626	0.645	0.647	0.645	0.671
		231.5	0.842	0.805	0.627	0.634	0.636	0.640	0.626	0.653
		241.5	0.832	0.783	0.625	0.618	0.632	0.626	0.637	0.657
		251.5	0.830	0.794	0.631	0.639	0.660	0.657	0.652	0.696
		261.5	0.847	0.814	0.640	0.638	0.641	0.646	0.652	0.658
		271.5	0.833	0.798	0.637	0.640	0.666	0.663	0.667	0.700
		281.5	0.849	0.811	0.634	0.628	0.648	0.651	0.649	0.670
		291.5	0.832	0.810	0.635	0.634	0.689	0.671	0.674	0.722
		301.5	0.837	0.814	0.641	0.647	0.661	0.665	0.654	0.699
	Dump-tank		0.006	0.006	0.004	0.004	0.005	0.005	0.008	0.004
m_{st}/m_{feed}		(Total)	5.4	6.9	10.9	10.5	8.2	7.9	7.4	6.5
		(Hydrocarbon Only)	21.9	28.2	12.4	11.9	9.4	9.1	8.6	7.5

	Location		Run 67	68	69	70	71	72	73	74
Temperature, °C	Top of Pebble Bed		-	-	-	-	-	-	-	-
	Ethane Heater Exit		369	633	634	631	653	647	644	653
	Transition Section	(Near wall))	898	-	-	-	-	-	1121	1109
		(Centerline)	990	1220	1216	1220	1220	1220	1223	1212
	Feed Line		126	543	543	545	553	551	548	557
	Nozzle Feed Manifold		176	466	461	474	486	476	473	475
	Nozzle Wall (peak)		785	-	-	-	-	-	-	-
	X (cm) =	96.5	-	-	-	-	-	-	-	-
		196.5	834	946	948	950	935	954	954	917
		276.5	796	896	895	898	879	901	904	857
		296.5	-	-	-	-	-	-	-	-
		408.1	742	819	817	819	799	824	826	783
Presssure, bar	Top of Pebble Bed		2.259	2.282	2.272	2.265	-	-	2.278	2.242
	Nozzle Manifold		0.113	0.773	0.819	0.870	0.767	0.949	0.872	0.629
	X section		2.166	2.191	2.182	2.172	2.193	2.185	2.189	2.152
	X (cm) =	21.5	0.108	0.132	0.131	0.131	0.131	0.132	0.132	0.126
		31.5	0.125	0.132	0.130	0.131	0.129	0.129	0.132	0.121
		41.5	0.116	0.140	0.141	0.141	0.139	0.140	0.141	0.134
		51.5	0.134	0.147	0.148	0.146	0.142	0.147	0.148	0.135
		61.5	0.128	0.345	0.153	0.152	0.153	0.152	0.155	0.146
		71.5	0.139	0.459	0.285	0.332	0.253	0.161	0.336	0.148
		81.5	0.169	0.531	0.411	0.449	0.420	0.390	0.453	0.301
		91.5	0.379	0.557	0.495	0.516	0.495	0.460	0.518	0.415
		101.5	0.413	0.563	0.484	0.504	0.503	0.506	0.534	0.486
		111.5	0.466	0.616	0.551	0.563	0.570	0.555	0.585	0.520
		121.5	0.489	0.610	0.568	0.587	0.568	0.553	0.587	0.524
		131.5	0.511	0.640	0.591	0.601	0.596	0.575	0.615	0.546
		141.5	0.525	0.654	0.607	0.621	0.611	0.595	0.624	0.560
		161.5	0.555	0.662	0.634	0.641	0.634	0.630	0.648	0.600
		171.5	0.553	0.683	0.647	0.653	0.640	0.625	0.661	0.571
		181.5	0.567	0.664	0.637	0.638	0.645	0.637	0.651	0.612
		191.5	0.576	0.679	0.648	0.662	0.648	0.642	0.657	0.615
		201.5	0.576	0.670	0.641	0.652	0.648	0.635	0.654	0.615
		221.5	0.595	0.680	0.654	0.661	0.654	0.648	0.666	0.624
		231.5	0.581	0.683	0.649	0.661	0.654	0.642	0.660	0.615
		241.5	0.575	0.693	0.660	0.665	0.662	0.633	0.664	0.621
		251.5	0.615	0.692	0.663	0.670	0.673	0.656	0.673	0.633
		261.5	0.589	0.698	0.660	0.676	0.666	0.656	0.679	0.627
		271.5	0.611	0.704	0.678	0.687	0.679	0.673	0.694	0.645
		281.5	0.591	0.691	0.650	0.664	0.660	0.657	0.673	0.637
		291.5	0.634	0.729	0.689	0.684	0.689	0.676	0.696	0.655
		301.5	0.616	0.703	0.665	0.695	0.682	0.660	0.676	0.632
	Dump-tank		0.005	0.243	0.245	0.264	0.271	0.251	0.227	0.257
m_{st}/m_{feed}		(Total)	53.1	7.2	6.6	6.2	7.2	5.4	5.9	9.5
		(Hydrocarbon Only)	61.2	24.1	25.4	23.9	12.7	12.7	13.8	9.5

Appendix H. Proof-of-Concept Experiment Chemical Data

Run	Location, cm	Partial Pressure, kPa																				% Conversion	% Selectivity
		CH_4		C_2H_2		C_2H_4		C_2H_6		C_3H_4		C_3H_6		C_3H_8		CO_2	H_2	Ar	N_2	Ne			
		FID	TCD	FID	TCD	FID	TCD	FID	TCD	FID	TCD	FID	TCD	FID	TCD	TCD	TCD	TCD	TCD	TCD			
35	136.5	0.00	0.00	0.00	0.00	0.00	0.00	0.06	1.99	-	-	-	-	-	-	0.00	0.00	-	-	0.00		0.6	100.0
		0.00	0.00	0.00	0.00	0.04	0.00	7.23	6.36	-	-	-	-	-	-	0.00	0.00	-	-	0.00		0.5	100.0
	216.5	0.00	0.00	0.00	0.00	0.07	0.00	3.94	3.78	-	-	-	-	-	-	0.00	0.00	-	-	0.00		1.8	100.0
		0.00	0.00	0.00	0.00	0.09	0.00	5.05	4.59	-	-	-	-	-	-	1.63	0.00	-	-	0.00		1.8	99.1
	276.5	0.00	0.00	0.00	0.00	0.15	0.11	6.11	5.51	-	-	-	-	-	-	2.88	0.00	-	-	0.00		2.4	100.0
		0.00	0.00	0.00	0.00	0.13	0.09	5.31	4.80	-	-	-	-	-	-	2.39	0.00	-	-	0.00		2.5	99.4
		0.00	-	0.00	-	0.16	-	6.83	-	-	-	-	-	-	-	-	-	-	-	0.00		2.3	99.1
	Front Ballast	0.00	0.00	0.00	0.00	0.37	0.29	164.8	76.18	-	-	-	-	-	-	0.00	0.00	6.11	0.00	0.00		0.0	0.0
	Rear Ballast	0.00	0.00	0.00	0.00	0.38	0.56	163.1	76.09	-	-	-	-	-	-	0.00	0.00	6.20	0.00	0.00		0.0	0.0
37	296.5	0.01	0.00	0.00	0.00	0.23	0.14	2.48	2.53	-	-	-	-	-	-	2.50	0.00	-	-	0.00		8.5	98.8
	Ballast*	0.00	0.00	0.00	0.00	0.37	0.42	164.0	76.13	-	-	-	-	-	-	0.00	0.00	6.15	0.00	0.00		0.0	0.0
39	216.5	0.00	0.00	0.00	0.00	0.03	0.00	3.00	2.55	-	-	-	-	-	-	0.00	0.00	-	-	0.00		1.0	100.0
	Dump-tank	0.00	0.00	0.00	0.00	0.05	0.00	3.39	2.95	-	-	-	-	-	-	0.00	0.00	-	-	0.00		1.4	100.0
	Rear Ballast*	0.00	0.00	0.00	0.00	0.37	0.42	164.0	76.13	-	-	-	-	-	-	0.00	0.00	6.15	0.00	0.00		0.0	0.0
40	136.5	0.00	0.00	0.00	0.00	0.02	0.00	3.99	3.44	-	-	-	-	-	-	0.00	0.00	-	-	0.00		0.6	100.0
	216.5	0.00	0.00	0.00	0.00	0.13	0.00	3.02	2.74	-	-	-	-	-	-	0.00	0.00	-	-	0.00		4.1	100.0
	296.5	0.00	0.00	0.00	0.00	0.23	0.00	3.23	3.12	-	-	-	-	-	-	0.00	0.00	-	-	0.00		6.6	100.0
	Dump-tank	0.00	0.00	0.00	0.00	0.18	0.00	2.06	2.05	-	-	-	-	-	-	0.00	0.00	3.11	11.49	0.00		8.0	100.0
	Front Ballast	0.00	0.00	0.00	0.00	0.20	0.00	96.91	47.99	-	-	-	-	-	-	0.00	0.00	45.30	0.00	0.00		0.0	0.0
	Rear Ballast	0.00	0.00	0.00	0.00	0.22	0.00	100.8	47.60	-	-	-	-	-	-	0.00	0.00	46.45	0.00	0.00		0.0	0.0
41	136.5	0.03	0.00	0.00	0.00	0.48	0.00	0.83	0.78	-	-	-	-	-	-	0.00	0.00	-	-	0.00		37.1	97.3
	276.5	0.04	0.00	0.01	0.00	0.67	0.00	0.61	0.00	-	-	-	-	-	-	0.00	0.00	-	-	0.00		53.7	95.8
	296.5	0.04	0.00	0.01	0.00	0.68	0.00	0.62	0.00	-	-	-	-	-	-	0.00	0.00	-	-	0.00		53.4	95.8
	Dump-tank	0.02	0.00	0.00	0.00	0.23	0.00	0.22	0.00	-	-	-	-	-	-	0.00	0.00	-	-	0.00		52.3	95.7
	Ballast	0.00	0.00	0.00	0.00	0.10	0.00	40.94	23.29	-	-	-	-	-	-	0.00	0.00	71.21	0.00	0.00		0.0	0.0
		0.00	0.00	0.00	0.00	0.10	0.00	40.69	23.44	-	-	-	-	-	-	0.00	0.00	74.42	0.00	0.00		0.0	0.0
42	136.5	0.00	0.00	0.00	0.00	0.05	0.00	1.20	1.12	-	-	-	-	-	-	0.00	0.00	4.37	6.42	0.00		4.3	98.3
	276.5	0.02	0.00	0.00	0.00	0.40	0.00	0.76	1.02	-	-	-	-	-	-	0.00	0.00	3.18	5.26	0.00		34.8	97.6
	296.5	0.02	0.00	0.00	0.00	0.42	0.00	0.81	0.91	-	-	-	-	-	-	0.00	0.00	4.32	5.42	0.00		34.6	97.4
	Dump-tank	0.01	0.00	0.00	0.00	0.12	0.00	0.23	0.00	-	-	-	-	-	-	0.00	0.00	-	-	0.00		34.8	97.1
	Ballast*	0.00	0.00	0.00	0.00	0.10	0.00	40.81	23.36	-	-	-	-	-	-	0.00	0.00	72.82	0.00	0.00		0.0	0.0
44	216.5	0.04	0.00	0.01	0.00	1.09	0.81	1.85	1.60	-	-	-	-	-	-	2.99	0.00	-	-	0.00		37.6	97.4
	296.5	0.04	0.00	0.02	0.00	1.11	0.81	1.11	1.05	-	-	-	-	-	-	0.00	0.00	-	-	0.00		50.8	96.7
		0.15	0.00	0.03	0.00	1.82	1.44	1.83	1.73	-	-	-	-	-	-	1.03	0.00	-	-	0.00		51.2	94.6
	Ballast	0.00	0.00	0.00	0.00	0.07	0.00	29.01	17.36	-	-	-	-	-	-	0.00	0.00	52.76	0.00	0.00		0.0	0.0
		0.00	0.00	0.00	0.00	0.08	0.00	34.13	16.09	-	-	-	-	-	-	0.00	0.00	52.98	0.00	0.00		0.0	0.0

Run	Location, cm	Partial Pressure, kPa																				% Conversion	% Selectivity
		CH_4		C_2H_2		C_2H_4		C_2H_6		C_3H_4		C_3H_6		C_3H_8		CO_2	H_2	Ar	N_2	Ne			
		FID	TCD	FID	TCD	FID	TCD	FID	TCD	FID	TCD	FID	TCD	FID	TCD	TCD	TCD	TCD	TCD	TCD			
45	116.5	0.01	0.95	0.00	0.00	0.25	0.47	3.05	3.06	-	-	-	-	-	-	0.00	0.00	-	-	0.00		7.8	97.5
	116.5*	0.05	0.11	0.00	0.34	0.64	0.50	8.46	6.26	-	-	-	-	-	-	0.73	0.00	-	-	0.00		7.3	96.5
	216.5	0.04	0.00	0.01	0.00	0.91	0.71	1.20	1.35	-	-	-	-	-	-	0.00	0.00	-	-	0.00		43.9	96.7
	216.5*	0.10	0.13	0.03	0.22	1.80	1.39	2.37	2.13	-	-	-	-	-	-	2.07	0.00	-	-	0.00		44.3	95.9
	296.5	0.05	0.72	0.02	0.00	1.04	0.83	0.87	0.99	-	-	-	-	-	-	0.00	0.00	-	-	0.00		55.3	95.9
	296.5*	0.09	0.14	0.05	0.20	1.99	1.54	1.58	1.49	-	-	-	-	-	-	1.85	0.25	-	-	0.00		56.8	95.5
	Dump-tank	0.02	0.00	0.01	0.00	0.45	0.00	0.26	0.00	-	-	-	-	-	-	0.00	0.00	-	-	0.00		64.6	94.7
	Dump-tank+	0.07	0.13	0.04	0.00	1.09	0.88	0.60	0.66	-	-	-	-	-	-	1.52	0.00	-	-	0.00		66.0	93.5
	Ballast*	0.00	0.00	0.00	0.00	0.07	0.00	31.57	16.73	-	-	-	-	-	-	0.00	0.00	52.87	0.00	0.00		0.0	0.0
46	116.5	0.05	0.00	0.00	0.15	0.92	0.84	17.79	11.36	-	-	-	-	-	-	3.87	0.00	-	-	0.00		5.0	97.3
	216.5	0.06	0.10	0.01	0.00	1.66	1.32	4.53	3.69	-	-	-	-	-	-	1.91	0.00	-	-	0.00		27.3	97.5
	296.5	0.06	0.37	0.02	0.00	1.83	1.39	2.69	2.26	-	-	-	-	-	-	2.66	0.00	-	-	0.00		41.2	97.0
	Dump-tank	0.01	0.00	0.00	0.09	0.28	0.13	0.27	0.06	-	-	-	-	-	-	3.45	0.00	-	-	0.00		51.7	96.8
	Ballast*	0.00	0.00	0.00	0.00	0.07	0.00	31.57	16.73	-	-	-	-	-	-	0.00	0.00	52.87	0.00	0.00		0.0	0.0
47	116.5	0.09	0.21	0.00	0.15	1.56	1.22	18.38	11.79	-	-	-	-	-	-	3.21	0.00	44.04	4.47	0.00		8.0	97.1
	216.5	0.09	0.18	0.03	0.15	2.53	1.92	4.83	3.97	-	-	-	-	-	-	4.29	0.00	20.57	3.12	0.00		35.0	97.1
	296.5	0.12	0.20	0.07	0.10	2.98	2.29	3.06	2.73	-	-	-	-	-	-	2.72	0.25	18.54	3.77	0.00		50.3	95.8
	367.46	0.10	0.17	0.07	0.18	2.43	1.92	1.92	1.76	-	-	-	-	-	-	3.13	0.00	15.27	5.01	0.00		57.0	95.4
	408.1	0.10	0.11	0.05	0.00	2.33	1.77	1.91	1.68	-	-	-	-	-	-	1.09	0.00	15.70	5.14	0.00		56.1	95.7
	Dump-tank	0.06	0.12	0.03	0.00	1.20	0.87	0.82	0.72	-	-	-	-	-	-	3.79	0.00	11.68	28.88	0.00		60.6	95.2
	Ballast*	0.00	0.00	0.00	0.00	0.07	0.00	31.57	16.73	-	-	-	-	-	-	0.00	0.00	52.87	0.00	0.00		0.0	0.0
48	116.5	0.06	0.11	0.00	0.00	1.17	0.91	12.40	8.57	-	-	-	-	-	-	8.71	0.00	33.73	2.93	0.00		8.8	97.1
	216.5	0.11	0.13	0.04	0.10	2.82	2.11	4.10	3.45	-	-	-	-	-	-	3.87	0.00	20.56	2.97	0.00		41.6	96.6
	296.5	0.14	0.17	0.09	0.18	3.25	2.45	2.81	2.41	-	-	-	-	-	-	2.72	0.00	18.63	3.57	0.00		54.8	95.5
	367.46	0.11	0.15	0.07	0.00	2.52	1.91	1.83	1.65	-	-	-	-	-	-	2.42	0.00	16.60	5.27	0.00		59.1	95.2
	408.1	0.11	0.12	0.08	0.10	2.60	1.99	1.65	1.49	-	-	-	-	-	-	2.19	0.70	15.15	5.37	0.00		62.4	95.0
	Dump-tank	0.06	0.00	0.04	0.10	1.24	1.01	0.68	0.73	-	-	-	-	-	-	4.13	0.00	11.64	28.36	0.00		65.9	94.5
	Ballast*	0.00	0.00	0.00	0.00	0.07	0.00	31.57	16.73	-	-	-	-	-	-	0.00	0.00	52.87	0.00	0.00		0.0	0.0
50	116.5	0.25	0.32	0.16	0.23	4.66	3.74	3.17	3.06	-	-	-	-	-	-	16.09	0.00	24.55	1.98	0.00		60.9	94.2
	216.5	0.34	0.42	0.42	0.64	5.38	4.25	1.72	1.63	-	-	-	-	-	-	7.34	0.00	25.38	3.40	0.00		77.7	90.0
	296.5	0.33	0.41	0.43	0.66	4.90	3.91	1.24	1.37	-	-	-	-	-	-	8.48	0.00	24.30	2.64	0.00		81.6	89.1
	367.46	0.25	0.34	0.34	0.69	3.54	2.89	0.77	0.77	-	-	-	-	-	-	5.64	0.25	17.89	2.65	0.00		83.8	88.4
	408.1	0.21	0.39	0.25	0.29	2.90	2.46	0.61	0.64	-	-	-	-	-	-	3.99	0.37	14.72	2.90	0.00		84.2	89.1
	Dump-tank	0.11	0.16	0.11	0.22	1.29	0.95	0.26	0.14	-	-	-	-	-	-	3.64	0.00	10.72	24.31	0.00		85.0	88.4
	Ballast	0.00	0.00	0.00	0.00	0.06	0.00	24.31	15.52	-	-	-	-	-	-	0.00	0.00	48.04	0.00	0.00		0.0	0.0
		0.00	0.00	0.00	0.00	0.05	0.00	21.47	13.92	-	-	-	-	-	-	0.00	0.00	44.26	0.00	0.00		0.0	0.0
51	116.5	0.15	0.15	0.13	0.18	3.23	2.18	3.11	2.61	-	-	-	-	-	-	2.20	0.27	14.15	2.94	0.00		52.5	93.9
	216.5	0.31	0.35	0.33	0.25	5.65	3.90	2.88	2.35	-	-	-	-	-	-	2.36	0.49	18.29	2.72	0.00		68.0	92.1
	367.46	0.32	0.57	0.45	0.53	5.10	3.62	1.48	1.17	-	-	-	-	-	-	1.01	0.25	16.44	5.37	0.00		79.5	89.4
	408.1	0.27	0.28	0.29	0.41	4.22	3.05	1.32	1.37	-	-	-	-	-	-	2.38	0.34	12.65	4.72	0.00		77.9	90.9
	Dump-tank	0.14	0.17	0.15	0.23	1.75	1.41	0.48	0.21	-	-	-	-	-	-	4.39	0.00	11.81	38.33	0.00		80.5	88.9
	Ballast*	0.00	0.00	0.00	0.00	0.06	0.00	22.89	14.72	-	-	-	-	-	-	0.00	0.00	46.15	0.00	0.00		0.0	0.0

Run	Location, cm	Partial Pressure, kPa																		% Conversion	% Selectivity
		CH_4		C_2H_2		C_2H_4		C_2H_6		C_3H_4		C_3H_6		C_3H_8		CO_2	H_2	Ar	N_2	Ne	
		FID	TCD	FID	TCD	FID	TCD	FID	TCD	FID	TCD	FID	TCD	FID	TCD	TCD	TCD	TCD	TCD	TCD	
53	116.5	0.07	-	0.01	-	1.08	-	8.96	-	-	-	-	-	-	-	-	-	-	-	0.00	11.2 96.1
	216.5	0.12	-	0.07	-	2.76	-	3.82	-	-	-	-	-	-	-	-	-	-	-	0.00	43.1 95.6
	296.5	0.01	-	0.00	-	0.10	-	0.04	-	-	-	-	-	-	-	-	-	-	-	0.00	74.4 96.4
		0.00	-	0.00	-	0.06	-	0.02	-	-	-	-	-	-	-	-	-	-	-	0.00	73.9 96.6
		0.01	-	0.00	-	0.12	-	0.04	-	-	-	-	-	-	-	-	-	-	-	0.00	74.0 96.6
	367.46	0.13	-	0.20	-	2.64	-	1.00	-	-	-	-	-	-	-	-	-	-	-	0.00	74.4 90.9
		0.08	-	0.12	-	1.68	-	0.63	-	-	-	-	-	-	-	-	-	-	-	0.00	74.4 91.3
	408.1	0.16	-	0.23	-	3.16	-	1.09	-	-	-	-	-	-	-	-	-	-	-	0.00	76.1 91.0
		0.08	-	0.12	-	1.67	-	0.60	-	-	-	-	-	-	-	-	-	-	-	0.00	75.3 91.3
	Dump-tank	0.02	-	0.02	-	0.33	-	4.48	-	-	-	-	-	-	-	-	-	-	-	0.00	7.4 92.4
		0.01	-	0.01	-	0.21	-	2.77	-	-	-	-	-	-	-	-	-	-	-	0.00	7.5 92.8
	Ballast	0.00	0.00	0.00	0.00	0.13	0.00	30.09	29.97	-	-	-	-	-	-	0.00	0.00	77.22	0.00	0.00	0.0 0.0
54	116.5	0.10	-	0.01	-	1.45	-	8.95	-	-	-	-	-	-	-	-	-	-	-	0.00	14.4 96.0
		0.06	-	0.00	-	0.85	-	5.36	-	-	-	-	-	-	-	-	-	-	-	0.00	14.1 96.3
	216.5	0.12	-	0.06	-	2.80	-	3.57	-	-	-	-	-	-	-	-	-	-	-	0.00	45.0 95.8
		0.08	-	0.04	-	1.96	-	2.42	-	-	-	-	-	-	-	-	-	-	-	0.00	45.7 96.1
	296.5	0.01	-	0.01	-	0.25	-	0.09	-	-	-	-	-	-	-	-	-	-	-	0.00	74.3 94.4
		0.01	-	0.00	-	0.15	-	0.05	-	-	-	-	-	-	-	-	-	-	-	0.00	73.8 95.1
		0.01	-	0.01	-	0.28	-	0.10	-	-	-	-	-	-	-	-	-	-	-	0.00	74.3 94.8
	367.46	0.14	-	0.20	-	2.86	-	1.04	-	-	-	-	-	-	-	-	-	-	-	0.00	75.1 91.4
		0.08	-	0.11	-	1.73	-	0.61	-	-	-	-	-	-	-	-	-	-	-	0.00	75.4 92.0
	408.1	0.15	-	0.19	-	2.95	-	0.94	-	-	-	-	-	-	-	-	-	-	-	0.00	77.3 91.8
		0.10	-	0.11	-	1.88	-	0.60	-	-	-	-	-	-	-	-	-	-	-	0.00	77.4 92.0
	Dump-tank	0.05	-	0.07	-	0.87	-	0.25	-	-	-	-	-	-	-	-	-	-	-	0.00	79.7 90.0
	Dump-tank (cont'd)	0.05	-	0.07	-	0.82	-	0.23	-	-	-	-	-	-	-	-	-	-	-	0.00	79.5 90.1
	Ballast	0.00	0.00	0.00	0.00	0.14	0.00	32.15	30.50	-	-	-	-	-	-	0.00	0.00	73.52	0.00	0.00	0.0 0.0
55	116.5	0.01	-	0.00	-	0.23	-	5.02	-	-	-	-	-	-	-	-	-	-	-	0.00	4.4 98.3
		0.01	-	0.00	-	0.14	-	2.97	-	-	-	-	-	-	-	-	-	-	-	0.00	4.7 98.3
	216.5	0.15	-	0.08	-	3.14	-	3.40	-	-	-	-	-	-	-	-	-	-	-	0.00	49.2 95.3
		0.09	-	0.05	-	1.99	-	2.05	-	-	-	-	-	-	-	-	-	-	-	0.00	50.4 95.5
	296.5	0.15	-	0.11	-	2.75	-	1.20	-	-	-	-	-	-	-	-	-	-	-	0.00	70.9 93.6
		0.10	-	0.08	-	1.86	-	0.80	-	-	-	-	-	-	-	-	-	-	-	0.00	71.4 93.7
	367.46	0.15	-	0.21	-	2.66	-	0.81	-	-	-	-	-	-	-	-	-	-	-	0.00	78.5 90.2
		0.08	-	0.12	-	1.50	-	0.45	-	-	-	-	-	-	-	-	-	-	-	0.00	78.6 90.4
	408.1	0.16	-	0.21	-	2.80	-	0.74	-	-	-	-	-	-	-	-	-	-	-	0.00	80.7 90.5
		0.10	-	0.13	-	1.66	-	0.43	-	-	-	-	-	-	-	-	-	-	-	0.00	81.0 90.5
	Dump-tank	0.02	-	0.02	-	0.26	-	0.07	-	-	-	-	-	-	-	-	-	-	-	0.00	80.7 91.0
		0.02	-	0.02	-	0.27	-	0.07	-	-	-	-	-	-	-	-	-	-	-	0.00	80.8 91.5
	Ballast	0.00	0.00	0.00	0.00	0.13	0.00	31.05	30.77	-	-	-	-	-	-	0.00	0.00	76.81	0.00	0.00	0.0 0.0

Run	Location, cm	Partial Pressure, kPa																				% Conversion	% Selectivity
		CH_4		C_2H_2		C_2H_4		C_2H_6		C_3H_4		C_3H_6		C_3H_8		CO_2	H_2	Ar	N_2	Ne		
		FID	TCD	FID	TCD	FID	TCD	FID	TCD	FID	TCD	FID	TCD	FID	TCD	TCD	TCD	TCD	TCD	TCD		
56	116.5	0.04	0.11	0.00	0.00	0.98	1.06	7.24	7.99	-	-	-	-	-	-	1.90	0.00	24.18	3.25	0.00	12.1	97.8
	216.5	0.19	0.32	0.10	0.20	3.91	4.14	3.43	4.02	-	-	-	-	-	-	2.83	0.45	23.53	3.40	0.00	54.5	95.3
	367.46	0.18	0.39	0.19	0.50	3.08	3.22	0.95	1.29	-	-	-	-	-	-	2.85	0.54	13.29	4.34	0.00	78.0	91.6
	408.1	0.07	0.00	0.06	0.18	1.25	1.24	0.32	0.46	-	-	-	-	-	-	0.00	0.00	5.84	1.71	0.00	80.7	92.9
	Dump-tank	0.04	0.00	0.03	0.16	0.66	0.61	0.14	0.18	-	-	-	-	-	-	1.60	0.00	4.73	15.29	0.00	83.3	92.4
	Ballast*	0.00	0.00	0.00	0.00	0.13	0.00	31.05	30.77	-	-	-	-	-	-	0.00	0.00	76.81	0.00	0.00	0.0	0.0
57	116.5	0.03	0.00	0.00	0.15	0.83	0.72	6.34	6.18	-	-	-	-	-	-	9.65	0.00	17.46	2.01	0.00	11.8	97.7
	216.5	0.22	0.29	0.12	0.32	4.77	4.38	3.94	3.93	-	-	-	-	-	-	1.90	0.32	24.09	3.56	0.00	55.9	95.3
	296.5	0.18	0.34	0.11	0.37	3.37	3.05	1.31	1.76	-	-	-	-	-	-	2.34	0.43	14.37	4.49	0.00	73.2	94.5
	367.46	0.18	0.24	0.22	0.40	3.36	3.01	0.94	1.25	-	-	-	-	-	-	1.39	0.25	14.26	4.70	0.00	79.5	91.5
	408.1	0.24	0.33	0.25	0.62	4.14	3.56	1.02	1.36	-	-	-	-	-	-	1.47	0.72	15.55	4.57	0.00	81.5	91.8
	Dump-tank	0.04	0.00	0.03	0.00	0.68	0.61	0.15	0.08	-	-	-	-	-	-	2.94	0.00	4.74	19.76	0.00	83.1	93.2
	Ballast*	0.00	0.00	0.00	0.00	0.13	0.00	31.05	30.77	-	-	-	-	-	-	0.00	0.00	76.81	0.00	0.00	0.0	0.0
58	116.5	0.10	0.19	0.02	0.16	2.54	2.41	8.00	8.10	-	-	-	-	-	-	2.72	0.00	28.95	5.92	0.00	24.6	97.1
	216.5	0.30	0.46	0.25	0.51	5.60	5.57	3.32	3.52	-	-	-	-	-	-	3.15	0.63	27.20	4.70	0.00	64.4	93.3
	296.5	0.23	0.44	0.18	0.37	4.18	4.20	1.35	1.74	-	-	-	-	-	-	2.80	0.32	17.23	6.57	0.00	76.9	93.3
	367.46	0.22	0.34	0.29	0.69	3.68	3.54	0.92	1.17	-	-	-	-	-	-	2.17	0.23	14.00	7.07	0.00	81.6	90.3
	408.1	0.15	0.24	0.18	0.34	2.51	2.54	0.54	0.71	-	-	-	-	-	-	0.92	0.28	8.55	4.40	0.00	83.7	90.8
	Dump-tank	0.10	0.21	0.14	0.22	1.53	1.39	0.29	0.17	-	-	-	-	-	-	4.24	0.00	10.50	87.87	0.00	85.7	88.8
	Ballast*	0.00	0.00	0.00	0.00	0.13	0.00	31.05	30.77	-	-	-	-	-	-	0.00	0.00	76.81	0.00	0.00	0.0	0.0
59	116.5	0.27	0.40	0.22	0.42	5.20	5.25	3.56	3.90	-	-	-	-	-	-	13.70	0.43	27.17	2.69	0.00	60.9	93.7
	216.5	0.50	0.76	0.58	0.83	7.11	7.82	2.49	2.79	-	-	-	-	-	-	4.57	0.69	29.94	3.84	0.00	76.1	89.5
	296.5	0.34	0.60	0.30	0.91	5.17	5.28	1.27	1.64	-	-	-	-	-	-	3.32	0.58	22.02	5.08	0.00	81.7	91.6
	367.46	0.31	0.49	0.40	0.71	4.61	4.73	0.97	1.15	-	-	-	-	-	-	4.51	0.45	17.36	5.40	0.00	84.2	89.3
	408.1	0.35	0.56	0.42	0.82	5.00	5.09	0.97	1.39	-	-	-	-	-	-	1.36	0.52	21.41	7.28	0.00	85.2	89.4
	Dump-tank	0.18	0.30	0.22	0.46	2.57	2.47	0.52	0.26	-	-	-	-	-	-	1.85	0.00	17.61	58.06	0.00	84.8	89.2
	Ballast*	0.00	0.00	0.00	0.00	0.13	0.00	31.05	30.77	-	-	-	-	-	-	0.00	0.00	76.81	0.00	0.00	0.0	0.0
60	116.5	0.35	0.66	0.31	0.23	6.12	6.60	3.93	4.37	-	-	-	-	-	-	1.20	0.47	30.59	4.16	0.00	62.7	92.7
	216.5	0.48	0.63	0.68	1.18	6.59	6.88	1.79	2.15	-	-	-	-	-	-	2.17	0.61	27.71	4.04	0.00	80.7	87.7
	296.5	0.33	0.65	0.34	0.34	4.67	4.76	0.91	1.18	-	-	-	-	-	-	3.26	0.52	18.87	3.57	0.00	85.0	90.2
	367.46	0.29	0.39	0.43	0.64	3.98	3.89	0.64	0.86	-	-	-	-	-	-	11.25	0.00	14.74	4.82	0.00	87.7	87.3
	408.1	0.31	0.63	0.44	0.65	4.28	4.28	0.64	0.78	-	-	-	-	-	-	5.71	0.56	16.23	4.83	0.00	88.4	87.7
	Dump-tank	0.16	0.28	0.23	0.57	2.04	2.11	0.27	0.47	-	-	-	-	-	-	13.45	0.00	14.45	47.50	0.00	89.8	86.9
	Ballast*	0.00	0.00	0.00	0.00	0.13	0.00	31.05	30.77	-	-	-	-	-	-	0.00	0.00	76.81	0.00	0.00	0.0	0.0
61	116.5	0.04	0.00	0.00	0.00	1.02	1.00	13.43	13.37	-	-	-	-	-	-	16.77	0.00	1.83	1.06	0.00	7.2	98.0
	216.5	0.05	0.00	0.01	0.22	1.27	1.16	1.47	1.68	-	-	-	-	-	-	21.52	0.00	18.54	77.96	0.00	47.0	97.4
	367.46	0.22	0.45	0.12	0.51	5.33	5.22	5.46	5.59	-	-	-	-	-	-	13.32	0.00	1.39	2.36	0.00	50.5	95.8
	408.1	0.23	0.27	0.13	0.23	5.63	5.52	5.60	5.82	-	-	-	-	-	-	6.96	0.00	2.05	3.39	0.00	51.2	95.8
	Dump-tank	0.25	0.30	0.17	0.26	5.41	5.39	4.14	4.34	-	-	-	-	-	-	1.52	0.50	7.64	35.27	0.00	57.9	94.9
	Ballast	0.00	0.00	0.00	0.00	0.49	0.43	167.1	78.00	-	-	-	-	-	-	0.00	0.00	10.10	0.00	0.00	0.0	0.0

Run	Location, cm	Partial Pressure, kPa																				% Conversion	% Selectivity
		CH_4		C_2H_2		C_2H_4		C_2H_6		C_3H_4		C_3H_6		C_3H_8		CO_2	H_2	Ar	N_2	Ne			
		FID	TCD	FID	TCD	FID	TCD	FID	TCD	FID	TCD	FID	TCD	FID	TCD	TCD	TCD	TCD	TCD	TCD			
62	116.5	0.16	0.25	0.01	0.00	3.48	3.24	16.03	15.01	-	-	-	-	-	-	13.28	0.00	3.24	4.61	0.00		18.2	97.5
	216.5	0.03	0.05	0.00	0.00	0.72	0.70	0.71	0.87	-	-	-	-	-	-	3.28	0.07	16.54	72.28	0.00		51.1	97.6
	296.5	0.28	0.39	0.14	0.20	6.10	6.06	6.70	6.42	-	-	-	-	-	-	7.60	0.41	4.65	11.89	0.00		48.8	95.7
	367.46	0.27	0.36	0.18	0.34	6.03	5.84	5.37	5.25	-	-	-	-	-	-	1.50	0.37	2.75	7.14	0.00		54.2	95.1
	408.1	0.25	0.35	0.15	0.25	5.86	5.56	5.16	5.02	-	-	-	-	-	-	4.74	0.41	2.59	5.27	0.00		54.3	95.5
	Dump-tank	0.30	0.40	0.26	0.39	6.06	5.64	4.13	4.28	-	-	-	-	-	-	13.41	0.40	12.30	57.43	0.00		61.0	93.7
	Ballast*	0.00	0.00	0.00	0.00	0.49	0.43	167.1	78.00	-	-	-	-	-	-	0.00	0.00	10.10	0.00	0.00		0.0	0.0
63	116.5	0.14	0.21	0.01	0.00	3.59	3.16	22.33	18.62	-	-	-	-	-	-	1.99	0.28	3.51	3.81	0.00		14.1	97.9
	216.5	0.01	0.00	0.00	0.00	0.19	0.18	0.25	0.33	-	-	-	-	-	-	0.58	0.00	17.20	72.66	0.00		44.2	98.2
	296.5	0.30	0.46	0.13	0.29	7.88	7.20	11.28	9.77	-	-	-	-	-	-	2.97	0.49	4.23	10.50	0.00		42.0	96.6
	367.46	0.21	0.31	0.11	0.25	6.01	5.24	6.93	6.08	-	-	-	-	-	-	1.98	0.43	2.55	4.10	0.00		47.3	96.6
	408.1	0.27	0.37	0.15	0.33	7.47	6.43	8.51	7.06	-	-	-	-	-	-	4.79	0.40	2.44	4.15	0.00		47.7	96.3
	Dump-tank	0.27	0.47	0.23	0.42	6.82	5.65	5.90	5.32	-	-	-	-	-	-	0.00	0.00	8.33	51.27	0.00		54.9	94.8
	Ballast*	0.00	0.00	0.00	0.00	0.49	0.43	167.1	78.00	-	-	-	-	-	-	0.00	0.00	10.10	0.00	0.00		0.0	0.0
64	116.5	0.07	0.27	0.01	0.00	1.34	1.27	2.65	2.91	-	-	-	-	-	-	14.29	0.00	0.59	0.76	0.00		34.4	96.7
	216.5	0.13	0.21	0.07	0.00	3.46	2.93	4.57	4.79	-	-	-	-	-	-	0.80	0.26	6.63	24.98	0.00		44.0	96.3
	296.5	0.32	0.50	0.14	0.33	7.96	7.52	8.91	7.83	-	-	-	-	-	-	4.29	0.56	4.88	12.75	0.00		48.1	96.4
	367.46	0.24	0.37	0.13	0.28	6.27	5.54	6.27	5.85	-	-	-	-	-	-	1.49	0.64	2.38	4.27	0.00		51.0	96.1
	408.1	0.29	0.50	0.14	0.35	7.27	6.48	6.86	6.24	-	-	-	-	-	-	2.48	0.76	2.20	3.70	0.00		52.4	96.2
	Dump-tank	0.35	0.70	0.28	0.50	7.70	6.95	6.09	5.60	-	-	-	-	-	-	4.39	0.50	9.80	47.20	0.00		57.2	94.5
	Ballast*	0.00	0.00	0.00	0.00	0.49	0.43	167.1	78.00	-	-	-	-	-	-	0.00	0.00	10.10	0.00	0.00		0.0	0.0
65	116.5	0.37	0.48	0.09	0.13	6.73	6.15	14.55	12.74	-	-	-	-	-	-	0.00	0.00	3.36	4.35	0.00		32.5	96.1
	216.5	0.21	0.30	0.09	0.17	5.67	4.98	11.66	9.70	-	-	-	-	-	-	0.00	0.00	2.41	3.38	0.00		33.5	96.6
	296.5	0.30	0.42	0.12	0.22	7.18	6.69	7.94	7.22	-	-	-	-	-	-	5.49	0.61	4.32	11.21	0.00		48.4	96.4
	367.46	0.27	0.37	0.14	0.24	6.68	5.86	7.17	6.53	-	-	-	-	-	-	1.20	0.60	2.54	4.77	0.00		49.2	96.0
	408.1	0.17	0.29	0.08	0.27	4.63	4.08	4.40	4.22	-	-	-	-	-	-	0.00	0.00	1.82	3.48	0.00		52.2	96.6
	Dump-tank	0.37	0.51	0.31	0.45	8.06	7.33	6.84	6.05	-	-	-	-	-	-	1.92	0.00	10.24	48.69	0.00		55.6	94.2
	Ballast*	0.00	0.00	0.00	0.00	0.49	0.43	167.1	78.00	-	-	-	-	-	-	0.00	0.00	10.10	0.00	0.00		0.0	0.0
66	116.5	0.00	0.04	0.00	0.00	0.07	0.09	8.37	7.36	-	-	-	-	-	-	17.54	0.00	1.02	1.35	0.00		0.9	99.3
	176.5	0.00	0.03	0.00	0.00	0.11	0.11	7.06	6.12	-	-	-	-	-	-	2.75	0.00	0.96	1.52	0.00		1.5	99.4
	216.5	0.00	0.04	0.00	0.00	0.29	0.28	8.50	7.30	-	-	-	-	-	-	12.35	0.00	1.66	4.09	0.00		3.3	99.4
	296.5	0.00	0.08	0.00	0.03	0.40	0.32	8.54	7.25	-	-	-	-	-	-	2.64	0.00	1.74	4.46	0.00		4.4	99.4
	408.1	0.00	0.12	0.00	0.01	0.45	0.42	6.52	5.76	-	-	-	-	-	-	1.38	0.06	0.82	1.09	0.00		6.4	99.5
	Dump-tank	0.00	0.10	0.00	0.04	0.39	0.36	4.76	4.46	-	-	-	-	-	-	6.79	0.04	3.88	18.21	0.00		7.6	99.5
	Ballast*	0.00	0.00	0.00	0.00	0.49	0.43	167.1	78.00	-	-	-	-	-	-	0.00	0.00	10.10	0.00	0.00		0.0	0.0
67	116.5	0.00	0.00	0.00	0.00	0.04	0.00	3.55	3.42	-	-	-	-	-	-	7.14	0.00	0.42	0.91	0.00		1.0	100.0
	176.5	0.00	0.00	0.00	0.00	0.08	0.00	7.03	6.04	-	-	-	-	-	-	0.61	0.00	1.00	1.90	0.00		1.1	99.5
	216.5	0.00	0.00	0.00	0.00	0.25	0.22	9.34	8.01	-	-	-	-	-	-	2.94	0.00	1.73	4.28	0.00		2.6	99.4
	296.5	0.00	0.00	0.00	0.00	0.28	0.33	7.04	6.07	-	-	-	-	-	-	0.70	0.00	1.66	4.46	0.00		3.9	99.4
	408.1	0.01	0.07	0.00	0.00	1.14	1.20	21.40	16.45	-	-	-	-	-	-	10.91	0.09	3.28	7.13	0.00		5.1	99.5
	Dump-tank	0.00	0.00	0.00	0.00	0.15	0.14	1.68	1.89	-	-	-	-	-	-	1.04	0.00	1.68	32.42	0.00		8.4	99.4
	Ballast*	0.00	0.00	0.00	0.00	0.49	0.43	167.1	78.00	-	-	-	-	-	-	0.00	0.00	10.10	0.00	0.00		0.0	0.0

Run	Location, cm	Partial Pressure, kPa																				% Conversion	% Selectivity
		CH_4		C_2H_2		C_2H_4		C_2H_6		C_3H_4		C_3H_6		C_3H_8		CO_2	H_2	Ar	N_2	Ne			
		FID	TCD	FID	TCD	FID	TCD	FID	TCD	FID	TCD	FID	TCD	FID	TCD	TCD	TCD	TCD	TCD	TCD			
68	116.5	0.02	0.04	0.00	0.00	0.44	0.41	0.58	0.73	-	-	-	-	-	-	7.43	0.00	-	-	0.00		43.8	96.5
		0.03	0.04	0.01	0.00	0.57	0.52	0.77	0.88	-	-	-	-	-	-	3.17	0.00	-	-	0.00		43.3	96.5
		0.03	0.04	0.01	0.04	0.49	0.44	0.67	0.82	-	-	-	-	-	-	5.66	0.00	-	-	0.00		43.5	96.5
	176.5	0.06	0.12	0.04	0.07	1.07	1.01	0.78	0.91	-	-	-	-	-	-	1.53	0.08	-	-	0.00		59.4	94.2
		0.05	0.12	0.03	0.05	0.96	0.93	0.70	0.85	-	-	-	-	-	-	1.82	0.08	-	-	0.00		59.3	94.3
		0.04	0.09	0.03	0.03	0.84	0.80	0.60	0.74	-	-	-	-	-	-	0.79	0.08	-	-	0.00		59.9	94.3
	216.5	0.15	0.23	0.17	0.28	2.29	2.18	0.63	0.78	-	-	-	-	-	-	2.29	0.19	-	-	0.00		80.1	90.5
		0.13	0.19	0.14	0.21	2.02	1.91	0.55	0.72	-	-	-	-	-	-	2.42	0.19	-	-	0.00		80.2	90.6
		0.12	0.17	0.13	0.20	1.76	1.67	0.48	0.58	-	-	-	-	-	-	2.11	0.17	-	-	0.00		80.4	90.5
	Dump-tank	0.07	0.09	0.10	0.20	0.91	0.88	0.17	0.26	-	-	-	-	-	-	1.56	0.12	-	-	0.00		86.0	87.0
		0.07	0.10	0.10	0.18	0.92	0.86	0.18	0.28	-	-	-	-	-	-	0.54	0.00	-	-	0.00		85.7	87.4
		0.07	-	0.10	-	0.93	-	0.18	-	-	-	-	-	-	-	-	-	-	-	0.00		85.7	87.7
	Ballast	0.00	0.00	0.00	0.00	0.03	0.00	6.76	6.84	-	-	-	-	-	-	0.00	0.00	12.55	0.00	0.00		0.0	0.0
		0.00	0.00	0.00	0.00	0.03	0.00	6.95	6.96	-	-	-	-	-	-	0.00	0.00	12.40	0.00	0.00		0.0	0.0
		0.00	0.00	0.00	0.00	0.03	0.00	6.97	7.01	-	-	-	-	-	-	0.00	0.00	12.61	0.00	0.00		0.0	0.0
		0.00	0.00	0.00	0.00	0.03	0.00	6.77	6.81	-	-	-	-	-	-	0.00	0.00	12.68	0.00	0.00		0.0	0.0
		0.00	0.00	0.00	0.00	0.03	0.00	6.83	6.95	-	-	-	-	-	-	0.00	0.00	11.56	0.00	0.00		0.0	0.0
		0.00	0.00	0.00	0.00	0.03	0.00	6.85	6.96	-	-	-	-	-	-	0.00	0.00	11.54	0.00	0.00		0.0	0.0
		0.00	0.00	0.00	0.00	0.03	0.00	6.82	7.08	-	-	-	-	-	-	0.00	0.00	12.58	0.00	0.00		0.0	0.0
		0.00	0.00	0.00	0.00	0.03	0.00	6.76	6.85	-	-	-	-	-	-	0.00	0.00	12.55	0.00	0.00		0.0	0.0
		0.00	0.00	0.00	0.00	0.03	0.00	6.95	7.12	-	-	-	-	-	-	0.00	0.00	12.39	0.00	0.00		0.0	0.0
		0.00	0.00	0.00	0.00	0.03	0.00	6.97	7.16	-	-	-	-	-	-	0.00	0.00	12.58	0.00	0.00		0.0	0.0
		0.00	0.00	0.00	0.00	0.03	0.00	6.77	6.81	-	-	-	-	-	-	0.00	0.00	12.69	0.00	0.00		0.0	0.0
69	116.5	0.02	-	0.00	-	0.39	-	0.66	-	-	-	-	-	-	-	-	-	-	-	-		38.0	96.7
		0.02	-	0.00	-	0.43	-	0.73	-	-	-	-	-	-	-	-	-	-	-	-		38.0	96.7
	176.5	0.04	-	0.02	-	0.74	-	0.76	-	-	-	-	-	-	-	-	-	-	-	-		50.3	95.7
		0.03	-	0.01	-	0.66	-	0.66	-	-	-	-	-	-	-	-	-	-	-	-		51.0	95.7
	216.5	0.10	0.16	0.09	0.15	1.74	1.78	0.63	0.83	-	-	-	-	-	-	3.14	0.00	-	-	2.11		74.8	92.6
		0.09	-	0.08	-	1.56	-	0.56	-	-	-	-	-	-	-	-	-	-	-	-		75.2	92.4
	296.5	0.04	-	0.03	-	0.68	-	0.18	-	-	-	-	-	-	-	-	-	-	-	-		80.3	93.5
		0.05	-	0.03	-	0.72	-	0.19	-	-	-	-	-	-	-	-	-	-	-	-		80.3	93.3
		0.04	-	0.03	-	0.68	-	0.18	-	-	-	-	-	-	-	-	-	-	-	-		80.4	93.4
		0.11	-	0.10	-	1.60	-	0.42	-	-	-	-	-	-	-	-	-	-	-	-		80.8	91.4
	408.1	0.07	-	0.07	-	1.04	-	0.24	-	-	-	-	-	-	-	-	-	-	-	-		82.9	90.8
		0.05	-	0.06	-	0.80	-	0.18	-	-	-	-	-	-	-	-	-	-	-	-		82.9	90.8
		0.06	-	0.06	-	0.92	-	0.21	-	-	-	-	-	-	-	-	-	-	-	-		82.9	90.7
	Dump-tank	0.00	0.07	0.00	0.13	0.01	0.70	0.00	0.16	-	-	-	-	-	-	0.23	0.17	-	-	0.52		86.6	86.3
	Ballast	0.00	-	0.00	-	0.14	-	32.19	-	-	-	-	-	-	-	-	-	-	0.00	-		0.0	0.0
		0.00	-	0.00	-	0.05	-	14.01	-	-	-	-	-	-	-	-	-	-	0.00	-		0.0	0.0

Run	Location, cm	Partial Pressure, kPa																				% Conversion	% Selectivity
		CH_4		C_2H_2		C_2H_4		C_2H_6		C_3H_4		C_3H_6		C_3H_8		CO_2	H_2	Ar	N_2	Ne			
		FID	TCD	FID	TCD	FID	TCD	FID	TCD	FID	TCD	FID	TCD	FID	TCD	TCD	TCD	TCD	TCD	TCD			
70	296.5	0.08	-	0.09	-	1.10	-	0.20	-	-	-	-	-	-	-	-	-	-	-	-		86.0	89.7
	408.1	0.07	-	0.08	-	0.93	-	0.18	-	-	-	-	-	-	-	-	-	-	-	-		85.7	89.3
		0.06	-	0.07	-	0.84	-	0.15	-	-	-	-	-	-	-	-	-	-	-	-		85.8	89.4
	Ballast*	0.00	-	0.00	-	0.09	-	23.10	-	-	-	-	-	-	-	-	-	-	0.00	-		0.0	0.0
71	408.1	0.11	-	0.09	-	2.11	-	0.87	-	-	-	-	-	-	-	-	-	-	-	-		72.0	93.8
		0.12	-	0.10	-	2.38	-	1.00	-	-	-	-	-	-	-	-	-	-	-	-		71.6	93.8
		0.14	-	0.11	-	2.72	-	1.16	-	-	-	-	-	-	-	-	-	-	-	-		71.5	93.7
	Ballast*	0.00	-	0.00	-	0.09	-	23.10	-	-	-	-	-	-	-	-	-	-	0.00	-		0.0	0.0
72	176.5	0.39	0.58	0.00	0.11	0.73	0.69	0.21	0.32	0.00	0.00	0.08	0.00	1.59	1.73	0.00	0.00	-	-	0.00		34.6	57.9
	408.1	0.75	-	0.04	-	1.26	-	0.17	-	0.00	-	0.21	-	0.66	-	-	-	-	-	0.00		68.6	58.7
	Dump-tank	0.49	0.70	0.04	0.08	0.85	0.84	0.11	0.12	0.00	-	0.06	-	0.36	-	-	-	-	-	0.00		70.9	64.1
		0.50	0.69	0.04	0.00	0.85	0.84	0.10	0.12	0.00	-	0.12	-	0.35	-	-	-	-	-	0.00		72.9	60.2
	Ballast	0.13	0.19	0.00	0.00	0.00	0.00	0.53	0.88	0.00	0.00	0.02	0.00	11.50	13.23	0.00	0.00	21.48	0.00	0.00		0.0	0.0
73	408.1	0.63	-	0.04	-	1.07	-	0.13	-	0.00	-	0.15	-	0.38	-	-	-	-	-	0.00		75.6	60.2
		0.71	-	0.05	-	1.21	-	0.14	-	0.00	-	0.17	-	0.43	-	-	-	-	-	0.00		75.6	60.3
		0.96	-	0.06	-	1.54	-	0.19	-	0.00	-	0.21	-	0.56	-	-	-	-	-	0.00		75.4	59.7
	Ballast	0.13	0.19	0.00	0.00	0.00	0.00	0.53	0.88	0.00	0.00	0.02	0.00	11.50	13.23	0.00	0.00	21.48	0.00	0.00		0.0	0.0
74	116.5	0.07	0.10	0.01	0.03	1.52	1.32	4.85	4.74	0.00	0.00	0.00	0.00	0.01	0.00	12.28	0.09	-	-	0.61		24.5	96.6
	176.5	0.06	0.09	0.01	0.00	1.54	1.37	4.54	4.39	0.00	0.00	0.00	0.00	0.01	0.00	3.69	0.11	-	-	0.48		26.0	97.0
	216.5	0.32	0.42	0.13	0.16	7.05	7.02	9.04	8.52	0.00	0.00	0.01	0.00	0.02	0.00	2.29	0.39	-	-	1.21		44.9	95.5
	296.5	0.21	0.27	0.07	0.13	5.04	4.52	4.58	4.39	0.00	0.00	0.01	0.00	0.01	0.00	1.70	0.00	-	-	1.11		53.3	96.3
	408.1	0.14	0.19	0.07	0.12	3.33	3.11	2.36	2.52	0.00	0.00	0.00	0.00	0.00	0.00	0.22	0.19	-	-	0.53		59.6	95.7
		-	0.19	-	0.12	-	3.07	-	2.49	-	0.00	-	0.00	-	0.00	0.24	0.25	-	-	0.54		-	-
	Dump-tank	0.08	0.12	0.05	0.08	1.87	1.76	1.14	1.32	0.00	0.00	0.00	0.00	0.01	0.00	0.92	0.14	-	-	0.31		63.3	94.6
	Ballast*	0.00	0.00	0.00	0.00	0.09	0.00	23.10	6.96	0.00	0.00	0.00	0.00	0.00	0.00	0.00	0.00	12.37	0.00	0.00		0.0	0.0

- Not measured
* Ballast mixture identical to and computed from average of measurements from previous case.
+ These samples an all in subsequent runs were additionally compressed prior to analysis.

Appendix I. Recompression Study Data with Computed Characteristic Parameters*

Case 1

X (cm) =																									
	x_o = -11.4 cm								x_o = -12.1 cm														Pressure (bar)	
																							Plenum	
8.075	8.032	7.509	6.649	6.634	6.034	4.731	4.706	4.612	3.165	8.548	8.548	8.536	8.060	6.631	5.392	4.820	4.248						-13.34	
0.881	0.876	0.817	0.726	0.727	0.665	0.665	0.659	0.677	0.550	0.943	0.922	0.928	0.877	0.731	0.666	0.709	0.740							
0.958	0.950	0.898	0.783	0.787	0.714	0.564	0.561	0.565	0.512	0.987	0.994	0.997	0.966	0.788	0.657	0.618	0.797						-12.70	
0.890	0.878	0.818	0.745	0.756	0.787	0.737	0.728	0.734	0.502	0.945	0.935	0.937	1.064	0.761	0.907	0.912	0.884						-12.07	
1.071	1.039	0.964	0.927	0.999	0.916	0.594	0.579	0.787	0.392	1.122	1.212	1.320	1.633	1.001	1.043	1.166	1.074						-11.43	
1.071	1.039	0.964	0.927	0.999	0.916	0.594	0.579	0.787	0.392	1.122	1.212	1.320	1.633	1.001	1.043	1.166	1.074						-10.80	
1.794	1.735	1.559	1.617	1.693	1.540	1.143	1.102	1.192	0.798	2.008	2.123	2.172	2.188	1.715	1.431	1.387	1.240						-10.16	
2.092	2.155	1.910	1.771	1.766	1.634	1.316	1.260	1.325	0.911	2.266	2.323	2.300	2.333	1.833	1.585	1.462	1.308						-9.53	
2.092	2.155	1.910	1.771	1.766	1.634	1.316	1.260	1.325	0.911	2.266	2.323	2.300	2.333	1.833	1.585	1.462	1.308						-8.89	
2.245	2.247	2.067	1.912	1.893	1.716	1.331	1.320	1.368	0.956	2.451	2.410	2.399	2.194	1.922	1.577	1.456	1.330						-8.26	
2.283	2.277	2.162	1.871	1.899	1.744	1.408	1.396	1.395	0.989	2.346	2.356	2.372	2.248	1.893	1.616	1.531	1.359						-7.62	
2.250	2.233	2.068	1.959	1.974	1.758	1.433	1.412	1.425	1.015	2.363	2.395	2.401	2.267	1.947	1.647	1.565	1.378						-6.99	
2.360	2.352	2.189	1.973	1.987	1.816	1.457	1.466	1.467	1.080	2.479	2.499	2.550	2.382	1.972	1.693	1.638	1.432						-6.35	
2.407	2.390	2.207	2.023	2.024	1.856	1.494	1.487	1.488	1.114	2.555	2.562	2.572	2.460	1.985	1.736	1.689	1.459						-5.72	
2.420	2.422	2.245	2.056	2.069	1.901	1.520	1.520	1.519	1.143	2.578	2.622	2.622	2.503	2.023	1.768	1.722	1.486						-5.08	
2.420	2.422	2.245	2.056	2.069	1.901	1.520	1.520	1.519	1.143	2.578	2.622	2.622	2.503	2.023	1.768	1.722	1.486						-4.45	
2.433	2.429	2.262	2.084	2.103	1.884	1.544	1.552	1.533	1.165	2.593	2.607	2.628	2.515	2.078	1.791	1.757	1.511						-3.81	
2.424	2.435	2.243	2.075	2.078	1.924	1.560	1.553	1.563	1.163	2.604	2.620	2.641	2.530	2.058	1.815	1.770	1.515						-3.18	
2.419	2.453	2.271	2.094	2.058	1.989	1.619	1.590	1.598	1.173	2.660	2.619	2.685	2.537	2.082	1.882	1.799	1.542						-2.54	
2.419	2.453	2.271	2.094	2.058	1.989	1.619	1.590	1.598	1.173	2.660	2.619	2.685	2.537	2.082	1.882	1.799	1.542						-1.91	
2.553	2.636	2.443	2.276	2.230	2.058	1.712	1.638	1.651	1.169	2.833	2.875	2.722	2.730	2.219	1.926	1.853	1.574						-1.27	
2.859	2.924	2.650	2.446	2.459	2.255	1.800	1.779	1.763	1.227	3.140	3.117	3.162	2.985	2.445	2.085	1.944	1.665						-0.64	
-11.0	-11.5	-11.0	-11.6	-11.8	-11.6	-11.4	-11.3	-11.6	-11.4	-11.6	-11.7	-11.8	-12.2	-11.7	-12.6	-12.7	-12.3						x_o (cm)	
1.344	1.563	1.283	1.316	1.301	1.087	0.941	0.960	0.770	0.769	1.626	1.653	1.660	1.500	1.296	1.118	1.138	0.689						Δp_o (bar)	
1.20	1.57	1.21	1.47	1.45	1.39	1.56	1.63	1.49	1.90	1.41	1.36	1.41	1.41	1.26	1.97	2.31	2.03						L (cm)	

Case 1 (continued)

x_o = -8.8 cm			x_o = -10.9 cm																X (cm) =
4.682	4.560	3.128	8.548	8.542	8.536	8.063	8.053	8.032	7.557	7.509	6.689	6.680	6.655	6.652	5.414	5.395	4.872	4.847	4.823	4.802	Plenum
0.646	0.655	0.549	0.930	0.943	0.931	0.889	0.875	0.875	0.826	0.821	0.731	0.729	0.727	0.727	0.651	0.643	0.664	0.666	0.662	0.666	-13.34
0.555	0.542	0.517	1.000	0.999	0.996	0.952	0.958	0.960	0.898	0.896	0.795	0.794	0.780	0.787	0.642	0.641	0.584	0.579	0.574	0.573	-12.70
0.688	0.672	0.454	0.927	0.932	0.932	0.884	0.881	0.872	0.817	0.809	0.731	0.731	0.731	0.728	0.779	0.783	0.732	0.736	0.738	0.732	-12.07
0.511	0.494	0.387	1.041	1.027	1.013	0.981	0.955	0.929	0.903	0.874	0.847	0.860	0.838	0.841	0.662	0.656	0.559	0.565	0.564	0.559	-11.43
0.511	0.494	0.387	1.041	1.027	1.013	0.981	0.955	0.929	0.903	0.874	0.847	0.860	0.838	0.841	0.662	0.656	0.559	0.565	0.564	0.559	-10.80
0.458	0.441	0.330	1.733	1.657	1.722	1.539	1.286	1.135	1.296	1.568	1.316	1.402	1.231	1.215	1.101	1.145	0.972	1.041	1.088	1.082	-10.16
0.594	0.582	0.467	2.152	2.168	2.180	1.951	1.824	1.721	1.633	1.811	1.710	1.693	1.648	1.571	1.374	1.377	1.185	1.229	1.230	1.258	-9.53
0.594	0.582	0.467	2.152	2.168	2.180	1.951	1.824	1.721	1.633	1.811	1.710	1.693	1.648	1.571	1.374	1.377	1.185	1.229	1.230	1.258	-8.89
0.584	0.557	0.504	2.329	2.286	2.328	2.125	2.014	1.999	1.935	2.076	1.791	1.838	1.778	1.742	1.514	1.541	1.352	1.367	1.371	1.361	-8.26
0.815	0.746	0.616	2.459	2.471	2.438	2.285	2.288	2.239	2.117	2.098	1.886	1.875	1.898	1.899	1.542	1.547	1.398	1.431	1.443	1.450	-7.62
1.062	0.938	0.743	2.365	2.343	2.382	2.241	2.223	2.213	2.094	2.195	1.928	1.925	1.914	1.915	1.593	1.595	1.460	1.461	1.458	1.463	-6.99
1.290	1.194	0.880	2.482	2.467	2.501	2.360	2.353	2.343	2.196	2.194	1.992	1.991	1.982	1.978	1.636	1.652	1.534	1.528	1.516	1.543	-6.35
1.292	1.263	0.884	2.534	2.495	2.529	2.372	2.371	2.319	2.203	2.280	2.013	2.010	1.987	1.991	1.696	1.701	1.579	1.564	1.560	1.579	-5.72
1.341	1.295	0.877	2.589	2.573	2.581	2.420	2.424	2.429	2.264	2.334	2.041	2.045	2.009	2.005	1.735	1.739	1.615	1.596	1.591	1.605	-5.08
1.341	1.295	0.877	2.589	2.573	2.581	2.420	2.424	2.429	2.264	2.334	2.041	2.045	2.009	2.005	1.735	1.739	1.615	1.596	1.591	1.605	-4.45
1.384	1.315	0.941	2.647	2.610	2.622	2.436	2.458	2.440	2.285	2.368	2.078	2.069	2.039	2.008	1.751	1.758	1.622	1.616	1.611	1.652	-3.81
1.433	1.365	0.932	2.616	2.587	2.606	2.420	2.425	2.438	2.282	2.385	2.076	2.084	2.021	2.007	1.780	1.784	1.666	1.644	1.631	1.664	-3.18
1.481	1.408	0.935	2.571	2.542	2.635	2.469	2.385	2.438	2.258	2.387	2.110	2.152	2.019	2.023	1.805	1.837	1.707	1.716	1.660	1.734	-2.54
1.481	1.408	0.935	2.571	2.542	2.635	2.469	2.385	2.438	2.258	2.387	2.110	2.152	2.019	2.023	1.805	1.837	1.707	1.716	1.660	1.734	-1.91
1.595	1.497	0.928	2.804	2.774	2.750	2.601	2.563	2.644	2.414	2.615	2.213	2.319	2.146	2.074	1.866	1.916	1.769	1.739	1.735	1.774	-1.27
1.699	1.591	0.865	3.103	3.078	3.140	2.878	2.857	2.874	2.714	2.888	2.441	2.483	2.404	2.396	2.073	2.073	1.887	1.876	1.855	1.888	-0.64
-8.7	-8.6	-8.6	-11.0	-10.9	-10.9	-10.9	-10.5	-10.3	-10.6	-11.0	-10.9	-10.9	-10.8	-10.6	-11.0	-11.1	-11.0	-11.0	-11.1	-11.2	x_o (cm)
0.844	0.817	0.430	1.555	1.539	1.567	1.444	1.458	1.475	1.355	1.473	1.221	1.195	1.196	1.136	1.098	1.103	1.097	1.062	1.045	1.093	Δp_- (bar)
1.38	1.45	1.10	1.29	1.23	1.19	1.31	1.16	1.16	1.35	1.45	1.34	1.31	1.33	1.13	1.64	1.58	1.82	1.63	1.58	1.81	L (cm)

Pressure (bar)

Case 1 (continued)

x_o = -7.9 cm									x_o = -8.8 cm												X (cm) =
8.053	7.536	6.701	5.986	5.986	5.417	5.383	4.823	4.750	8.542	6.683	6.683	6.646	6.007	5.392	4.826	4.799	4.796	4.784	4.774	4.706	Plenum
0.879	0.822	0.732	0.671	0.670	0.645	0.649	0.652	0.647	0.940	0.724	0.723	0.725	0.663	0.645	0.662	0.658	0.657	0.664	0.659	0.652	-13.34
0.956	0.893	0.794	0.699	0.699	0.643	0.638	0.572	0.565	0.988	0.795	0.792	0.783	0.705	0.640	0.579	0.568	0.570	0.569	0.571	0.560	-12.70
0.870	0.818	0.724	0.671	0.668	0.753	0.758	0.719	0.699	0.929	0.720	0.724	0.721	0.672	0.751	0.722	0.711	0.715	0.712	0.714	0.696	-12.07
0.915	0.862	0.790	0.697	0.697	0.637	0.618	0.538	0.524	0.960	0.784	0.787	0.786	0.707	0.623	0.539	0.531	0.531	0.533	0.535	0.517	-11.43
0.915	0.862	0.790	0.697	0.697	0.637	0.618	0.538	0.524	0.960	0.784	0.787	0.786	0.707	0.623	0.539	0.531	0.531	0.533	0.535	0.517	-10.80
0.847	0.799	0.753	0.645	0.645	0.553	0.551	0.482	0.465	0.854	0.759	0.761	0.733	0.652	0.556	0.480	0.476	0.475	0.479	0.480	0.458	-10.16
0.780	0.705	0.690	0.589	0.589	0.614	0.624	0.606	0.597	0.884	0.697	0.698	0.668	0.614	0.635	0.606	0.611	0.608	0.623	0.643	0.596	-9.53
0.780	0.705	0.690	0.589	0.589	0.614	0.624	0.606	0.597	0.884	0.697	0.698	0.668	0.614	0.635	0.606	0.611	0.608	0.623	0.643	0.596	-8.89
0.842	0.843	0.833	0.701	0.702	0.652	0.662	0.583	0.579	0.914	0.860	0.889	0.863	0.829	0.701	0.605	0.621	0.630	0.715	0.724	0.583	-8.26
1.050	0.999	0.788	0.873	0.878	0.847	0.847	0.739	0.741	1.180	1.232	1.273	1.077	1.215	0.974	0.827	0.919	0.882	0.994	0.974	0.795	-7.62
1.234	1.164	1.128	0.959	0.986	0.932	1.007	0.921	0.933	1.766	1.543	1.559	1.462	1.466	1.185	1.082	1.148	1.121	1.189	1.173	0.994	-6.99
1.918	1.779	1.655	1.468	1.461	1.369	1.382	1.240	1.222	2.203	1.845	1.852	1.778	1.680	1.437	1.300	1.333	1.309	1.326	1.318	1.237	-6.35
2.011	1.870	1.803	1.547	1.550	1.423	1.464	1.316	1.280	2.301	1.883	1.895	1.852	1.705	1.519	1.361	1.351	1.339	1.375	1.366	1.328	-5.72
2.188	1.990	1.846	1.650	1.648	1.498	1.479	1.332	1.339	2.350	1.929	1.941	1.856	1.741	1.519	1.368	1.398	1.377	1.399	1.395	1.320	-5.08
2.188	1.990	1.846	1.650	1.648	1.498	1.479	1.332	1.339	2.350	1.929	1.941	1.856	1.741	1.519	1.368	1.398	1.377	1.399	1.395	1.320	-4.45
2.206	2.073	1.910	1.682	1.685	1.487	1.517	1.404	1.368	2.368	1.965	1.985	1.917	1.796	1.544	1.409	1.414	1.422	1.470	1.434	1.362	-3.81
2.183	1.956	1.934	1.708	1.701	1.555	1.557	1.423	1.415	2.434	2.051	2.062	1.981	1.871	1.630	1.459	1.458	1.459	1.492	1.482	1.417	-3.18
2.242	2.081	2.003	1.769	1.734	1.603	1.635	1.514	1.468	2.530	2.153	2.150	2.017	1.978	1.692	1.487	1.510	1.510	1.588	1.484	1.462	-2.54
2.242	2.081	2.003	1.769	1.734	1.603	1.635	1.514	1.468	2.530	2.153	2.150	2.017	1.978	1.692	1.487	1.510	1.510	1.588	1.484	1.462	-1.91
2.507	2.238	2.119	1.967	1.927	1.641	1.757	1.556	1.545	2.636	2.270	2.310	2.205	2.009	1.794	1.568	1.590	1.596	1.674	1.551	1.531	-1.27
2.731	2.482	2.361	2.093	2.079	1.844	1.878	1.677	1.656	3.036	2.507	2.515	2.388	2.251	1.942	1.721	1.708	1.722	1.758	1.728	1.653	-0.64
-7.8	-7.8	-8.0	-7.7	-7.8	-7.8	-7.9	-8.6	-8.6	-8.5	-8.8	-9.1	-8.6	-9.2	-8.7	-8.7	-8.9	-8.8	-8.9	-8.9	-8.7	x_o (cm)
1.197	1.076	1.159	0.856	0.849	0.719	0.711	0.900	0.891	1.494	1.177	1.349	1.101	1.238	0.913	0.851	0.851	0.835	0.777	0.746	0.836	Δp_o (bar)
1.16	1.20	1.14	1.21	1.24	1.22	1.12	1.80	1.84	1.07	1.40	1.48	1.23	1.43	1.39	1.34	1.35	1.41	1.44	1.42	1.41	L (cm)

Pressure (bar)

Case 1 (continued)																					X (cm) =
x_o = -6.2 cm									x_o = -7.1 cm										x_o = -7.9 cm		
6.013	5.986	5.986	5.983	5.401	4.872	4.847	4.536	3.275	8.545	8.075	6.649	6.640	6.628	5.377	4.863	4.278	3.217	3.184	8.548	8.539	Plenum
0.670	0.663	0.656	0.665	0.637	0.665	0.660	0.657	0.569	0.926	0.887	0.722	0.728	0.734	0.653	0.661	0.655	0.561	0.556	0.943	0.946	-13.34
0.706	0.706	0.711	0.707	0.643	0.579	0.575	0.538	0.570	0.997	0.950	0.783	0.788	0.781	0.641	0.582	0.506	0.547	0.527	0.992	0.981	-12.70
0.674	0.672	0.677	0.673	0.753	0.724	0.717	0.666	0.434	0.937	0.874	0.717	0.720	0.717	0.761	0.714	0.618	0.435	0.450	0.928	0.932	-12.07
0.707	0.709	0.711	0.704	0.623	0.548	0.540	0.491	0.422	0.967	0.914	0.772	0.781	0.781	0.619	0.544	0.467	0.409	0.390	0.950	0.961	-11.43
0.707	0.709	0.711	0.704	0.623	0.548	0.540	0.491	0.422	0.967	0.914	0.772	0.781	0.781	0.619	0.544	0.467	0.409	0.390	0.950	0.961	-10.80
0.645	0.641	0.639	0.643	0.553	0.483	0.478	0.438	0.355	0.860	0.849	0.737	0.731	0.734	0.551	0.481	0.457	0.341	0.336	0.861	0.854	-10.16
0.585	0.582	0.582	0.578	0.615	0.595	0.597	0.570	0.475	0.863	0.772	0.650	0.645	0.649	0.620	0.602	0.555	0.465	0.465	0.879	0.859	-9.53
0.585	0.582	0.582	0.578	0.615	0.595	0.597	0.570	0.475	0.863	0.772	0.650	0.645	0.649	0.620	0.602	0.555	0.465	0.465	0.879	0.859	-8.89
0.696	0.681	0.686	0.684	0.639	0.587	0.582	0.534	0.471	0.874	0.806	0.796	0.806	0.799	0.648	0.582	0.546	0.468	0.475	0.905	0.884	-8.26
0.775	0.797	0.800	0.795	0.801	0.685	0.670	0.628	0.520	1.095	1.058	0.802	0.803	0.784	0.784	0.699	0.624	0.528	0.527	1.182	1.155	-7.62
0.820	0.829	0.830	0.825	0.775	0.795	0.777	0.747	0.594	1.152	1.185	0.969	0.946	0.941	0.797	0.839	0.739	0.595	0.599	1.616	1.289	-6.99
0.890	0.928	0.888	0.905	1.033	0.875	0.818	0.736	0.609	1.674	1.667	1.423	1.439	1.349	1.124	1.104	0.989	0.746	0.807	2.160	2.023	-6.35
1.144	1.225	1.138	1.136	1.290	1.060	0.988	0.874	0.745	1.958	1.925	1.597	1.612	1.613	1.296	1.238	1.086	0.870	0.847	2.275	2.125	-5.72
1.330	1.420	1.389	1.346	1.370	1.209	1.167	1.061	0.877	2.072	2.005	1.732	1.758	1.686	1.423	1.324	1.174	0.899	0.914	2.341	2.310	-5.08
1.330	1.420	1.389	1.346	1.370	1.209	1.167	1.061	0.877	2.072	2.005	1.732	1.758	1.686	1.423	1.324	1.174	0.899	0.914	2.341	2.310	-4.45
1.470	1.501	1.487	1.541	1.499	1.340	1.262	1.220	0.930	2.205	2.114	1.783	1.788	1.794	1.488	1.364	1.206	0.914	0.903	2.357	2.304	-3.81
1.611	1.617	1.618	1.624	1.495	1.361	1.339	1.257	0.919	2.305	2.156	1.804	1.820	1.797	1.497	1.396	1.245	0.917	0.916	2.376	2.236	-3.18
1.600	1.615	1.614	1.558	1.539	1.392	1.362	1.294	0.918	2.193	2.081	1.842	1.860	1.780	1.506	1.391	1.276	0.915	0.920	2.466	2.377	-2.54
1.600	1.615	1.614	1.558	1.539	1.392	1.362	1.294	0.918	2.193	2.081	1.842	1.860	1.780	1.506	1.391	1.276	0.915	0.920	2.466	2.377	-1.91
1.708	1.803	1.655	1.655	1.633	1.414	1.475	1.317	0.927	2.391	2.351	1.996	2.007	2.002	1.644	1.460	1.333	0.922	0.929	2.674	2.523	-1.27
1.818	1.925	1.817	1.829	1.754	1.576	1.537	1.433	0.876	2.684	2.598	2.189	2.204	2.156	1.770	1.602	1.423	0.870	0.868	2.998	2.811	-0.64
-6.1	-6.3	-6.1	-6.1	-6.7	-6.1	-6.1	-6.0	-6.4	-6.9	-7.1	-7.3	-7.3	-7.3	-7.1	-7.0	-7.1	-7.0	-7.0	-8.0	-7.3	x_o (cm)
0.783	0.757	0.782	0.795	0.729	0.532	0.574	0.592	0.366	1.091	1.014	0.906	0.920	0.964	0.761	0.582	0.533	0.361	0.324	1.193	1.020	Δp_- (bar)
1.21	1.13	1.08	1.13	1.26	0.97	1.06	1.07	1.00	1.49	1.11	1.26	1.14	1.42	1.29	1.08	1.24	1.06	0.74	0.94	0.78	L (cm)

Pressure (bar)

Case 2															Case 1 (continued)					x (cm) =
x_o = -12.4 cm															x_o = -6.2 cm					
6.830	6.827	6.824	6.815	6.812	6.809	4.920	4.920	4.908	4.306	4.302	3.125	3.118	2.921	2.918	2.916	8.056	8.053	8.044	7.560	6.661	Plenum
1.202	1.189	1.194	1.194	1.166	1.201	0.873	0.866	0.864	0.759	0.762	0.577	0.578	0.565	0.570	0.599	0.873	0.875	0.885	0.820	0.730	-13.34
1.091	1.113	1.083	1.084	1.085	1.072	0.966	0.963	0.965	0.875	0.867	0.638	0.637	0.599	0.598	0.651	0.960	0.954	0.961	0.903	0.794	-12.70
1.675	1.751	1.212	1.223	1.526	1.255	0.902	1.134	0.993	1.087	1.044	0.768	0.758	0.663	0.682	0.905	0.880	0.871	0.879	0.817	0.724	-12.07
2.184	2.212	1.844	1.844	2.042	1.889	1.364	1.510	1.419	1.380	1.323	0.992	0.994	0.858	0.879	1.042	0.918	0.915	0.936	0.866	0.782	-11.43
2.184	2.212	1.844	1.844	2.042	1.889	1.364	1.510	1.419	1.380	1.323	0.992	0.994	0.858	0.879	1.042	0.918	0.915	0.936	0.866	0.782	-10.80
2.707	2.719	2.485	2.472	2.620	2.483	1.802	1.868	1.816	1.666	1.630	1.215	1.229	1.128	1.134	1.206	0.850	0.850	0.848	0.800	0.739	-10.16
2.850	2.826	2.708	2.734	2.847	2.785	1.960	1.995	1.944	1.776	1.714	1.295	1.307	1.215	1.214	1.276	0.767	0.767	0.780	0.710	0.651	-9.53
2.850	2.826	2.708	2.734	2.847	2.785	1.960	1.995	1.944	1.776	1.714	1.295	1.307	1.215	1.214	1.276	0.767	0.767	0.780	0.710	0.651	-8.89
2.860	2.884	2.789	2.827	2.879	2.832	2.023	2.065	2.022	1.824	1.795	1.357	1.356	1.273	1.273	1.331	0.787	0.786	0.810	0.808	0.804	-8.26
2.953	2.978	2.865	2.842	2.937	2.816	2.098	2.124	2.095	1.870	1.857	1.408	1.407	1.322	1.323	1.376	1.048	1.051	1.002	0.963	0.795	-7.62
3.001	3.006	2.914	2.946	2.994	2.909	2.143	2.178	2.157	1.909	1.915	1.453	1.449	1.365	1.369	1.404	1.157	1.157	1.121	1.113	0.941	-6.99
3.089	3.111	3.043	3.038	3.077	2.982	2.228	2.259	2.253	1.980	1.998	1.508	1.496	1.430	1.433	1.459	1.339	1.432	1.264	1.112	1.008	-6.35
3.137	3.170	3.098	3.090	3.147	3.032	2.274	2.307	2.295	2.016	2.039	1.530	1.522	1.447	1.452	1.471	1.757	1.782	1.613	1.406	1.307	-5.72
3.188	3.212	3.129	3.138	3.201	3.081	2.310	2.323	2.334	2.040	2.063	1.552	1.539	1.463	1.469	1.485	1.935	1.919	1.876	1.672	1.574	-5.08
3.188	3.212	3.129	3.138	3.201	3.081	2.310	2.323	2.334	2.040	2.063	1.552	1.539	1.463	1.469	1.485	1.935	1.919	1.876	1.672	1.574	-4.45
3.234	3.299	3.176	3.163	3.268	3.152	2.344	2.349	2.356	2.067	2.086	1.567	1.568	1.475	1.477	1.486	2.037	2.042	2.064	1.889	1.767	-3.81
3.275	3.290	3.202	3.221	3.295	3.194	2.372	2.396	2.402	2.090	2.110	1.562	1.552	1.475	1.477	1.484	2.186	2.163	2.175	2.011	1.811	-3.18
3.301	3.317	3.302	3.270	3.316	3.194	2.430	2.405	2.398	2.134	2.130	1.582	1.568	1.493	1.481	1.494	2.120	2.130	2.111	1.929	1.801	-2.54
3.301	3.317	3.302	3.270	3.316	3.194	2.430	2.405	2.398	2.134	2.130	1.582	1.568	1.493	1.481	1.494	2.120	2.130	2.111	1.929	1.801	-1.91
3.356	3.345	3.235	3.369	3.337	3.259	2.481	2.474	2.442	2.122	2.150	1.558	1.556	1.477	1.488	1.474	2.147	2.228	2.369	2.025	1.929	-1.27
3.441	3.449	3.397	3.407	3.464	3.355	2.518	2.501	2.504	2.188	2.216	1.599	1.591	1.507	1.514	1.514	2.515	2.585	2.548	2.243	2.067	-0.64
-12.7	-12.7	-12.3	-12.3	-12.6	-12.4	-12.1	-12.1	-12.2	-12.5	-12.0	-12.4	-12.4	-12.2	-12.1	-12.8	-6.3	-6.3	-6.2	-6.1	-6.1	x_o (cm)
2.117	2.117	2.124	2.127	2.159	2.094	1.404	1.236	1.415	1.178	1.049	0.938	0.933	0.909	0.828	0.887	0.888	0.804	0.961	0.947	0.890	Δp_o (bar)
1.85	1.83	2.06	2.07	1.98	2.01	2.18	2.13	2.20	1.99	2.17	2.22	2.26	2.38	2.40	2.05	1.10	1.15	1.04	1.08	1.04	L (cm)

Pressure (bar)

Case 2 (continued)

x_o = -10.5 cm				x_o = -11.2 cm											x_o = -12.4 cm						X (cm) =
4.266	4.251	3.165	3.141	7.671	5.558	5.550	5.538	4.940	4.933	4.920	4.911	3.153	2.918	2.914	7.604	7.592	7.592	7.583	7.580	6.836	Plenum
0.748	0.756	0.571	0.558	1.308	0.980	0.983	0.981	0.868	0.870	0.867	0.864	0.562	0.556	0.558	1.294	1.295	1.281	1.303	1.320	1.201	-13.34
0.837	0.841	0.629	0.627	1.215	0.948	0.952	0.946	0.971	0.966	0.963	0.957	0.629	0.589	0.590	1.249	1.268	1.229	1.207	1.191	1.080	-12.70
0.686	0.684	0.504	0.504	1.306	0.936	0.922	0.924	0.822	0.810	0.813	0.820	0.512	0.569	0.572	2.047	1.999	1.829	1.316	1.357	1.581	-12.07
0.809	0.833	0.622	0.617	1.312	0.953	0.940	0.962	0.894	0.832	0.932	0.972	0.621	0.568	0.566	2.524	2.476	2.426	1.970	2.075	2.111	-11.43
0.809	0.833	0.622	0.617	1.312	0.953	0.940	0.962	0.894	0.832	0.932	0.972	0.621	0.568	0.566	2.524	2.476	2.426	1.970	2.075	2.111	-10.80
0.739	0.736	0.727	0.776	2.026	1.644	1.629	1.740	1.599	1.264	1.597	1.600	0.853	0.787	0.868	3.064	3.064	3.002	2.742	2.762	2.652	-10.16
1.040	1.085	0.961	0.989	2.447	1.900	1.865	1.918	1.771	1.585	1.777	1.754	1.050	1.007	1.055	3.196	3.159	3.138	3.007	2.977	2.797	-9.53
1.040	1.085	0.961	0.989	2.447	1.900	1.865	1.918	1.771	1.585	1.777	1.754	1.050	1.007	1.055	3.196	3.159	3.138	3.007	2.977	2.797	-8.89
1.338	1.343	1.107	1.133	2.719	2.098	2.077	2.147	1.908	1.737	1.917	1.901	1.168	1.110	1.132	3.240	3.269	3.214	3.095	3.127	2.869	-8.26
1.495	1.480	1.203	1.222	2.960	2.220	2.205	2.239	2.010	1.893	2.007	2.017	1.253	1.191	1.201	3.309	3.347	3.296	3.151	3.223	2.931	-7.62
1.598	1.609	1.267	1.286	3.089	2.347	2.302	2.319	2.064	1.997	2.105	2.052	1.307	1.234	1.249	3.386	3.417	3.356	3.262	3.261	2.963	-6.99
1.746	1.742	1.360	1.379	3.277	2.460	2.452	2.476	2.210	2.127	2.216	2.186	1.403	1.315	1.332	3.471	3.532	3.466	3.359	3.396	3.075	-6.35
1.818	1.805	1.406	1.421	3.378	2.529	2.515	2.538	2.251	2.195	2.272	2.249	1.437	1.349	1.364	3.542	3.593	3.524	3.430	3.452	3.132	-5.72
1.866	1.860	1.441	1.450	3.442	2.576	2.571	2.575	2.302	2.238	2.314	2.288	1.475	1.374	1.389	3.588	3.667	3.597	3.475	3.511	3.168	-5.08
1.866	1.860	1.441	1.450	3.442	2.576	2.571	2.575	2.302	2.238	2.314	2.288	1.475	1.374	1.389	3.588	3.667	3.597	3.475	3.511	3.168	-4.45
1.907	1.907	1.480	1.478	3.560	2.622	2.593	2.573	2.326	2.322	2.341	2.342	1.493	1.392	1.404	3.647	3.690	3.615	3.512	3.519	3.213	-3.81
1.954	1.945	1.490	1.493	3.567	2.667	2.658	2.637	2.367	2.324	2.377	2.374	1.512	1.410	1.416	3.694	3.726	3.671	3.584	3.575	3.253	-3.18
1.969	1.967	1.520	1.501	3.606	2.693	2.686	2.689	2.376	2.347	2.416	2.413	1.531	1.411	1.428	3.801	3.732	3.748	3.652	3.596	3.289	-2.54
1.969	1.967	1.520	1.501	3.606	2.693	2.686	2.689	2.376	2.347	2.416	2.413	1.531	1.411	1.428	3.801	3.732	3.748	3.652	3.596	3.289	-1.91
1.951	1.982	1.489	1.505	3.649	2.756	2.707	2.692	2.401	2.346	2.422	2.410	1.508	1.407	1.446	3.768	3.784	3.750	3.646	3.689	3.423	-1.27
2.028	2.031	1.521	1.524	3.780	2.805	2.800	2.772	2.484	2.434	2.503	2.489	1.555	1.441	1.458	3.898	3.876	3.858	3.780	3.792	3.457	-0.64
-10.2	-10.3	-10.7	-10.8	-10.9	-11.2	-10.7	-11.5	-11.6	-10.9	-11.6	-11.7	-10.8	-10.8	-11.0	-12.7	-12.7	-12.7	-12.2	-12.3	-12.6	x_o (cm)
1.279	1.304	1.011	0.983	2.286	1.740	1.392	1.725	1.549	1.525	1.570	1.546	0.930	0.888	0.892	2.300	2.352	2.379	2.357	2.384	2.114	Δp_c (bar)
2.28	2.10	2.05	1.99	2.10	2.21	2.07	2.17	2.18	2.17	2.21	2.19	2.24	2.29	2.30	1.78	1.88	1.90	2.08	2.08	1.89	L (cm)

Pressure (bar)

Case 2 (continued)

Pressure (bar)

x_o = -9.9 cm						x_o = -10.5 cm														X (cm) =
4.254	4.254	3.187	2.916	2.904	2.328	6.769	6.764	5.555	5.553	4.933	4.933	4.930	4.928	4.902	4.896	4.896	4.896	4.896	4.327	4.321	Plenum
0.753	0.746	0.564	0.555	0.560	0.511	1.198	1.195	0.983	0.994	0.873	0.871	0.880	0.869	0.860	0.865	0.869	0.869	0.866	0.759	0.764	-13.34
0.850	0.839	0.634	0.591	0.590	0.470	1.076	1.080	0.950	0.941	0.959	0.966	0.961	0.956	0.953	0.947	0.963	0.962	0.951	0.857	0.854	-12.70
0.692	0.690	0.506	0.570	0.569	0.515	1.152	1.146	0.927	0.925	0.800	0.799	0.808	0.804	0.800	0.793	0.798	0.797	0.793	0.700	0.692	-12.07
0.818	0.816	0.614	0.556	0.556	0.439	1.140	1.119	0.948	0.933	0.824	0.822	0.820	0.822	0.819	0.817	0.818	0.829	0.819	0.833	0.822	-11.43
0.818	0.816	0.614	0.556	0.556	0.439	1.140	1.119	0.948	0.933	0.824	0.822	0.820	0.822	0.819	0.817	0.818	0.829	0.819	0.833	0.822	-10.80
0.710	0.707	0.628	0.612	0.613	0.453	1.072	1.108	1.018	1.024	0.945	1.021	1.124	1.100	0.955	0.854	0.906	1.063	1.132	1.126	0.808	-10.16
0.908	0.958	0.643	0.581	0.588	0.450	1.539	1.575	1.557	1.469	1.356	1.397	1.483	1.462	1.379	1.240	1.406	1.373	1.498	1.372	1.162	-9.53
0.908	0.958	0.643	0.581	0.588	0.450	1.539	1.575	1.557	1.469	1.356	1.397	1.483	1.462	1.379	1.240	1.406	1.373	1.498	1.372	1.162	-8.89
1.082	1.226	0.887	0.722	0.796	0.599	2.025	2.062	1.824	1.768	1.632	1.658	1.673	1.668	1.628	1.545	1.652	1.613	1.679	1.546	1.412	-8.26
1.324	1.425	1.079	0.895	1.001	0.732	2.313	2.297	1.982	1.933	1.778	1.792	1.822	1.830	1.801	1.689	1.767	1.757	1.820	1.668	1.548	-7.62
1.479	1.551	1.166	1.051	1.083	0.842	2.421	2.415	2.153	2.087	1.919	1.918	1.907	1.939	1.909	1.835	1.901	1.905	1.936	1.752	1.650	-6.99
1.655	1.692	1.278	1.153	1.171	0.918	2.645	2.666	2.284	2.249	2.052	2.059	2.081	2.080	2.056	1.993	2.029	2.036	2.086	1.884	1.793	-6.35
1.723	1.748	1.325	1.196	1.214	0.952	2.729	2.761	2.357	2.329	2.125	2.138	2.153	2.147	2.119	2.072	2.112	2.115	2.156	1.951	1.857	-5.72
1.788	1.804	1.360	1.220	1.248	0.972	2.817	2.839	2.415	2.393	2.187	2.194	2.203	2.209	2.173	2.122	2.149	2.169	2.213	1.990	1.915	-5.08
1.788	1.804	1.360	1.220	1.248	0.972	2.817	2.839	2.415	2.393	2.187	2.194	2.203	2.209	2.173	2.122	2.149	2.169	2.213	1.990	1.915	-4.45
1.863	1.863	1.374	1.251	1.263	1.003	2.892	2.903	2.456	2.459	2.253	2.262	2.240	2.266	2.207	2.163	2.205	2.239	2.263	2.045	1.958	-3.81
1.904	1.905	1.415	1.284	1.299	1.010	2.963	2.992	2.536	2.520	2.288	2.292	2.302	2.309	2.258	2.222	2.272	2.281	2.302	2.077	2.006	-3.18
1.933	1.948	1.433	1.318	1.312	1.028	2.880	3.028	2.525	2.587	2.347	2.329	2.316	2.355	2.305	2.233	2.289	2.340	2.338	2.098	2.048	-2.54
1.933	1.948	1.433	1.318	1.312	1.028	2.880	3.028	2.525	2.587	2.347	2.329	2.316	2.355	2.305	2.233	2.289	2.340	2.338	2.098	2.048	-1.91
1.947	1.983	1.460	1.307	1.328	0.986	3.107	3.067	2.615	2.625	2.367	2.352	2.328	2.365	2.355	2.245	2.328	2.329	2.346	2.093	2.054	-1.27
2.004	2.015	1.467	1.335	1.328	0.950	3.100	3.150	2.667	2.662	2.430	2.429	2.408	2.433	2.397	2.306	2.401	2.399	2.404	2.157	2.103	-0.64
-9.7	-10.0	-9.6	-9.4	-9.5	-9.5	-10.2	-10.3	-10.4	-10.4	-10.4	-10.5	-10.7	-10.6	-10.4	-10.3	-10.4	-10.6	-10.7	-10.8	-10.4	x_o (cm)
1.199	1.214	0.813	0.731	0.713	0.584	2.013	2.017	1.633	1.634	1.501	1.507	1.511	1.492	1.468	1.443	1.468	1.523	1.501	1.312	1.322	Δp_{-} (bar)
1.96	1.98	1.94	1.91	1.93	1.88	2.03	2.09	1.91	2.11	2.09	2.19	2.30	2.28	1.96	2.08	1.98	2.41	2.23	2.35	2.15	L (cm)

Case 2 (continued)

x_o = -9.9 cm

Pressure (bar)																			X (cm) =
8.111	7.622	7.619	7.616	7.572	7.572	6.863	6.860	6.854	6.762	6.752	6.750	5.548	5.543	5.541	5.538	4.896	4.896	4.312	4.254	Plenum
1.391	1.282	1.290	1.291	1.318	1.337	1.186	1.186	1.197	1.176	1.203	1.203	0.994	0.984	0.978	0.980	0.869	0.860	0.759	0.756	-13.34
1.276	1.208	1.201	1.206	1.216	1.215	1.095	1.085	1.078	1.084	1.083	1.085	0.949	0.960	0.948	0.960	0.953	0.960	0.848	0.834	-12.70
1.382	1.327	1.319	1.309	1.277	1.289	1.176	1.168	1.175	1.166	1.143	1.140	0.926	0.925	0.917	0.921	0.793	0.804	0.697	0.685	-12.07
1.366	1.320	1.300	1.312	1.273	1.303	1.167	1.167	1.181	1.153	1.150	1.141	0.935	0.919	0.936	0.929	0.811	0.809	0.826	0.819	-11.43
1.366	1.320	1.300	1.312	1.273	1.303	1.167	1.167	1.161	1.153	1.150	1.141	0.935	0.919	0.936	0.929	0.811	0.809	0.826	0.819	-10.80
1.258	1.158	1.162	1.179	1.165	1.177	1.070	1.051	1.068	1.075	1.078	1.082	0.899	0.891	0.902	0.937	0.823	0.826	0.740	0.721	-10.16
1.886	1.468	1.520	1.517	1.366	1.429	1.508	1.335	1.491	1.440	1.533	1.542	1.191	1.121	1.213	1.275	1.134	1.179	1.032	0.997	-9.53
1.886	1.468	1.520	1.517	1.366	1.429	1.508	1.335	1.491	1.440	1.533	1.542	1.191	1.121	1.213	1.275	1.134	1.179	1.032	0.997	-8.89
2.410	2.069	2.134	2.083	1.757	1.975	1.996	1.810	1.966	1.928	1.951	1.979	1.530	1.422	1.594	1.678	1.441	1.469	1.326	1.321	-8.26
2.758	2.533	2.572	2.490	2.203	2.407	2.368	2.208	2.277	2.254	2.222	2.237	1.850	1.791	1.893	1.891	1.663	1.668	1.517	1.480	-7.62
2.923	2.687	2.684	2.679	2.517	2.610	2.435	2.357	2.390	2.344	2.377	2.398	1.953	1.946	2.006	2.044	1.773	1.781	1.597	1.598	-6.99
3.131	2.939	2.932	2.904	2.737	2.870	2.648	2.641	2.661	2.600	2.633	2.651	2.166	2.157	2.207	2.205	1.959	1.966	1.771	1.724	-6.35
3.196	3.005	2.990	2.971	2.917	2.903	2.772	2.694	2.752	2.722	2.696	2.719	2.254	2.208	2.260	2.293	2.031	2.036	1.828	1.792	-5.72
3.284	3.068	3.063	3.041	2.926	3.013	2.825	2.788	2.842	2.778	2.769	2.795	2.315	2.288	2.318	2.359	2.095	2.099	1.887	1.843	-5.08
3.284	3.068	3.063	3.041	2.926	3.013	2.825	2.788	2.842	2.778	2.769	2.795	2.315	2.288	2.318	2.359	2.095	2.099	1.887	1.843	-4.45
3.412	3.128	3.099	3.140	3.078	3.084	2.904	2.867	2.937	2.838	2.782	2.806	2.428	2.364	2.392	2.457	2.131	2.167	1.918	1.892	-3.81
3.475	3.235	3.246	3.221	3.153	3.178	2.973	2.951	2.992	2.945	2.913	2.932	2.471	2.424	2.454	2.503	2.195	2.216	1.975	1.945	-3.18
3.616	3.278	3.318	3.298	3.113	3.193	3.089	2.965	3.033	2.892	2.982	2.997	2.496	2.503	2.535	2.533	2.231	2.287	1.974	1.983	-2.54
3.616	3.278	3.318	3.298	3.113	3.193	3.089	2.965	3.033	2.892	2.982	2.997	2.496	2.503	2.535	2.533	2.231	2.287	1.974	1.983	-1.91
3.527	3.392	3.330	3.191	3.189	3.309	3.066	3.067	3.201	3.012	2.908	2.973	2.523	2.445	2.593	2.604	2.232	2.270	2.001	2.003	-1.27
3.692	3.392	3.394	3.361	3.299	3.352	3.145	3.127	3.154	3.068	3.080	3.081	2.592	2.574	2.629	2.631	2.322	2.363	2.048	2.044	-0.64
-10.2	-9.8	-9.9	-9.9	-9.7	-9.8	-10.1	-9.9	-10.1	-10.0	-10.2	-10.3	-10.0	-9.9	-10.0	-10.1	-10.1	-10.2	-9.5	-9.5	x_o (cm)
2.241	2.065	2.026	2.043	2.104	1.996	1.916	1.945	2.003	1.913	1.891	1.975	1.631	1.607	1.569	1.586	1.390	1.420	0.951	0.945	Δp_c (bar)
1.85	1.61	1.55	1.75	2.31	1.75	1.85	2.02	2.19	2.09	2.17	2.11	2.24	2.22	1.95	2.01	1.99	2.00	1.87	1.86	L (cm)

Case 2 (continued)

x_o = -7.4 cm			x_o = -8.8 cm																	X (cm) =
4.248	2.921	2.449	8.096	7.565	6.866	6.752	6.737	5.538	5.538	5.535	4.917	4.917	4.917	4.902	4.893	4.887	4.257	4.254	2.921	2.921	Plenum
0.755	0.556	0.516	1.384	1.300	1.191	1.182	1.204	0.992	0.979	0.975	0.868	0.863	0.867	0.865	0.861	0.866	0.750	0.758	0.559	0.555	-13.34
0.835	0.592	0.492	1.275	1.209	1.108	1.085	1.079	0.960	0.963	0.961	0.958	0.943	0.951	0.966	0.960	0.952	0.842	0.848	0.597	0.596	-12.70
0.681	0.574	0.557	1.382	1.293	1.179	1.160	1.152	0.908	0.930	0.917	0.798	0.793	0.800	0.804	0.806	0.788	0.682	0.683	0.573	0.571	-12.07
0.806	0.560	0.465	1.383	1.280	1.154	1.162	1.169	0.907	0.949	0.920	0.820	0.826	0.841	0.818	0.826	0.801	0.818	0.816	0.560	0.562	-11.43
0.806	0.560	0.465	1.383	1.280	1.154	1.162	1.169	0.907	0.949	0.920	0.820	0.826	0.841	0.818	0.826	0.801	0.818	0.816	0.560	0.562	-10.80
0.673	0.592	0.492	1.234	1.169	1.057	1.060	1.051	0.892	0.883	0.884	0.799	0.786	0.792	0.796	0.784	0.792	0.685	0.688	0.605	0.608	-10.16
0.871	0.589	0.435	1.405	1.387	1.215	1.233	1.227	1.072	1.049	1.059	1.038	1.014	1.044	1.011	1.021	1.010	0.891	0.885	0.585	0.584	-9.53
0.871	0.589	0.435	1.405	1.387	1.215	1.233	1.227	1.072	1.049	1.059	1.038	1.014	1.044	1.011	1.021	1.010	0.891	0.885	0.585	0.584	-8.89
0.770	0.648	0.569	1.585	1.726	1.371	1.431	1.406	1.183	1.150	1.149	1.036	1.011	1.043	0.954	0.947	0.951	0.788	0.792	0.664	0.682	-8.26
0.940	0.600	0.500	2.019	2.183	1.618	1.608	1.633	1.535	1.332	1.368	1.364	1.361	1.386	1.215	1.232	1.226	1.040	1.088	0.669	0.746	-7.62
0.871	0.692	0.598	2.567	2.545	2.085	2.075	2.052	1.884	1.695	1.677	1.609	1.637	1.647	1.497	1.479	1.475	1.271	1.321	0.899	0.967	-6.99
1.307	0.847	0.793	2.786	2.755	2.348	2.333	2.370	2.061	1.948	2.002	1.821	1.843	1.843	1.766	1.762	1.738	1.528	1.560	1.092	1.117	-6.35
1.446	1.017	0.886	3.023	2.866	2.607	2.492	2.521	2.147	2.098	2.085	1.941	1.894	1.924	1.854	1.864	1.857	1.615	1.640	1.154	1.168	-5.72
1.542	1.096	0.944	3.067	2.913	2.619	2.574	2.576	2.202	2.136	2.157	1.971	1.979	1.975	1.926	1.914	1.897	1.650	1.693	1.190	1.212	-5.08
1.542	1.096	0.944	3.067	2.913	2.619	2.574	2.576	2.202	2.136	2.157	1.971	1.979	1.975	1.926	1.914	1.897	1.650	1.693	1.190	1.212	-4.45
1.606	1.164	0.989	3.117	3.049	2.740	2.654	2.711	2.254	2.233	2.258	2.049	2.064	2.052	1.968	2.011	1.985	1.715	1.747	1.199	1.256	-3.81
1.715	1.197	1.008	3.253	3.150	2.808	2.746	2.753	2.351	2.328	2.321	2.121	2.107	2.118	2.061	2.060	2.048	1.787	1.789	1.253	1.276	-3.18
1.753	1.240	1.018	3.366	3.177	2.816	2.828	2.842	2.326	2.404	2.462	2.129	2.131	2.227	2.121	2.161	2.022	1.778	1.877	1.272	1.291	-2.54
1.753	1.240	1.018	3.366	3.177	2.816	2.828	2.842	2.326	2.404	2.462	2.129	2.131	2.227	2.121	2.161	2.022	1.778	1.877	1.272	1.291	-1.91
1.761	1.174	0.983	3.362	3.188	3.028	2.776	2.833	2.500	2.404	2.467	2.127	2.180	2.164	2.109	2.056	2.114	1.922	1.848	1.295	1.261	-1.27
1.785	1.229	0.950	3.482	3.292	2.953	2.905	2.882	2.486	2.481	2.437	2.239	2.191	2.220	2.187	2.188	2.149	1.904	1.868	1.297	1.312	-0.64
-7.6	-7.0	-7.2	-9.1	-9.4	-8.6	-8.6	-8.6	-9.1	-8.6	-8.7	-8.9	-8.9	-8.9	-8.8	-8.9	-8.9	-8.8	-8.9	-8.3	-8.5	x_o (cm)
0.953	0.585	0.445	1.900	1.821	1.502	1.369	1.406	1.310	1.214	1.226	1.135	1.148	1.102	1.152	1.197	1.200	1.060	1.030	0.594	0.617	Δp_- (bar)
2.08	1.68	1.37	1.79	2.09	1.76	1.83	1.78	1.84	1.91	1.97	2.00	1.99	1.86	1.96	2.16	2.26	2.05	1.78	1.43	1.65	L (cm)

Pressure (bar)

Case 2 (continued)

x_o = -5.9 cm			x_o = -7.4 cm																X (cm) =
2.927	2.807	2.529	8.105	7.671	7.631	7.628	7.557	7.554	6.872	6.866	6.695	5.564	5.523	5.523	5.520	5.514	4.884	4.872	4.251	4.251	Plenum
0.556	0.551	0.526	1.398	1.351	1.302	1.307	1.323	1.325	1.202	1.201	1.191	0.983	0.983	0.990	0.985	0.981	0.870	0.869	0.748	0.743	-13.34
0.592	0.565	0.513	1.285	1.217	1.201	1.204	1.199	1.201	1.091	1.095	1.071	0.948	0.948	0.955	0.969	0.958	0.949	0.956	0.849	0.838	-12.70
0.575	0.574	0.568	1.382	1.315	1.315	1.316	1.277	1.287	1.171	1.177	1.120	0.940	0.924	0.917	0.933	0.925	0.784	0.788	0.678	0.683	-12.07
0.560	0.534	0.500	1.404	1.324	1.288	1.335	1.280	1.289	1.169	1.171	1.126	0.966	0.934	0.934	0.920	0.914	0.814	0.822	0.813	0.826	-11.43
0.560	0.534	0.500	1.404	1.324	1.288	1.335	1.280	1.289	1.169	1.171	1.126	0.966	0.934	0.934	0.920	0.914	0.814	0.822	0.813	0.826	-10.80
0.592	0.565	0.508	1.229	1.171	1.165	1.160	1.163	1.150	1.050	1.063	1.052	0.862	0.877	0.870	0.870	0.872	0.778	0.778	0.680	0.674	-10.16
0.591	0.561	0.453	1.392	1.329	1.300	1.303	1.329	1.323	1.212	1.202	1.191	0.989	1.000	1.003	0.989	0.992	0.984	0.978	0.882	0.869	-9.53
0.591	0.561	0.453	1.392	1.329	1.300	1.303	1.329	1.323	1.212	1.202	1.191	0.989	1.000	1.003	0.989	0.992	0.984	0.978	0.882	0.869	-8.89
0.652	0.629	0.580	1.434	1.365	1.353	1.350	1.375	1.362	1.294	1.288	1.309	1.121	1.111	1.102	1.110	1.101	0.911	0.912	0.780	0.771	-8.26
0.600	0.572	0.509	1.710	1.617	1.644	1.630	1.577	1.593	1.449	1.431	1.371	1.118	1.097	1.101	1.107	1.102	1.039	1.054	0.908	0.923	-7.62
0.648	0.631	0.575	1.610	1.487	1.546	1.533	1.450	1.473	1.375	1.343	1.296	1.212	1.146	1.186	1.130	1.144	1.003	1.016	0.865	0.839	-6.99
0.683	0.667	0.600	2.422	2.071	2.449	2.408	2.155	2.114	2.215	2.001	1.899	1.837	1.714	1.762	1.747	1.688	1.490	1.580	1.321	1.225	-6.35
0.671	0.698	0.609	2.719	2.507	2.590	2.620	2.495	2.514	2.369	2.312	2.243	1.930	1.887	1.873	1.888	1.901	1.685	1.700	1.487	1.422	-5.72
0.798	0.893	0.808	2.812	2.631	2.731	2.719	2.606	2.559	2.444	2.366	2.327	2.052	1.965	2.018	1.990	1.964	1.749	1.784	1.579	1.530	-5.08
0.798	0.893	0.808	2.812	2.631	2.731	2.719	2.606	2.559	2.444	2.366	2.327	2.052	1.965	2.018	1.990	1.964	1.749	1.784	1.579	1.530	-4.45
1.007	0.997	0.944	2.989	2.709	2.835	2.920	2.738	2.836	2.594	2.604	2.441	2.131	2.163	2.132	2.079	2.101	1.895	1.871	1.665	1.645	-3.81
1.133	1.096	0.989	3.107	2.815	2.947	2.992	2.864	2.887	2.658	2.658	2.539	2.215	2.180	2.201	2.170	2.189	1.943	1.938	1.723	1.680	-3.18
1.147	1.125	1.008	3.218	2.952	2.971	3.037	2.877	2.866	2.763	2.743	2.606	2.310	2.298	2.246	2.212	2.167	1.995	2.020	1.754	1.730	-2.54
1.147	1.125	1.008	3.218	2.952	2.971	3.037	2.877	2.866	2.763	2.743	2.606	2.310	2.298	2.246	2.212	2.167	1.995	2.020	1.754	1.730	-1.91
1.172	1.105	0.997	3.303	3.005	3.065	3.156	2.968	2.949	2.802	2.658	2.669	2.374	2.223	2.272	2.245	2.261	2.031	2.054	1.769	1.795	-1.27
1.151	1.105	0.966	3.231	2.962	3.082	3.099	3.003	3.016	2.739	2.780	2.622	2.321	2.320	2.329	2.258	2.275	2.058	2.067	1.787	1.749	-0.64
-5.3	-5.8	-5.5	-7.3	-7.2	-7.6	-7.4	-7.4	-7.3	-7.4	-7.4	-7.3	-7.5	-7.4	-7.6	-7.3	-7.3	-7.4	-7.5	-7.4	-7.3	x_o (cm)
0.490	0.486	0.393	1.517	1.472	1.441	1.505	1.523	1.651	1.265	1.414	1.333	1.028	1.125	1.115	1.042	1.100	1.027	0.954	0.924	0.944	Δp_- (bar)
0.78	1.15	0.57	1.24	1.42	1.41	1.35	1.54	1.86	1.05	1.57	1.45	1.40	1.60	1.80	1.20	1.48	1.63	1.37	1.51	1.70	L (cm)

Pressure (bar)

Case 3				Case 2 (continued)																X (cm) =
x_o = -12.7 cm				x_o = -5.9 cm																
4.768	3.682	3.663	3.663	8.117	8.111	8.108	8.105	7.641	7.634	7.631	7.539	6.680	6.671	6.668	6.661	5.573	4.872	4.860	3.305	3.281	Plenum
1.319	1.007	1.006	1.020	1.419	1.425	1.436	1.419	1.319	1.304	1.320	1.331	1.197	1.208	1.190	1.183	0.981	0.861	0.854	0.584	0.590	-13.34
1.345	1.026	1.065	1.174	1.301	1.288	1.295	1.279	1.207	1.206	1.201	1.209	1.072	1.075	1.082	1.072	0.953	0.947	0.957	0.657	0.657	-12.70
1.985	1.454	1.483	1.636	1.370	1.387	1.384	1.389	1.315	1.300	1.310	1.291	1.128	1.130	1.138	1.135	0.935	0.781	0.787	0.524	0.521	-12.07
2.304	1.733	1.733	1.829	1.408	1.390	1.389	1.395	1.320	1.302	1.331	1.283	1.143	1.124	1.132	1.139	0.946	0.817	0.806	0.640	0.640	-11.43
2.304	1.733	1.733	1.829	1.408	1.390	1.389	1.395	1.320	1.302	1.331	1.283	1.143	1.124	1.132	1.139	0.946	0.817	0.806	0.640	0.640	-10.80
2.578	1.951	1.964	2.010	1.239	1.234	1.240	1.238	1.163	1.151	1.155	1.158	1.051	1.055	1.056	1.049	0.859	0.776	0.782	0.634	0.629	-10.16
2.640	2.032	2.021	2.063	1.394	1.390	1.391	1.395	1.321	1.311	1.304	1.324	1.188	1.194	1.190	1.189	0.978	0.971	0.969	0.646	0.638	-9.53
2.640	2.032	2.021	2.063	1.394	1.390	1.391	1.395	1.321	1.311	1.304	1.324	1.188	1.194	1.190	1.189	0.978	0.971	0.969	0.646	0.638	-8.89
2.690	2.056	2.067	2.098	1.441	1.436	1.437	1.441	1.360	1.342	1.341	1.366	1.292	1.292	1.303	1.292	1.120	0.907	0.903	0.704	0.701	-8.26
2.728	2.091	2.087	2.119	1.689	1.712	1.710	1.697	1.607	1.626	1.603	1.569	1.363	1.356	1.362	1.354	1.106	1.021	1.016	0.702	0.696	-7.62
2.744	2.111	2.122	2.138	1.546	1.535	1.542	1.533	1.453	1.459	1.462	1.411	1.240	1.236	1.247	1.229	1.093	0.942	0.940	0.700	0.705	-6.99
2.786	2.134	2.134	2.155	1.690	1.699	1.686	1.729	1.528	1.541	1.552	1.608	1.370	1.376	1.373	1.352	1.180	1.070	1.026	0.775	0.753	-6.35
2.789	2.138	2.133	2.150	1.985	1.981	1.993	2.056	1.767	1.833	1.804	1.959	1.732	1.710	1.660	1.636	1.382	1.351	1.294	0.835	0.774	-5.72
2.789	2.139	2.134	2.148	2.514	2.496	2.518	2.587	2.155	2.268	2.223	2.417	2.103	2.116	2.064	2.057	1.668	1.566	1.518	1.004	0.961	-5.08
2.789	2.139	2.134	2.148	2.514	2.496	2.518	2.587	2.155	2.268	2.223	2.417	2.103	2.116	2.064	2.057	1.668	1.566	1.518	1.004	0.961	-4.45
2.766	2.128	2.128	2.141	2.949	2.771	2.872	2.823	2.532	2.668	2.549	2.630	2.310	2.403	2.336	2.282	1.945	1.696	1.715	1.147	1.131	-3.81
2.702	2.070	2.071	2.080	2.957	2.966	2.971	2.969	2.808	2.825	2.789	2.781	2.505	2.488	2.474	2.476	2.088	1.848	1.833	1.255	1.263	-3.18
2.706	2.067	2.061	2.062	3.061	3.081	3.065	2.978	2.850	2.889	2.857	2.823	2.504	2.551	2.511	2.538	2.137	1.957	1.912	1.302	1.297	-2.54
2.706	2.067	2.061	2.062	3.061	3.081	3.065	2.978	2.850	2.889	2.857	2.823	2.504	2.551	2.511	2.538	2.137	1.957	1.912	1.302	1.297	-1.91
2.640	2.027	2.008	2.045	3.127	3.081	3.061	3.163	2.922	2.932	2.925	3.025	2.565	2.672	2.488	2.532	2.127	1.941	1.858	1.311	1.316	-1.27
2.701	2.071	2.058	2.078	3.028	3.003	2.987	2.998	2.836	2.915	2.868	2.836	2.529	2.555	2.535	2.546	2.172	1.975	1.937	1.302	1.319	-0.64
-12.8	-12.7	-12.8	-12.9	-5.9	-6.0	-5.9	-5.9	-5.9	-6.0	-6.0	-6.0	-6.1	-6.0	-6.0	-6.0	-6.0	-6.4	-6.2	-5.9	-5.7	x_o (cm)
1.456	1.101	1.130	1.120	1.380	1.412	1.380	1.264	1.485	1.416	1.410	1.230	1.199	1.183	1.174	1.230	1.031	1.032	0.955	0.594	0.621	Δp_o (bar)
1.25	1.24	1.33	1.15	0.79	1.08	0.89	0.76	1.41	1.10	1.33	0.88	1.03	0.90	0.95	1.09	1.27	2.02	1.45	1.57	1.47	L (cm)

Pressure (bar)

Case 3 (continued)

x_o = -12.7 cm

																				X (cm) =
7.557	7.530	6.716	6.722	6.716	6.710	6.722	5.676	5.676	5.658	5.655	5.655	5.655	4.759	4.756	4.762	4.765	3.666	5.655	4.771	4.768	Plenum
1.970	1.968	1.796	1.806	1.821	1.832	1.804	1.532	1.552	1.545	1.553	1.544	1.547	1.320	1.320	1.306	1.326	1.012	1.552	1.310	1.333	-13.34
2.076	2.122	1.820	1.816	1.815	1.805	1.815	1.580	1.602	1.564	1.572	1.565	1.575	1.377	1.394	1.393	1.403	1.029	1.568	1.401	1.408	-12.70
2.999	3.127	1.956	1.974	1.951	2.016	1.995	2.291	2.404	2.223	2.328	2.275	2.315	2.072	2.065	2.042	2.088	1.478	2.267	2.029	2.117	-12.07
3.582	3.661	2.816	2.776	2.748	2.817	2.878	2.745	2.782	2.703	2.756	2.734	2.744	2.358	2.363	2.326	2.365	1.745	2.734	2.348	2.393	-11.43
3.582	3.661	2.816	2.776	2.748	2.817	2.878	2.745	2.782	2.703	2.756	2.734	2.744	2.358	2.363	2.326	2.365	1.745	2.734	2.348	2.393	-10.80
4.051	4.067	3.411	3.421	3.421	3.438	3.420	3.067	3.069	3.035	3.076	3.057	3.062	2.593	2.600	2.590	2.603	1.960	3.060	2.589	2.612	-10.16
4.178	4.140	3.571	3.560	3.587	3.552	3.547	3.145	3.141	3.120	3.155	3.124	3.137	2.655	2.657	2.645	2.660	2.012	3.130	2.667	2.669	-9.53
4.178	4.140	3.571	3.560	3.587	3.552	3.547	3.145	3.141	3.120	3.155	3.124	3.137	2.655	2.657	2.645	2.660	2.012	3.130	2.667	2.669	-8.89
4.243	4.225	3.652	3.639	3.644	3.674	3.646	3.209	3.198	3.174	3.204	3.180	3.198	2.706	2.716	2.700	2.711	2.060	3.195	2.706	2.717	-8.26
4.279	4.292	3.731	3.713	3.728	3.742	3.711	3.255	3.247	3.232	3.252	3.242	3.251	2.744	2.754	2.748	2.757	2.083	3.251	2.744	2.755	-7.62
4.339	4.322	3.734	3.755	3.736	3.774	3.745	3.285	3.286	3.260	3.268	3.264	3.263	2.755	2.763	2.784	2.783	2.116	3.256	2.770	2.763	-6.99
4.368	4.363	3.856	3.852	3.844	3.831	3.844	3.323	3.310	3.285	3.301	3.285	3.299	2.796	2.796	2.784	2.797	2.138	3.305	2.783	2.795	-6.35
4.384	4.378	3.854	3.860	3.860	3.856	3.838	3.309	3.303	3.289	3.304	3.291	3.303	2.800	2.801	2.785	2.797	2.139	3.310	2.791	2.798	-5.72
4.373	4.367	3.854	3.860	3.851	3.863	3.845	3.319	3.290	3.291	3.297	3.293	3.301	2.787	2.794	2.782	2.793	2.130	3.301	2.788	2.785	-5.08
4.373	4.367	3.854	3.860	3.851	3.863	3.845	3.319	3.290	3.291	3.297	3.293	3.301	2.787	2.794	2.782	2.793	2.130	3.301	2.788	2.785	-4.45
4.332	4.334	3.876	3.863	3.821	3.851	3.833	3.293	3.261	3.267	3.279	3.265	3.284	2.766	2.771	2.777	2.790	2.114	3.288	2.758	2.783	-3.81
4.239	4.228	3.729	3.752	3.735	3.752	3.744	3.205	3.212	3.192	3.214	3.192	3.211	2.699	2.706	2.697	2.706	2.067	3.217	2.701	2.709	-3.18
4.211	4.183	3.771	3.764	3.720	3.716	3.737	3.167	3.154	3.164	3.237	3.200	3.209	2.692	2.713	2.691	2.686	2.073	3.220	2.656	2.680	-2.54
4.211	4.183	3.771	3.764	3.720	3.716	3.737	3.167	3.154	3.164	3.237	3.200	3.209	2.692	2.713	2.691	2.686	2.073	3.220	2.656	2.680	-1.91
4.077	4.124	3.698	3.722	3.662	3.694	3.668	3.178	3.119	3.119	3.123	3.129	3.087	2.657	2.640	2.629	2.664	2.014	3.102	2.600	2.642	-1.27
4.214	4.189	3.711	3.778	3.740	3.732	3.704	3.204	3.181	3.183	3.220	3.191	3.206	2.700	2.702	2.680	2.705	2.062	3.213	2.690	2.698	-0.64
-12.8	-12.8	-12.2	-12.2	-12.1	-12.2	-12.2	-12.8	-12.8	-12.6	-12.7	-12.7	-12.7	-12.8	-12.8	-12.8	-12.8	-12.7	-12.7	-12.8	-12.8	x_o (cm)
2.422	2.372	1.992	2.004	1.995	2.003	1.980	1.791	1.736	1.694	1.702	1.699	1.724	1.443	1.450	1.466	1.443	1.103	1.704	1.465	1.428	Δp_- (bar)
1.30	1.14	1.14	1.20	1.15	1.14	1.13	1.29	1.16	1.11	1.09	1.11	1.13	1.08	1.10	1.15	1.08	1.23	1.10	1.16	1.00	L (cm)

Pressure (bar)

Case 3 (continued)

x_o = -12.0 cm												x_o = -12.7 cm									X (cm) =
6.701	6.716	5.670	5.661	5.658	4.748	4.252	3.657	3.657	3.003	2.994	1.816	9.017	9.026	9.023	9.026	8.234	8.237	8.231	7.533	7.536	Plenum
1.798	1.812	1.540	1.543	1.530	1.279	1.118	0.984	0.988	0.815	0.809	0.493	2.283	2.299	2.288	2.290	2.103	2.116	2.111	1.961	1.974	-13.34
1.852	1.844	1.574	1.577	1.593	1.316	1.154	1.025	1.043	0.851	0.848	0.509	2.547	2.488	2.448	2.462	2.316	2.355	2.296	2.042	2.060	-12.70
1.935	1.946	1.706	1.648	1.674	1.338	1.169	1.052	1.095	0.927	0.933	0.641	3.837	3.756	3.669	3.653	3.349	3.577	3.325	2.937	3.012	-12.07
2.269	2.239	2.304	1.880	1.918	1.625	1.398	1.234	1.394	1.212	1.234	0.781	4.402	4.373	4.323	4.299	3.944	4.063	3.919	3.602	3.627	-11.43
2.269	2.239	2.304	1.880	1.918	1.625	1.398	1.234	1.394	1.212	1.234	0.781	4.402	4.373	4.323	4.299	3.944	4.063	3.919	3.602	3.627	-10.80
3.119	3.137	2.846	2.644	2.669	2.197	1.871	1.660	1.767	1.471	1.482	0.917	4.871	4.850	4.857	4.808	4.407	4.449	4.357	4.018	4.041	-10.16
3.294	3.300	2.923	2.765	2.801	2.311	1.984	1.757	1.832	1.519	1.526	0.945	5.023	4.992	4.980	4.952	4.514	4.569	4.506	4.107	4.138	-9.53
3.294	3.300	2.923	2.765	2.801	2.311	1.984	1.757	1.832	1.519	1.526	0.945	5.023	4.992	4.980	4.952	4.514	4.569	4.506	4.107	4.138	-8.89
3.392	3.399	3.005	2.846	2.905	2.390	2.065	1.824	1.876	1.570	1.573	0.965	5.088	5.053	5.070	5.049	4.605	4.632	4.573	4.218	4.216	-8.26
3.481	3.468	3.074	2.920	2.970	2.446	2.133	1.870	1.923	1.594	1.601	0.981	5.186	5.134	5.155	5.123	4.685	4.724	4.661	4.260	4.278	-7.62
3.534	3.541	3.123	3.012	3.026	2.512	2.169	1.912	1.976	1.624	1.621	1.003	5.198	5.168	5.197	5.139	4.721	4.745	4.678	4.341	4.301	-6.99
3.653	3.648	3.171	3.090	3.107	2.589	2.242	1.980	2.014	1.663	1.667	1.014	5.243	5.228	5.241	5.204	4.773	4.793	4.741	4.365	4.354	-6.35
3.686	3.674	3.177	3.106	3.127	2.610	2.267	1.999	2.016	1.666	1.668	1.016	5.226	5.226	5.237	5.197	4.767	4.787	4.741	4.373	4.354	-5.72
3.659	3.699	3.189	3.064	3.106	2.608	2.272	2.019	2.030	1.662	1.667	1.021	5.220	5.209	5.225	5.198	4.766	4.785	4.747	4.358	4.364	-5.08
3.659	3.699	3.189	3.064	3.106	2.608	2.272	2.019	2.030	1.662	1.667	1.021	5.220	5.209	5.225	5.198	4.766	4.785	4.747	4.358	4.364	-4.45
3.669	3.686	3.166	3.095	3.105	2.609	2.262	1.989	2.027	1.653	1.666	1.015	5.204	5.154	5.196	5.144	4.746	4.707	4.710	4.313	4.293	-3.81
3.559	3.632	3.119	3.026	3.070	2.583	2.233	1.967	1.970	1.612	1.612	0.974	5.047	5.046	5.050	5.032	4.603	4.633	4.597	4.229	4.199	-3.18
3.581	3.529	3.060	3.022	3.017	2.499	2.191	1.916	1.935	1.583	1.577	0.934	5.074	5.013	5.015	5.010	4.640	4.556	4.600	4.176	4.203	-2.54
3.581	3.529	3.060	3.022	3.017	2.499	2.191	1.916	1.935	1.583	1.577	0.934	5.074	5.013	5.015	5.010	4.640	4.556	4.600	4.176	4.203	-1.91
3.630	3.568	3.123	3.052	3.065	2.554	2.235	1.969	1.972	1.611	1.616	0.900	4.949	4.872	4.918	4.977	4.540	4.489	4.499	4.089	4.090	-1.27
5.766	5.949	5.067	5.046	4.984	4.321	3.774	3.370	3.460	2.941	2.927	1.815	5.018	5.010	4.997	4.988	4.559	4.562	4.567	4.186	4.174	-0.64
-11.8	-11.7	-12.2	-11.7	-11.7	-11.9	-11.8	-11.8	-12.1	-12.2	-12.2	-12.1	-12.8	-12.8	-12.8	-12.8	-12.8	-12.8	-12.8	-12.8	-12.8	x_o (cm)
1.736	1.724	1.589	1.466	1.447	1.283	1.116	0.951	0.934	0.817	0.814	0.374	2.916	2.887	2.937	2.898	2.639	2.601	2.601	2.408	2.387	Δp_{-} (bar)
1.46	1.43	1.26	1.51	1.38	1.65	1.75	1.68	1.55	1.46	1.37	1.47	1.05	1.12	1.20	1.21	1.21	0.98	1.22	1.30	1.28	L (cm)

Pressure (bar)

Case 3 (continued)

Pressure (bar)

x_o = -10.2 cm									x_o = -12.0 cm											X (cm) =
4.774	4.780	4.735	3.648	3.642	3.639	2.973	2.969	2.960	9.029	9.039	9.020	9.023	9.017	8.234	8.222	8.139	7.613	7.549	7.509	6.719	Plenum
1.319	1.323	1.317	1.005	1.012	1.005	0.824	0.828	0.823	2.397	2.404	2.401	2.408	2.402	2.186	2.178	2.171	2.038	2.026	2.008	1.798	-13.34
1.298	1.288	1.276	0.980	0.980	0.984	0.806	0.803	0.800	2.324	2.313	2.340	2.334	2.315	2.130	2.152	2.112	2.011	2.023	2.007	1.788	-12.70
1.331	1.328	1.309	1.024	1.021	1.016	0.826	0.827	0.817	2.454	2.358	2.358	2.343	2.364	2.294	2.359	2.314	2.308	2.291	2.177	1.925	-12.07
1.334	1.329	1.309	1.027	1.026	1.022	0.851	0.841	0.831	3.529	3.067	3.076	2.970	3.003	3.211	3.328	3.269	3.045	3.105	2.629	2.377	-11.43
1.334	1.329	1.309	1.027	1.026	1.022	0.851	0.841	0.831	3.529	3.067	3.076	2.970	3.003	3.211	3.328	3.269	3.045	3.105	2.629	2.377	-10.80
1.544	1.512	1.512	1.213	1.247	1.198	1.035	0.988	0.987	4.360	4.194	4.191	4.085	4.234	4.048	4.062	4.033	3.780	3.806	3.569	3.187	-10.16
1.926	1.883	1.818	1.441	1.523	1.443	1.240	1.237	1.177	4.496	4.384	4.363	4.279	4.340	4.174	4.152	4.130	3.925	3.915	3.726	3.339	-9.53
1.926	1.883	1.818	1.441	1.523	1.443	1.240	1.237	1.177	4.496	4.384	4.363	4.279	4.340	4.174	4.152	4.130	3.925	3.915	3.726	3.339	-8.89
2.163	2.130	2.067	1.591	1.665	1.591	1.356	1.333	1.302	4.645	4.515	4.467	4.374	4.477	4.292	4.282	4.255	4.013	4.020	3.804	3.434	-8.26
2.265	2.270	2.221	1.701	1.738	1.689	1.430	1.406	1.382	4.736	4.635	4.581	4.478	4.575	4.367	4.365	4.310	4.091	4.071	3.890	3.517	-7.62
2.355	2.376	2.332	1.777	1.801	1.774	1.481	1.467	1.447	4.841	4.728	4.692	4.600	4.689	4.460	4.448	4.396	4.157	4.152	4.008	3.620	-6.99
2.495	2.482	2.444	1.868	1.886	1.878	1.546	1.538	1.520	4.929	4.847	4.820	4.777	4.825	4.555	4.526	4.493	4.229	4.228	4.109	3.693	-6.35
2.536	2.532	2.497	1.912	1.921	1.918	1.578	1.567	1.552	4.948	4.877	4.864	4.846	4.862	4.584	4.532	4.503	4.246	4.225	4.122	3.713	-5.72
2.545	2.562	2.531	1.932	1.946	1.934	1.598	1.578	1.568	4.955	4.898	4.877	4.824	4.903	4.559	4.499	4.557	4.257	4.249	4.099	3.705	-5.08
2.545	2.562	2.531	1.932	1.946	1.934	1.598	1.578	1.568	4.955	4.898	4.877	4.824	4.903	4.559	4.499	4.557	4.257	4.249	4.099	3.705	-4.45
2.581	2.564	2.498	1.939	1.962	1.915	1.609	1.599	1.567	4.945	4.855	4.859	4.815	4.860	4.535	4.537	4.460	4.181	4.160	4.086	3.700	-3.81
2.524	2.538	2.492	1.916	1.914	1.906	1.579	1.565	1.548	4.820	4.753	4.738	4.688	4.697	4.538	4.463	4.418	4.183	4.165	3.970	3.651	-3.18
2.512	2.490	2.497	1.922	1.898	1.945	1.575	1.590	1.560	4.776	4.763	4.674	4.714	4.667	4.405	4.409	4.324	4.088	4.044	3.933	3.574	-2.54
2.512	2.490	2.497	1.922	1.898	1.945	1.575	1.590	1.560	4.776	4.763	4.674	4.714	4.667	4.405	4.409	4.324	4.088	4.044	3.933	3.574	-1.91
2.457	2.430	2.456	1.889	1.857	1.909	1.541	1.533	1.523	4.815	4.755	4.697	4.656	4.703	4.459	4.456	4.378	4.139	4.112	3.962	3.614	-1.27
2.507	2.509	2.496	1.905	1.913	1.901	1.568	1.547	1.543	7.659	7.798	7.652	7.628	7.676	6.856	6.887	6.992	6.481	6.426	6.405	5.778	-0.64
-10.2	-10.2	-10.2	-10.2	-10.2	-10.2	-10.2	-10.2	-10.2	-12.2	-11.9	-12.0	-11.9	-11.9	-12.2	-12.2	-12.2	-12.3	-12.2	-11.8	-11.9	x_o (cm)
1.031	1.060	1.045	0.781	0.760	0.779	0.628	0.629	0.627	2.586	2.513	2.488	2.480	2.481	2.405	2.344	2.348	2.222	2.181	1.938	1.788	Δp_o (bar)
1.66	1.74	1.85	1.87	1.43	1.82	1.49	1.54	1.76	1.25	1.43	1.45	1.63	1.42	1.27	1.19	1.19	1.34	1.21	1.43	1.47	L (cm)

Case 3 (continued)

$x_o \approx$ -7.6 cm					$x_o \approx$ -10.2 cm														X (cm) =
2.898	2.877	1.960	1.969	1.972	9.003	9.011	9.026	8.997	8.201	8.201	8.187	7.463	7.602	6.707	6.704	6.707	5.658	5.640	5.637	5.634	Plenum
0.803	0.803	0.533	0.542	0.548	2.323	2.347	2.333	2.326	2.151	2.162	2.154	1.989	2.004	1.827	1.818	1.838	1.578	1.564	1.566	1.569	-13.34
0.779	0.780	0.531	0.526	0.526	2.405	2.393	2.397	2.407	2.188	2.192	2.175	2.007	2.025	1.817	1.809	1.820	1.526	1.527	1.521	1.527	-12.70
0.800	0.795	0.525	0.526	0.524	2.322	2.321	2.338	2.340	2.129	2.132	2.128	1.996	1.990	1.844	1.849	1.842	1.566	1.580	1.574	1.567	-12.07
0.811	0.805	0.532	0.528	0.525	2.335	2.359	2.374	2.378	2.178	2.158	2.188	2.061	2.045	1.882	1.906	1.906	1.600	1.597	1.596	1.583	-11.43
0.811	0.805	0.532	0.528	0.525	2.335	2.359	2.374	2.378	2.178	2.158	2.188	2.061	2.045	1.882	1.906	1.906	1.600	1.597	1.596	1.583	-10.80
0.896	0.894	0.589	0.589	0.589	2.758	2.764	2.799	2.694	2.550	2.496	2.471	2.310	2.367	2.020	2.085	2.114	1.833	1.791	1.799	1.810	-10.16
0.904	0.899	0.616	0.615	0.619	3.523	3.595	3.603	2.894	3.417	3.133	3.184	2.982	3.046	2.324	2.698	2.860	2.294	2.158	2.295	2.243	-9.53
0.904	0.899	0.616	0.615	0.619	3.523	3.595	3.603	2.894	3.417	3.133	3.184	2.982	3.046	2.324	2.698	2.860	2.294	2.158	2.295	2.243	-8.89
0.927	0.920	0.639	0.628	0.641	4.017	4.063	4.115	3.408	3.786	3.634	3.604	3.442	3.516	2.912	3.106	3.156	2.582	2.509	2.559	2.530	-8.26
1.057	1.063	0.704	0.695	0.706	4.191	4.230	4.221	3.935	3.909	3.818	3.770	3.555	3.636	3.165	3.232	3.275	2.713	2.701	2.691	2.684	-7.62
1.010	0.991	0.684	0.688	0.703	4.291	4.380	4.379	4.161	3.993	3.950	3.923	3.649	3.762	3.279	3.337	3.378	2.803	2.789	2.793	2.762	-6.99
1.366	1.370	0.909	0.897	0.914	4.566	4.591	4.609	4.437	4.203	4.187	4.145	3.881	3.930	3.471	3.504	3.517	2.949	2.931	2.947	2.924	-6.35
1.415	1.409	0.940	0.932	0.944	4.653	4.667	4.695	4.547	4.283	4.253	4.233	3.945	4.005	3.529	3.549	3.574	3.000	2.983	2.994	2.977	-5.72
1.443	1.434	0.960	0.956	0.967	4.709	4.711	4.739	4.622	4.337	4.309	4.274	3.969	4.025	3.570	3.600	3.608	3.039	3.011	3.027	2.997	-5.08
1.443	1.434	0.960	0.956	0.967	4.709	4.711	4.739	4.622	4.337	4.309	4.274	3.969	4.025	3.570	3.600	3.608	3.039	3.011	3.027	2.997	-4.45
1.467	1.467	0.978	0.979	0.980	4.726	4.737	4.796	4.674	4.357	4.299	4.335	3.925	3.999	3.558	3.577	3.612	3.033	3.062	3.036	3.032	-3.81
1.445	1.442	0.969	0.972	0.970	4.661	4.667	4.670	4.634	4.271	4.271	4.256	3.927	3.979	3.533	3.522	3.551	2.984	2.980	2.984	2.983	-3.18
1.438	1.445	0.980	0.961	0.977	4.598	4.707	4.683	4.559	4.295	4.144	4.225	3.997	4.003	3.415	3.504	3.522	3.014	2.986	2.954	2.968	-2.54
1.438	1.445	0.980	0.961	0.977	4.598	4.707	4.683	4.559	4.295	4.144	4.225	3.997	4.003	3.415	3.504	3.522	3.014	2.986	2.954	2.968	-1.91
1.362	1.405	0.909	0.912	0.914	4.617	4.558	4.566	4.602	4.233	4.102	4.191	3.848	3.836	3.390	3.399	3.448	2.938	2.943	3.032	2.926	-1.27
1.394	1.410	0.864	0.863	0.859	4.591	4.564	4.575	4.572	4.257	4.151	4.165	3.941	3.923	3.499	3.510	3.508	2.995	2.969	2.980	2.970	-0.64
-7.6	-7.6	-7.5	-7.5	-7.5	-10.2	-10.2	-10.2	-9.7	-10.2	-10.2	-10.2	-10.2	-10.2	-9.8	-10.2	-10.2	-10.2	-10.2	-10.2	-10.2	x_o (cm)
0.410	0.399	0.288	0.292	0.271	1.942	1.916	1.923	2.058	1.698	1.768	1.756	1.599	1.592	1.557	1.442	1.408	1.214	1.277	1.227	1.237	Δp_- (bar)
0.91	0.86	0.70	0.88	0.64	1.58	1.43	1.46	1.69	1.31	1.73	1.82	1.48	1.41	1.19	1.48	1.23	1.50	1.78	1.56	1.62	L (cm)

Pressure (bar)

Case 3 (continued)

x_o = -7.6 cm

																				X (cm) =
7.549	7.442	7.423	6.749	6.750	6.731	5.628	5.655	5.652	5.649	5.652	5.628	4.814	4.731	4.731	4.728	3.636	3.636	3.636	2.924	2.918	Plenum
2.022	2.022	2.013	1.803	1.815	1.801	1.566	1.556	1.548	1.566	1.564	1.566	1.340	1.299	1.309	1.300	1.005	1.008	1.012	0.817	0.812	-13.34
2.017	2.004	2.014	1.808	1.813	1.807	1.527	1.523	1.540	1.529	1.532	1.527	1.292	1.292	1.278	1.274	0.981	0.983	0.980	0.789	0.784	-12.70
1.995	2.009	2.035	1.800	1.792	1.796	1.570	1.556	1.564	1.571	1.582	1.561	1.340	1.334	1.322	1.318	1.021	1.019	1.018	0.813	0.805	-12.07
2.056	2.047	2.061	1.846	1.846	1.859	1.572	1.577	1.572	1.571	1.574	1.570	1.342	1.340	1.347	1.325	1.022	1.011	1.017	0.828	0.828	-11.43
2.056	2.047	2.061	1.846	1.846	1.859	1.572	1.577	1.572	1.571	1.574	1.570	1.342	1.340	1.347	1.325	1.022	1.011	1.017	0.828	0.828	-10.80
2.234	2.217	2.196	1.982	1.979	1.971	1.701	1.700	1.702	1.704	1.708	1.706	1.462	1.445	1.438	1.442	1.137	1.137	1.138	0.915	0.901	-10.16
2.324	2.283	2.271	2.050	2.051	2.052	1.716	1.728	1.727	1.726	1.730	1.725	1.477	1.451	1.447	1.451	1.124	1.124	1.127	0.917	0.904	-9.53
2.324	2.283	2.271	2.050	2.051	2.052	1.716	1.728	1.727	1.726	1.730	1.725	1.477	1.451	1.447	1.451	1.124	1.124	1.127	0.917	0.904	-8.89
2.495	2.409	2.310	2.183	2.200	2.209	1.738	1.818	1.814	1.810	1.788	1.796	1.567	1.503	1.500	1.508	1.170	1.166	1.157	0.941	0.906	-8.26
2.667	2.609	2.348	2.294	2.309	2.308	1.835	2.073	2.042	2.044	2.020	2.056	1.806	1.699	1.736	1.713	1.341	1.348	1.329	1.074	0.981	-7.62
2.774	2.648	2.568	2.409	2.438	2.423	2.001	2.018	2.045	2.048	2.008	2.017	1.812	1.667	1.688	1.685	1.281	1.293	1.288	1.045	1.047	-6.99
3.681	3.590	3.139	3.210	3.243	3.273	2.380	2.727	2.737	2.707	2.728	2.722	2.362	2.236	2.282	2.245	1.751	1.735	1.702	1.380	1.237	-6.35
3.766	3.692	3.478	3.330	3.356	3.347	2.650	2.808	2.823	2.812	2.817	2.816	2.423	2.333	2.346	2.324	1.810	1.792	1.775	1.429	1.373	-5.72
3.844	3.742	3.616	3.411	3.423	3.414	2.769	2.855	2.868	2.853	2.855	2.860	2.458	2.377	2.377	2.385	1.837	1.827	1.810	1.459	1.414	-5.08
3.844	3.742	3.616	3.411	3.423	3.414	2.769	2.855	2.868	2.853	2.855	2.860	2.458	2.377	2.377	2.385	1.837	1.827	1.810	1.459	1.414	-4.45
3.837	3.804	3.643	3.480	3.487	3.452	2.818	2.863	2.850	2.923	2.907	2.878	2.487	2.394	2.435	2.408	1.836	1.863	1.855	1.471	1.447	-3.81
3.848	3.794	3.659	3.425	3.447	3.433	2.802	2.856	2.892	2.886	2.856	2.875	2.461	2.404	2.408	2.394	1.850	1.854	1.834	1.468	1.446	-3.18
3.873	3.784	3.666	3.483	3.427	3.478	2.878	2.860	2.922	2.894	2.838	2.875	2.464	2.383	2.449	2.387	1.858	1.854	1.875	1.459	1.448	-2.54
3.873	3.784	3.666	3.483	3.427	3.478	2.878	2.860	2.922	2.894	2.838	2.875	2.464	2.383	2.449	2.387	1.858	1.854	1.875	1.459	1.448	-1.91
3.836	3.831	3.625	3.416	3.389	3.419	2.755	2.759	2.822	2.761	2.908	2.758	2.432	2.359	2.434	2.307	1.829	1.810	1.764	1.398	1.424	-1.27
3.829	3.847	3.648	3.400	3.460	3.446	2.788	2.845	2.910	2.878	2.872	2.834	2.471	2.402	2.404	2.346	1.837	1.837	1.806	1.427	1.439	-0.64
-7.8	-7.7	-6.9	-7.7	-7.8	-7.7	-6.9	-7.5	-7.6	-7.5	-7.6	-7.5	-7.7	-7.5	-7.6	-7.5	-7.5	-7.5	-7.5	-7.5	-7.0	x_o (cm)
1.209	1.196	1.172	1.172	1.199	1.138	0.952	0.846	0.842	0.859	0.884	0.861	0.670	0.755	0.731	0.737	0.570	0.562	0.559	0.437	0.464	Δp_{-} (bar)
0.76	0.77	0.66	0.90	1.04	0.67	0.71	0.59	0.67	0.79	0.76	0.65	0.71	0.86	0.73	0.84	0.55	0.67	0.80	0.82	0.79	L (cm)

Pressure (bar)

Case 3 (continued)

x_o = -5.7 cm												x_o = -7.6 cm								X (cm) =
5.618	5.615	4.799	4.802	4.799	4.718	4.706	3.688	3.636	3.042	3.042	3.042	9.090	9.028	9.099	9.057	9.004	8.258	8.249	8.177	8.171	Plenum
1.570	1.564	1.332	1.334	1.326	1.306	1.288	1.021	1.004	0.845	0.848	0.850	2.327	2.343	2.331	2.304	2.350	2.151	2.132	2.156	2.149	-13.34
1.522	1.523	1.297	1.293	1.291	1.269	1.273	0.989	0.979	0.820	0.825	0.820	2.414	2.412	2.425	2.407	2.389	2.181	2.206	2.187	2.168	-12.70
1.570	1.561	1.333	1.344	1.334	1.324	1.322	1.030	1.022	0.842	0.841	0.840	2.347	2.316	2.331	2.318	2.333	2.130	2.134	2.162	2.127	-12.07
1.593	1.563	1.329	1.336	1.319	1.334	1.326	1.035	1.031	0.850	0.859	0.848	2.361	2.344	2.354	2.329	2.342	2.161	2.157	2.178	2.161	-11.43
1.593	1.563	1.329	1.336	1.319	1.334	1.326	1.035	1.031	0.850	0.859	0.848	2.361	2.344	2.354	2.329	2.342	2.161	2.157	2.178	2.161	-10.80
1.704	1.715	1.458	1.467	1.467	1.450	1.450	1.153	1.134	0.952	0.950	0.947	2.712	2.683	2.709	2.705	2.669	2.446	2.451	2.416	2.417	-10.16
1.710	1.712	1.459	1.463	1.461	1.438	1.439	1.131	1.121	0.944	0.942	0.941	2.763	2.768	2.724	2.736	2.757	2.552	2.532	2.505	2.500	-9.53
1.710	1.712	1.459	1.463	1.461	1.438	1.439	1.131	1.121	0.944	0.942	0.941	2.763	2.768	2.724	2.736	2.757	2.552	2.532	2.505	2.500	-8.89
1.721	1.721	1.467	1.463	1.467	1.439	1.434	1.124	1.118	0.927	0.930	0.927	3.209	3.076	2.975	2.968	2.924	2.695	2.590	2.670	2.655	-8.26
1.688	1.692	1.449	1.458	1.461	1.437	1.443	1.142	1.169	0.952	0.944	0.945	3.251	3.165	3.050	3.067	3.004	2.762	2.562	2.740	2.740	-7.62
1.834	1.847	1.583	1.587	1.590	1.563	1.567	1.263	1.298	1.059	1.051	1.049	3.965	3.825	3.216	3.250	3.180	2.929	2.813	2.888	2.883	-6.99
1.782	1.776	1.506	1.501	1.512	1.480	1.484	1.129	1.234	0.943	0.940	0.940	4.382	4.384	4.307	4.272	4.265	3.926	3.466	3.842	3.903	-6.35
1.848	1.847	1.594	1.603	1.630	1.551	1.586	1.268	1.613	1.069	1.070	1.051	4.501	4.476	4.419	4.392	4.390	4.042	3.868	3.996	4.001	-5.72
2.333	2.337	2.017	2.035	2.075	1.904	2.017	1.589	1.716	1.290	1.315	1.271	4.582	4.573	4.483	4.485	4.460	4.107	3.987	4.075	4.089	-5.08
2.333	2.337	2.017	2.035	2.075	1.904	2.017	1.589	1.716	1.290	1.315	1.271	4.582	4.573	4.483	4.485	4.460	4.107	3.987	4.075	4.089	-4.45
2.615	2.578	2.233	2.255	2.266	2.124	2.176	1.709	1.750	1.391	1.403	1.395	4.633	4.603	4.560	4.569	4.567	4.238	4.064	4.166	4.139	-3.81
2.664	2.647	2.275	2.278	2.295	2.199	2.228	1.745	1.754	1.428	1.427	1.412	4.611	4.590	4.528	4.552	4.508	4.194	4.073	4.120	4.112	-3.18
2.664	2.654	2.244	2.300	2.321	2.238	2.212	1.762	1.765	1.420	1.421	1.407	4.632	4.571	4.579	4.576	4.666	4.261	4.028	4.227	4.121	-2.54
2.664	2.654	2.244	2.300	2.321	2.238	2.212	1.762	1.765	1.420	1.421	1.407	4.632	4.571	4.579	4.576	4.666	4.261	4.028	4.227	4.121	-1.91
2.617	2.618	2.200	2.328	2.263	2.250	2.152	1.753	1.702	1.412	1.420	1.368	4.456	4.434	4.496	4.436	4.621	4.276	3.959	4.020	4.037	-1.27
2.606	2.556	2.244	2.259	2.285	2.204	2.183	1.707	1.713	1.380	1.378	1.354	4.528	4.516	4.484	4.471	4.470	4.262	4.049	4.169	4.046	-0.64
-5.8	-5.8	-5.8	-5.8	-5.8	-5.8	-5.8	-5.9	-6.4	-5.9	-5.9	-5.9	-8.2	-8.3	-7.7	-7.7	-7.7	-7.7	-6.9	-7.7	-7.8	x_o (cm)
0.934	0.906	0.806	0.811	0.810	0.775	0.777	0.636	0.558	0.504	0.501	0.498	1.393	1.535	1.515	1.513	1.549	1.474	1.326	1.436	1.392	Δp_- (bar)
0.70	0.67	0.66	0.62	0.58	0.82	0.61	0.59	0.51	0.69	0.57	0.67	0.98	0.97	0.83	0.85	0.82	0.90	0.73	0.92	0.81	L (cm)

Pressure (bar)

Case 3 (continued)

X (cm) =	Pressure (bar)																				
x_o = -5.7 cm																					
9.075	9 084	8 997	9.006	8 988	8 967	7.347	8 178	8 166	7.689	7.399	7.393	7 387	6 728	6 70:	6 698	6 692	6 695	5 618	Plenum		
2.309	2.330	2 332	2 353	2.345	2 326	1 884	2 161	2 149	2 028	2 050	2 017	2 025	1 807	1 849	1 859	1 845	1 849	1 569	-13 34		
2 421	2 405	2 393	2 405	2 387	2 387	1.934	2 177	2 174	2 042	1 996	2 001	1 995	1 809	1 800	1 790	1 803	1 814	1 522	-12 70		
2 324	2 332	2 327	2 331	2 337	2 325	1 884	2 132	2 132	2 006	2 031	2 025	2 033	1 812	1 867	1 856	1 878	1 870	1 559	-12 07		
2 326	2 358	2 355	2 344	2 371	2 343	1.899	2 160	2 178	2 077	2 061	2 071	2 063	1 860	1 897	1 893	1 872	1 884	1 585	-11 43		
2.326	2.358	2 355	2 344	2 371	2 343	1 899	2 160	2 178	2 077	2 061	2 071	2 063	1 860	1 897	1 893	1 872	1 884	1 585	-10 80		
2 714	2.694	2 662	2 678	2.656	2 654	2 148	2 419	2 406	2 257	2 213	2 189	2 211	1 976	1 971	1 989	1 982	1 981	1 702	-10 16		
2 723	2.715	2 741	2 755	2.763	2 751	2 225	2 488	2 473	2 342	2 273	2 258	2 263	2 034	2 042	2 047	2 048	2 049	1 713	-9 53		
2 723	2.715	2 741	2 755	2 763	2 751	2 225	2 488	2 473	2 342	2 273	2 258	2 263	2 034	2 042	2 047	2 048	2 049	1 713	-8 89		
2 766	2.770	2 790	2 803	2.788	2 772	2 239	2 522	2 515	2 349	2 265	2 262	2 269	2 084	2 050	2 057	2 054	2 055	1 705	-8 26		
2 714	2.716	2 653	2 672	2.653	2 649	2 120	2 401	2 382	2 276	2 162	2 153	2 175	1 936	1 985	1.994	1 987	1 987	1 695	-7 62		
2 768	2.777	2 821	2 837	2.827	2 810	2 265	2 598	2 589	2 422	2 433	2 393	2 403	2 122	2 160	2 174	2 159	2 154	1 832	-6 99		
2 780	2.802	2 751	2 764	2.785	2 746	2 226	2 486	2 502	2 324	2 381	2 366	2 361	2 100	2 109	2 118	2 110	2 108	1 799	-6 35		
2 854	2.771	2 854	2 843	2.754	2 744	2 224	2 575	2 560	2 434	2 469	2 459	2 471	2 105	2 210	2 239	2 197	2 229	1 813	-5 72		
3 826	3 640	3 773	3 822	3 488	3 484	2 871	3 449	3 315	3 113	3 140	3 183	3 090	2 676	2 793	2 896	2 770	2 794	2 350	-5 08		
3 826	3 640	3 773	3 822	3 488	3 484	2 871	3 449	3 315	3 113	3 140	3 183	3 090	2 676	2 793	2 896	2 770	2 794	2 350	-4 45		
4 120	4.146	4.119	4 230	3 956	3 959	3 284	3 727	3 748	3 477	3 368	3 428	3 395	3 054	3 087	3 121	3 055	3 068	2 595	-3 81		
4 278	4 233	4 239	4 251	4 162	4 153	3 362	3 802	3 819	3 609	3 491	3 500	3 498	3 178	3 192	3 176	3 150	3 178	2 662	-3 18		
4 296	4 327	4 185	4 284	4 232	4 166	3 371	3 903	3 864	3 641	3 541	3 573	3 472	3 202	3 228	3 211	3 220	3 191	2 744	-2 54		
4 296	4 327	4 185	4 284	4 232	4 166	3 371	3 903	3 864	3 641	3 541	3 573	3 472	3 202	3 228	3 211	3 220	3 191	2 744	-1 91		
4 219	4 296	4 029	4 042	4 176	4 036	3 241	3 788	3 708	3 616	3 415	3 560	3 414	3 181	3 210	3 255	3 093	3 130	2 631	-1 27		
4 185	4 123	4 052	4 141	4 130	3 935	3 266	3 731	3 631	3 499	3 462	3 471	3 368	3 133	3 173	3 132	3 097	3 147	2 639	-0 64		
-5 7	-5.4	-5 8	-5.7	-5 5	-5 5	-5.4	-5 8	-5.7	-5 8	-5 8	-5 8	-5 8	-5.4	-5 8	-5 8	-5 5	-5 8	-5.7	x_o (cm)		
1 535	1.483	1.547	1.552	1.457	1.432	1.138	1.344	1.400	1 350	1.136	1 167	1 176	1 104	1 144	1 074	0 981	1 133	0 902	Δp_o (bar)		
0 59	0.37	0.61	0.54	0.57	0.56	0 36	0 53	0 70	0 75	0 62	0 56	0 69	0 48	0 73	0 53	0 50	0 73	0 66	L (cm)		

* Each table entry represents the average of eight measurements taken for very nearly matched shock locations (~±1 mm) as per description in Section 4.4.

VITA

Robert K. Masse

6/91 **Bachelor of Science**
University of California, Los Angeles
Department of Mechanical, Aerospace, and Nuclear Engineering

6/93 **Master of Science**
University of Washington
Department of Aeronautics and Astronautics

3/00 **Doctor of Philosophy**
University of Washington
Department of Aeronautics and Astronautics